Using Two-Dimensional Infrared Spectroscopy as a Tool for Studying Amyloid and Membrane Proteins

by Emily Blanco Dunkelberger

A dissertation submitted in partial fulfillment
of the requirements for the degree of

Doctor of Philosophy
(Chemistry)

at the
University of Wisconsin-Madison
2013

Date of final oral examination: May 17, 2013

The dissertation is approved by the following members of the Final Oral Committee:

Martin T. Zanni, Professor, Chemistry
Edwin L. Sibert, Professor, Chemistry
Silvia Cavagnero, Professor, Chemistry
J.R. Schmidt, Associate Professor, Chemistry
Etienne Garand, Assistant Professor, Chemistry

Using Two-Dimensional Infrared Spectroscopy as a Tool for Studying Amyloid and Membrane Proteins

Emily Blanco Dunkelberger

Under the supervision of Professor Martin T. Zanni

At the University of Wisconsin-Madison

Abstract

Two-dimensional infrared (2D IR) spectroscopy has become a useful tool for studying the structure and dynamics of difficult to study biological systems, such as amyloid and membrane proteins. The goals of my research involved measuring the structure of the causative agent in Type 2 diabetes, human amylin, and measuring the structure of the membrane-bound anti-microbial peptide, ovispirin. Human amylin misfolds into β-sheets, while ovispirin is an α-helix on bilayers. In both cases, we exploited vibrational couplings between synthetically incorporated isotope labeled amino acids. Doing so, we achieved site-specific resolution, and when combined with our ability to measure spectra on-the-fly, we were able to monitor previously difficult to observe structural changes in both peptides.

Table of Contents ii

List of Figures

Chapter 5

Chapter 6

Chapter 7

Appendix 1

Appendix 2

List of Tables

Acknowledgements

My journey as a scientist started in high school. Growing up, I loved playing with a chemistry set that my parents bought me for Christmas. It turns out that chromatography of Crayola markers is fascinating for a 3rd grader. It wasn't until high school, however, that I found myself really enjoying science and possibly gravitating towards going to college as a science major. Dissecting cats in anatomy and lighting things on fire in chemistry really excited me, and I went to college wanting to be a forensic chemist. Trendy, I know (but I still haven't watched an entire episode of CSI!).

When I arrived at Michigan State University, I took Honor's Freshman Chemistry. We learned about the Schrodinger Equation, the particle in a box problem, and Group Theory. It was all so interesting (and hard), but I had so much fun learning physical chemistry. Sometime towards the end of my first semester of college, the author of my chemistry textbook visited the department for an evening seminar. My fellow chemistry enthusiasts and I decided to go to the seminar, expecting not to understand a word, but wanting to get our textbooks signed by the speaker. We chickened out of asking for his autograph, and we didn't understand most of the material. But, I was incredibly interested in everything the speaker had to say. That night, I decided I wasn't going to become a forensic chemist, despite the physical chemistry tools they use; instead, I decided I wanted to go to graduate school to study physical chemistry. The rest is history.

Succeeding in graduate school and earning a PhD takes a village. First, I want to thank Marty. When I was visiting graduate schools and trying to decide what kind of

research I wanted to do, I got so excited about using 2D IR spectroscopy to study proteins. I couldn't imagine joining another group. I am grateful to you, Marty, for your guidance, your patience, and your willingness to take me as a first year graduate student. I also want to thank you for being a role model for being a great scientist, spouse, parent, and mentor. Your enthusiasm for the research we do is contagious, and I have always appreciated that. I also want to thank the entire Zanni group, both past and present. When I joined the group in 2007, Sudipta Mukherjee and I were group members 7 and 8. We were a small group who would go out to breakfast together before Monday morning group meetings. The group has changed so much since I've been in Madison, and now, we are a large group of 16 people who have the most fun cooking together in Marty's kitchen. Ann Woys was my first mentor in the group, and she was patient with me as I learned how to tweak an OPA and was so good at keeping a conversation going in the cold dark laser lab. I thank her for teaching me to be fearless and adventurous both in and out of lab. My next mentors were Dave Strasfeld and Chris Middleton, not to be confused with the Backstreet Boys. Dave and Chris were so encouraging while I was part of the team tasked with building the Wyvern laser table. They always kept the atmosphere light in lab, even when the oscillator wasn't mode-locking or when the Wyvern wasn't lasing. Chris in particular was a great resource in the lab, and I feel fortunate to have spent time with him building a laser table and troubleshooting laser problems. He was a great source of information and became a good friend. Other former group members, Prabuddha Mukherjee, Sang-Hee Shim, Yun Ling, and Wei Xiong were

such a pleasure to work with and learn from, and I feel fortunate that I got to spend time with them.

For the past several years, I have worked most closely with Lauren Buchanan, and need to thank her for many of the finest, if not funniest times in lab. Together, I think we learned the hard way about temperature gradients in laser boxes, plumbing, and air conditioners, all things I never imagined I'd be exposed to during graduate school. We also learned how (not) to caramelize amino acids, and how (not) to synthesize peptides. There have been many great laughs shared with her, and I thank her for those moments. I also want to thank Sean Moran. Sean, you have become a good friend over the past couple years. I will sincerely miss talking to you about science just as much as I'll miss cutting a rug with you to the Cash Box Kings.

Other group members have had an influence over my graduate school career include Maxsim Grechko, Jennifer Laaser, and Huong Tran. Maxsim, you invented a new way to measure transition dipole strengths. Thank you for your patience and willingness to help me work through your new technique. Jenny, thanks for being a friend and for always being willing to talk about science questions I have, even if they don't have anything to do what you think about. Huong, it has been a pleasure working with you the past few months. You will continue to excel with these projects, and I'll miss you and your Texas cooking.

To Sudipta, we joined the group together on November 1, 2007, and we are defending within days of each other. Good luck, dude. You are fun to work with. I'll miss your stressed out hair-dos. Ha Dong, you were a nice officemate and I wish you

luck with whatever comes next for you. David Skoff, it has been a total pleasure talking college football and basketball with you, even if we don't see eye to eye about, well, anything. Randy Mehlenbacher, it has been a delight knowing you for the past three years, and I think you are a really good guy; you are so helpful, especially when it comes to instant messaging ThorLabs tech support, or steering me down the river in a canoe. Tianqi Zhang, you have proven to be such a hard worker, and you are so kind. Tracey Oudenhoven, you are such a great addition to the group and we are lucky to have you. Tom McDonough, thanks for taking the plunge as a zombie this year. Jia-Jung Ho, good luck in graduate school, I know you'll do well. Arnaldo Serrano, you are the newest member of the Zanni group. Keep the rest of them in line. Maybe someday I'll learn who Boba Fett is.

There are several more people both inside and outside the building that kept me on this journey. Being an experimentalist means I am a plumber and electrician, studying proteins means I should probably learn some mass spectrometry, and being a student at UW-Madison means that the staff who keep the department running are kind and personable. As such, I want to thank Rick Pfeifer, and Kendall Schneider for teaching me bits and pieces of the fun art of machining, Dr. Martha Vestling for teaching me about mass spectrometry and for taking enough of an interest in my project to send me interesting papers, Teresa Knudson for being as close to a mom as possible in the department, and April Leslie for being a breath of fresh air in physical chemistry and for being so proactive with everything that happens in the department. I also want to thank the Crim group for being a second group to me. Over the years, I've gotten to know so

many of you so well, and I have truly enjoyed eating lunch and doing crossword puzzles with you. Fleming, I thank you for your encouragement, guidance, and support both in science and otherwise.

Science and creating new knowledge requires a team. Outside of the Zanni group, I had a couple collaborators who made large parts of this thesis possible. The Dan Raleigh group at SUNY-Stonybrook and graduate students Peter Marek, Ping Cao, Cynthia Tu, and Hui Wang each helped me either by synthesizing and purifying peptides that I used, or by teaching me how synthesize and purify peptides myself. They are experts, and I learned a lot from them. Also, the James Nowick group and graduate students Jing Zheng and Pin-Nan Cheng at the University of California-Irvine synthesized a new class of amyloid inhibitors. They were kind enough to share their inhibitors with us, and we have learned a lot about hIAPP in the process. I also want to thank Ned Sibert and Silvia Cavagnero for being on my TBO committee, JR Schmidt for being on my RP committee, and Etienne Garand for being on my Thesis committee. You have all asked tough questions that made me think deeper about my research.

The memories I've made in Madison are so special, partly because Madison such a special place to live, but also because of the people I've met along the way. To Adam Dunkelberger, Craig Tainter, Kacie Louis, Rob Sturm, Brie Sturm, Danielle Stacy, Lauren Michael, and Eugenia Turov, it was a wild first year of graduate school, and I thank you for being such good classmates, great friends, and fun people. I miss you already. To the Mighty Hucks, thank you for accepting me onto your Ultimate team and teaching me how to throw a flick. Each of you made my last couple summers and falls in

Madison so fun, and I feel fortunate that I got to play on a team where I consider each teammate a good friend. To the Thursday lunch club, including Joe Yeager, Ryan Kieda, and Brett Marsh, thanks for the weekly break, regardless of the service.

Besides Ultimate, I also took up two other hobbies during graduate school, one old and one new. My old hobby, tap dancing, was made extra special by the people in my class. To my teacher, Donna Peckett, thank you for teaching me how to be a better performer, and for providing me an outlet once a week where I could sweat and forget about graduate school. My brain, body, and soul needed it. Also, thank you Simone, Lisa, Kim, Courtney, and Dorrie for giving me the best pep talks in preparation for my interview talk in DC. You are fabulous, encouraging, and I will miss you. My new hobby, distance running, was much more solitary, but I thank Danielle, Kacie, Brie, Katie Freeman, Cornelia Heid, Justin Wiens, Ken Barns, Shannon McNierney, Huong and Eugenia for being running buddies and/or cheerleaders. It has changed my life for the better.

Last but not least, I want to thank the people who have been my cheerleaders since the beginning. Growing up, my parents always encouraged me to pursue my interests and to never stop learning. I don't think they necessarily meant that I should go to graduate school and not drop the "student" part of my job title until the age of 27. Nevertheless, my parents taught me the value of education, and I am always grateful for that. Thank you for constant support with everything I do and every choice I make. Think of this book as partly yours; it is a culmination of my hard work as a student, and your hard work as parents. I am lucky and proud to have you as my mom and dad. I love

you. Also, thank you to my brother and sister, David and Suzi. You two are some of my favorite people in this word and I'm so proud of everything you've accomplished. You two make me want to be a better person. Finally, to Adam: little did I know that I would meet my future husband during the UW recruiting weekend, but I am so glad I did. You have been my rock for the past six years, first as a friend and then as a husband. Your encouragement and straight talk kept me (at least somewhat) rational during the hard times, your sense of humor and singing kept me laughing when I didn't think I could, and your love and support helped me accomplish so many things I never thought I could do. I could not be more proud of you and what you've accomplished and I cannot wait for our future together as the Drs. Dunkelberger. You are *my* favorite scientist. I love you.

CHAPTER 1

Introduction

1.1 Introduction

One of the great questions in biophysical chemistry is, 'how do the structure and dynamics of a protein affect its function?'. Proteins can be thought of as long linear chains of amino acids. These chains fold, and sometimes misfold, into myriad biologically relevant structures. Proteins in cell membranes can act as channels to allow ions to pass into and out of cells.[1-3] Proteins in blood transport oxygen throughout the body.[4,5] Sometimes, when proteins misfold, they cause disease.[6-8] Understanding the structure and dynamics of how proteins fold (and as equally important, misfold) can help pave the way towards rationally designed drugs. A better understanding of the cause of

disease may someday lead to elimination of large-scale drug screening and promotion of more logically designed therapeutics.

1.2 Amyloid peptides

Amyloid peptides are a class of peptides that all share the same structural motif, cross-β-sheet, and are known to be the causative agents in over 20 human diseases including Alzheimer's disease, Parkinson's disease, Huntington's disease, cataracts, and Type II diabetes.[6] In vivo, amyloids are known to misfold into long β-sheet fibers that can extend in length to the nanometer or micron scale.[6,10] When amyloid fibers form, plaques build up in the organs in which they lie (the brain for the Alzheimer's peptide, the eye for the cataract peptide, and the pancreas for the Type II diabetes peptide).[6,11,12] The amyloid peptide I have spent most of my graduate career working on is human islet amyloid polypeptide, also commonly referred to as hIAPP or human amylin. Human amylin is a 37-residue polypeptide hormone co-secreted with insulin in the pancreas.[13,14] Fibers are formed when two columns of hIAPP monomers each form turns near the middle of the peptide chain, as shown in Figure 1.1. The monomers stack through hydrogen bonds to form four parallel β-sheets that run parallel to the fiber axis.

There is still much debate over whether or not the final fiber structure is the most toxic species, or if it is the intermediate structures along the folding pathway that are the most toxic.[6,15-17] Thus, it is critical to determine the folding mechanism of amyloid fibers and to decipher the structures of the intermediate species that may cause the most harm in the body. The problem lies in the fact that hIAPP is one of the most amyloidogenic peptides and folds very quickly, making early and intermediate-stage structures difficult

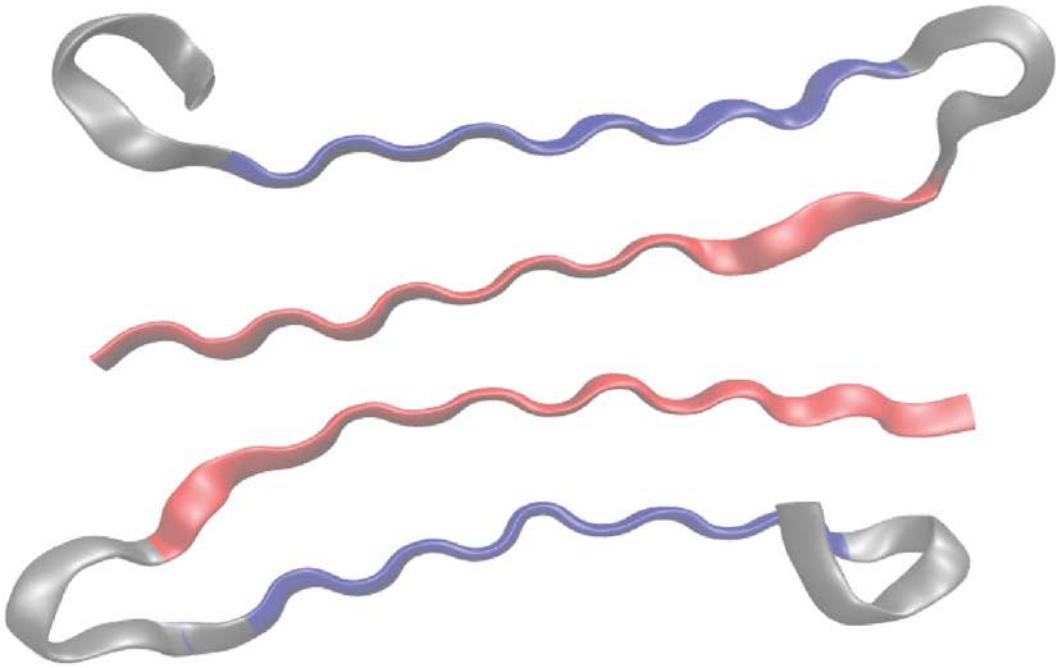

Figure 1.1 Cross β-sheet structure of hIAPP fibers derived from the solid-state NMR structure.[9] The perspective is looking down the fiber axis. Two U-shaped monomers fold nearly in half. A total of four β-sheets form: the two blue N-terminal external sheets and the two red C-terminal internal sheets. The grey region on the N-terminus is the result of disorder caused by the disulfide bond between Cys-2 and Cys-7. The grey area connecting the N and C-termini is due to the disordered turn region.

to characterize. The ideal technique for studying such molecules would have the ability to collect measurements on-the-fly so that early, intermediate, and late structures in the folding pathway can be distinguished, while also getting high structure resolution so that if different parts of the peptide are behaving differently, their individual folding pathways can be deciphered.

1.3 Membrane peptides

Membrane peptides are another class of peptides that are involved in many biological processes and diseases.[18,19] However, their structure can be very difficult to study due to the difficulty in studying membranes themselves. Lipid bilayers are composed of two layers of lipid molecules; each lipid molecule is composed of a polar head group and a non-polar hydrocarbon tail. Bilayers assemble such that the head groups form the outer edges of the bilayer and the tails form the inner layers. This allows the hydrophilic head groups to protect the hydrophobic tails from surrounding water molecules. One way to study the structure and dynamics of peptides and proteins that bind to membranes is to study their hydration levels. Figure 1.2 shows an example of three different types of membrane peptides: a surface-bound peptide, a transmembrane peptide, and a transmembrane channel. In the first example, the surface bound peptide has amino acids that lie within the polar head groups and sometimes may lie in the hydrophobic tails. Other residues are completely exposed to water. The water exposure at each residue in the peptide oscillates with environment, and for an α-helix, oscillates every 3.6 residues. The second example, a transmembrane peptide, has some residues near the water-lipid interface that are in a hydrophilic environment and has some residues

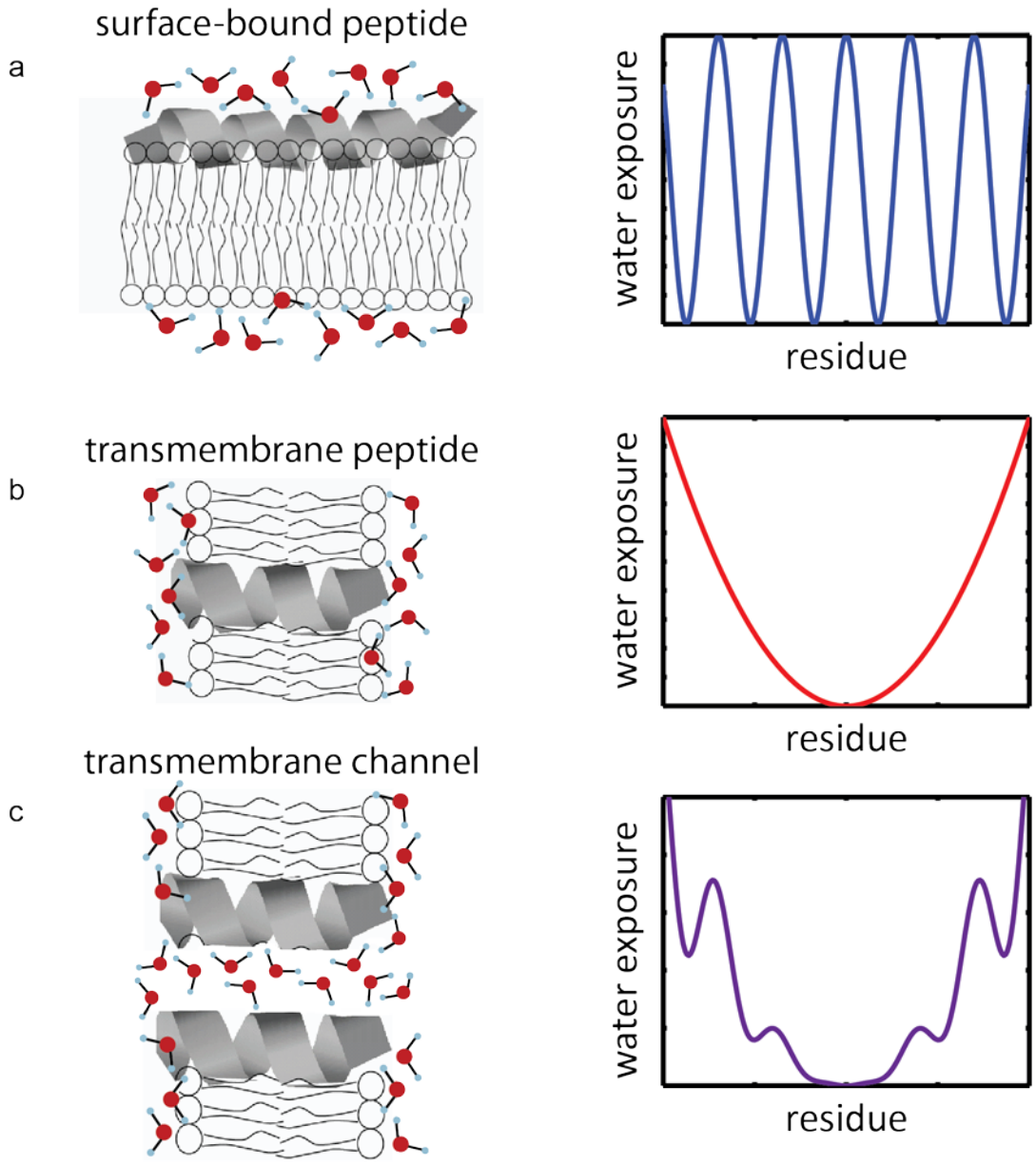

Figure 1.2 Hydration of membrane peptides. (a) For a surface-bound α-helix, some amino acids are located in the hydrophobic membrane while others lie outside the membrane in a more hydrophilic environment. If the peptide is a perfect helix and lies perfectly flat on the membrane, the environment and water exposure at each residue will oscillate with the same frequency as that of a helix: every 3.6 residues. (b) For a transmembrane peptide, the amino acids on the N and C termini will be more exposed to water than the residues that span the hydrophobic membrane core. The water exposure will be dramatically different than that of a surface-bound peptide. (c) For a transmembrane channel, the residues in contact with water will be similar to that of the transmembrane peptide in that the N and C-termini are more exposed to water than the residues in the bilayer. However, water exposure of the residues that line the channel will be similar to that of a surface-bound peptide in that the residues that face the channel are more exposed to water than those that face away from the channel. Measuring site-specific water exposure in a peptide gives secondary and tertiary structural information.

deep in the membrane that are in a hydrophobic environment. The water exposure at each residue will be different than that of a surface-bound peptide. Rather than oscillations, the residues at the N and C-termini are highly exposed to water, and the residues in the middle of the bilayer are less exposed to water. The third example, a transmembrane channel, is a hybrid of the previous two examples. Amino acids at the N and C-termini are more exposed to water than those in the center of the bilayer, but residues that line the channel will be more exposed to water than those facing away from the channel.

Using hydration levels of the peptide to determine its structure has been shown to be an effective way to get secondary and tertiary structural information.[20-26] However, many of the technical difficulties in these measurements lie in the fact that lipids are inherently disordered molecules that are fantastic at scattering light. Ideally, a technique would be used that could measure the hydration levels in membrane peptides without sacrificing residue-specific structural resolution.

1.4 Infrared spectroscopy of peptides

Proteins are dynamic systems. Some fluctuations occur on the femtosecond to picosecond timescale, while others occur on the microsecond to millisecond timescale, or even longer, on the minute to hour timescale.[27] For instance, molecular vibrations and solution phase collisions occur in picoseconds, proton transfer and sidechain rotation in proteins happens in nanoseconds, and on the order of milliseconds, large scale structural motions occur, which can persist to seconds, minutes, and hours.[27-29] In order to gain insight into the molecular structure of a protein as it folds, several techniques have been

developed that can spatially and temporally probe protein structure and folding dynamics. X-ray crystallography provides the best structural resolution of any technique; however, in order to use X-ray crystallography, the protein must crystallize.[30-32] While this may not be problematic for globular proteins, amyloid proteins and membrane proteins are very difficult to crystallize. In addition, crystallizing a protein typically removes the protein from its natural, dynamic state, possibly removing physiological relevance from the measurement. Solution and solid-state nuclear magnetic resonance (NMR) spectroscopy are also common techniques for studying protein structure.[1,10,33-36] However, limitations arise when trying to study membrane proteins and amyloids. Solution NMR requires the use of micelles, not membranes, while solid-state NMR can measure membrane proteins and amyloid fibers, at the cost of lower structural resolution. Although protein dynamics can be observed using NMR, the timescale is on the order of milliseconds, not femto or picoseconds. Transmission electron microscopy (TEM) and fluorescence measurements are popular techniques for studying amyloid proteins because with TEM you can get images of entire fibers[6,10,37] and using thioflavin-T as a fluorescent dye you can monitor the kinetics of aggregation; as amyloid β-sheets form, ThT thioflavin-T fluorescence increases.[38-42] However, these techniques do not give high-level structural resolution to the process of aggregation; ThT fluorescence measures real-time kinetics, but only of the bulk peptide, and TEM images measure highly resolved structure, but cannot measure structure of kinetically changing species. Circular dichroism and linear infrared spectroscopies are also used to identify protein secondary structure, but again, the spectra have very low structural resolution that only report on the

bulk properties of the protein.[37,43-46] In order to glean meaningful information from these techniques, the spectra must be deconvoluted to tease apart the congestion from overlapping peaks. In all, several techniques exist that are used to study protein structure and dynamics. Solving protein structure, especially for dynamic systems, is a huge challenge, and each of these techniques has its place.

That being said, infrared spectroscopy, most specifically two-dimensional infrared (2D IR) spectroscopy, has emerged in the past fifteen years as a way to measure protein structure that provides more spatial and temporal resolution than traditional linear infrared spectroscopy, while still being able to measure physiologically relevant samples.[24,25,47-49] Spectroscopy is the study of the interaction of light with matter, and in IR spectroscopies, mid-IR wavelengths of light are used to interrogate the sample.

In protein samples, the amide I mode is the vibrational mode that is most often probed.[9] The amide I mode, composed mostly of the carbonyl stretch on every amino acid, is quite sensitive to protein secondary structure (Figure 1.3a).[9] For instance, the amide I mode of unfolded, random coil proteins absorbs near 1645 cm^{-1} (Figure 1.3b), membrane-bound α-helical proteins absorb near 1655 cm^{-1} (Figure 1.3c), and amyloid fibers that have folded into parallel β-sheets absorb near 1620 cm^{-1} (Figure 1.3d). Using 2D IR spectroscopy, the spectra obtained are now separated into two dimensions and provide higher structural resolution. When proteins fold into ordered secondary structure, such as α-helices or β-sheets, the amide I mode vibrationally couples, most strongly with adjacent residues in an α-helix and with in-register amino acids in neighboring strands in β-sheets, the latter example shown Figure 1.4a.[50-53] The

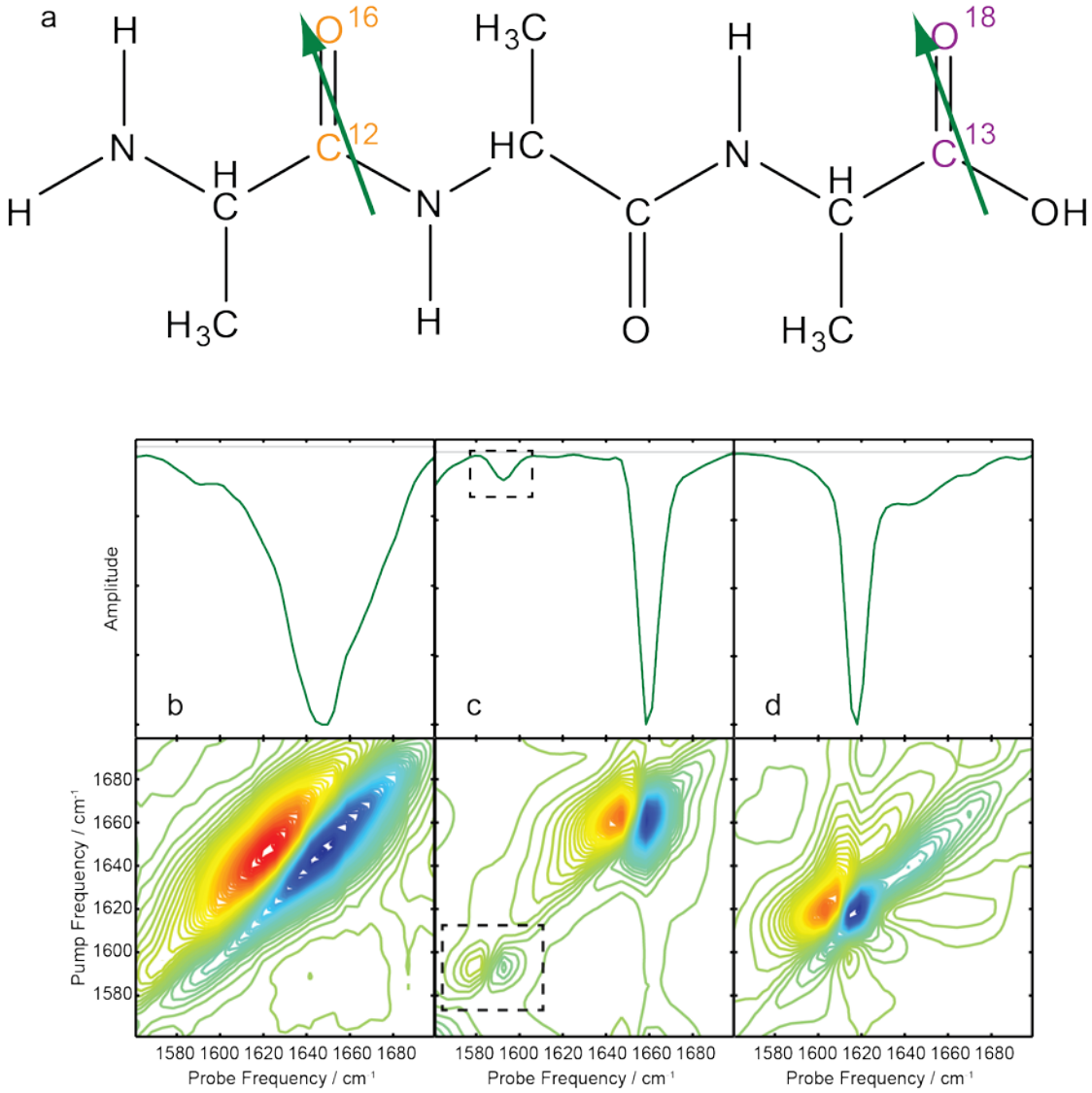

Figure 1.3 (a) Model peptide. Two carbonyl groups are labeled in orange and purple to highlight their differences. The orange carbonyl group contains natural abundance $^{12}C^{16}O$, which the purple carbonyl group is $^{13}C^{18}O$ isotope labeled. The green arrows represent the amide I transition dipole moment, which is predominantly composed of C=O stretch, but also contains some CN stretch and NH bend.[9] (b) 2D IR spectrum and diagonal slice of a random coil peptide that has a maximum absorbance near 1645 cm^{-1}. (c) 2D IR spectrum and diagonal slice of a surface-bound α-helix peptide. The unlabeled amide I mode absorbs near 1655 cm^{-1}. The dashed boxes enclose the isotope labeled amide I mode. The frequency of the label is ~1595 cm^{-1}, red shifted from the unlabeled amide I mode. (d) 2D IR spectrum and diagonal slice of an amyloid fiber. The amide I mode absorbs near 1620 cm^{-1}.

vibrational modes then delocalize over several residues. Strong coupling gives the unique infrared frequencies for each secondary structure; this is part of the reason that the carbonyl group in a protein can absorb at a large range of frequencies, despite no change in composition.

A 2D IR spectrum can be thought of as a linear FTIR spectrum spread over two dimensions. The peaks in a linear IR spectrum are analogous to the peaks along the diagonal of a 2D IR spectrum. However, 2D IR spectroscopy is dependent on the transition dipole strength, $|\mu|^4$, whereas linear FTIR spectroscopy is dependent on $|\mu|^2$.[51] This allows for the measurement of smaller signals, which has in turn lead to the development of small, non-invasive vibrational probes that can be attached to or synthesized into proteins, providing site-specific resolution as in NMR spectroscopy.[38,54-57] In 2D IR spectroscopy, three ultrashort laser pulses interact with the sample. When the sample absorbs energy from the mid-IR light, it becomes vibrationally excited. By watching the molecular vibrations evolve with time, one can learn about the structure of the sample.

1.5 Isotope labeling amino acids

In order to use infrared spectroscopy to get information about individual amino acids, a straightforward isotope labeling technique can be used. One vibrational probe that has become popular is attaching a nitrile group to phenylalanine.[56,57] This technique is quite useful for studying amino acid sidechains, and nitrile groups absorb in an otherwise blank part of a peptide absorption spectrum, making them easier to detect. However, we are interested in the motions of peptide backbones, not sidechains, and thus

isotope labeling the carbonyl groups in amino acids, rather than adding a nitrile group, has become our and others method of getting site-specific structural backbone information.[25,48,54,55,58] Vibrational frequencies are dependent on many factors, such as solvent effects, hydrogen bonding, and coupling. However, the characteristic vibrational frequency is also dependent on the mass of the group that is vibrating. In the case of the amide I mode, by isotope labeling the carbonyl group with $^{13}C^{18}O$, the frequency of the amide I shifts to lower frequency by ~66 cm^{-1} (Figure 1.3a).[53] This is a large enough shift to spectroscopically separate the peak from the single isotope labeled amino acid from the much larger peak from the rest of the natural abundance, $^{12}C^{16}O$, amino acids, as shown in the small box in Figure 1.3c.

1.6 Coupled vibrational modes and kinetics of amyloids

For a β-sheet protein with a single isotope labeled amino acid, the frequency of the isotope labeled residue appears at ~1595 cm^{-1}.[48,59] In the special situation of amyloid fibers, the amyloidogenic protein into parallel β-sheets, and the isotope labeled amino acid aligns in register (Figure 1.4a). The coupling between the strands is strong, and the vibrational modes become delocalized over several β-strands. The result is that the frequency of the isotope label residue moves to lower frequency, this time by twice the coupling constant, β.[50,51,59] For a typical amyloid parallel β-sheet, the coupling constant between two in-register residues in neighboring strands is -9 to -11 cm^{-1}, and thus for a well-coupled amino acid, the frequency of the isotope label peak could be as low as ~1575 cm^{-1}.[59] The coupling constant is not uniform for every residue in a β-sheet. Residues near disordered turns or at the ends of the protein may be more disordered and

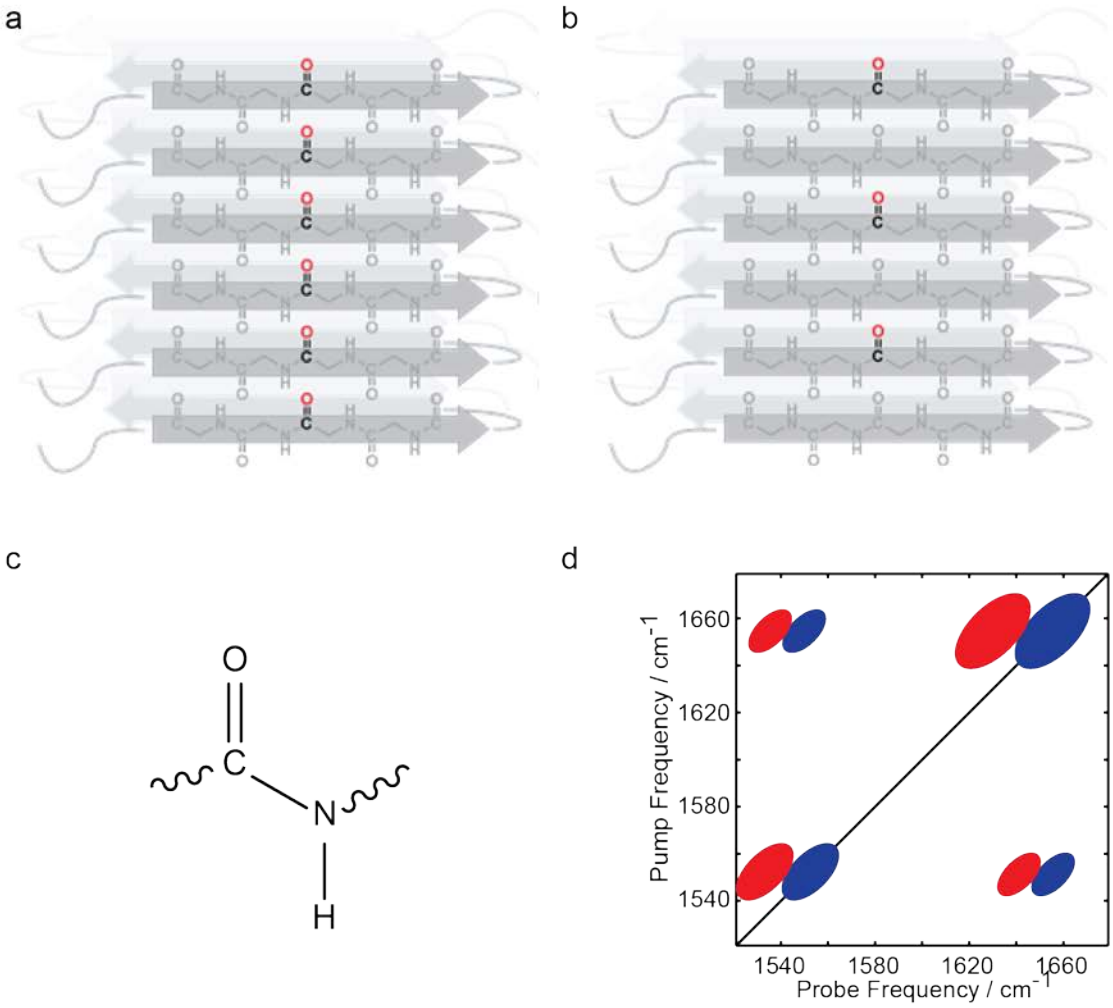

Figure 1.4 (a) A model parallel β-sheet in which one amino acid in the chain contains a $^{13}C^{18}O$ isotope label. When the peptide folds into a parallel β-sheet, the isotope label aligns in register, couples to labeled residues on adjacent strands, and the frequency of the label shifts by twice the coupling constant. (b) If the sample composition changes, such as adding a peptide-like inhibitor molecule, the isotope labeled amino acid may become 'dilute', in which case it does not couple to the amide I modes on adjacent strands, and the frequency does not shift. (c) Model peptide unit. (d) Representative 2D IR of an α-helix surface-bound peptide. The peaks along the diagonal correspond to the amide I mode (1650 cm^{-1}) and amide II mode (1550 cm^{-1}). The peaks on the off diagonal are cross peaks that indicate that the amide I and amide II modes are coupled.

would couple less strongly that residues firmly located in a β-sheet. In that case, the coupling constant would be smaller, resulting in a higher frequency for the isotope labeled amino acid. By measuring the frequency shift caused by coupling, as a function of residue, the overall structure of the β-sheet can be determined.

By extension, if a perturbation is applied to a β-sheet, one could observe if the perturbation causes coupling at a particular amino acid to change. If so, the change in coupling would provide insight into how the perturbation changed the protein structure. We observed three different types of perturbations to hIAPP in three separate projects. The first perturbation to hIAPP that caused a change in the expected coupling in hIAPP was deamidation (Chapter 3).[7] Deamidation is the most common non-enzymatic post-translational modification in proteins, and has been well-studied in a variety of other amyloid peptides and proteins.[60-66] When a protein deamidates, asparagine and glutamine residues undergo a structure change to form iso/aspartic acid and iso/glutamic acid. This is a very tiny change to the protein sequence that can have large structural implications. We were able to observe a change in coupling at four isotope labeled residues throughout the hIAPP and we determined what effects these modifications have on the overall structure, as well as on the kinetics of amyloid formation. The second perturbation to hIAPP involved mutating hIAPP to the rat form of the peptide (rIAPP) and learning how those mutations affected the transition dipole strength in the peptide (Chapter 4). We found that the transition dipole strength of hIAPP fibers and rIAPP in solution are dramatically different. Even rIAPP in solution, micelle, and membranes exhibited different transition dipole strengths, suggesting that all of these samples contain different

secondary structures.[52] The third perturbation to hIAPP that caused a change in coupling was the addition of small β-sheet macrocycles that were designed to inhibit hIAPP aggregation (Chapter 5). The current trend in studying amyloids is to mix potential inhibitor molecules with amyloid monomers with hope that that the inhibitors will prevent fiber formation.[39,59,67-73] By observing either strong isotope coupling (Figure 1.4a) or broken isotope coupling (1.4b), the structure of hIAPP mixed with inhibitory molecules was measured.

In order to observe these changes in coupling of the isotope label, we use ultrafast femtosecond laser spectroscopy. By using ultrafast femtosecond laser pulses, the dynamics of a protein can be measured on the picosecond timescale. With our rapid-scan technology and pulse shaping abilities, we can measure kinetic spectra on-the-fly.[74,75] This enables us to measure both ultrafast dynamics of proteins, such as hydrogen bonding and electrostatics, which occur in picoseconds, and ultraslow dynamics, such as large structural rearrangements, which occur in minutes and hours. By monitoring the change in intensity of particular features in a 2D IR spectrum, the kinetics of both the unlabeled residues and of the isotope labeled residue can be measured simultaneously. Figure 1.5 shows three 2D IR spectra collected during the lag phase (a), growth phase (b), and elongation phase (c) of amyloid fiber growth. The black box encloses the region of the spectrum where unlabeled residues in β-sheets absorb, and the intensity of the blue box is plotted as a function of time (Figure 1.5d, blue). After fiber initiation, the peptide is mostly random coil and there is very little β-sheet character (Figure 1.5a). After ~1 h of lag phase, the β-sheet intensity in the 2D IR spectrum increases, and the peptide begins to

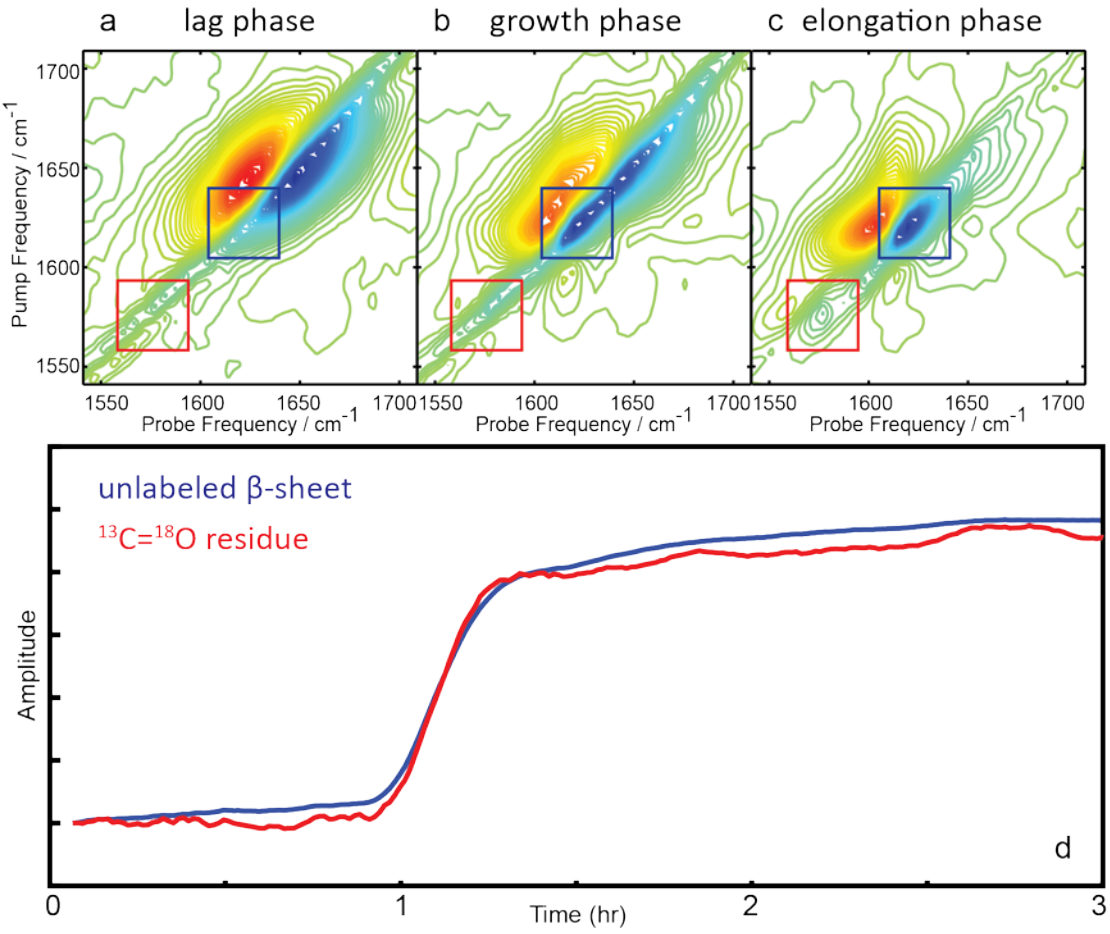

Figure 1.5 Amyloid fiber aggregation kinetics, as monitored by 2D IR spectroscopy. (a) 2D IR spectrum collected during the lag phase (0-1 h) of aggregation, when the peptide is mostly random coil (~1645 cm^{-1}) and there is no appreciable β-sheet peak in the spectrum. (b) 2D IR spectrum collected during the growth phase (1-2 h) of aggregation, when the peptide begins to form β-sheets (~1620 cm^{-1}). (c) 2D IR spectrum collected during the elongation phase (2-3 h), when the peptide β-sheets are growing. The blue boxes enclose the region of the 2D IR spectra where unlabeled β-sheets absorb. The red boxes enclose the region of the 2D IR spectra where the isotope labeled residue absorbs, if it is part of the β-sheet. (d) The intensity of the blue and red boxes, plotted as a function of time.

grow into fibers (Figure 1.5b). Following the growth phase of the fiber, the fiber continues to elongate and the unlabeled β-sheet peak equilibrates (Figure 1.5c). The kinetics of the unlabeled residues measured using 2D IR spectroscopy mimic those measured by ThT fluorescence, but the added advantage is that the kinetics of the isotope labeled amino acid are also measured. If the label folds faster or slower than or at the same time as the unlabeled residues, that will be measured and structural information can be gleaned. The red boxes in Figure 1.5 shows the region of the spectrum where a coupled isotope labeled amino acid absorbs in a β-sheet. The intensity of 2D IR spectra at that frequency can be plotted as a function of time, and is shown in Figure 1.5d, red. The isotope labeled amino acid trace closely matches that of the unlabeled β-sheet peak. These traces may closely match, or they may look very different, depending on the sample; regardless, using the unique combination of isotope labeling and 2D IR spectroscopy, we can measure the kinetics of hIAPP aggregation on-the-fly with higher structural resolution than can be collected from ThT fluorescence measurements.

1.7 Using hydrogen-deuterium exchange to get membrane peptide structure

For an α-helical protein with a single isotope labeled amino acid, the frequency of the label shifts to ~1595 cm^{-1}.[25] The frequency of the unlabeled residues is ~1655 cm^{-1} and the diagonal linewidth of the unlabeled amino acids is narrow enough that the unlabeled peak does not overlap with the labeled peak (Figure 1.3c). This allows for the measurement of the diagonal linewidth of just the one isotope labeled amino acid. Diagonal linewidth measurements can give information about the electrostatic

environment of the amino acid, whether it is solvent exposed, or if it lies in the hydrophobic part of a membrane bilayer.[24-26]

The coupling in an α-helix is different from that in a β-sheet in that coupling is strongest between two adjacent residues in the peptide chain, rather than two residues on neighboring strands.[51] Rather than learning about the structure through excitonic coupling between adjacent β-strands in amyloids, the structure of α-helical surface-bound peptides manifests itself through cross peaks in a 2D IR spectrum. Cross peaks appear on the off-diagonal of a 2D IR spectrum and are the result of two modes with two different frequencies that are coupled. The coupling strength depends on the relative orientation and distance between the two coupled modes. In an α-helix, the amide I and amide II modes are strongly coupled. The amide I, composed of mostly C=O stretching vibrations, and the amide II, composed of CN stretch and NH bending motions are strongly coupled and in a 2D IR spectrum, cross peaks between these two modes are evident in an α-helical peptide.[9] Figure 1.4c shows a single peptide unit and Figure 1.4d shows a representative 2D IR spectrum for this peptide unit if it was contained in an α-helix. Pairs of peaks would show up at high frequency (~1650 cm^{-1}) for the amide I mode and at low frequency (~1550 cm^{-1}) for the amide II mode. Cross peaks on the off diagonal would indicate that the amide I and amide II modes are coupled.

Including a single isotope labeled residue in a surface-bound α-helix adds an additional peak along the diagonal of a 2D IR spectrum at the frequency of the isotope label (~1595cm^{-1}). Since the isotope labeled amino acid is also still strongly coupled to an amide II mode, additional cross peaks between the isotope label and amide II mode

would appear in the 2D IR spectrum (not shown). We exploited the cross peaks between an isotope labeled amino acid and the amide II mode to measure the water exposure in the surface-bound antimicrobial peptide, ovispirin (Chapter 6). We used hydrogen-deuterium exchange experiments to measure the exchange rate of the amide hydrogen atom for deuterium atom, which is measure of that particular residue's water exposure.

1.8 Summary

Using the unique combination of 2D IR spectroscopy and isotope labeling, I performed several experiments that benefitted from observation of coupling, whether it be between isotope labeled amino acids in β-sheets or between an isotope labeled amino acid and other unlabeled residues in an α-helix. By measuring coupling, the structures of different peptide systems were clarified. Hopefully, these techniques will be used in the future to gain more knowledge of amyloid and membrane peptides.

1.9 References

(1) Cady, S. D.; Hong, M. *Proceedings of the National Academy of Sciences* **2008**, *105*, 1483-1488.

(2) Ghosh, A.; Qiu, J.; DeGrado, W. F.; Hochstrasser, R. M. *Proceedings of the National Academy of Sciences* **2011**, *108*, 6115-6120.

(3) Manor, J.; Feldblum, E. S.; Zanni, M. T.; Arkin, I. T. *Journal of Physical Chemistry Letters* **2012**, *3*, 939-944.

(4) Eaton, W. A.; Hofrichter, J. In *Adv. Protein Chem.*; C.B. Anfinsen, J. T. E. F. M. R., David, S. E., Eds.; Academic Press: 1990; Vol. Volume 40, p 63-279.

(5) Schechter, A. N. *Blood* **2008**, *112*, 3927-3938.

(6) Chiti, F.; Dobson, C. M. *Annu. Rev. Biochem.* **2006**, *75*, 333-366.

(7) Dunkelberger, E. B.; Buchanan, L. E.; Marek, P.; Cao, P.; Raleigh, D. P.; Zanni, M. T. *J. Am. Chem. Soc.* **2012**, *134*, 12658-12667.

(8) Yam, A. Y.; Wang, X.; Gao, C. M.; Connolly, M. D.; Zuckermann, R. N.; Bleu, T.; Hall, J.; Fedynyshyn, J. P.; Allauzen, S.; Peretz, D.; Salisbury, C. M. *Biochemistry* **2011**, *50*, 4322-4329.

(9) Krimm, S.; Bandekar, J. In *Adv. Protein Chem.*; C.B. Anfinsen, J. T. E., Frederic, M. R., Eds.; Academic Press: 1986; Vol. Volume 38, p 181-364.

(10) Luca, S.; Yau, W.-M.; Leapman, R.; Tycko, R. *Biochemistry* **2007**, *46*, 13505-13522.

(11) Hamley, I. W. *Chem. Rev. (Washington, DC, U. S.)* **2012**.

(12) Moran, S. D.; Woys, A. M.; Buchanan, L. E.; Bixby, E.; Decatur, S. M.; Zanni, M. T. *Proceedings of the National Academy of Sciences* **2012**, *109*, 3329-3334.

(13) Lorenzo, A.; Yankner, B. A. *Ann. N. Y. Acad. Sci.* **1996**, *777*, 89-95.

(14) Höppener, J. W. M.; Ahrén, B.; Lips, C. J. M. *N. Engl. J. Med.* **2000**, *343*, 411-419.

(15) Härd, T.; Lendel, C. *J. Mol. Biol.* **2012**, *421*, 441-465.

(16) Greenwald, J.; Riek, R. *J. Mol. Biol.* **2012**, *421*, 417-426.

(17) Fändrich, M. *J. Mol. Biol.* **2012**, *421*, 427-440.

(18) Sachs, J. N.; Engelman, D. M. *Annu. Rev. Biochem.* **2006**, *75*, 707-712.

(19) Engel, A.; Gaub, H. E. *Annu. Rev. Biochem.* **2008**, *77*, 127-148.

(20) Hubbell, W. L.; Gross, A.; Langen, R.; Lietzow, M. A. *Curr. Opin. Struct. Biol.* **1998**, *8*, 649-656.

(21) White, S. H.; Wimley, W. C. *Annu. Rev. Biophys. Biomol. Struct.* **1999**, *28*, 319-365.

(22) Krishna, M. M. G.; Hoang, L.; Lin, Y.; Englander, S. W. *Methods* **2004**, *34*, 51-64.

(23) Englander, S. W.; Krishna, M. M. G. *Nat. Struct. Mol. Biol.* **2001**, *8*, 741-742.

(24) Mukherjee, P.; Kass, I.; Arkin, I. T.; Zanni, M. T. *Proc. Natl. Acad. Sci. U. S. A.* **2006**, *103*, 3528-3533.

(25) Woys, A. M.; Lin, Y.-S.; Reddy, A. S.; Xiong, W.; de Pablo, J. J.; Skinner, J. L.; Zanni, M. T. *J. Am. Chem. Soc.* **2010**, *132*, 2832-2838.

(26) Wang, L.; Middleton, C. T.; Singh, S.; Reddy, A. S.; Woys, A. M.; Strasfeld, D. B.; Marek, P.; Raleigh, D. P.; de Pablo, J. J.; Zanni, M. T.; Skinner, J. L. *J. Am. Chem. Soc.* **2011**, *133*, 16062-16071.

(27) Fleming, G. R.; Wolynes, P. G. *Physics Today* **1990**, *43*, 36-43.

(28) Frauenfelder, H.; Sligar, S.; Wolynes, P. *Science* **1991**, *254*, 1598-1603.

(29) Lewandowski, J. R. *Acc. Chem. Res.* **2013**.

(30) Makin, O. S.; Atkins, E.; Sikorski, P.; Johansson, J.; Serpell, L. C. *Proc. Natl. Acad. Sci. U. S. A.* **2005**, *102*, 315-320.

(31) Sunde, M.; Serpell, L. C.; Bartlam, M.; Fraser, P. E.; Pepys, M. B.; Blake, C. C. F. *J. Mol. Biol.* **1997**, *273*, 729-739.

(32) Sumner Makin, O.; Serpell, L. C. *J. Mol. Biol.* **2004**, *335*, 1279-1288.

(33) Yamaguchi, S.; Huster, D.; Waring, A.; Lehrer, R. I.; Kearney, W.; Tack, B. F.; Hong, M. *Biophys. J.* **2001**, *81*, 2203-2214.

(34) Paravastu, A. K.; Leapman, R. D.; Yau, W.-M.; Tycko, R. *Proceedings of the National Academy of Sciences* **2008**, *105*, 18349-18354.

(35) Tycko, R.; Wickner, R. B. *Acc. Chem. Res.* **2013**.

(36) Cotten, M.; Fu, R.; Cross, T. A. *Biophys. J.* **1999**, *76*, 1179-1189.

(37) Goldsbury, C.; Goldie, K.; Pellaud, J.; Seelig, J.; Frey, P.; Müller, S. A.; Kistler, J.; Cooper, G. J. S.; Aebi, U. *J. Struct. Biol.* **2000**, *130*, 352-362.

(38) Marek, P.; Mukherjee, S.; Zanni, M. T.; Raleigh, D. P. *J. Mol. Biol.* **2010**, *400*, 878-888.

(39) Meng, F.; Abedini, A.; Plesner, A.; Verchere, C. B.; Raleigh, D. P. *Biochemistry* **2010**, *49*, 8127-8133.

(40) Meng, F.; Raleigh, D. P.; Abedini, A. *J. Am. Chem. Soc.* **2010**, *132*, 14340-14342.

(41) Padrick, S. B.; Miranker, A. D. *Biochemistry* **2002**, *41*, 4694-4703.

(42) Engel, M. F. M.; Khemtémourian, L.; Kleijer, C. C.; Meeldijk, H. J. D.; Jacobs, J.; Verkleij, A. J.; de Kruijff, B.; Killian, J. A.; Höppener, J. W. M. *Proceedings of the National Academy of Sciences* **2008**, *105*, 6033-6038.

(43) Jayasinghe, S. A.; Langen, R. *Biochemistry* **2005**, *44*, 12113-12119.

(44) Vigano, C.; Smeyers, M.; Raussens, V.; Scheirlinckx, F.; Ruysschaert, J. M.; Goormaghtigh, E. *Biopolymers* **2004**, *74*, 19-26.

(45) Wu, Y.; Murayama, K.; Ozaki, Y. *The Journal of Physical Chemistry B* **2001**, *105*, 6251-6259.

(46) Ludlam, C. F.; Arkin, I. T.; Liu, X. M.; Rothman, M. S.; Rath, P.; Aimoto, S.; Smith, S. O.; Engelman, D. M.; Rothschild, K. J. *Biophys. J.* **1996**, *70*, 1728-1736.

(47) Hamm, P.; Lim, M.; Hochstrasser, R. M. *The Journal of Physical Chemistry B* **1998**, *102*, 6123-6138.

(48) Kim, Y. S.; Liu, L.; Axelsen, P. H.; Hochstrasser, R. M. *Proceedings of the National Academy of Sciences* **2008**, *105*, 7720-7725.

(49) DeFlores, L. P.; Ganim, Z.; Nicodemus, R. A.; Tokmakoff, A. *J. Am. Chem. Soc.* **2009**, *131*, 3385-3391.

(50) *Examining Amyloid Structure and Kinetics with 1D and 2D Infrared Spectroscopy and Isotope Labeling*; 1 ed.; Buchanan, L., Dunkelberger, EB, Zanni, MT, Ed.; Springer: Heidelberg, 2011; Vol. 1.

(51) Hamm, P. a. Z., Martin T.; Cambridge University Press, New York: 2011.

(52) Grechko, M.; Zanni, M. T. *The Journal of Chemical Physics* **2012**, *137*, 184202.

(53) Woys, A. M.; Almeida, A. M.; Wang, L.; Chiu, C.-C.; McGovern, M.; de Pablo, J. J.; Skinner, J. L.; Gellman, S. H.; Zanni, M. T. *J. Am. Chem. Soc.* **2012**.

(54) Torres, J.; Adams, P. D.; Arkin, I. T. *J. Mol. Biol.* **2000**, *300*, 677-685.

(55) Torres, J.; Kukol, A.; Goodman, J. M.; Arkin, I. T. *Biopolymers* **2001**, *59*, 396-401.

(56) Urbanek, D. C.; Vorobyev, D. Y.; Serrano, A. L.; Gai, F.; Hochstrasser, R. M. *The Journal of Physical Chemistry Letters* **2010**, *1*, 3311-3315.

(57) Chung, J. K.; Thielges, M. C.; Fayer, M. D. *Proceedings of the National Academy of Sciences* **2011**, *108*, 3578-3583.

(58) Shim, S.-H.; Gupta, R.; Ling, Y. L.; Strasfeld, D. B.; Raleigh, D. P.; Zanni, M. T. *Proceedings of the National Academy of Sciences* **2009**, *106*, 6614-6619.

(59) Middleton, C. T.; Marek, P.; Cao, P.; Chiu, C.-c.; Singh, S.; Woys, A. M.; de Pablo, J. J.; Raleigh, D. P.; Zanni, M. T. *Nat Chem* **2012**, *advance online publication*.

(60) Robinson, N. E.; Robinson, A. B. *Mechanisms of Ageing and Development* **2004**, *125*, 259-267.

(61) Scotchler, J. W.; Robinson, A. B. *Anal. Biochem.* **1974**, *59*, 319-322.

(62) Robinson, N. E.; Robinson, A. B. *Proc. Natl. Acad. Sci. U. S. A.* **2001**, *98*, 12409-12413.

(63) Robinson, N. E.; Robinson, M. L.; Schulze, S. E. S.; Lai, B. T.; Gray, H. B. *Protein Sci.* **2009**, *18*, 1766-1773.

(64) Flaugh, S. L.; Mills, I. A.; King, J. *J. Biol. Chem.* **2006**, *281*, 30782-30793.

(65) Nilsson, M. R.; Driscoll, M.; Raleigh, D. P. *Protein Sci.* **2002**, *11*, 342-349.

(66) Robinson, N. E.; Robinson, A. B. *Proc. Natl. Acad. Sci. U. S. A.* **2001**, *98*, 944-949.

(67) Mishra, R.; Sellin, D.; Radovan, D.; Gohlke, A.; Winter, R. *ChemBioChem* **2009**, *10*, 445-449.

(68) Mishra, R.; Bulic, B.; Sellin, D.; Jha, S.; Waldmann, H.; Winter, R. *Angewandte Chemie International Edition* **2008**, *47*, 4679-4682.

(69) Sellin, D.; Yan, L.-M.; Kapurniotu, A.; Winter, R. *Biophys. Chem.* **2010**, *150*, 73-79.

(70) Abedini, A.; Meng, F.; Raleigh, D. P. *J. Am. Chem. Soc.* **2007**, *129*, 11300-11301.

(71) Cheng, P.-N.; Liu, C.; Zhao, M.; Eisenberg, D.; Nowick, J. S. *Nat Chem* **2012**, *advance online publication*.

(72) Cheng, P.-N.; Spencer, R.; Woods, R. J.; Glabe, C. G.; Nowick, J. S. *J. Am. Chem. Soc.* **2012**.

(73) Zheng, J.; Liu, C.; Sawaya, M. R.; Vadla, B.; Khan, S.; Woods, R. J.; Eisenberg, D.; Goux, W. J.; Nowick, J. S. *J. Am. Chem. Soc.* **2011**, *133*, 3144-3157.

(74) Shim, S.-H.; Strasfeld, D. B.; Ling, Y. L.; Zanni, M. T. *Proceedings of the National Academy of Sciences* **2007**, *104*, 14197-14202.

(75) Strasfeld, D. B.; Ling, Y. L.; Shim, S.-H.; Zanni, M. T. *J. Am. Chem. Soc.* **2008**, *130*, 6698-6699.

CHAPTER 2

Experimental Methods: Tips and Tricks

2.1 Introduction

In this chapter, I aim to add additional details to some experimental procedures that I have performed during graduate school. Many details of the experiments I performed are included in later chapters. However, there are many tips and tricks to these experiments that might become useful in the future. During my time in the group, I learned some synthesis and purification techniques: isotope labeling amino acids and synthesizing and purifying amyloidogenic proteins. I also developed ways to best prepare amyloidogenic proteins for 2D IR spectroscopy measurements and to prepare micelle and membrane samples for amyloid and hydrogen-deuterium exchange (HDX) experiments. In addition, I spent approximately 15% of my graduate career building a

laser table. Several former group members have described how an ultrafast laser works; my intent is to offer advice to those who may have to design and build an optical setup in the future.

2.2 Isotope labeling procedure

One advantage to using infrared spectroscopy to study peptides is that there are relatively simple and non-invasive ways to observe single amino acids in the peptide. The technique we use relies on the fact that isotopes of amino acids have different frequencies than natural abundance amino acids. Natural abundance amino acids have $^{12}C^{16}O$ in the carbonyl position, while the $^{13}C^{16}O$ isotope naturally occurs at ~1% in nature, and the $^{13}C^{18}O$ isotope occurs at <1% in nature. The $^{13}C^{16}O$ isotope absorbs ~40 cm^{-1} lower than the $^{12}C^{16}O$ carbonyl group, but this peak can be in the region where sidechains absorb. In addition, in large proteins of 100 amino acids, the $^{13}C^{16}O$ isotope is likely to occur at 1 random position in the peptide. However, by synthetically incorporating a $^{13}C^{18}O$ carbonyl group into one amino acid, the frequency of that residue shifts by ~66 cm^{-1} from the frequency of the natural abundance amino acid.[1] The 66 cm^{-1} shift is larger than the one caused by just ^{13}C or just ^{18}O, and is enough to make the isotope labeled residue appear in an otherwise featureless part of a peptide IR spectrum.[2,3] In addition, this isotope naturally occurs less often, giving us control over which residue contains the label. Thus, by incorporating isotope labeled amino acids into different positions in a peptide, we can obtain site-specific information about different parts of the peptide. Figure 2.1a shows a schematic of the isotope labeling scheme we use, and how it affects the frequency of the carbonyl group in an amino acid.

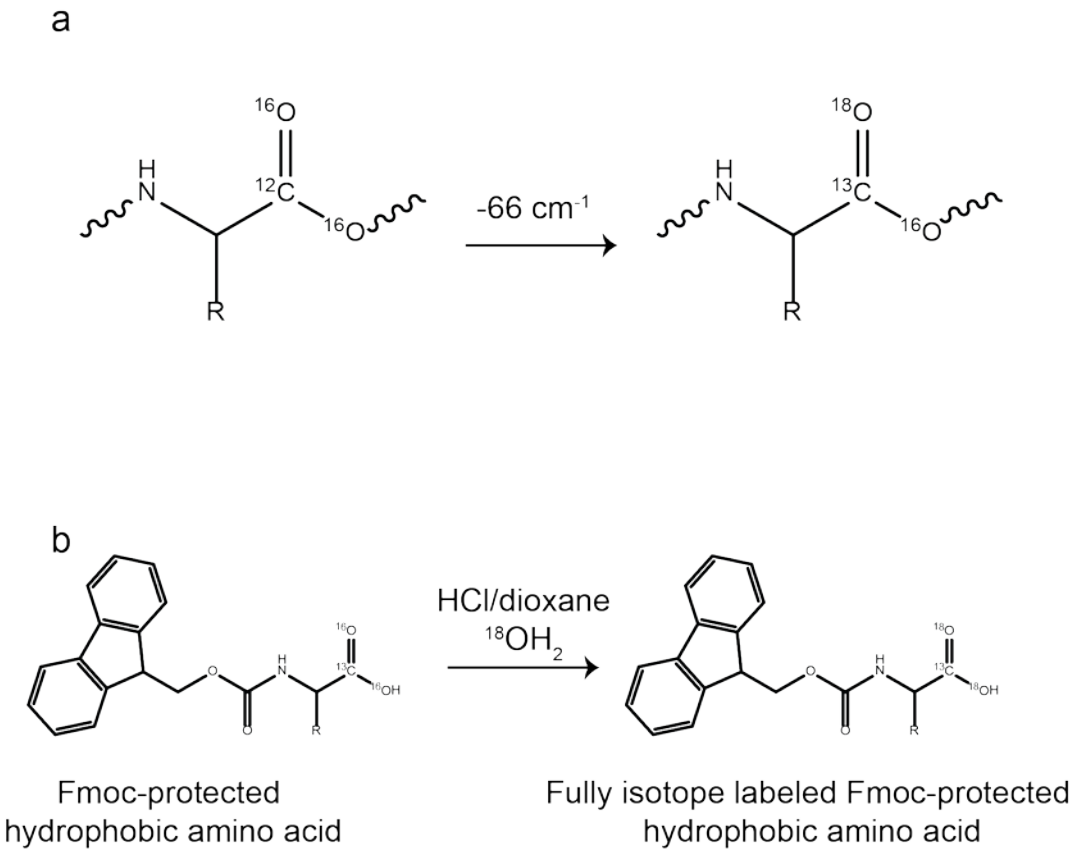

Figure 2.1 (a) Incorporating a $^{13}C^{18}O$ group into the carbonyl group of an amino acids shifts the peak to lower frequency by ~54 cm^{-1}. (b) The isotope labeling procedure for an Fmoc-protected amino acid is best achieved under acidic conditions. Under this procedure both ^{16}O atoms should exchange for ^{18}O in order to yield the best results of incorporating a label into a peptide.

The details for $^{13}C^{18}O$ isotope labeling amino acids have been previously published several times over, and so I will not go into great detail here.[2,4-6] The easiest amino acids to label are the ones with non-reactive hydrophobic sidechains (Gly, Val, Ala, Phe, Leu, Ile). They are cheaper to purchase with a ^{13}C in the C_α position than amino acids with reactive side chains, and they can be purchased 9-fluorenylmethyloxycarbonyl (Fmoc) protected. The Fmoc group protects the amine group on amino acids and since it is base-labile, it is easily removed under basic conditions without disturbing the acid labile linking group between the peptide and solid state resin. When isotope labeling an amino acid, the ^{18}O can and should exchange in both oxygen positions in the carboxyl group in order to have the highest rate of ^{18}O incorporation into the peptide (Figure 2.1b). One way to yield better rates for isotope exchange is to use dry reagents. If possible, it is best to purchase small amounts of each reagent and to use it completely soon after the bottles are open. This will help prevent water uptake. Oftentimes, it is best to isotope label a couple amino acids simultaneously in order to use up the reagents before they take up too much water.

Previously, most of the isotope labeling procedures suggested isotope labeling the carbonyl group of the amino acid first, and then Fmoc-protecting the residue for use in peptide synthesis. However, this strategy is disadvantageous in that the isotope labeling reaction can be reversed under the experimental conditions for adding the Fmoc group and the yield can drop. The exchange of ^{16}O for ^{18}O in the carbonyl group is acid-catalyzed, whereas addition of the Fmoc group is base-catalyzed.[7] Attaching the Fmoc group to the amino acid first, before isotope labeling, will not interfere with the labeling

efficiency; since the Fmoc group is base-labile it will also not back-exchange under the acidic conditions of isotope labeling. However, if the Fmoc group is added first, the isotope label can be reversed upon neutralization of the newly Fmoc protected amino acid. The best option, though it is more expensive, is to purchase amino acids with the $^{13}C_{\alpha}$ and the Fmoc group already attached. Shown in Figure 2.1b is a schematic of the isotope labeling procedure for a general Fmoc-protected hydrophobic amino acid.

Liquid chromatography-mass spectrometry (LC-MS) is typically used to access the isotope exchange yield. To prepare the sample, the dioxane/water solution from the isotope labeling reaction is pulled off the sample using the vacuum trap on the Schlenk line. First, freeze, the sample to prevent bumping, and then pull a vacuum on the reaction flask. Typically, this process takes 12-16 hours, and if the sample is not completely dry after that amount of time, the sample can be dried on the lypohilizer. For LC-MS analysis, a visible amount of amino acid should be dissolved in 1 mL of acetonitrile (ACN). The standard LC-MS protocol that is sufficient for amino acids samples is Std_100_1000.lcm. This protocol will run a 0-100% binary gradient of 0.1% formic acid in water (solvent A) and 0.1% formic acid in ACN (solvent B) at 0.200 mL/min for 12 min. A liquid chromatogram of isotope labeled Leu is shown in Figure 2.2a. The primary products of the isotope labeling procedure have a retention time of just over 10 min on this gradient (shown by a red line). To access the masses of the products of the main peak in the chromatogram, the mass spectrum at the maximum of the chromatogram is measured. To calculate the percent of isotope exchange, the intensity of the peak that includes $^{13}C^{18}O^{18}O$, the fully labeled carboxyl group, should be added to ½ of the

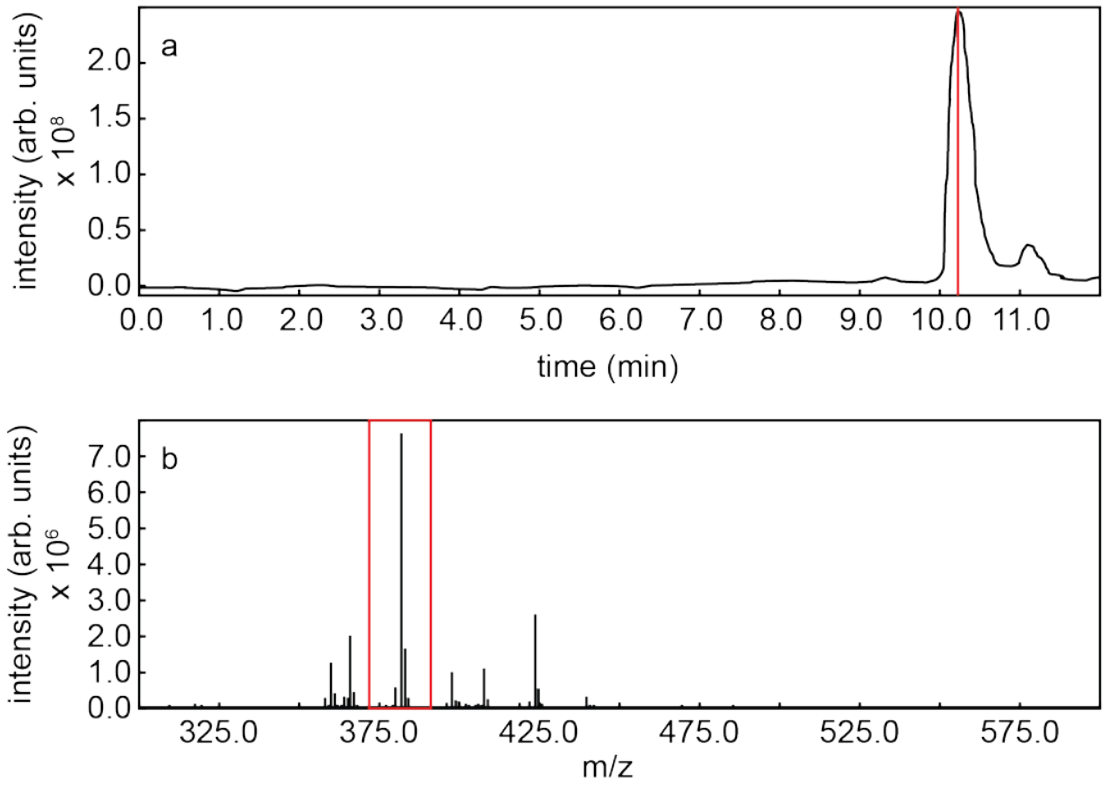

Figure 2.2 (a) Liquid chromatogram of an isotope labeled amino acid on a 0-100%B in 12 min binary gradient of 0.1% formic acid in water and 0.1% formic acid in ACN. The red line marks the maximum intensity in the chromatogram and the eluent at that retention time is most likely to contain the labeled amino acid. (b) Mass spectrum from the eluent at the retention time marked by the red line in (a). The red box surrounds the isotope pattern of the $^{13}C^{18}O^{18}O$, $^{13}C^{18}O^{16}O$, and $^{13}C^{16}O^{16}O$ isotopes.

intensity of the $^{13}C^{18}O^{16}O$, the half-labeled carboxyl group. The sum of these quantities should be divided by the sum of the intensity of the fully labeled carboxyl group, the intensity of the half-labeled carboxyl group, and the intensity of the non-oxygen labeled carboxyl group, according to Equation 2.1.

$$\frac{Intensity\ (^{13}C^{18}O^{18}O) + \frac{1}{2}Intensity\ (^{13}C^{18}O^{16}O)}{Intensity\ (^{13}C^{18}O^{18}O) + Intensity\ (^{13}C^{18}O^{16}O) + Intensity\ (^{13}C^{16}O^{16}O)} \quad (2.1)$$

Figure 2.2b shows a representative LC-MS spectrum for isotope labeled Leu. Highlighted in the red box are the peaks due to isotope labeled Leu. Fmoc-protected $^{13}C^{18}O^{18}O$ labeled Leu has a molecular weight of 381.1 g/mol, and is the largest peak in the red box. Fmoc protected $^{13}C^{18}O^{16}O$ has a molecular weight of 379.1 g/mol, and the $^{13}C^{16}O^{16}O$ isotope has a mass of 377.1 g/mol. Commonly during LC-MS, a sodium ion (Na^+) will bind to the isotope labeled amino acid and will shift the mass of the sample by 23 amu. As a result, it is a good idea to check for a peak at that additional mass in the spectrum as well as the isotope pattern for partially exchanged amino acids. The LC-MS software is unable to integrate peak heights, and so the intensity of these three peaks should be measured by hand. Based upon the equation for labeling efficiency described above, this sample of Leu is 95.15% isotope labeled. The isotope labeling procedure must be repeated until the labeling efficiency is greater than 90%. Otherwise, the label will be too dilute and will not effectively couple in β-sheets.

2.3 Peptide synthesis and cleavage

Amyloidgenic peptides are notoriously difficult to synthesize via solid-state methods because of their natural tendency to aggregate on the solid support. Previously,

we relied on our collaborators at SUNY-Stonybrook to synthesize hIAPP for our measurements. However, after an unfortunate series of events when all of our isotope labeled hIAPP deamidated, we elected to begin synthesizing our own peptides. Microwave-assisted peptide synthesis has become an efficient way to synthesize difficult peptides. The reagents used in this technique are identical to those used in traditional synthesis protocols. However, the use of microwave energy assists the synthesis and increases the yield. It is still unclear exactly how microwave energy produces higher yields; however, the yield of hIAPP under standard synthesis conditions is ~5%, while the yield using microwave synthesis is at least 15%. This is a significant difference in yield, particularly when the peptide has an expensive isotope label incorporated into it.

Figure 2.3 shows a schematic of standard solid-phase Fmoc synthesis. A polystyrene bead attaches to the first amino acid through a linker, and each amino acid is protected on the amide group by a large heterocyclic Fmoc group. First, the Fmoc group is removed by a deprotection solution of dimethylformamide, piperidine, and hydroxybenzotriazole (HOBt). Then, the deprotected amino acid is activated by o-benzotriazole-N,N,N',N'-tetramethyl-uronium-hexafluoro-phosphate (HBTU) and N,N-diisopropylethylamine (DIEA). Last, the next amino acid, which is also Fmoc protected on the amide group couples to the deprotected peptide. During a typical coupling step, the microwave is turned on for up to 3 min and the temperature of the synthesis solution increases up to 50°C. The amide group of the first amino acid forms a peptide bond with the free carboxyl group on the second amino acid. Peptide synthesis proceeds from C-

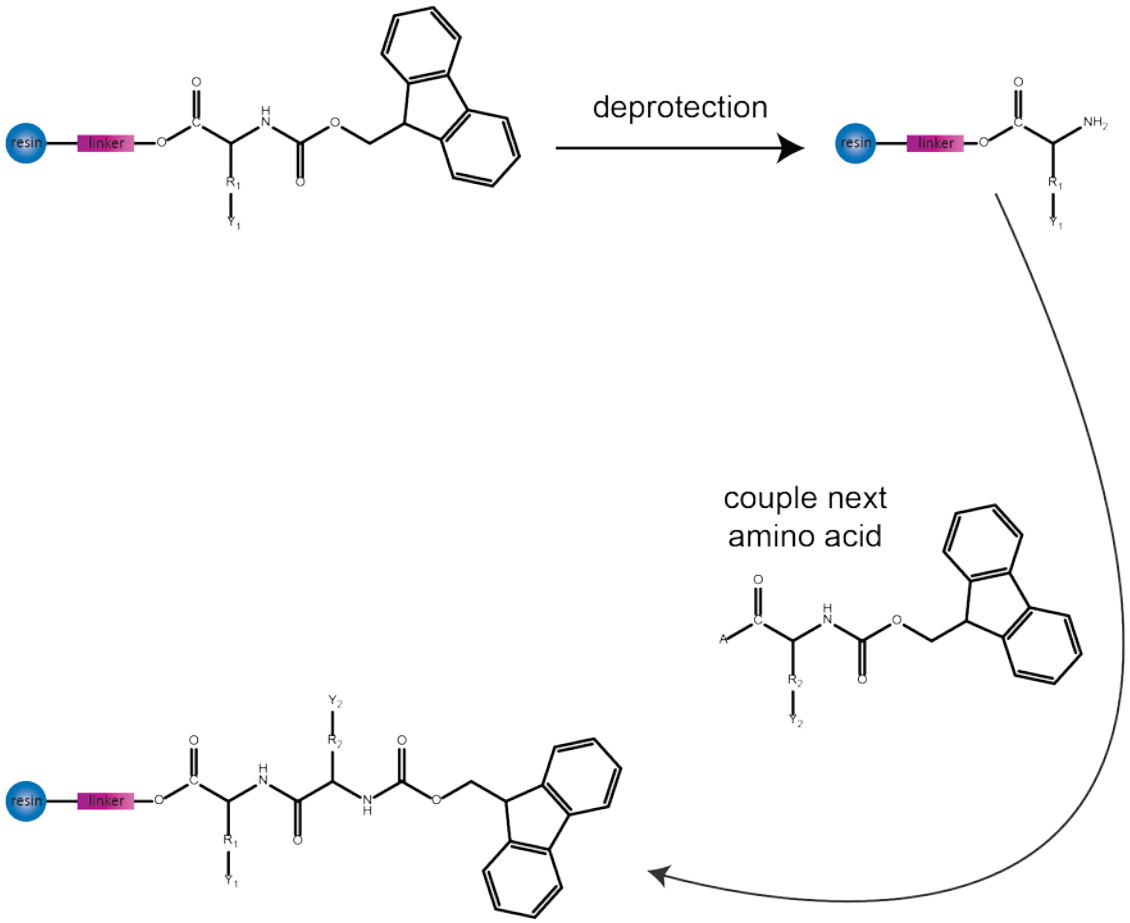

Figure 2.3 General scheme for Fmoc peptide synthesis. The C-terminal amino acids are attached through a linking group to a solid state resin. The Fmoc group is deprotected, the next amino acid is activated, and then finally, the amino acid is coupled to the peptide already attached to the resin.

terminus to N-terminus, and this cycle of deprotection and coupling is repeated until all of the amino acids have been added.

The protocol I have used for synthesizing hIAPP and rIAPP follows closely with the protocol published by Dan Raleigh.[4,8] PAL-PEG-PS resin is used to ensure an amidated C-terminus. Two pseudoproline derivatives are incorporated into Ala-13-Thr-14 and Leu-27-Ser-28 in hIAPP, while only the Ala-13-Thr-14 pseudoproline is incorporated into rIAPP. In addition, the Raleigh group typically incorporates a pseudoproline derivative into Ser-19-Ser20.[8] Pseudoprolines are useful for synthesis because they temporarily protect the sidechains on Ser, Thr, and Cys during synthesis. Sidechain protection allows for better solubility and therefore better coupling. In addition, pseudoprolines limit peptide aggregation during synthesis. After synthesis, pseudoprolines are easily converted to the amino acids it has replaced through cleavage and deprotection by trifluoroacetic acid (TFA).

Following synthesis, any solid-state synthesized peptide must be cleaved from the resin. Typically, it is unwise and unnecessary to cleave an entire synthesis worth of resin. For large-scale syntheses of hIAPP (0.1 mmol), only a third of the resin should cleaved. The remaining resin should be stored dry in the freezer. By storing the majority of the peptide dry and on the resin, all of the reactive sidechains remain protected by their protecting group. This prevents any post-translational modifications, such as deamidation of asparagine and glutamine sidechains, from occurring. These conditions should, in theory, render the peptides completely inert until later cleavages. Dichloromethane (DCM) is used to transfer the resin from the microwave synthesis

reaction vessel into a centrifuge tube. The DCM can be blown off with nitrogen or removed using a vacuum pump. Regardless, the DCM should be removed before cleavage and freezer storage.

I tested several cleavage cocktails, but one cocktail stood out as producing the largest and purest yield of hIAPP. The best cleavage cocktail for hIAPP synthesis is 90% TFA, 5% ethanedithiol, 2.5 % thioanisole, and 2.5% anisole. TFA cleaves the peptide from the solid resin as well as removes all sidechain protecting groups. Several amino acids in hIAPP have reactive sidechains; during synthesis, these sidechains are protected by an acid-labile group that is inert in the synthesis solvents that are basic, but during cleavage, TFA removes them. Ethanedithiol, thioanisole, and anisole act as scavengers for the sidechain protecting groups that are removed. If there are no scavengers, the protecting groups will reattach to the peptide.

The cleavage procedure should be performed in a hood and anything that touches the cleavage cocktail should be doused in dilute bleach and left in the hood to dry for at least one week before disposal. The scavengers in the cleavage cocktail contain thiol groups and therefore smell terrible. The cleavage procedure is as follows:

1. Prepare a fresh batch of cleavage cocktail. To cleave ~500 mg of resin, no more than 10 mL of cleavage cocktail is necessary.

2. Punch a 1” diameter filter from thick filter paper. Place the filter in the bottom of a 30 mL syringe. Attach a 3-way stopcock to the bottom of the syringe and ensure the stopcock is set to prevent liquid from flowing through it. Attach a syringe needle to the other end of the stopcock.

3. Attach a rubber septum to the top of a 50 mL sidearm flask. Punch the syringe needle through the stopcock.

4. Place ~500 mg of resin in the syringe. Add ~5-7 mL of cleavage cocktail in the syringe using a Pasteur pipet. The cleavage cocktail should swell the resin slightly, as well as make the solution bright yellow. Brownish solution is ok too.

5. Seal the syringe with the syringe plunger and gently swirl the syringe.

6. Every 30 minutes for 3 hours, swirl the syringe. Cleavage of hIAPP should not last more than 3 h. Any longer and Cys and Trp sidechains may start reacting, even in the presence of scavengers.[8]

7. Following cleavage, pull the cleavage solution through the syringe needle by opening the stopcock and pulling a vacuum on the flask. Use the remaining 3-5 mL of cleavage cocktail to rinse the resin. The solid resin should remain in the syringe and the peptide should now be in the yellow solution in the flask. The resin should be pale yellow.

8. Dry the peptide solution with nitrogen. This typically takes ~1 h. After 1 h, carefully use a heat gun to dry the remaining solvent from the peptide. The heat gun can get very hot and can actually caramelize and burn the peptide if left unattended. The dry peptide should form a pale yellow-clear film on the bottom of the flask.

9. Once the peptide is dry, chill a bottle of ether in the freezer for 10 minutes. Once chilled, add 2-3 capfuls of ether to the peptide. The peptide will precipitate out of the ether while the scavengers and other organic molecules will dissolve in the ether. Use a spatula to scrape the peptide from the walls of the flask and to break up large chunks of solid.

10. Pour the ether-peptide mixture into a 50 mL centrifuge tube and centrifuge the sample for 5-10 min at 3000 rpm.

11. Carefully decant the ether from the peptide.

12. Repeat steps 9, 10, and 11 two more times.

13. After decanting the ether the third time, leave the centrifuge tube open to air until the remaining ether has completely evaporated.

14. Dissolve a visible amount of peptide in water or methanol. Use MALDI-MS to ensure the mass of the crude peptide is correct.

15. If the mass of hIAPP is correct, dissolve the peptide in dimethylsulfoxide (DMSO) at 5 mg/2 mL. Let the peptide (if hIAPP or rIAPP) sit in DMSO for at least 48 h to form a disulfide bond is formed between Cys-2 and Cys-7.

Dan Raleigh's group performs a couple extra steps in the cleavage process of hIAPP. At the time I am writing this, a couple steps have been implemented, but it would be useful to explore these steps further to determine if they are useful. One step the Raleigh group does, but that I never tried, is to add cold ether to the cleaved and dried peptide and let the mixture sit on an ice bath for 2-3 hours until the solid is clear, not yellow (before step 9). The peptide will precipitate out, and the absence of yellow means that the scavengers are probably more separated from the peptide, yielding a higher purity crude peptide. The other step during the cleavage process that the Raleigh group performs is that after checking the crude peptide mass by MALDI-MS (step 14), they dissolve the peptide in 20% acetic acid and stir until there are no obvious particles in the solution. This step increases the solubility of the crude peptide. After the peptide is

completely dissolved, the solution is lyophilized and the peptide is then dissolved in DMSO at 5 mg/mL (step 15).

Several things can go wrong during peptide synthesis; most are simply instrument error, and most do not have any effect on the synthesis. One common problem is that solvent lines may not be properly calibrated to dispense the correct amount of reagent. If that is the case, the solvents could run out mid-synthesis. This will likely not affect the yield of the synthesis, unless the instrument is calibrated to dispense too little solvents, and instructions for adding more reagents mid-synthesis are in the peptide synthesizer manual. Another common problem is that the N_2 pressure in all the lines is too low. If that is the case, reagents will not be delivered to the reaction vessel in appropriate amounts of time. This problem will also not likely affect the yield. If this problem occurs, the N_2 tank is probably empty. In that case, replace the tank and recalibrate the instrument to ensure proper delivery of all of the reagents.

Two other things are important to note about the peptide synthesizer. The synthesizer does not have the capability to do Boc synthesis. Fmoc synthesis is performed under basic conditions, while Boc synthesis is in acidic solvents. Doing Boc synthesis with our instrument will permanently contaminate the lines. Also, reagents dissolved in DMSO should be avoided. DMSO is viscous and very difficult to clean and remove from the lines. If left in the lines, the lines and connections can start to degrade. DMSO solvents should be avoided.

2.4 Peptide purification

Once hIAPP (or rIAPP) has been sitting in DMSO for 48 hours, the disulfide bond has likely been formed and the peptide can be purified. It is best to start by running a 5-95%B over 90 min two buffer gradient system: solvent A is 100% water and 0.045% HCl, and solvent B is 80% water, 20% ACN, and 0.045% HCl. The wavelengths to monitor are 220 nm and 280 nm. Any peaks at 280 nm include peptide with Tyr-37, or any aromatic sidechain, and any peaks at 220 nm are due to peptide backbone bonds. The easiest way to prepare buffers is to prepare 4 L batches; doing so means exactly 6 mL of HCl should be added to solvents A and B. To prepare the peptide for high-performance liquid chromatography (HPLC), 1 mL of the peptide/DMSO solution and 1 mL of 20% acetic acid should be mixed in a 2 mL glass vial for the HPLC autosampler. It is ok to use the prep column rather than the analytical column for the first HPLC run; however, all peaks should be collected, lyophilized, and tested with MALDI-MS to determine which peaks are due to full length peptide. Figure 2.4a shows a trace at 280 nm of hIAPP purified on a C18 preparative column with a gradient of 5-95%B for 90 min. The large peak from 7-15 min is due to the injection peak of DMSO. The peak near 45 min is due to full-length, oxidized hIAPP. All other small peaks are due to impurities. Once the peak with full-length hIAPP has been determined, narrow the gradient both in the %B that is spanned, and in the time of the full gradient. Doing so allows for faster purification and less waste of solvents. Shown in Figure 2.4b is a trace at 280 nm of a 25-60%B over 35 min gradient on a C18 preparative column. The first peak is due to DMSO injection, and the peak near 27 min is due to pure hIAPP eluting from the column.

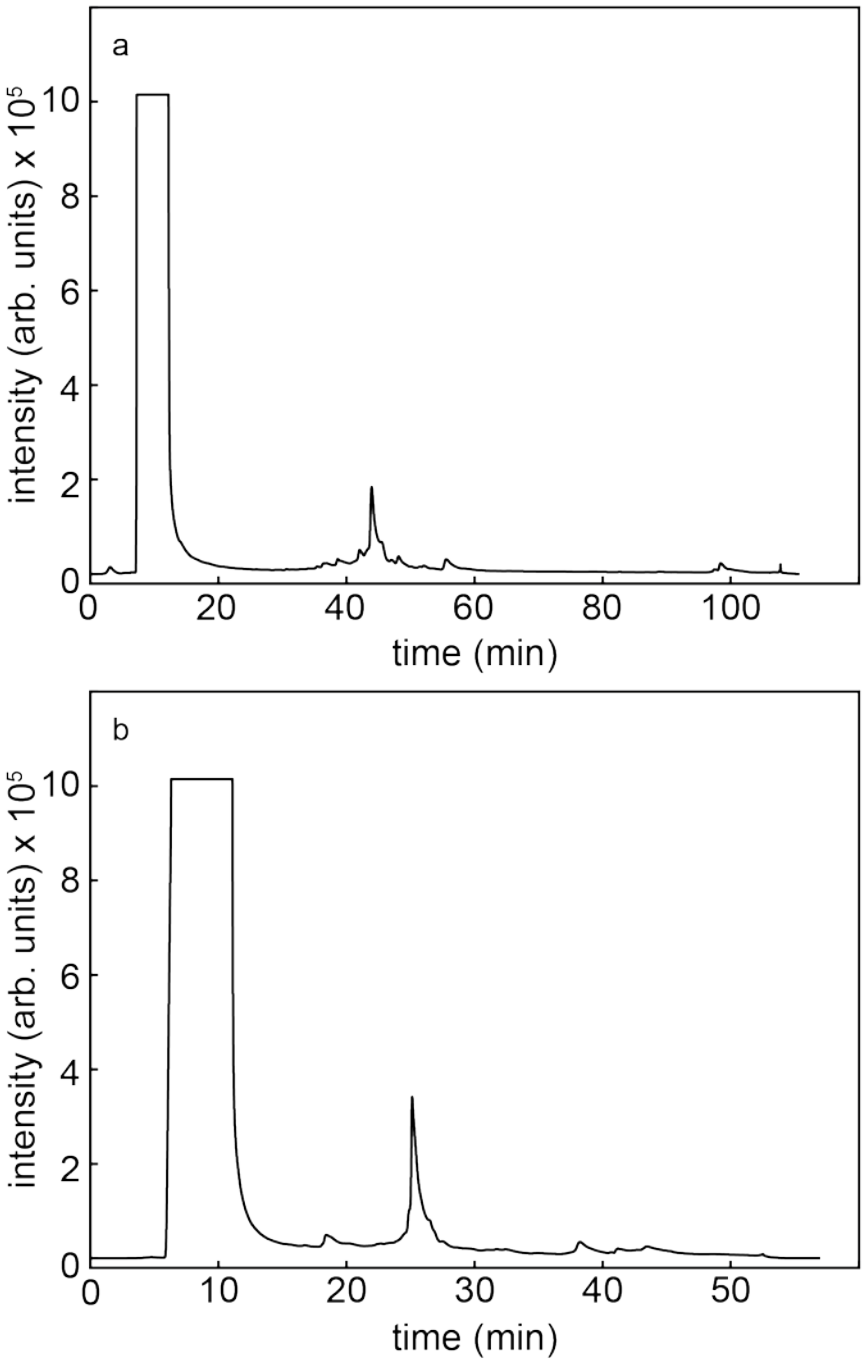

Figure 2.4 (a) HPLC chromatogram at 280 nm of crude hIAPP. The characteristic oxidized hIAPP retention time is ~45 min in a binary gradient of 5-95%B in 90 min in 100% water, 0.045% HCl and 80% ACN, 20% water, and 0.045% HCl. (b) HPLC chromatogram at 2880 nm of crude hIAPP. The solvent system is identical to that in (a), but the gradient has been shortened to 25-60%B in 35 min.

The hIAPP peak in Figure 2.4b is sharper and less congested than the hIAPP peak in Figure 2.4a. Narrowing the gradient is the best way to purify large batches of hIAPP.

Following purification of each HPLC run, the collected fractions should be lyophilized until dry. It is best to lyophilize the fractions as few times as possible, and then freeze the fractions until they can be combined. After all the fractions are dry, they should be dissolved in a small amount of water, combined into one centrifuge tube, and lyophilized one final time. After the recombined peptide is dry, it can take on many phases. Sometimes the peptide is white and fluffy, other times it is a pale yellow film, and sometimes it looks like pale yellow sand.

The Raleigh group performs an additional purification step that at this point is probably beneficial towards improving the solubility of hIAPP. After the purification described above, hIAPP is sometimes yellowish, indicating the presence of scavengers that were not removed in the ether step of cleavage or during purification. Scavengers might increase the aggregation rate and reduce the solubility of hIAPP; thus it is important to ensure they are completely removed from the sample. The Raleigh group dissolves hIAPP in hexafluoroisopropanol (HFIP) at 5-6 mg/mL. The solution is pale yellow and clear. Then, the HFIP solution is diluted into DI water at 0.8 mL HFIP into 10 mL water. This diluted HFIP solution is then injected into the HPLC and purified using the same buffer system as before. The peptide should elute from the column without scavengers, and after lyophilization should be a white powder.

Purifying hIAPP can be tedious because you cannot inject too much peptide onto the column; the peptide will readily aggregate and the chromatogram should be

monitored during wash cycles to ensure that no peptide is sticking to the column. During the first purification step, the DMSO and 20% acetic acid help to prevent aggregation on the column and should not be omitted. If the second purification step is deemed necessary, the HFIP should help keep hIAPP disaggregated. Following purification of the entire batch of cleaved peptide, the column should be washed several times with a 5-95% gradient, 100% B, and methanol to guarantee that the column is free from hIAPP and other contaminants.

2.5 Sample preparation for 2D IR spectroscopy measurements

Following the last lyophilization of the combined fractions, hIAPP (and any peptide) should first be verified by MALDI-MS and then be aliquoted into Eppendorf tubes, each containing ~1 mg of peptide. Figure 2.5a shows an example of a MALDI-MS spectrum of singly-isotope labeled and oxidized hIAPP. The main peak appears at 3906 m/z, better shown in Figure 2.5b. However, masses greater than 3906 may be acceptable. Sometimes, the peptide is attached to a sodium or potassium ion, and the detected mass is 23 or 39 units larger, respectively.

Additionally, the instrument sometimes needs calibrated so the detected mass could be inaccurate. One way to verify the calibration is to measure a MALDI-MS spectrum of a known sample of hIAPP and compare that to the recently purified sample.

Excess peptide that is not aliquoted should be sealed and stored at -80°C. The peptide that will be used in experiments should then be dissolved in deuterated hexafluoroisopropanol (d-HFIP); by dissolving in d-HFIP, the amide hydrogen atoms exchange for deuterium atoms and cause the amide II mode in the peptide to absorb

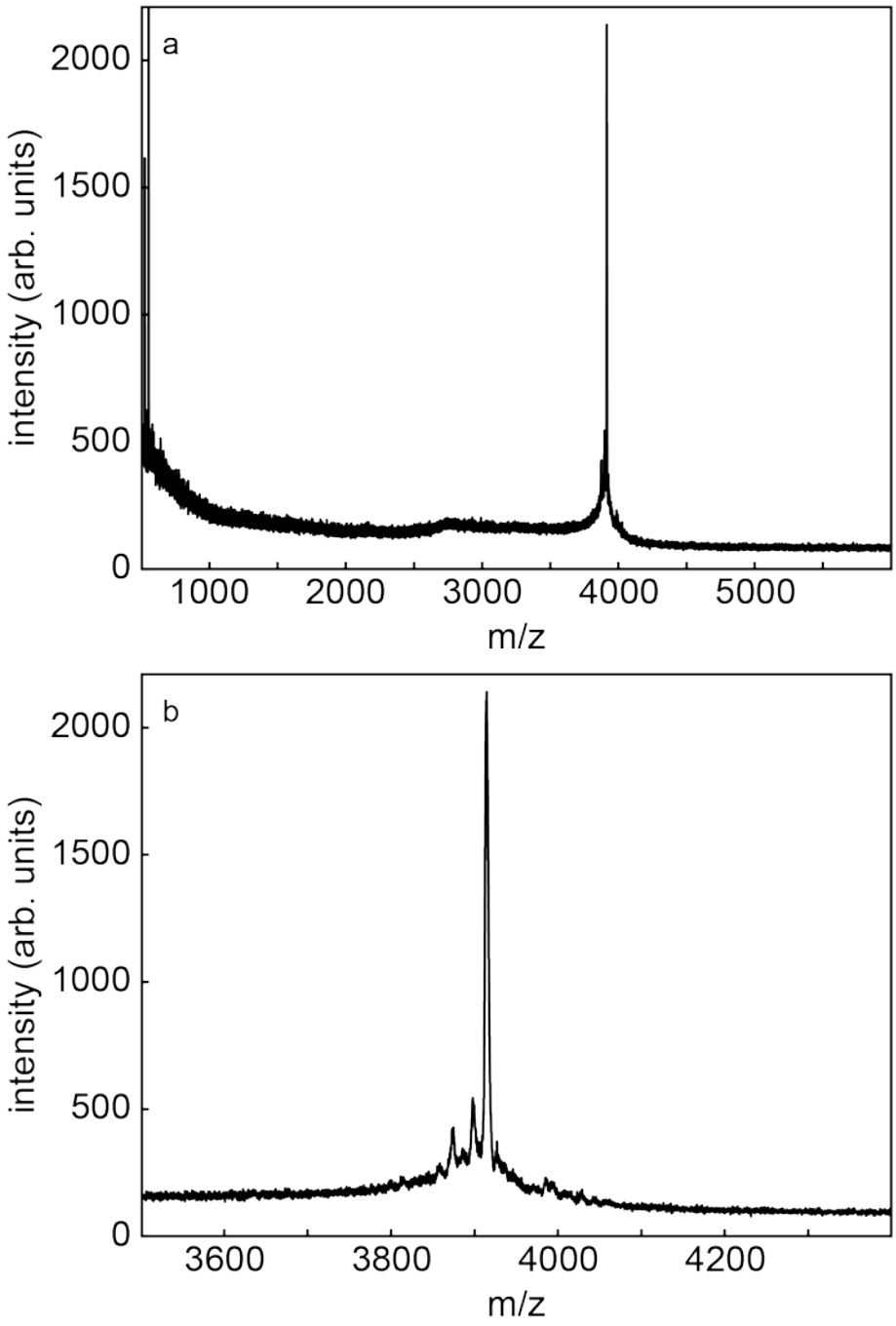

Figure 2.5 (a) MALDI-MS spectrum of purified hIAPP. The parent peak is 3906 m/z, which corresponds to hIAPP that contains a disulfide bond beteween Cys-2 and Cys-7, as well as a single $^{13}C^{18}O$ carbonyl group. (b) Enlarged MALDI-MS spectrum of purified hIAPP. A MALDI-MS spectrum with this little amount of extraneous peaks indicates the peptide has been well-purified.

outside the bandwidth of the laser. In addition, d-HFIP (and HFIP) prevents hIAPP from aggregating and evaporates easily; these are two characteristics that make it a good solvent in which to make stock solutions. The hIAPP/d-HFIP stock solution should be sonicated without heat for 4 h. After 4 h, the amide hydrogen atoms should be sufficiently exchanged for deuterium atoms. If the peptide has completely dissolved, it can be sealed and stored in the freezer (-20°C) until use.

However, if the peptide has not completely dissolved, several other steps may be necessary to solubilize hIAPP. Oftentimes when this happens, the first thing I do is continue sonicating the sample, but this time over gentle heat. HFIP evaporates near 60°C, and so I try not to heat the sample above 40°C. At this point, I have seen the peptide look like small white chunks, like long white strands, or look like a gel at the top of the solution. The next step is to lyophilize and remove the d-HFIP. I then add D_2O to make sure the peptide will dissolve in a more hydrophobic solvent. This may take a few hours of sonication to achieve. After dissolving hIAPP in D_2O, I lyophilize the sample. hIAPP should not be stored in D_2O as a long-term solution because the peptide will aggregate and will need to be disaggregated for kinetics experiments. After lyophilizing from D_2O, I try dissolving the sample in d-HFIP and sonicating again. If after 8 h of sonication, and additional heating if thought necessary, hIAPP still has not dissolved, the sample should be centrifuged for 30 minutes at $\geq$ 14,000 rpm. hIAPP and d-HFIP have similar densities, and thus the higher the rpm, the better separation will occur. After centrifugation, the supernatant can be removed from undissolved hIAPP that should form a pellet in the bottom of the tube. The supernatant can be sealed and stored in the freezer

(-20°C). Remaining work should be done on the pellet to get it to dissolve; another round of HPLC may be necessary, though by routinely including the Raleigh group's extra purification step, hIAPP will hopefully become more soluble.

After hIAPP has completely dissolved in d-HFIP, either by simply dissolving, or by being separated by centrifugation, the stock solution concentration should be measured. Previously, the concentration of stock solutions was not measured in our group. The ~1 mg aliquots of hIAPP massed after lyophilization will likely include many salts that will distort the true concentration of the sample. In addition, if the Eppendorf tube has been exposed to air or heated, some d-HFIP has evaporated. It is therefore critical to measure the concentration of the stock solution. To measure the concentration, remove 5 µL of the solution and place it into a small PCR tube. Lyophilize the sample for 30 min, and redissolve the sample in 5 µL of H_2O. The concentration of the sample can then be measured using UV-Vis detection at 280 nm. The absorbance at 280 nm is due to the Tyr-37 sidechain in hIAPP, and the molar extinction coefficient, ε, is 1300 $M^{-1}cm^{-1}$. It is fine if the stock solution is not 1 mM. It is better to work with the stock solution as is, rather than try to dilute it or make it more concentrated. If those steps are taken, it can sometimes be difficult to solubilize the peptide again in HFIP, and time will be wasted.

To prepare a 1 mM sample for 2D IR spectroscopy measurements, an aliquot of hIAPP should be removed from the stock solution and placed in a small PCR tube. The sample is then lyophilized for at least 30 min. If the sample will be used for kinetics measurements, any trace amounts of d-HFIP will enhance aggregation rates. It is

therefore better to lyophilize the sample for 6 h. If steady-state fiber measurements are all that is necessary, 30-60 min of lyophilization is sufficient. Following lyophlization, the sample should be redissolved in buffer to final concentration of 1 mM. The peptide will be a clear film on the walls of the tube, and care should be taken to dissolve the entire film. Once dissolved, the sample should be placed between two CaF_2 windows, the sample cell should be assembled, and the sample should be placed in the spectrometer for 2D IR spectroscopy measurements. If the sample is not to be measured immediately, it should be placed in a purge box in order to prevent water uptake into the sample.

hIAPP sample preparation can be tricky due to its solubility in d-HFIP. When hIAPP dissolves completely in d-HFIP, the turn-around between the last purification run and measuring a 2D IR spectrum is only 1 day. However, if hIAPP is not dissolving, it can take a week to prepare a stock of hIAPP for spectroscopy measurements. Thus, it is important moving forward to know if the additional steps the Raleigh group takes to purify their peptides aids in their solubility.

2.6 Preparation of micelles and membranes

Many interesting and difficult to study peptides and proteins are biologically relevant when attached to or imbedded in membranes. Samples containing membranes, however, can be quite challenging to work with, in particular because of their inhomogeneity and their ability to scatter light. Scatter is a huge problem when trying to measure 2D IR spectra of small peptides on a membrane because scatter can make it difficult to identify a good spot in the sample and in order to eliminate as much scatter as possible, it is necessary for the signal to average for at least 30 min. As a result, I have

developed a technique that produces low amounts of scatter and allows for easier data collection.

Membrane lipids should be purchased as chloroform solutions. While the lipids are still in chloroform, they should only be handled with glass syringes and should be stored in glass vials. Lipid mixtures, such as those used in Chapters 4 and 6, should be mixed in an appropriate ratio in a glass vial, and the bulk of the chloroform should be dried under a gentle stream of nitrogen for 4 h. Then, the lipids should dry under the strongest vacuum possible for an additional 24 h. After the chloroform has been removed, the lipids should be rehydrated in an appropriate amount of water. In order to form vesicles, the lipid solution should be subjected to 5 freeze-thaw cycles and then sonicated for 30 min above the phase transition temperature of the lipid. This will produce small unilamellar vesicles (15-50 nm). During the freeze-thaw cycles and sonication, the solution should become increasingly more clear. It will never become completely clear, however. After sonication, the solution should be aliquoted into small PCR tubes. Then, the tubes should be lyophilized to dryness, sealed, and frozen. Hydrated lipid membranes begin to degrade after ~7 days. It is best to only thaw one aliquot of lipids per experiment in order to maintain the integrity of the membrane. After thawing an aliquot for experimentation, rehydrate the lipids with D_2O or buffer, perform 5 freeze-thaw cycles, and sonicate as described previously. After sonication, the lipids can be added to the peptide of interest. Once the lipids and peptide are combined, they should be sonicated together for 30 min at a temperature above the phase transition temperature.

In order to make samples for 2D IR spectroscopy measurements with the least scatter, it is best to add the lipids to the sample cell when the lipids are at an elevated temperature. In addition, the CaF_2 windows should also be heated on a hot plate to ~50°C. By making the sample at an elevated temperature, the lipids form a more clear sample on the windows. The lipids are more ordered and they produce less scatter for 2D IR spectroscopy measurements.

Lipid bilayers cause more scatter and are more difficult to prepare than micelles; for that reason, many peptides are studied in micelles. To prepare micelle samples, micelles should be purchased as solids, dissolved to an appropriate concentration in chloroform, dried under nitrogen for 4 h, and lyophilized under a strong vacuum for 24 h. Once dry, the film should be rehydrated in D_2O and sonicated above the phase transition temperature for 1 h. After sonication, the solution should be completely clear. Again, the solution should be aliquoted into smaller portions and be lyophilized, sealed, and stored in a freezer until use, so that only a small amount of micelles are thawed for each experiment. After thawing one aliquot for an experiment, it should be rehydrated, sonicated for 1 h, and added to the peptide. Micelles are generally much more uniform that lipid bilayers and do not contribute scatter to 2D IR measurements. For these reasons, it is not critical to make micelle samples at elevated temperatures.

2.7 Preparation of samples for hydrogen-deuterium exchange measurements

Chapter 6 will concern a series of a HDX experiments I performed on the membrane-bound peptide, ovispirin. HDX experiments are commonly performed on

proteins using nuclear magnetic resonance (NMR) spectroscopy and mass spectrometry. These techniques can be very powerful for determining HDX rates and therefore structures of proteins. However, one characteristic they lack is the ability to measure HDX rates on-the-fly under physiological conditions. To this end, I have developed a method using our existing sample cell design to enable HDX measurements without any additional instruments and without using costly techniques such as quenching.

Figure 2.6 shows a diagram of our of traditional sample cell from both the front and side perspectives. The only difference between a traditional sample cell and one that can be used for HDX measurements is the CaF_2 windows. In a regular cell, two 1" diameter windows are used. In a cell for HDX, one 1" diameter window is used as the bottom window, and one 1" diameter window that has been cut in half is used as the top window. After placing the sample (with all hydrogen atoms in the amide II position) on the bottom window, the half-window is placed on top and the rest of the cell is assembled as usual. As a result, half of the sample is exposed to air, while half of the sample is still smashed between two windows.

When placing the sample cell in the spectrometer, it is important that the helium-neon (HeNe) and mid-IR beams are well-overlapped at the sample. This is important for all samples, but especially for HDX measurements. The reason is that when positioning the cell in the spectrometer, the cell should be aligned such that the HeNe beam passes through both windows, albeit at the edge of the half window. If both the HeNe and mid-IR are well-overlapped, this will ensure that the mid-IR is passing through both windows and will pass through sample that will be exposed to deuterated buffer. Once the sample

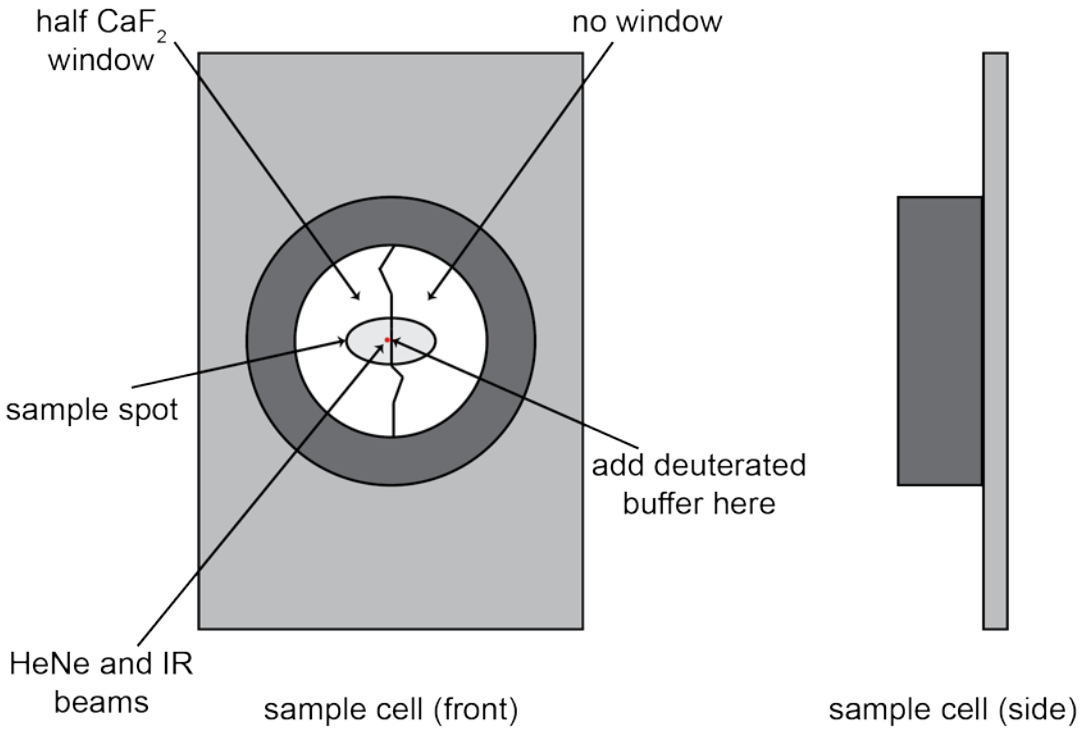

Figure 2.6 A typical sample cell used for HDX experiments from the front and side views. Instead of two full CaF_2 windows, the sample is placed between a full and a half CaF_2 window. The sample cell should be aligned such that the HeNe and mid-IR beams pass through both windows and the sample, albeit at the edge of the half window (red spot). The deuterated buffer for HDX can then be added to sample cell directly at the edge of the half window, without having to disassemble the sample cell. Data collection can proceed as the deuterated buffer is added, eliminating any experimental dead time.

cell is in place and a spectrum of the sample has been averaged, deuterated buffer can be added directly to the sample cell. Deuterated buffer should be added to the edge of the half-window. The buffer will be whisked between the windows and the sample will begin exchanging.

2.8 Tips for building a stable optical parametric amplifier

During part of my second and third years of graduate school, I had the opportunity to design and build a laser table. The KMLabs-designed oscillator was pumped by a Spectra-Physics Millennia. A Spectra-Physics Empower pump laser pumped the KMLabs-designed regenerative amplifier (regen), and the stretcher and compressor were designed by KMLabs, as well. The first design of these components included housing the Millennia in the same box as the oscillator, stretcher, regen, and compressor. After several months, it was discovered that the Millennia output too much heat and was causing a temperature gradient inside the box. Lauren Buchanan and I ended up moving the Millennia outside the box. It is my suggestion that pump lasers never sit in the same box as other optics unless there is a clear way to expel the heat they produce.

Since the laser was a prototype system, intending to run at 5 kHz, there was no manual with details on aligning the stretcher or regen. An optical layout was provided, and Appendix 1 contains the beam path and optics labels for the stretcher, regen, and compressor on the Wyvern table. In addition, there are detailed instructions on stretcher and regen alignment. I am including the details in Appendix 1, though after I graduate, it

would be a good idea to consult Sudipta Mukherjee's, Lauren Buchanan's, and David Skoff's theses to see if they have included additional alignment details.

Once the laser system was consistently outputting high power (~4.5 W at 1 kHz), the optical parametric amplifier (OPA) was much easier to build and align. Below is a schematic of the OPA (Figure 2.7). P-polarized 800 nm light is emitted from the compressor. After passing through a periscope (not shown), the polarization switches to s-polarized light. First the 800 nm light reflects off an s-polarized 800 nm high reflector, and then 2% of the light is split to produce white light continuum (BS2R). The white light passes through a half-waveplate to rotate its polarization to p-polarized light, then through a lens (L1), and then through a thin film polarizer (TFP) to ensure only p-polarized light is allowed on this pass. The white light then passes through a 30% neutral density filter (F) to block even more of the light. Then, the white light is focused onto a sapphire crystal, recollimated by another lens (L2), passes through a manual translation stage with silver mirrors (TS, Ag), and is focused on a Type II β-barium borate (BBO) crystal. After the white light is split off, 10% of the remaining s-polarized light is transmitted through a beam splitter to make the first pass and the remaining light is reflected to make the second pass (BS90R). The first pass is then focused (L3) into the BBO crystal. The white light transmits through a long wave pass filter (LWP1) and the first pass reflects off of it; the two beams should be overlapped in space and time at the BBO in order to produce signal and idler beams. When they are overlapped, white light continuum is produced on the crystal and green wings form (Figure 2.8a). To ensure that the white light and first pass are properly overlapped, block the white light pass with your

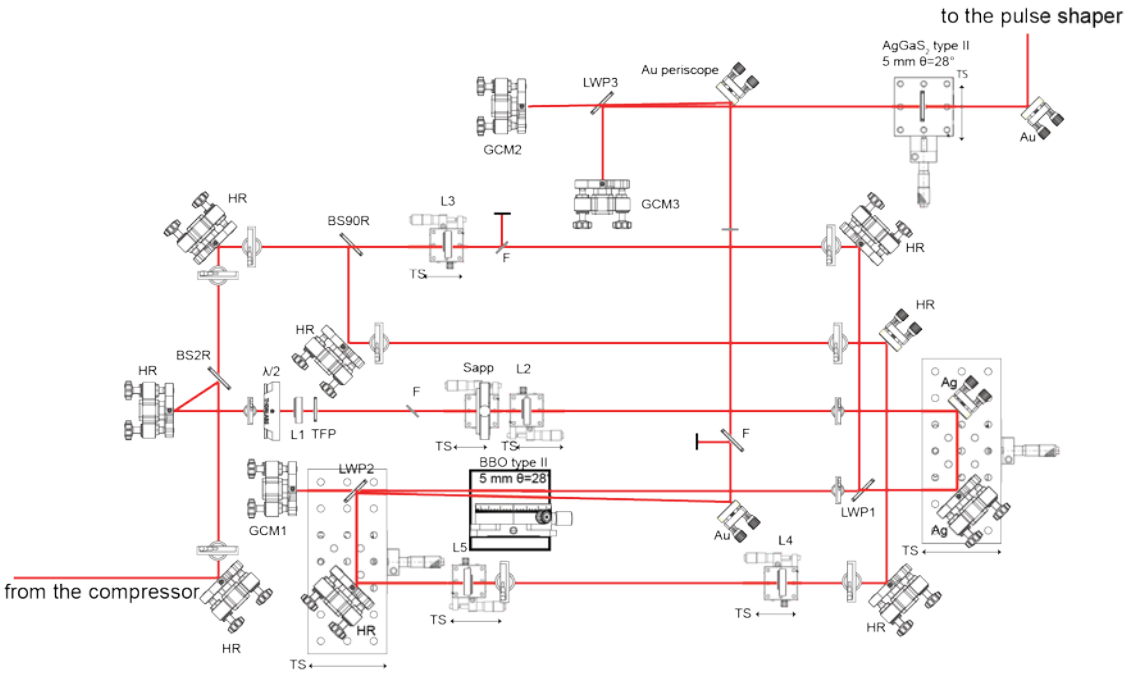

HR = high reflector mirror for 800 nm light
TS = translation stage
Ag = silver mirror
Au = gold mirror
TFP = thin film polarizer
λ/2 = half-waveplate
F = filter
Sapp = sapphire window
BS2R = beam splitter, reflects 2%, transmits 98%
BS90R = beam splitter, reflects 90%, transmits 10%
BBO = β-barium borate crystal
$AgGaS_2$ = silver gallium sulfide crystal
GCMx = gold curved mirror with a set focal length
GCM1 = 25 cm
GCM2 = 30 cm
GCM3 = 30 cm

Lx = lens with variable focal lengths
L1 = 20 cm
L2 = 3.5 cm
L3 = 75 cm
L4 = 30 cm
L5 = -10 cm

LWPx = long wave pass filter (set at 45˚)
LWP1 = reflect s-polarized 800 nm light
transmit p-polarized 1240-1530 nm light
LWP2 = relfect s-polarized 800 nm light
transmit p-polarized 1240-1530 nm light
LWP3 = reflect s polarized 1385 ± 70 nm
transmit p-polarized 1680 ± 22 nm

Figure 2.7 Optical layout and beam path of an OPA. Light enters the OPA after being ejected from the compressor and passing through a periscope. Light exits the OPA and difference frequency generation setup and then goes to a pulse shaper. A guide for the abbreviations of the optics in the OPA is given as well.

hand; if this causes the wings in Figure 2.8a to disappear (Figure 2.8b), then the white light and first pass are overlapped in space and time and signal and idler beams are being generated.

After the white light and first pass generate signal and idler beams, the signal and idler transmit through another long wave pass filter (LWP2), and reflect off of a gold curved mirror (GCM1) that collimates each beam. The signal and idler are then sent back through the BBO crystal and overlapped with the remaining 800 nm light, called the second pass. Before reaching the BBO crystal, the second pass passes through a pair of lenses that telescope to half its original diameter (~0.5 cm), and then through a delay stage so the timing can be controlled. When the second pass and signal and idler are overlapped spatial and temporally at the BBO crystal, the signal and idler pulses are amplified. The signal and idler pass through a filter to absorbs extraneous 800 nm light, and then through a periscope that switches their polarizations. Then, the signal and idler are separated by a long wave pass filter (LWP3), are reflected off of two curved mirrors (GCM2 and GCM3), are recombined, and then overlapped spatially and temporally at a $AgGaS_2$ crystal. The difference in frequency of the signal and idler beams yields mid-IR light.

The OPA described above and shown in Figure 2.7 is generally the same as all the home-built OPAs in the group. One tip towards building an OPA is to thoughtfully and liberally place irises throughout the beam paths. In this OPA, irises were placed before and after several high-reflector (HR) mirrors and before and after lenses in order to be sure the beams were hitting the center of the lenses. Variables that can change from OPA

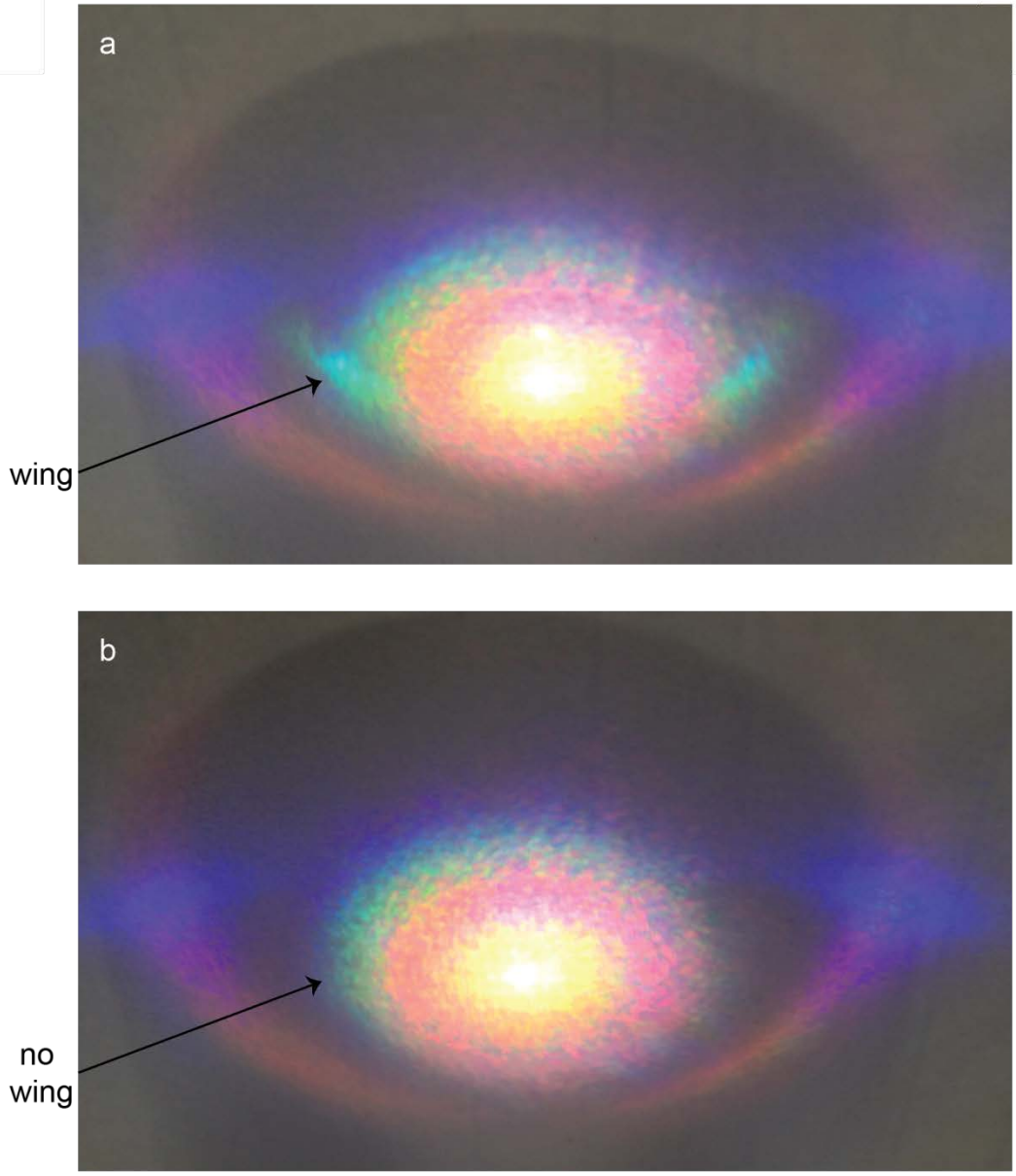

Figure 2.8 A card has been placed after the BBO crystal in the OPA and the second pass has been completely blocked. (a) Photograph of the continuum generated when the white light and first passes are overlapped in space and time at the BBO crystal. Green wings form. (b) Photograph of the continuum generated when the white light and first passes are not overlapped at the BBO crystal. When aligning the OPA, the continuum will look like (b) until the correct timing and spatial overlap has been achieved (a). To double check that the wings are real, block the white light with a notecard. If the wings are truly generated from white light/first pass overlap, the wings will disappear when the white light is blocked or when the timing of the white light translation stage is changed.

to OPA include thickness of the sapphire window and lens focal length. When building an OPA, these are some of the least expensive optics. It is beneficial to have a variety of lenses and sapphire windows on hand to see what works best.

There have been two major changes to the OPA since I stopped working with it. One is that the sapphire window has been replaced by a YAG window, for better stability. The other major change is that a cube polarizer has been placed in the narrow region between LWP2 and GCM1 (Figure 2.7). Cube polarizers work by allowing one polarization of light to transmit, while the polarization(s) of light get reflects orthogonal to the transmitted light. This cube polarizer only allows the idler beam to transmit through the cube, reflect off GCM1, and transmit back through the cube to overlap with the second pass at the BBO. By rejecting the signal beam and transmitting the idler beam, there is less destructive interference between the two beams and the second pass is more efficiently converted to signal and idler when overlapped in the BBO. Adding this cube polarizer more than doubled the amount of mid-IR generation in the OPA, and enhanced stability. I point out this particular optic because not every OPA uses a cube polarizer in that position; however, it should always be considered as a possible way to increase the amount of mid-IR light being generated.

2.9 References

(1) Woys, A. M.; Almeida, A. M.; Wang, L.; Chiu, C.-C.; McGovern, M.; de Pablo, J. J.; Skinner, J. L.; Gellman, S. H.; Zanni, M. T. *J. Am. Chem. Soc.* **2012**.

(2) Torres, J.; Adams, P. D.; Arkin, I. T. *J. Mol. Biol.* **2000**, *300*, 677-685.

(3) Torres, J.; Kukol, A.; Goodman, J. M.; Arkin, I. T. *Biopolymers* **2001**, *59*, 396-401.

(4) Marek, P.; Woys, A. M.; Sutton, K.; Zanni, M. T.; Raleigh, D. P. *Org. Lett.* **2010**, *12*, 4848-4851.

(5) Middleton, C. T.; Woys, A. M.; Mukherjee, S. S.; Zanni, M. T. *Methods* **2010**, *52*, 12-22.

(6) Woys, A. M.; Lin, Y.-S.; Reddy, A. S.; Xiong, W.; de Pablo, J. J.; Skinner, J. L.; Zanni, M. T. *J. Am. Chem. Soc.* **2010**, *132*, 2832-2838.

(7) Cruz, L. J.; Beteta, N. G.; Ewenson, A.; Albericio, F. *Org. Process Res. Dev.* **2004**, *8*, 920-924.

(8) Abedini, A.; Raleigh, D. P. *Org. Lett.* **2005**, *7*, 693-696.

CHAPTER 3*

Deamidation Accelerates Amyloid Formation and Alters Amylin Fiber Structure

3.1 Abstract

Deamidation of asparagine and glutamine is the most common non-enzymatic, post-translational modification. Deamidation can influence the structure, stability, folding, and aggregation of proteins and has been proposed to play a role in amyloid formation. However there are no structural studies of the consequences of deamidation on amyloid fibers, in large part because of the difficulty of studying these materials using conventional methods. Here we examine the effects of deamidation on the kinetics of amyloid formation by amylin, the causative agent of type 2 diabetes. We find that deamidation accelerates amyloid formation and the deamidated material is able to seed

* This chapter was originally published as the following: Dunkelberger, Emily B., Buchanan, Lauren E., Marek, Peter, Cao, Ping, Raleigh, Daniel P., Zanni, Martin T., "Deamidation Accelerates Amyloid Formation and Alters Amylin Fiber Structure", *J. Am. Chem. Soc.*, 2012, *134* (30), 12658.

amyloid formation by unmodified amylin. Using site-specific isotope labeling and two-dimensional infrared (2D IR) spectroscopy, we show that fibers formed by samples that contain deamidated polypeptide contain reduced amounts of β-sheet. Deamidation leads to disruption of the N-terminal β-sheet between Ala-8 and Ala-13, but β-sheet is still retained near Leu-16. The C-terminal sheet is disrupted near Leu-27. Analysis of potential sites of deamidation together with structural models of amylin fibers reveals that deamidation in the N-terminal β-sheet region may be the cause for the disruption of the fiber structure at both the N- and C-terminal β-sheet. Thus, deamidation is a post-translational modification that creates fibers which have an altered structure, but can still act as a template for amylin aggregation. Deamidation is very difficult to detect with standard methods used to follow amyloid formation, but isotope labeled IR spectroscopy provides a means for monitoring sample degradation and investigating the structural consequences of deamidation.

3.2 Introduction

Post-translational modifications are common steps in polypeptide and protein biosynthesis. They include phosphorylation, glycoslyation, lipidation, amidation of the C-terminus and acetylation, as well as disulfide bond formation.[2-4] These post-translational modifications occur *in vivo* in a myriad of proteins and are under careful biological control. Deamidation of Asn and Gln side chains is a common spontaneous, non-enzymatic post translation modification *in vivo* and *in vitro*, and is caused by a reaction of asparagine or glutamine side chains with the protein backbone.[5-8] Deamidation can influence the structure, stability, folding, and aggregation of proteins

and is proposed to play a role in amyloid formation.[7,9-12] Deamidation is also a concern with protein and polypeptide based pharmaceuticals.[13] Under physiological conditions deamidation proceeds through a 5-membered succinimide intermediate. The ring subsequently hydrolyzes into either aspartic or isoaspartic acid (from asparagine), while for glutamine, either glutamic or isoglutamic acid is formed (Figure 3.1). Deamidation favors the production of the L-forms of the products, but can racemize to the D-forms via the succinimide intermediate. The ratio of the iso-products to normal products is 3:1.[6] Deamidation can cause major perturbations to the structure and stability of a protein because it adds a negative charge. When the iso-product is formed, deamidation extends the length of the backbone by a CH_2 group and thus introduces another rotatable bond into the peptide backbone.

Deamidation has been implicated in amyloid formation by several proteins involved in human disease, including amyloid-β (Aβ) from Alzheimer's[7,9,12,14-16] and the crystallins[10,17,18] from cataracts. α-synuclein, which causes Parkinson's and other neurodegenerative diseases, also deamidates.[19,20] Some otherwise non-amyloidogenic peptides have been shown to become amyloidogenic upon deamidation.[21] Although not strictly deamidation, all three Asp residues in the Aβ polypeptide of Alzheimer's disease patients have been found to isomerize to isoAsp, thus adding an additional bond to the peptide backbone and causing structural disorder. It has been reported that 55% of Asp-7 in Aβ isomerizes to isoAsp-7 in senile plaques.[12] In addition, two common Aβ mutations, the Iowa mutation (Asn-23) and the Tottori-Japanese mutation (Asn-7) have both been found to deamidate to isoAsp in Alzheimer's disease patients.[7,14] While it is

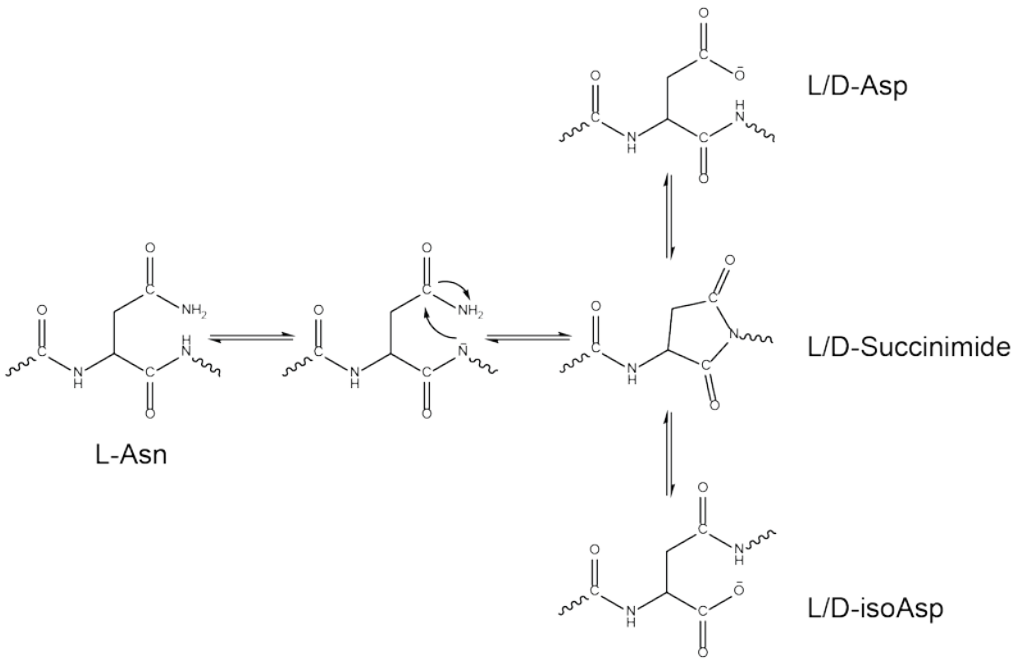

Figure 3.1 Mechanism for deamidation of L-Asn.

still not explicitly understood the role deamidation has in forming Alzheimer plaques, one hypothesis is that the mutation at Asp-23 to Asn-23 and the subsequent deamidation to isoAsp-23, in the turn region of Aβ, might cause a structural change to Aβ that initiates folding into β-sheets.[16] Deamidation may contribute to plaque formation through the isomerization to isoAsp that presumably prevents proper degradation of damaged peptides.[16] Regarding the crystallin proteins, King and coworkers showed that deamidation of Gln residues, which appear at the interface of two domains in γD-crystallin, lowered the barrier to unfolding, thus increasing the probability of populating partially unfolded states.[17] It is suggested that these partially unfolded states could be more likely to aggregate. Using non-cataractous lenses from human patients of varying ages, ten different residues of γD-crystallin were determined to deamidate (out of 167) and, in general, the amount of deamidation at each site increased with age of the protein. Thus, deamidation is thought to be an important cause of cataract formation.

Similar in sequence to human amylin is pramlintide, the synthetic drug used as replacement therapy in diabetics. The two peptides differ slightly in structure with mutations at A25P, S28P, and S29P.[22] A deamidation study was performed on pramlintide in which it was thermally stressed at 40°C for 45 days.[23,24] The results show that five of the six asparagine residues, with the exception of Asn-31 showed some amount of deamidation to either aspartic or isoaspartic acid. The residues with the most observed deamidation were Asn-21 and Asn-35. High levels of deamidation at Asn-21 were attributed to the hydrophilic Ser-Asn-Asn sequence and residues 20 and 22 aid in deamidation of Asn-21. Asn-35 was the second-most deamidated residue. It is thought

that Asn-Ser sequences are more prone to deamidation, and in fact have been measured to have deamidation half-lives has short as 16 days under physiological conditions.[25] It was speculated that Thr-36, being similar in structure to Ser, might allow Asn-35 to have higher amounts of deamidation than other Asn residues,[23,24] and the deamidation half-life for Asn-Thr is 47 days.[25] Deamidation rates are also closely correlated with peptide structure, and typically the deamidation rate slows with increasing three-dimensional structure.[26] Overall, the C-terminus of pramlintide had higher levels of deamidation than the N-terminus, with Asn-3, located in the sequence between the disulfide bond, having the lowest amount of deamidation products.

In this chapter, we focus on the effects of deamidation on the *in vitro* fiber structure and aggregation kinetics of human amylin (human islet amyloid polypeptide-hIAPP) the major component of the islet amyloid associated with type 2 diabetes. Amylin has been identified in all mammals examined and it is secreted together with insulin. The polypeptide normally acts as a partner to insulin[27-31], but it is responsible for islet amyloid in type-2 diabetes.[29-38] The factors which trigger amyloid formation by human amylin are not completely understood, but it is one of the most amyloidogenic polypeptides known and many studies have been done to understand its aggregation.[1,39-44] Aggregates of human IAPP are toxic to pancreatic β-cells, strongly suggesting that the process of amyloid formation by amylin contributes to islet cell death in type 2 diabetes. Islet amyloid has also been proposed to play an important role in the failure of transplanted islet cell grafts.[45,46] Human IAPP is a 37 residue peptide hormone that has a disulfide bridge between Cys-2 and Cys-7 and an amidated C-terminus (Figure 3.2a).

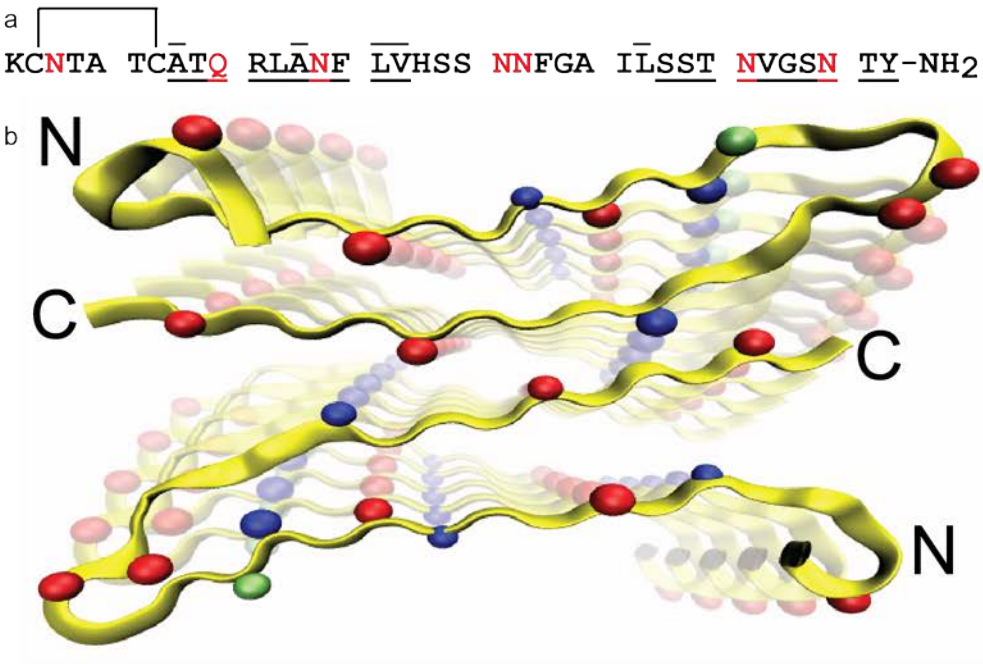

Figure 3.2 (a) Sequence of hIAPP. Potential sites for deamidation are shown in red and residues that were isotope labeled for this study are shown with an overbar. There is a disulfide bond between Cys-2 and Cys-7, and the C-terminus is amidated. Underlined amino acids have parallel β-sheet structure, according to Tycko.[1] (b) Structural model for an isomorphic structure of amylin fiber from solid-state NMR. Asparagines and glutamine are shown in red. The four isotope labeled residues incorporated into deamidated amylin are shown in blue. Val-17 is shown in green. The perspective of the figure is looking down the fiber axis.

The polypeptide contains six Asn residues and one Gln. Interactions involving Asn side chains have been proposed to be important in amyloid formation by human amylin and mutation of certain Asn residues to Leu, an approximately isoteric substitution, has been shown to have large effects on the kinetics of assembly.[47] While it is not known if amylin is deamidated in the plaques of the β-islet cells of type 2 diabetics, we report here that it readily deamidates under physiological conditions *in vitro*. Moreover, we discover that there is a major change to the fiber β-sheet structure which is not resolved with TEM, CD, or standard linear or 2D IR spectroscopy, all of which produce images or spectra that are indistinguishable from those of polypeptides that are not deamidated. We are able to identify the change in secondary structure by the combination of isotope labeling and 2D IR spectroscopy. $^{13}C^{18}O$ labeling allows the backbone amide I vibrational modes of individual residues to be spectroscopically identified. As described in more detail below, the isotope labeled amino acids are very strongly coupled to one another in the parallel β-sheet structure of amyloid fibers, which produces distinctive frequency shifts and cross peaks. These spectral signatures are a sensitive measure of structure change. While it is clear that the addition of a charge and the conversion of a standard amino acid to a β-amino acid could have repercussions for amyloid fiber structure and aggregation kinetics, ascertaining the location and extent of the structure change is difficult. Isotope edited 2D IR spectroscopy enables one to probe, residue-by-residue, the effects of deamidation.

3.3 Overview of how isotope labeling and 2D IR spectroscopy allow for the identification of parallel β-sheets with residue-specificity

Many amyloid polypeptides and proteins, including hIAPP, whose sequence and structure is shown in Figure 3.2, form parallel β-sheets when folded into amyloid fibers.[39,48,49] In particular, hIAPP fibers consist of two columns of hIAPP monomers that contain one turn. Intermolecular hydrogen bonds form between the stacked monomers, essentially creating a structure of four parallel β-sheets that run along the fiber axis. There are no intra-peptide hydrogen bonds between backbone groups. Amyloid fibers have a distinctive absorption band in their infrared spectra at about 1620 cm^{-1}, which is caused by vibrational coupling between the amide groups of the amino acids.[50] The strongest couplings are between in-register residues that span from one strand to the next, although the coupling is caused by electrostatics, not hydrogen bonding.[51] The couplings cause the vibrational modes to delocalize over several amino acids, so that they all vibrate in unison. Delocalized normal modes occur in β-sheets in globular proteins as well, but they are particularly evident in amyloid fibers, because the parallel β-sheets are very large and structurally well-ordered.

The strong coupling between β-strands provides an effective means of using isotope labeling to test for parallel β-sheet structure. If an amino acid is isotope labeled with a $^{13}C^{18}O$ backbone carbonyl, the frequency of that particular amide I mode is shifted ~54 cm^{-1} from the frequency of the unlabeled (random coil) amide I modes due to the change in its reduced mass.[50] In hIAPP, each polypeptide contributes one strand to each of the β-sheets. Thus, in the parallel β-sheets of the amyloid fiber, the isotope labeled amino acids align in register (Figure 3.3).[50,52] As mentioned above, the coupling between in-register residues is particularly strong, and so the vibrational modes of the labeled

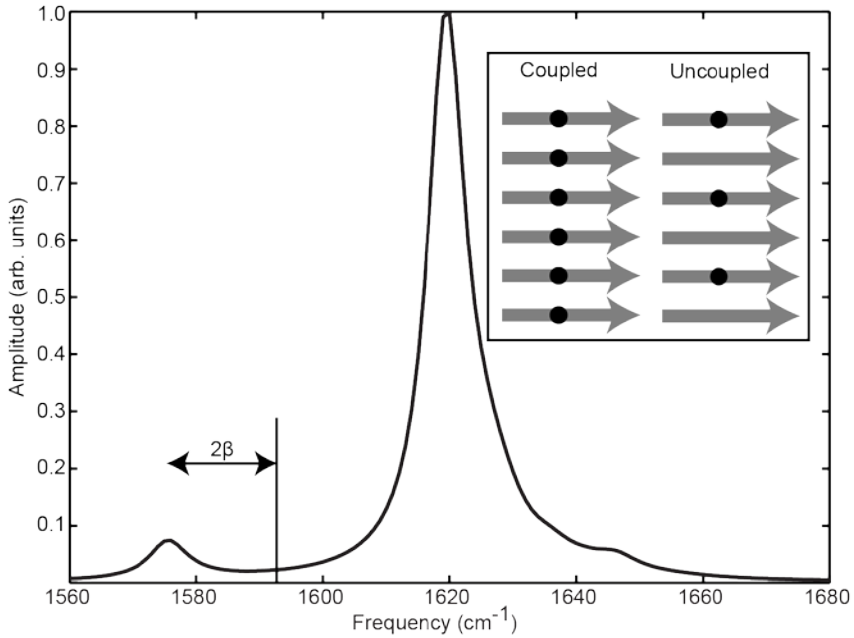

Figure 3.3 Model slice through the diagonal of a 2D IR spectrum of an isotopically labeled parallel β-sheet. The unlabeled amide I mode absorbs at 1620 cm^{-1}, while the strongly coupled, in-register isotope labeled amino acid absorbs at ~1575 cm^{-1}.

residues become delocalized into a chain that spans many β-strands. The result is a shift in frequency that is less than or equal to twice the coupling constant, β.[53,54] Typically, the coupling constant between two in-register residues in adjacent parallel β-strands is -9 to -11 cm^{-1}, and thus the frequency shift due to excitonic coupling can be as large as 20 cm^{-1} pacid experiences a different amount of structural disorder, which localizes the vibrations. Residues at the ends of the peptide where the β-sheet frays and residues in the turn region are less ordered and the effects of the coupling are small.[50] Moreover, the absolute frequency for each chain of residues may be different, even if the coupling strengths are the same, because of differences in electrostatic environments.

Electrostatic environments influence the frequencies of individual amino acids (local mode frequencies) and thus the diagonal linewidth. Measuring diagonal linewidths and overall lineshapes of isotope labeled amino acids in a peptide can be a useful experiment to determine the local environment of the labeled residue. For example, a narrower diagonal linewidth can be ascribed to a more homogeneous local environment and less electrostatics, whereas a larger diagonal linewidth means the residue lies in a more inhomogeneous environment and is subject to stronger electrostatic forces. This has been shown to be particularly useful when studying membrane peptides where the diagonal linewidths of residues that are located outside the membrane versus inside the membrane can vary by ~15 cm^{-1}.[40,55]

Thus, to obtain the frequency shift caused by coupling, we also need to know the local mode frequency of the individual amino acid, which we find by measuring fibers formed by a ~1:3 mixture of labeled and unlabeled peptides.[48,56] In isotope diluted

samples, the coupling is less effective across the linear chains, and so the vibrational modes localize. The frequency of the isotope labeled peak now reports the frequency when no coupling exists at that residue and is the intrinsic frequency of the labeled amino acid, which is a measure of its electrostatic environment. By measuring the frequency of fibers formed with 100% isotope labeled polypeptides and comparing it to the frequency of fibers formed from isotope diluted polypeptides, we obtain the frequency shift caused by coupling from which we can determine if the labeled amino acid residues in a parallel β-sheet. We have used this characteristic of parallel β-sheets to study the residue-specific aggregation kinetics, the stability, and the drug binding to amyloid fibers of hIAPP.[56,57]

3.4 Materials and Methods

3.4.1 Peptide synthesis and preparation of isotope labeled amino acids

hIAPP is a 37 residue polypeptide whose sequence and structure is shown in Figure 3.2. Peptides were prepared using standard FMOC solid phase peptide synthesis with a CEM Liberty 12-Channel Automated Peptide Synthesizer.[58] To produce an amidated C-terminus, PAL-PEG-PS resin was used. Pseudoproline dipeptides were incorporated to facilitate the synthesis as described elsewhere.[59] Standard trifluoroacetic acid (TFA) cleavage and deprotection protocols were used, and 1,2-ethanedithiol, anisole, and thioanisole served as scavengers. Crude peptide was dissolved overnight in dimethylsulfoxide (DMSO) at ~5 mg/mL to induce disulfide bond formation between Cys-2 and Cys-7. $^{13}C^{18}O$ isotope labeled alanine, leucine, and valine were individually incorporated into hIAPP at positions Ala-8, Ala-13, Leu-16, Leu-27, and Val-17. Fmoc-protected amino acids with the backbone carbonyl labeled with $^{13}C^{18}O$ were prepared as

described starting from ^{13}C C1 labeled amino acids (Cambridge Isotope Laboratories) and ^{18}O water.[57] The labeling levels were confirmed with LC-MS and greater than 90% labeling efficiency was achieved. Peptides were purified using reversed-phase HPLC with a C18 preparative column (Vydac) and absorbance was monitored at 200 nm and 280 nm. A two buffer system was used: buffer A consisted of H_2O and 0.045% HCl (v/v), and buffer B consisted of 80% acetonitrile (ACN), 20% H_2O, and 0.045% HCl (v/v). The gradient varied from 0-90% B over 90 minutes. TFA was not used as the counter ion to allow for the complete removal of residual TFA, which is required for IR spectroscopy. The molecular weight of all peptides was confirmed using MALDI-MS.

3.4.2 Detection of deamidation

Following synthesis, the peptides were allowed to age. Deamidation occurred spontaneously over the course of several months. Throughout this paper, all peptides that were allowed to age will be referred to as 'deamidated', whereas peptides that had not degraded and undergone deamidation will be referred to as 'unmodified'. To assess the degree of deamidation for each of the four samples, reverse-phase HPLC was performed with a C18 analytical column (Vydac) and absorbance was monitored at 220 nm and 280 nm. A two buffer gradient was used: buffer A consisted of H_2O and 0.1% (TFA) and buffer B consisted of 80% ACN, 20% H_2O, and 0.1% TFA. The gradient varied from 0-90% B over 90 minutes. Under these conditions (pH 2), hIAPP with native asparagine and deamidated hIAPP with isoaspartic acid will have identical retention times, while hIAPP that has had asparagine deamidated to aspartic acid will elute later.[21] Additionally, HPLC was performed at pH 5. Except for different buffers, HPLC at pH 5

was performed identically to that at pH 2. A two buffer gradient was used: buffer A consisted of 10 mM phosphate in H_2O and buffer B consisted of 10 mM phosphate in 80% ACN and 20% H_2O. Under these less acidic conditions, deamidated hIAPP with aspartic acid or isoaspartic acid has a shorter retention time than hIAPP with native asparagine.

3.4.3 Sample preparation

Samples for spectroscopy experiments were prepared by dissolving hIAPP in deuterated hexafluoroisopropanol (d-HFIP) to a final concentration of 1 mM. After four hours, hIAPP was completely deuterated. d-HFIP was evaporated under a stream of nitrogen and fiber formation was initiated by adding 20 mM deuterated potassium phosphate buffer at ~pH 7.4 to a final peptide concentration of 1 mM. The sample was then placed between two 2 mm thick CaF_2 windows separated by a 56 μm Teflon spacer. All samples were kept in a purge box until and during use. This method of fiber formation is known to create polymorphic fibers that differ near the turn region but have similar β-sheet forming regions.[1,56]

3.4.4 Two-dimensional infrared spectroscopy

The 2D IR spectroscopy experimental setup consists of a home-built Ti:sapphire oscillator that seeds a Nd:YLF-pumped regenerative amplifier as described in more detail elsewhere.[57] Briefly, the 800 nm output is sent to a home-built BBO-based optical parametric amplifier (OPA). The signal and idler beams generated from the OPA are difference frequency mixed in a $AgGaS_2$ crystal, producing broad-bandwidth 6 μm pulses. The resulting mid-infrared light is split into pump and probe pulses, and the

pump pulse passes through a Ge acousto-optic modulator (AOM)-based pulse shaper.[60,61] Finally, pump and probe beams are focused onto the sample. Steady-state spectra were collected 4 hours after aggregation was initiated at which time the fiber structure has equilibrated according to ThT and 2D IR kinetics.[39,62,63] No differences in 2D IR spectra are found at longer times.

3.4.5 Transmission electron microscopy

TEM was performed at the University of Wisconsin Medical School Electron Microscope Facility. Peptides were prepared as for spectroscopy experiments, except all samples were diluted from 1 mM to 0.1 mM with deuterated potassium phosphate buffer. The peptides were allowed to aggregate for 12 hours prior to TEM. The samples were then prepared using a two-step negative staining procedure. Nano-W (methylamine tungstate) (Nanoprobes, Inc.) was used as the negative stain. The samples were then placed on a pioloform coated 300 mesh thinbar Cu grid, and viewed on a Philips CM120 electron microscope at 80 kV. The images were documented with a SIS (Olympus-Soft Imaging Systems) MegaView III digital camera.

Multiple images were collected for each sample. Apparent widths of the fibers were measured using Adobe Illustrator.[56] Lines were drawn across the fibers and the lengths of the lines were converted to pixels and then into nanometers using the resolution of the image. Random sampling of the images was achieved. However, due to poor contrast, some fibers may not have been measured. For publication purposes, the contrast of the images was enhanced.

3.4.6 Circular dichroism spectroscopy

CD spectra of unmodified and deamidated $^{13}C^{18}O$ labeled Ala-13 hIAPP were collected using an Aviv 420 circular dichroism spectrophotometer at room temperature. Spectra were collected at 200-300 nm with 1 nm intervals and a 3 second sampling time. A 0.1 cm path length cuvette was used, and the total sample volume was 300 µL. Peptide samples were diluted from 1 mM d-HFIP stock solutions, dried under a stream of nitrogen, and redissolved into 5 mM deuterated potassium phosphate buffer to a final concentration of 25 µM (deamidated peptide) and 75 µM (unmodified peptide). Following addition of buffer, all peptides were allowed to aggregate for 48 hours. Prior to collecting spectra of peptides, a background spectrum was collected of deuterated potassium phosphate buffer. This spectrum was subtracted from all subsequent peptide spectra.

3.4.7 Aggregation kinetics and seeding experiments

Samples of unmodified and deamidated peptides were prepared for kinetics as described above. However, rather than waiting four hours to allow the peptides to fold following aggregation initiation with buffer, 2D IR spectra were collected immediately after initiation with buffer, leading to a dead time of ~10 minutes. The seeding experiment was performed by mixing deamidated hIAPP fibers with unmodified hIAPP monomers. Unmodified and deamidated peptides were prepared in separate tubes as described above. Deamidated Ala-13 was allowed to aggregate for 6 hours prior to mixing with unmodified Val-17. After 6 hours, the unmodified peptide monomers were rehydrated with buffer and quickly mixed with the deamidated fibers. Ala-13 fibers were

formed at 1 mM and Val-17 monomers were added for final concentrations of 0.1 mM Ala-13 deamidated fibers and 1 mM Val-17 unmodified monomers in buffer. 2D IR spectra were collected immediately following mixing, with a deadtime of ~5 minutes.

3.4.8 Methyl esterification of deamidated peptides

The methyl esterification procedure used to detect the presence of deamidation in the peptides was described by Raleigh and Tuong.[21,64] Methanolic HCl was prepared by the addition of 5 mL acetyl chloride to 30 mL anhydrous methanol under nitrogen at 0°C. Following stirring for five minutes, 500 µL methanolic HCl was added to 10 nmol of dried peptide. The mixture was briefly vortexed and brought to room temperature. Aliquots of the reaction were removed at various time intervals and quenched with 4 times excess volume of water. After quenching, all aliquots were stored at 0°C. Samples were then dried by speed-vac and dissolved in methanol for MALDI-MS preparation. All aliquots were measured using MALDI-MS and the ratio of the peak intensity of the native peptide to the peak intensity of the methylated peptide allowed for determination of deamidation.

3.5 Results

3.5.1 Amylin deamidation shown by HPLC and methyl esterification reaction

Table 3.1 lists the percent deamidation calculated for each peptide sample. These quantities are taken from Figures A2.1a-d in Appendix 2 that show HPLC chromatograms of Ala-8, Ala-13, Leu-16, and Leu-27 when purified using acidic buffers. The characteristic hIAPP retention time is approximately 45 minutes on a 0-90%B gradient over 90 minutes, and the shoulder attributed to asparagine deamidated to aspartic

Label	Frequency un-modified peptide isotope peak (cm^{-1})	Frequency un-modified peptide unlabeled peak (cm^{-1})	Frequency deamidated peptide isotope peak (cm^{-1})	Frequency deamidated peptide unlabeled peak (cm^{-1})	Frequency un-modified peptide unlabeled peak without coupling (cm-1)[56]	% Deamidated (from HPLC)
A8	1590	1618	~1600	1617	1600 ± 3	85 ± 5
A13	1579	1615	~1595	1620	1598 ±1	95 ± 5
L16	1581	1617	1585	1619	1588 ±1	69 ± 5
L27	1577	1614	NA	1620	1598 ± 2	64 ± 5

Table 3.1 Frequency of various features in 2D IR spectra and calculated percent deamidation from HPLC.

acid elutes 1-2 minutes after the main peak. Figure A2.2a-d in Appendix 2 shows the peptide peaks enlarged. The presence of these two peaks suggests that hIAPP monomers that contained asparagine and isoaspartic acid separated from monomers containing aspartic acid. From the HPLC chromatograms of each peptide, the percent deamidation of each sample is measured. The ratio of the peak heights was used to compare the amount of aspartic acid products to the total amount of asparagine and isoaspartic acid products. Using the known literature ratio of isoaspartic acid:aspartic acid deamidation products, the percent deamidation of each of the four peptides was calculated.[6] The rate of deamidation is not uniform for all residues in most proteins.[6,25,65,66] The calculated percentage is the average over all the residues and we estimate 5% error in the calculations resulting from integration of the HPLC peaks. Figure A2.3 in Appendix 2 shows the HPLC chromatogram of Ala-13 purified using buffers at pH 5. Between 40 and 50 minutes, there are two small peaks, the second being the shoulder on the main peak at 50 minutes. These two smaller peaks are two different deamidation products, containing Asp and isoAsp in place of Asn in the peptide. The presence of two deamidated peaks is indicative that some of the Ala-13 monomers could have more deamidated residues than others, resulting in multiple deamidation peaks in the chromatogram.

The methyl esterification reaction of amylin containing isotope labeled Ala-13 verifies the presence of a deamidated residue by converting any aspartic acid or isoaspartic acid residues to their methyl ester, which results in an increase in mass of 15 Da for each methyl group added.[21,64] Human amylin contains no aspartic acid or

glutamic acid residues and the C-terminus is amidated; therefore, the only sites at which this reaction can occur are at Asn or Gln residues that have deamidated. Although MALDI-MS cannot be used as a quantitative method for measuring the percent of peptide that is deamidated, the ratio of the intensity of the native peptide peak to the intensity of the methylated peptide peak should increase over the course of the reaction. In Appendix 2 Figure A2.4 shows MALDI-MS spectra collected from peptide aliquots after 1 and 3 hours of the esterification reaction. In Appendix 2 Figure A2.4a, the ratio of the peak at 3923 m/z (singly methylated hIAPP) to the peak at 3908 m/z (native hIAPP) after 1 hour of methylation is 0.29. In Appendix 2 Figure A2.4b, the ratio of the peak at 3922 m/z to the peak at 3907 m/z after 3 hours is 0.64. In addition, after 3 hours, a peak appears at 3937, suggesting that given enough time, hIAPP becomes doubly methylated. The ratio of the intensities of the doubly methylated peak to the native hIAPP peak is 0.31. MALDI-MS spectra were collected for an aliquot that was given 7.5 hours to react, however, after that amount of time; the peptide was degraded (not shown). In addition, under these conditions and given enough time, the peptide may have started to aggregate, thus preventing some deamidation sites from becoming methylated.

3.5.2 Neither TEM nor CD spectroscopy reveal a change in fibril structure upon deamidation

Deamidated hIAPP still aggregates into amyloid fibers as determined by TEM, which is shown in Figure 3.4a. These images were collected using samples of Ala-13 hIAPP, for which 95% of the peptides are deamidated (Table 3.1). For comparison, TEM of non-degraded hIAPP is shown in Figure 3.4b, prepared under identical conditions. To

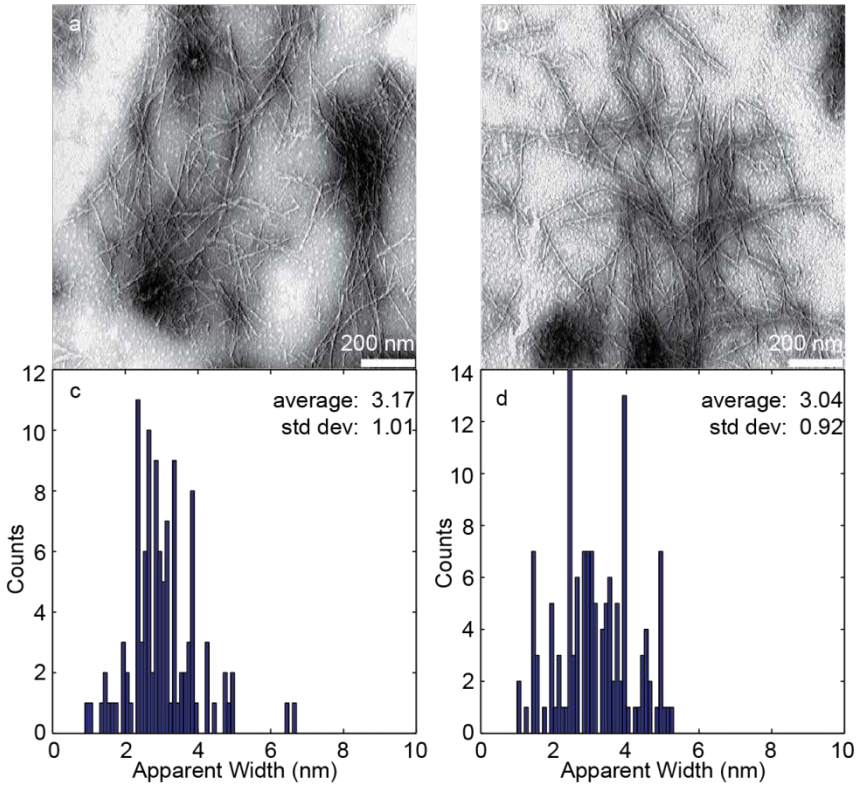

Figure 3.4 (a) TEM image of deamidated Ala-13 fibers. (b) TEM image of unmodified Ala-13 fibers. (c) Statistical analysis of the apparent width of deamidated Ala-13 fibers. (d) Statistical analysis of the apparent width of unmodified Ala-13 fibers. Scale bars on TEM represent 200 nm.

within the resolution of these TEM, we do not observe differences in morphologies between the two sets of fibers. A statistical analysis of the fiber full-width-at-half-maxima, place the widths of the deamidated fibers at 3.17 nm ± 1.01 nm (Figure 3.4c) and unmodified fibers at 3.04 nm ± 0.92 nm (Figure 3.4d).

Circular dichroism (CD) spectroscopy is often used to measure the secondary structure content of amyloid proteins. Normalized CD spectra of fibers formed from unmodified and deamidated hIAPP fibers are shown in Figure 3.5. These fibers are made from the same Ala-13 labeled stock as used for the TEM. The CD spectra of the unmodified and deamidated fibers exhibit a single peak at 220 nm and no shoulder at 208 nm. The experimental spectra are typical of those reported for amylin fibers and indicate β-sheet secondary structure.

3.5.3 Aggregation kinetics experiments reveal a difference in aggregation times

Shown in Figure 3.6 are kinetic traces for the aggregation of unmodified (Figure 3.6a) and deamidated (Figure 3.6b) Ala-13 hIAPP. The kinetic traces plot the increasing intensity of the fundamental of the amide I β-sheet peak that appears at 1615-1620 cm^{-1} in the 2D IR spectra. This peak intensity matches that of aggregation kinetics measured using the fluorescent dye ThT, so long as the dye binds to all β-sheets in the fiber.[56,63] In the unmodified peptides, there is consistently a lag time of 30 minutes to 1 hour before folding commences, for all samples measured from multiple peptide syntheses. In contrast, there is no lag time in the deamidated sample. The half-rise time of the unmodified samples are >1 hour and for deamidated peptides it is 30 minutes.

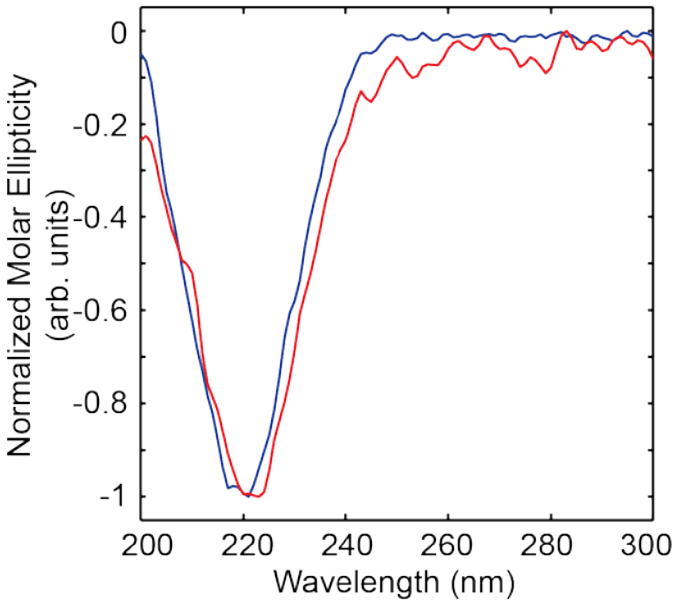

Figure 3.5 Normalized CD spectra of deamidated Ala-13 (blue) and unmodified Ala-13 (red).

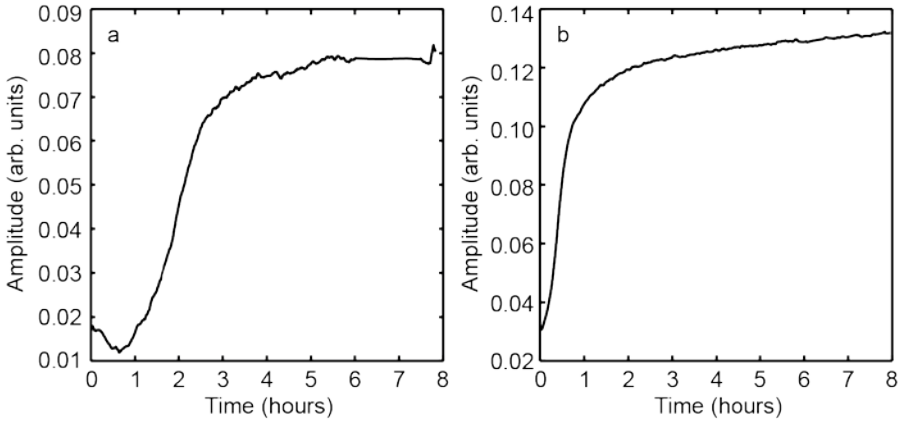

Figure 3.6 (a) Aggregation kinetics of human amylin monitored by following the amide I peak intensity in unmodified amylin. (b) Aggregation kinetics of human amylin monitored by following the amide I peak in deamidated amylin.

3.5.4 Isotope edited 2D IR reveals that deamidation alters the structure of the N-terminal β-sheet

The spectral features discussed in the introduction are illustrated in the 2D IR spectrum and diagonal slice in Figure 3.7 a and b, which was collected on a sample of Ala-13 labeled hIAPP fibers formed from polypeptides that have not deamidated. The peak at $\omega_{pump}=\omega_{probe}=1615$ cm^{-1} is due to the unlabeled amide I band of the parallel β-sheet amyloid fiber. The frequency of this peak can be as high as 1618 cm^{-1} for isotope labels that appear in the middle of the amyloid β-sheets.[39,56] The peak also appears higher for structurally disordered fibers in which the excitonic coupling is reduced. The intensity around 1645 cm^{-1} is mostly a measure of the random coil regions of the fiber, such as from residues 1-7 that are prevented from forming β-structure by the disulfide bond and residues ~18-22 in the turn region.[1,67] The isotope label for Ala-13 appears at 1579 cm^{-1}. Spectra of isotope diluted fibers absorb at 1598 cm^{-1} (not shown).[56] Thus, β=-10 cm^{-1}, which is consistent with a well-ordered β-sheet.

Having outlined the spectral signatures for isotope labeled hIAPP, we now compare 2D IR spectra collected for fibers formed from normal and deamidated peptides. Shown in Figure 3.7, c and d, are a 2D IR spectrum and its corresponding diagonal slice for Ala-13 labeled hIAPP fibers formed from a sample in which 95% of the peptides are deamidated, as measured by HPLC (see Table 3.1). In the 2D spectrum, the strong β-sheet mode from the unlabeled residues appears at 1620 cm^{-1}. The higher frequency for the unlabeled β-sheet peak indicates that the β-sheets in the deamidated fibers are particularly structurally disordered. The exact interpretation of the unlabeled features is

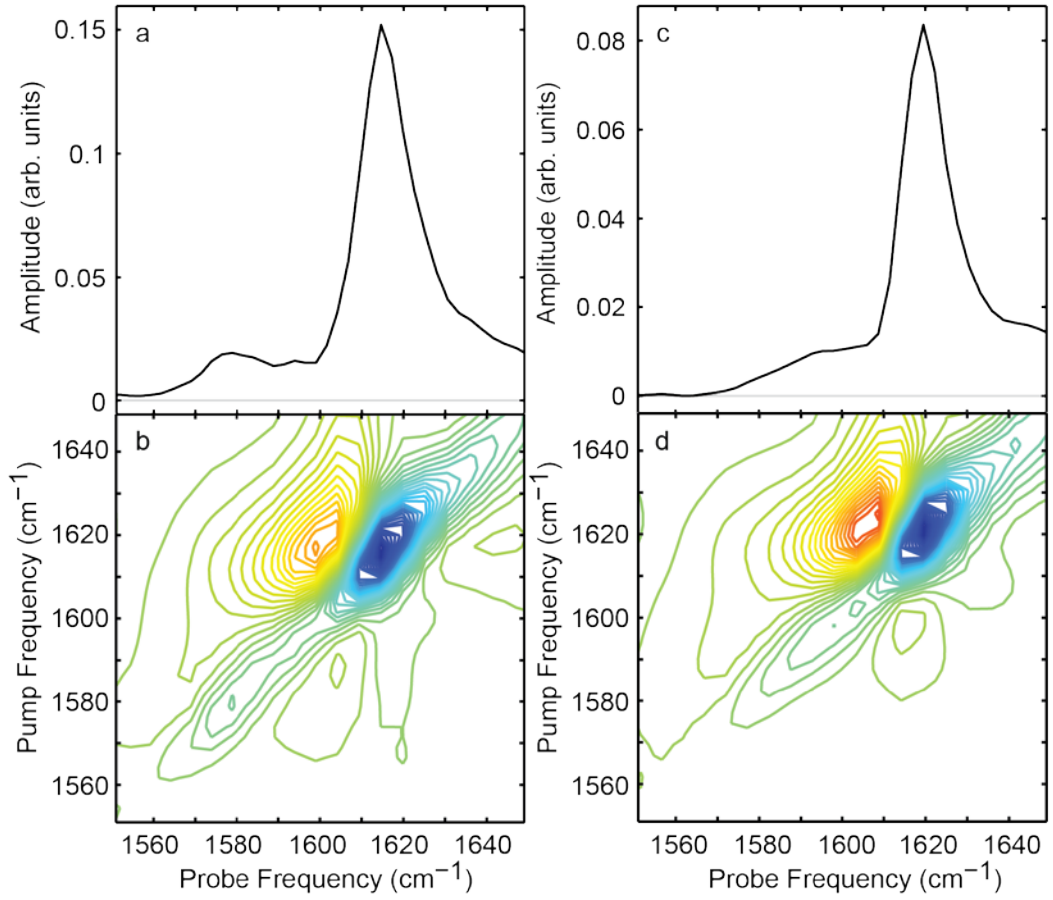

Figure 3.7 (a) Diagonal slice through the 2D IR spectrum of unmodified Ala-13. (b) 2D IR spectrum of unmodified Ala-13. (c) Diagonal slice through the 2D IR spectrum of deamidated Ala-13. (d) 2D IR spectrum of deamidated Ala-13.

difficult because the location of the isotope labels alters the unlabeled vibrational modes.[53] As for the Ala-13 isotope labeled peak in deamidated samples, it appears at 1595 cm^{-1}. 1595 cm^{-1} matches the frequency of the isotopically diluted sample, which indicates that the isotope labeled amide I peak is not shifted due to excitonic coupling.[56] Consequently, the strong coupling caused by parallel β-sheets is not present at the Ala-13 position in the deamidated sample. Therefore, even though amyloid fibers are formed as indicated by the 1620 cm^{-1} mode (and TEM and CD spectroscopy), the lack of the isotope frequency shift indicates that Ala-13 does not contribute to in-register parallel β-sheets in the deamidated sample. Exact values of the isotope and unlabeled β-sheet peaks in both the unmodified and deamidated spectra are given in Table 3.1. The linewidths and lineshapes of the isotope label were not measured in this set of experiments. The frequency assignments in Table 3.1 were made by inspection.

Similar experiments were performed for peptides isotope labeled at Ala-8, Leu-16 and Leu-27. Figure 3.8 shows slices through the diagonal of 2D IR spectra taken of fibers formed from both unmodified and deamidated samples. The full 2D IR spectra are given in Appendix 2 Figures A2.5 and A2.6. As discussed for Ala-13 above, all the samples have a strong amide I band near 1620 cm^{-1} that is the result of the unlabeled β-sheet while the isotope labels appear at 1579-1590 cm^{-1} when coupled and 1585-1600 cm^{-1} when not coupled. The range for these values spans ~15 cm^{-1} due to the variety of locations of the isotope labels in the peptide. Ala-13 and Leu-27 are some of the most ordered amino acids in the entire peptide, while Ala-8, adjacent to the disulfide bond is very disordered. The difference in the structure of hIAPP at these residues explains the

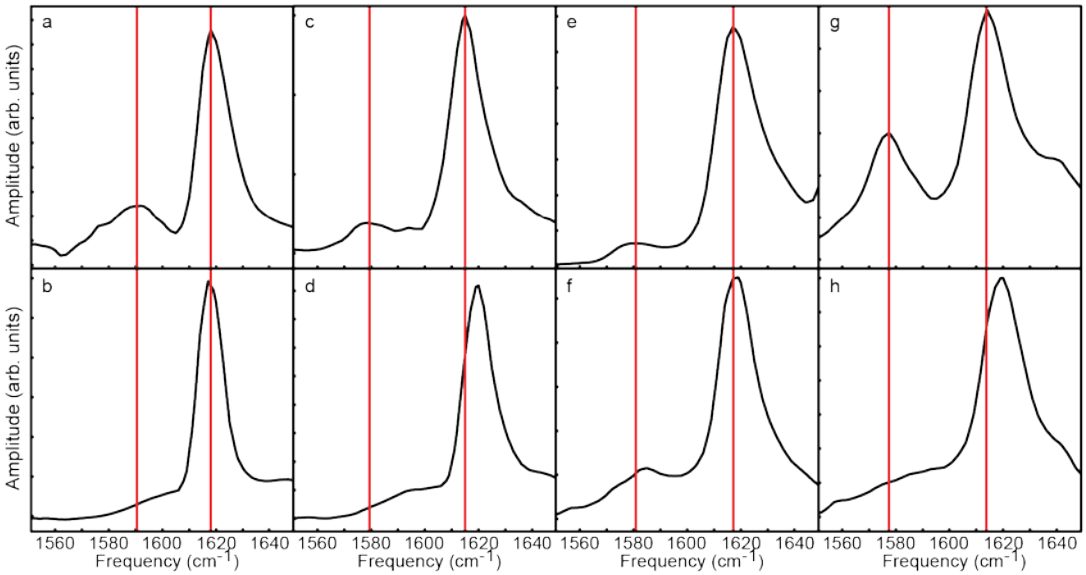

Figure 3.8 Slices through 2D IR spectra. (a) Unmodified Ala-8. (b) Deamidated Ala-8. (c) Unmodified Ala-13. (d) Deamidated Ala-13. (e) Unmodified Leu-16. (f) Deamidated Leu-16. (g) Unmodified Leu-27. (h) Deamidated Leu-27. Red lines are included as a guide to the eye for the frequencies of the unlabeled amide I and isotope label peaks.

large span of values for the isotope label frequency in the unmodified and deamidated spectra.

The red lines in Figure 3.8 mark the frequencies at which the isotope label and unlabeled β-sheet appear in the unmodified samples. For Ala-8 and Leu27, the data are similar to Ala-13. That is, the frequency of the isotope label in the deamidated samples appears at a much higher frequency and the peak is much weaker than in the spectrum of the unmodified peptide. Rather than the isotope label forming a discrete peak, it now becomes a shoulder on the side of the 1620 cm^{-1} β-sheet mode. The higher frequency and weaker intensity for these residues is a clear indication that the coupling between the isotope labels is much weaker than in the unmodified samples, which is again consistent with the loss of parallel β-sheet structure at these positions. That is not the case for Leu-16, for which there is only a 5 cm^{-1} frequency shift and the isotope label is still intense and well resolved in the deamidated spectrum. Thus, the coupling between Leu-16 residues is still significant for fibers formed from deamidated samples and the data are consistent with the deamidated samples containing parallel β-sheets at Leu-16. Comparing the unlabeled β-sheet peaks, in each sample there is a large amount of amyloid β-sheet secondary structure, evidenced by the lack of large random coil features at 1640 cm^{-1}. However, as in the case of Ala-13, the unlabeled β-sheet peak in Leu-27 is shifted to higher frequency (see Table 3.1), indicating that the β-sheets in the Leu-27 fibers are more structurally disordered.

3.5.5 Deamidated fibers seed amyloid formation by unmodified amylin

A seeding experiment was performed to determine if deamidated fibers could nucleate unmodified monomers.[11,21] These experiments were carried out using seeds created from deamidated peptides mixed with unmodified peptides isotope labeled at Val-17 in a ratio of 1:10. The Val-17 label was chosen in order to probe the structure of the seeded fibers near the location in which the deamidated fibers are known to possess parallel β-sheets (Figure 3.2). The seeds were created from deamidated peptides labeled at Ala-13, for which we know from HPLC that 95% of the peptides are deamidated and that the Ala-13 peak is very weak and broad (Figure 3.7c and d). Thus, the Ala-13 peak intensity is negligible in the interpretation of the 2D IR spectra presented below.

Shown in Figure 3.9 a and b are kinetic traces that measure β-sheet formation of seeded and unseeded aggregation. These traces are made by plotting the intensity of the unlabeled β-sheet at 1620 cm^{-1} over the course of aggregation. Seeding eliminates the lag time, which indicates that the seeds from deamidated peptides do indeed nucleate unmodified peptides into amyloid fibers. Figure 3.9 c and d shows slices through the 2D IR spectrum immediately after seeding and when the fibers have equilibrated at 2.5 hours. In the time-zero spectra, when less than half of the peptides are incorporated into fibers, the Val-17 isotope label is very broad and absorbs near 1590 cm^{-1}, consistent with most peptides adopting random coil structures in solution. In contrast, a very prominent and sharp isotope labeled peak appears in the equilibrated spectra at 1574 cm^{-1}, indicating that Val-17 residues, once they are nucleated into amyloid fibers, lie in-register by adopting a parallel β-sheet formation. Thus, unmodified peptides can be nucleated to

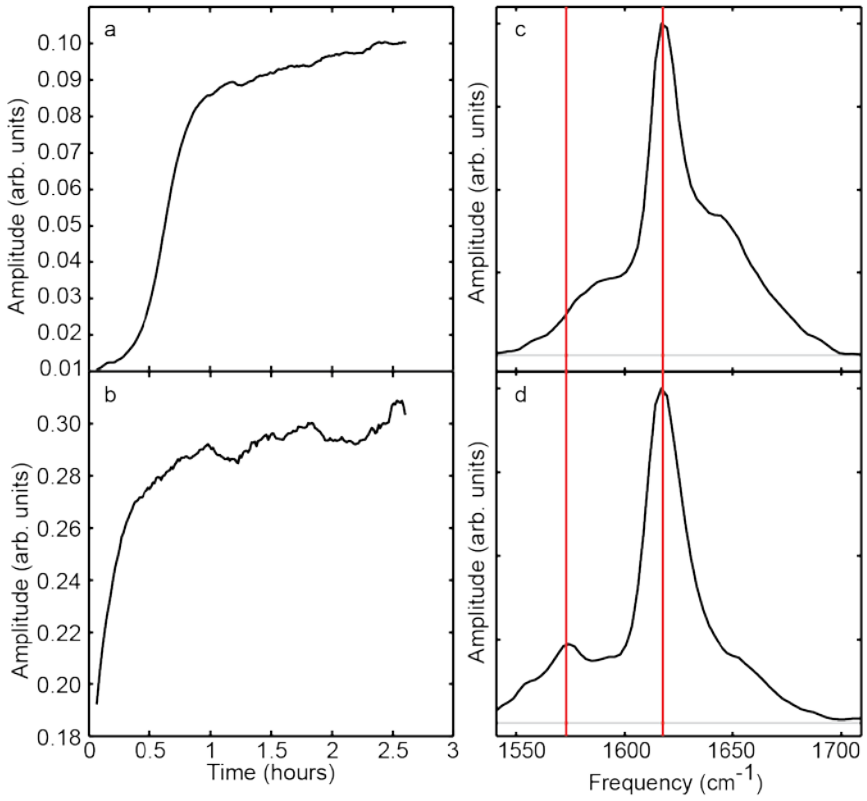

Figure 3.9 (a) Aggregation kinetics of unseeded Val-17 amide I folding monitored by following the amide I peak intensity in unmodified amylin. (b) Aggregation kinetics trace of seeded Val-17 amide I folding monitored by following the amide I peak intensity. (c) Slice through the diagonal of a 2D IR spectrum of unmodified Val-17 monomers seeded with deamidated Ala-13 fibers, averaged over the first 8 minutes following mixing. (d) Slice through the diagonal of a 2D IR spectrum averaged over 8 minutes 2.5 hours after mixing.

form fibers by deamidated seeds, and the seeded fibers have amyloid β-sheets at Val-17, which is in close proximity to the β-sheet region in deamidated fibers.

3.6 Discussion

Ascertaining the effect of deamidation on the structure of amyloid fibers is difficult. In fact, even recognizing that a polypeptide is deamidated is not easy. Deamidated amylin still aggregates into amyloid fibers, and the CD maximum of fibers formed from deamidated polypeptides are indistinguishable from unmodified peptides, as are the fiber widths measured by TEM. Deamidated polypeptides can be identified by HPLC purification and by mass spectrometry, but the differences are slight since the HPLC retention time is only slightly diminished and deamidation only produces a mass change of 1 Da.[21] Using 2D IR spectroscopy and isotope labeling, we are able to identify the changes deamidation induces to the amylin fibril structure. Moreover, we are able to probe the effect on fibril structure residue-by-residue as well as measure differences in fiber kinetics. Thus, we obtain insight into the effect of deamidation on the structure and folding kinetics of amylin fibers.

Shown in Figure 3.2b is a model for the fibrillar structure as determined by Tycko and co-workers using solid-state NMR.[1] Possible deamidation sites are shown in red and isotope labeled positions are shown in blue. The isotope labeled amino acids have been chosen to probe the inner and outer β-sheets, as well as near the disordered loop. The fibers in the Tycko study and ours probably differ in the number of stacked columns of peptides, but not in the locations of the β-sheets in each column. The parallel β-sheet structure of the fibers at Ala-8 and Ala-13 are broken, which lie adjacent to or 1 residue

away from a potential deamidation site. HPLC traces show that in samples of Ala-8 and Ala-13, nearly all of the peptides have some degree of deamidation. Thus, deamidation may cause a local loss of β-sheet structure due to puckering of the backbone with the addition of the extra CH_2 group. However, deamidation may be occurring in the C-terminal β-sheet as well. Leu-27 is positioned 3 or 4 residues away from the nearest possible deamidation site in the sequence (Figure 3.2). The study of deamidation of pramlintide showed that the residues with the highest degree of deamidation are Asn-21 and Asn-35.[23] Although those residues lie further from Leu-27, they may be more likely to deamidate. Deamidation of asparagine causes a negative charge, which may be the cause of this long-range effect.

The difference in lag times between unmodified Ala-13 and deamidated Ala-13 (Figure 3.6) is consistent with experiments on deamidated Aβ. ThT fluorescence experiments were performed on four different Aβ variants and compared to the fluorescence of native Aβ.[14] While one mutation, $Aβ_{1-42}$(L-isoAsp-23), produced more extensive aggregation over 24 hours, as shown as being almost twice as fluorescent at the end of the experiment, that and two other mutations, $Aβ_{1-42}$(isoAsp-7) and $Aβ_{1-42}$(E22Q), aggregated faster than wild-type Aβ. Although the three variants aggregated faster than wild-type Aβ, the E22Q mutation was by far the fastest. This mutant maximized ThT fluorescence after only 10 hours, compared to 20 hours for that of the wild-type. It is thought that the modifications at residues 22 and 23, located directly in the turn region, enhance aggregation due to the conformational changes that they cause. Asn-21 and

Asn-22, in the turn region of hIAPP could be deamidated, thus promoting a shorter lag time and faster folding in the deamidated sample.

While deamidation eliminates the N-terminal β-sheet between Ala-8 and Ala-13, as well as the C-terminal sheet near Leu-27, parallel β-sheets are still present in the deamidated fibers near Leu-16. Moreover, deamidated fibers can seed β-sheet formation. When unmodified Val-17 monomers are added to deamidated Ala-13 seeds, Val-17 fibers form faster than if they were unseeded. However, the structure of the deamidated fibers does not necessarily propagate to the unmodified monomers. After equilibration of Val-17 fiber formation, Val-17 is strongly coupled (Figure 3.9 d), suggesting that at Val-17, ordered, parallel β-sheets are formed. Val-17 lies adjacent to Leu-16, the residue that still retains some parallel β-sheet structure upon deamidation. Thus, while the β-sheet regions of deamidated fibers are much reduced, the β-sheet content is still sufficient to nucleate additional monomers. In addition, the unmodified fibers that are formed are more ordered than the deamidated seeds. This finding is interesting in light of the mechanism of amylin fiber formation. Previous studies have shown that amylin fibers nucleate somewhere in the disordered loop between Val-17 and Ala-25, with nucleation at Val-17 occurring faster than Ala-25.[39] Thus, even though deamidation decreases overall β-sheet content, deamidated peptides still retain the most critical region for nucleation. It is also interesting to note that the 20-29 fragment of amylin that shares a similar sequence range is induced to aggregate by as little as 5% deamidation impurity.[21] Thus, we hypothesize that in vivo post translational deamidation, if it occurs, still leads to amyloid deposits with much the same structure.

3.7 Conclusions

We find that deamidation has a major structural influence of fiber structure, by eliminating half of the N-terminal β-sheet and either disrupting the C-terminal β-sheet near Leu-27 or eliminating it entirely. The one region that it does not disrupt is the β-sheet structure is near Leu-16 and Val-17, which is why fibers formed from deamidated samples can still seed fiber formation of unmodified peptides. As we show, deamidation is very difficult to detect by either, CD spectroscopy or TEM. It is also not readily apparent in the FTIR or 2D IR spectra of un-isotope labeled peptides. Deamidation occurs spontaneously, even when peptides are carefully stored. As shown by HPLC, the peptides used in this study all displayed varying amounts of deamidation. However, all samples were synthesized, purified, stored, and aged in the same way. We therefore assume that while some samples may be more deamidated than others, the peptides are all undergoing the same deamidation process and the same residues are deamidating in each sample. Thus, our studies emphasize the need for careful monitoring of sample purity and the utility of isotope edited IR spectroscopy to not only easily identify sample degradation, but to also provide site-specific structural information on the structural consequences.

3.8 Appendix

Supporting information for this chapter includes HPLC chromatograms of deamidated peptides. Also included are MALDI-MS spectra from the methyl esterification reaction. 2D IR spectra and associated diagonal slices are also included for all unmodified and deamidated samples. This information can be found in Appendix 2.

3.9 Acknowledgments

Support for this research was provided by the NSF GRFP through grant DGE-0718123 for L.E.B., and the NIH through grant GM078114 for P.M., P.C., and D.P.R. and DK79895 for E.B.D. and M.T.Z. We thank Randall Massey at the University of Wisconsin Medical School Electron Microscope Facility for help with TEM and Lisa Johnson for help with CD spectroscopy. We also thank Dr. Robert Tycko for the coordinates for his structural model of human amylin fibers.

3.10 References

(1) Luca, S.; Yau, W. M.; Leapman, R.; Tycko, R. *Biochemistry* **2007**, *46*, 13505-13522.

(2) Walsh, C. T.; Garneau-Tsodikova, S.; Gatto, G. J. *Angewandte Chemie International Edition* **2005**, *44*, 7342-7372.

(3) Mann, M.; Jensen, O. N. *Nat Biotech* **2003**, *21*, 255-261.

(4) Witze, E. S.; Old, W. M.; Resing, K. A.; Ahn, N. G. *Nat Meth* **2007**, *4*, 798-806.

(5) Bischoff, R.; Kolbe, H. V. J. *Journal of Chromatography B: Biomedical Sciences and Applications* **1994**, *662*, 261-278.

(6) Geiger, T.; Clarke, S. *J. Biol. Chem.* **1987**, *262*, 785-794.

(7) Shimizu, T.; Matsuoka, Y.; Shirasawa, T. *Biol. Pharm. Bull.* **2005**, *28*, 1590-1596.

(8) Abedini, A.; Gupta, R.; Marek, P.; Meng, F.; Raleigh, D. P.; Taskent, H.; Tracz, S. In *Protein Misfolding Diseases*; John Wiley & Sons, Inc.: 2010, p 131-144.

(9) Shimizu, T.; Watanabe, A.; Ogawara, M.; Mori, H.; Shirasawa, T. *Arch. Biochem. Biophys.* **2000**, *381*, 225-234.

(10) Takata, T.; Oxford, J. T.; Demeler, B.; Lampi, K. J. *Protein Sci.* **2008**, *17*, 1565-1575.

(11) Nilsson, M. R.; Dobson, C. M. *Protein Sci.* **2003**, *12*, 2637-2641.

(12) Roher, A. E.; Lowenson, J. D.; Clarke, S.; Wolkow, C.; Wang, R.; Cotter, R. J.; Reardon, I. M.; Zürcher-Neely, H. A.; Heinrikson, R. L.; Ball, M. J. *J. Biol. Chem.* **1993**, *268*, 3072-3083.

(13) Xie, M.; Schowen, R. L. *J. Pharm. Sci.* **1999**, *88*, 8-13.

(14) Shimizu, T.; Fukuda, H.; Murayama, S.; Izumiyama, N.; Shirasawa, T. *Journal of Neuroscience Research* **2002**, *70*, 451-461.

(15) Fonseca, M. I.; Head, E.; Velazquez, P.; Cotman, C. W.; Tenner, A. J. *Exp. Neurol.* **1999**, *157*, 277-288.

(16) Sargaeva, N. P.; Lin, C.; O'Connor, P. B. *Anal. Chem.* **2009**, *81*, 9778-9786.

(17) Flaugh, S. L.; Mills, I. A.; King, J. *J. Biol. Chem.* **2006**, *281*, 30782-30793.

(18) Hanson, S. R. A.; Smith, D. L.; Smith, J. B. *Exp. Eye Res.* **1998**, *67*, 301-312.

(19) Robinson, N. E.; Robinson, M. L.; Schulze, S. E. S.; Lai, B. T.; Gray, H. B. *Protein Sci.* **2009**, *18*, 1766-1773.

(20) Nilsson, M. R. In *Amyloid Proteins*; Wiley-VCH Verlag GmbH: 2008, p 81-109.

(21) Nilsson, M. R.; Driscoll, M.; Raleigh, D. P. *Protein Sci.* **2002**, *11*, 342-349.

(22) Nonoyama, A.; Laurence, J. S.; Garriques, L.; Qi, H.; Le, T.; Middaugh, C. R. *Journal of Pharmaceutical Sciences* **2008**, *97*, 2552-2567.

(23) Hekman, C.; DeMond, W.; Dixit, T.; Mauch, S.; Nuechterlein, M.; Stepanenko, A.; Williams, J. D.; Ye, M. *Pharm. Res.* **1998**, *15*, 650-658.

(24) Hekman, C. M.; DeMond, W. S.; Kelley, P. J.; Mauch, S. F.; Williams, J. D. *J. Pharm. Biomed. Anal.* **1999**, *20*, 763-772.

(25) Robinson, N. E.; Robinson, A. B. *Proc. Natl. Acad. Sci. U. S. A.* **2001**, *98*, 944-949.

(26) Robinson, N. E.; Robinson, A. B. *Proc. Natl. Acad. Sci. U. S. A.* **2001**, *98*, 4367-4372.

(27) Hutton, J. C. *Diabetologia* **1989**, *32*, 271-281.

(28) Cooper, G. J. S. *Endocrine Reviews* **1994**, *15*, 163-201.

(29) Cooper, G. J. S.; Willis, A. C.; Clark, A.; Turner, R. C.; Sim, R. B.; Reid, K. B. M. *Proceedings of the National Academy of Sciences of the United States of America* **1987**, *84*, 8628-8632.

(30) Westermark, P.; Wernstedt, C.; Wilander, E.; Hayden, D. W.; Obrien, T. D.; Johnson, K. H. *Proceedings of the National Academy of Sciences of the United States of America* **1987**, *84*, 3881-3885.

(31) Nishi, M.; Sanke, T.; Nagamatsu, S.; Bell, G. I.; Steiner, D. F. *Journal of Biological Chemistry* **1990**, *265*, 4173-4176.

(32) Kahn, S. E.; Andrikopoulos, S.; Verchere, C. B. *Diabetes* **1999**, *48*, 241-253.

(33) Clark, A.; Cooper, G. J. S.; Morris, J. F.; Lewis, C. E.; Willis, A. C.; Reid, K. B. M.; Turner, R. C. *Lancet* **1987**, *2*, 231-234.

(34) Hull, R. L.; Westermark, G. T.; Westermark, P.; Kahn, S. E. *Journal of Clinical Endocrinology & Metabolism* **2004**, *89*, 3629-3643.

(35) Marzban, L.; Park, K.; Verchere, C. B. *Experimental Gerontology* **2003**, *38*, 347-351.

(36) Lorenzo, A.; Razzaboni, B.; Weir, G. C.; Yankner, B. A. *Nature* **1994**, *368*, 756-760.

(37) Clark, A.; Wells, C. A.; Buley, I. D.; Cruickshank, J. K.; Vanhegan, R. I.; Matthews, D. R.; Cooper, G. J. S.; Holman, R. R.; Turner, R. C. *Diabetes Research Clinical and Experimental* **1988**, *9*, 151-159.

(38) Butler, A. E.; Janson, J.; Bonner-Weir, S.; Ritzel, R.; Rizza, R. A.; Butler, P. C. *Diabetes* **2003**, *52*, 102-110.

(39) Shim, S.-H.; Gupta, R.; Ling, Y. L.; Strasfeld, D. B.; Raleigh, D. P.; Zanni, M. T. *Proceedings of the National Academy of Sciences* **2009**, *106*, 6614-6619.

(40) Wang, L.; Middleton, C. T.; Singh, S.; Reddy, A. S.; Woys, A. M.; Strasfeld, D. B.; Marek, P.; Raleigh, D. P.; de Pablo, J. J.; Zanni, M. T.; Skinner, J. L. *J. Am. Chem. Soc.* **2011**, null-null.

(41) Dupuis, N. F.; Wu, C.; Shea, J.-E.; Bowers, M. T. *J. Am. Chem. Soc.* **2011**, null-null.

(42) Dupuis, N. F.; Wu, C.; Shea, J.-E.; Bowers, M. T. *J. Am. Chem. Soc.* **2009**, *131*, 18283-18292.

(43) Apostolidou, M.; Jayasinghe, S. A.; Langen, R. *J. Biol. Chem.* **2008**, *283*, 17205-17210.

(44) Sellin, D.; Yan, L.-M.; Kapurniotu, A.; Winter, R. *Biophys. Chem.* **2010**, *150*, 73-79.

(45) Potter, K. J.; Abedini, A.; Marek, P.; Klimek, A. M.; Butterworth, S.; Driscoll, M.; Baker, R.; Nilsson, M. R.; Warnock, G. L.; Oberholzer, J.; Bertera, S.; Trucco, M.; Korbutt, G. S.; Fraser, P. E.; Raleigh, D. P.; Verchere, C. B. *Proceedings of the National Academy of Sciences* **2010**, *107*, 4305-4310.

(46) Westermark, G. T.; Westermark, P.; Berne, C.; Korsgren, O. *New England Journal of Medicine* **2008**, *359*, 977-979.

(47) Koo, B. W.; Hebda, J. A.; Miranker, A. D. *Protein Engineering Design and Selection* **2008**, *21*, 147-154.

(48) Kim, Y. S.; Liu, L.; Axelsen, P. H.; Hochstrasser, R. M. *Proceedings of the National Academy of Sciences* **2008**, *105*, 7720-7725.

(49) Moran, S. D.; Woys, A. M.; Buchanan, L. E.; Bixby, E.; Decatur, S. M.; Zanni, M. T. *Proceedings of the National Academy of Sciences* **2012**, *109*, 3329-3334.

(50) *Examining Amyloid Structure and Kinetics with 1D and 2D Infrared Spectroscopy and Isotope Labeling*; 1 ed.; Buchanan, L., Dunkelberger, EB, Zanni, MT, Ed.; Springer: Heidelberg, 2011; Vol. 1.

(51) Moran, A.; Mukamel, S. *Proc. Natl. Acad. Sci. U. S. A.* **2004**, *101*, 506-510.

(52) Decatur, S. M. *Acc. Chem. Res.* **2006**, *39*, 169-175.

(53) Strasfeld, D. B.; Ling, Y. L.; Gupta, R.; Raleigh, D. P.; Zanni, M. T. *Journal of Physical Chemistry B* **2009**, *113*, 15679-15691.

(54) Kim, Y. S.; Liu, L.; Axelsen, P. H.; Hochstrasser, R. M. *Proceedings of the National Academy of Sciences* **2009**, *106*, 17751-17756.

(55) Woys, A. M.; Lin, Y.-S.; Reddy, A. S.; Xiong, W.; de Pablo, J. J.; Skinner, J. L.; Zanni, M. T. *J. Am. Chem. Soc.* **2010**, *132*, 2832-2838.

(56) Middleton, C. T.; Marek, P.; Cao, P.; Chiu, C.-c.; Singh, S.; Woys, A. M.; de Pablo, J. J.; Raleigh, D. P.; Zanni, M. T. *Nat Chem* **2012**, *advance online publication*.

(57) Middleton, C. T.; Woys, A. M.; Mukherjee, S. S.; Zanni, M. T. *Methods* **2010**, *52*, 12-22.

(58) Marek, P.; Woys, A. M.; Sutton, K.; Zanni, M. T.; Raleigh, D. P. *Org. Lett.* **2010**, *12*, 4848-4851.

(59) Abedini, A.; Raleigh, D. P. *Org. Lett.* **2005**, *7*, 693-696.

(60) Shim, S.-H.; Strasfeld, D. B.; Fulmer, E. C.; Zanni, M. T. *Opt. Lett.* **2006**, *31*, 838-840.

(61) Shim, S.-H.; Strasfeld, D. B.; Zanni, M. T. *Opt. Express* **2006**, *14*, 13120-13130.

(62) Marek, P.; Gupta, R.; Raleigh, D. P. *ChemBioChem* **2008**, *9*, 1372-1374.

(63) Strasfeld, D. B.; Ling, Y. L.; Shim, S.-H.; Zanni, M. T. *J. Am. Chem. Soc.* **2008**, *130*, 6698-6699.

(64) Tuong, A.; Maftouh, M.; Ponthus, C.; Whitechurch, O.; Roitsch, C.; Picard, C. *Biochemistry* **1992**, *31*, 8291-8299.

(65) Robinson, N. E.; Robinson, A. B. *Proc. Natl. Acad. Sci. U. S. A.* **2001**, *98*, 12409-12413.

(66) Tyler-Cross, R.; Schirch, V. *J. Biol. Chem.* **1991**, *266*, 22549-22556.

(67) Wiltzius, J. J. W.; Sievers, S. A.; Sawaya, M. R.; Cascio, D.; Popov, D.; Riekel, C.; Eisenberg, D. *Protein Science* **2008**, *17*, 1467-1474.

CHAPTER 4*

Infrared Spectroscopy Provides Extended Vibrational Modes that Reveal Secondary Structures of Amyloid Proteins

4.1 Introduction

The aggregation mechanisms by which amyloid proteins misfold and assemble into long fibers is a perplexing issue. Ideally, one would continuously follow the structural changes associated with peptide or protein conformation throughout the process, from monomers, to oligomeric intermediates, and finally into the assembly of the fibers. Mapping the aggregation pathway in the presence of membrane bilayers or other protein constituents would also be valuable since the cytotoxic pathway may involve membrane permeation or binding to membrane proteins. However, the combination of structures, kinetics, and membranes is a difficult set of circumstances for

* This chapter will be submitted to the Journal of Chemical Physics in June 2013. It was prepared in collaboration with Maxsim Grechko and Martin T. Zanni.

many experimental techniques. Infrared, both FTIR and 2D IR spectroscopies, are proving to be very useful in this regard.[1-7] They provide secondary structure information as a function of time and can be applied to membranes and aggregates.[1,8-14] Structural information can be refined with isotope labeling either site-specifically or in domains.[13-16] IR spectroscopy is providing new insights into amyloid fiber structures[12,13], assembly process[1,17], small molecules and peptide inhibition[18-20], and membrane interactions.[2,9,11]

Usually, the interpretation of an IR spectrum relies solely on frequencies. Tables can be found listing frequencies of various secondary structures and sidechains.[21-23] The amide I mode, composed primarily of C=O stretch (~75%) but also of CN stretch (~10%) and NH in-plane bend (~10%), has a characteristic absorbance frequency based upon the local secondary structure.[21] For instance, in water, the amide I band absorbs near 1645 cm^{-1} for a random coil peptide, at 1635-1655 cm^{-1} for an α-helical[15,16] peptide, and β-sheets typically have a low frequency peak at 1620-1635 cm^{-1} and a higher frequency band at 1670-1680 cm^{-1}, depending on if the β-sheet is parallel or antiparallel.[21] It is important to note that these frequency ranges are compiled from empirical observations and that the frequency can vary by as much as 20 cm^{-1} since it depends on the electrostatic environment and vibrational couplings for the specific structure at hand. For instance, transmembrane helices typically absorb 20 cm^{-1} higher than soluble helical peptides. As a result, frequency assignments can oftentimes be subjective.

In this article we exploit transition dipole strengths, which we think is an underutilized quantity in the identification and assignment of secondary structures. The

transition dipole strength is the quantity responsible for the extinction coefficient, ε, that is central to Beers Law according to A = ε x c x l where A is absorbance, c is concentration, and l is pathlength. The extinction coefficient is related to the transition dipole strength, μ, by $\varepsilon = \mu^2$. The carbonyl stretch of the amide I mode has a very large transition dipole strength as do many sidechains.[22] What is interesting about these quantities is that their strengths depend on secondary structure, because secondary structures like α-helices and β-sheets places the backbone carbonyl groups, for example, into tightly packed arrangements that creates vibrational coupling between the amide I modes. This coupling causes a delocalization of the vibrational mode over multiple amide I units, which redistributes the oscillator strength.[24-26] Thus, if one observes a change of transition dipole, then one knows that vibrational coupling has occurred, and quantification of the transition dipole strength can help identify secondary structures and provide a lower limit to the number of residues contributing to the structure.

Let us provide some examples of how the transition dipole strength depends on structure. The classic example is the IR-allowed modes associated with a small molecule of high symmetry, such as gas-phase CO_2. CO_2 is a textbook example of a molecule that has symmetric and antisymmetric normal mode stretches formed by linear combinations of the local CO stretches. The transition dipoles of the normal modes are generated by vector sums of the local mode transition dipoles, $\mu_{\pm} = (1/\sqrt{2}) \times (\mu_1 \pm \mu_2)$, as shown in Figure 4.1a and b. Thus, the symmetric stretch of CO_2 is zero while the antisymmetric stretch is $\mu_+ = 2\mu/\sqrt{2}$. The resulting extinction coefficient of the CO_2 antisymmetric stretch is thus $\varepsilon_+ = 2$, which is twice as large as either of the local CO stretches. In CO_2,

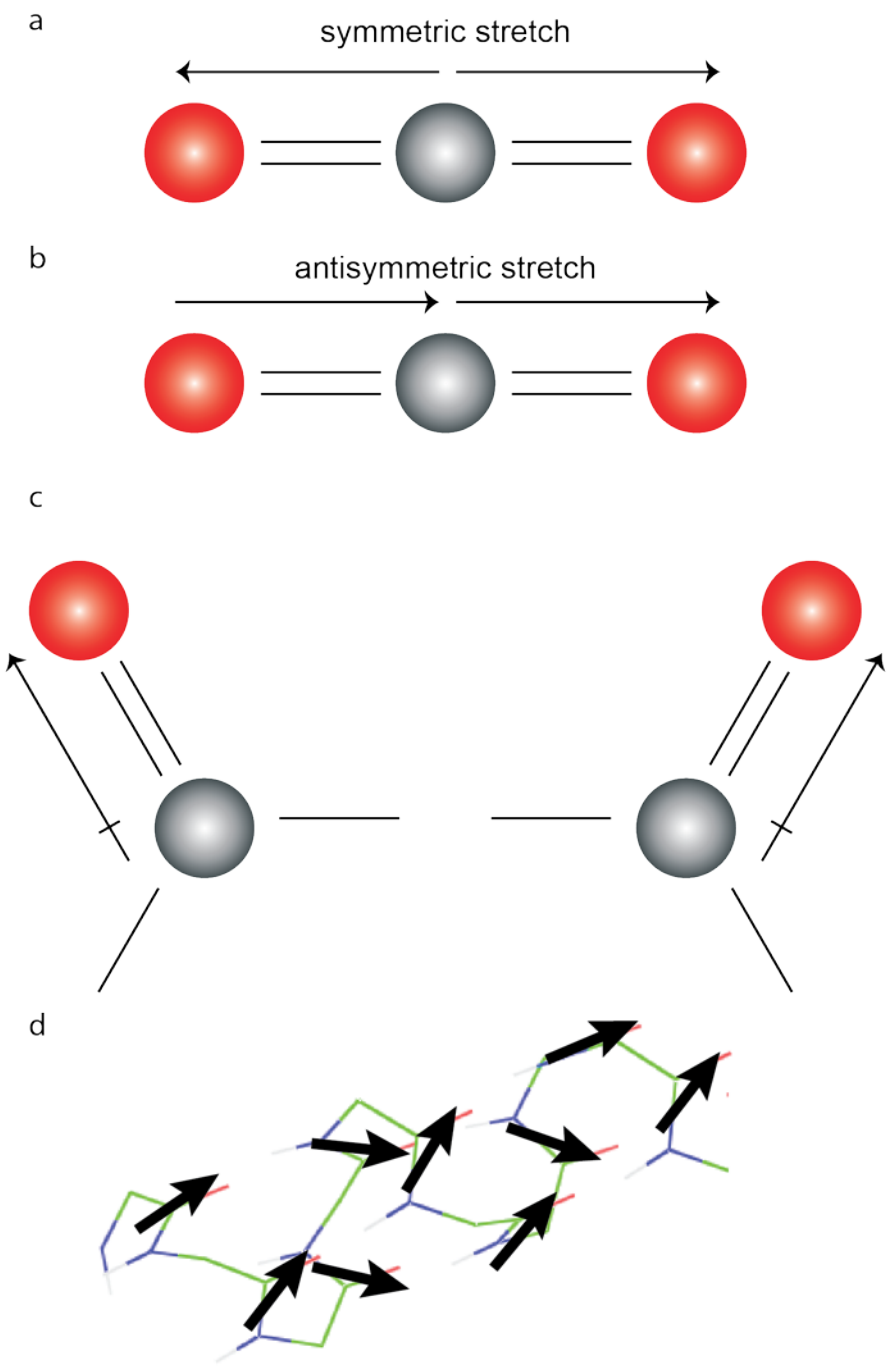

Figure 4.1 (a) Symmetric stretch vibration in carbon dioxide. (b) Antisymmetric stretch of carbon dioxide. (c) Coupled vibrational modes in two nearby acetone molecules. The coupling stretch between the two acetone molecules is dependent on the relative orientations and the distance between the two transition dipoles.

the two carbonyl stretches share a common carbon atom, and so splitting the molecule into two carbonyl groups is a conceptual construct that cannot occur in nature. Nonetheless, the same principle is applicable to two carbonyl groups on different molecules, such as two acetone molecules (Figure 4.1c). In that case, the coupling between the two molecules might occur by electrostatic forces that would depend on their distances and orientation. Nonetheless, the coupling will cause linear combinations of the two modes and a corresponding vector sum of the transition dipoles. If the molecules happen to be antiparallel (or parallel or collinear), then the vector sum will place all of the transition dipole intensity into one normal modes. In the more general case, both symmetric and antisymmetric modes will have a finite transition dipole strength, with one mode larger than the other. The point of outlining this simple situation is that, unless the coupled modes are orthogonal to one another, the appearance of a transition dipole strength that is either larger or smaller than the individual modes indicates that coupling is occurring.

We believe that the transition dipole strength is a particularly useful quantity to measure when vibrational frequencies are otherwise inconclusive. Consider an α-helix versus a random coil. Random coils typically absorb at 1645 cm^{-1} and α-helices range from 1635-1655 cm^{-1}. Thus, from the frequency alone, one cannot necessarily assign the spectrum of a peptide to an α-helix (it might help to measure other parameters such as linewidths and anharmonic shift). Like for CO_2, the normal modes are created from linear combinations of the local carbonyl (amide I) stretches (Figure 4.1d). The linear combination for the strongest mode in an α-helix is a sum of the coupling constants

between the residues, $\mu_A=1/\sqrt{N} \times \Sigma\mu_n$, which is referred to as the "A" mode in a perfect and infinitely long helix. The coupling constant between covalently bonded amide I modes (n and n+1) is about 8 cm^{-1}, while the rest of the coupling constants are positive with the largest about +5 cm^{-1} between hydrogen bonded residues (n and n+3).[24,27] Thus, when the sum is performed to obtain the normal mode, the negative and positive coupling constants largely cancel one another, which is why the frequency is very similar to that of the random coil. However, the vector addition of the amide I transition dipoles sum constructively, so that the transition dipole of an α-helix is equal to $\mu_A = N/\sqrt{N}$ and $\varepsilon_A = N$. Thus, the extinction coefficient of the A-mode becomes very large, because all of the residues contribute to the normal mode. In practice, the oscillator strength of the local modes is also partitioned into the E-modes (which lie orthogonal to the helix axis) and structural/environmental disorder prevents the normal mode from delocalizing along the entire helix. Nonetheless, the extinction coefficient would provide a clear signature of an α-helix even if there is not a clear frequency difference with the random coil.

The problem with utilizing transition dipole strengths to assess secondary structure (or the conformations of other molecules) is that it is often not possible to determine transition dipole strengths from FTIR spectroscopy because doing so requires knowing the concentration. Protein samples cannot always be prepared at precise concentrations, are not always homogeneous, like in aggregating or membrane systems, and in kinetics experiments the concentrations are constantly changing. Moreover, the integrated area of an FTIR spectrum is invariant under the redistribution of oscillator strengths. That is, for the same concentration, a random coil peptide of 30 residues has

the same integrated area as a helix with 30 residues. Thus, in a helix folding experiment, the extinction coefficient will change (we recently estimated that it changes by a factor of 2.2), but the intensity of the FTIR spectrum is constant aside from a possible frequency shift and spectral narrowing.[25] Thus, even if the concentration is known, the spectra may not resolvable conformations, which is necessary for computing the transition dipole strength(s).

In a previous paper, we described a method in which the relative amplitudes of FTIR and 2D IR spectra could be used to determine transition dipole strengths without prior knowledge of the concentration.[25] The essence of the approach uses the fact that an absorption spectrum scales as $c \times \mu^2$ while a 2D IR spectrum scales as $c \times \mu^4$. Thus, by dividing the two, one gets the transition dipole strength independent of concentration. In our previous publication, we tested the approach on a model helical peptide. In this paper, we apply it to measure the transition dipole strengths associated with the human islet amyloid polypeptide (hIAPP or amylin) in its fiber state, and with rat amylin in solution, micelles, and membranes. Human amylin, the causative agent in Type 2 diabetes misfolds; monomers form stacked columns with two parallel β-sheets connected by a flexible loop that runs along the fiber axis. There is considerable interest in understanding the structure of human amylin and how it forms fibers, especially in the presence of membranes, which catalyze fiber formation. In lipid membranes, it is thought that human amylin transitions through an α-helical intermediate en route to forming amyloid fibers. Rat amylin is a widely studied mutant of human amylin, whose sequence differs by only 6 residues. Rat amylin does not form amyloid fibers and so it is often

used as a model for human amylin micelle and membrane environments to which it binds but does not aggregate.[2,28-31] It is thought to also form an α-helical structure in the presence of membranes, as studied by NMR, EPR, and CD spectroscopies.[28,29,32-35] The amide I frequencies of rat amylin in solution, micelle, and membrane are so similar that it is not enough to determine their structure by amide I frequency alone (the anharmonic shift of the amide I band in 2D IR spectra did resolve helix formation in kinetics experiments of human amylin on bilayers).[2] In addition, rat amylin in micelles and bilayers is probably not wholly α-helical. Instead, it is likely that the peptide adopts a partially folded structure, which will further complicate structural analysis using frequencies. In this manuscript, we aim to use 1D and 2D IR spectroscopy to measure the transition dipole strength of human amylin fibers and rat amylin in solution, micelles, and membranes in order to determine the delocalization of the amide I normal modes. The goal is to build a knowledge about the transition dipole strengths of amylin in these situations to which we can then apply to kinetic aggregation experiments.

4.2 Materials and Methods

4.2.1 Amylin peptide synthesis

Human amylin is a 37 residue polypeptide with the sequence KCNTATCATQRLANFLGHSSNNFGAILSSTNVGSNTY. Human and rat amylin share the same sequence, with the exception of six mutations: H19R, F23L, A25P, I26V, S29P and S30P. Both peptides were prepared using standard FMOC solid phase peptide synthesis with a CEM Liberty 1 Microwave Peptide synthesizer. PAL-PEG-PS resin was used to ensure an amidated C-terminus. For hIAPP synthesis, a pseudoproline dipeptide

was incorporated into residues 13-14 and 27-28 to facilitate the synthesis as described elsewhere.[36] For rIAPP synthesis, only the pseudoproline at 13-14 was used. Following synthesis, cleavage and deprotection was performed using standard trifluoroacetic acid (TFA) protocols, and 1,2-ethanedithiol was used as a scavenger. Crude peptide was dissolved in dimethylsulfoxide (DMSO) at ~5 mg/mL overnight for the formation of a disulfide bond between Cys-2 and Cys-7. Both peptides were purified using reverse-phase high-performance liquid chromatography (HPLC, Jasco) with a C18 preparative column (Vydac). A two buffer gradient was used; Buffer A consisted of 100% water and 0.045% hydrocholoric acid (HCl) (v/v) and Buffer B consisted of 80% acetonitrile and 0.045% HCl (v/v). The gradient was varied from 0-90% B over 90 minutes and absorbance was monitored at 220 nm and 280 nm. The molecular weights of hIAPP and rIAPP were confirmed using MALDI-MS.

4.2.2 Lipid preparation

For membrane studies, 1-palmitoyl-2-oleoyl-*sn*-glycero-3-phosphocholine (POPC) and 1-palmitoyl-2-oleoyl-*sn*-glycero-3-phospho-(1'-*rac*-glycerol) (POPG) were purchased as chloroform solutions from Avanti Polar Lipids, Inc. The two lipid solutions were mixed at a molar ratio of 3:1. The mixture was dried under a gentle stream of nitrogen for 4 hours and then lyophilized overnight. The dry film was rehydrated in D_2O at a concentration of 80 mM and subjected to 5 freeze-thaw cycles. The lipids were then sonicated at 40°C for 30 minutes to form vesicles. For micelle experiments, n-dodecylphosphocholine (DPC) was purchased as a powder from Avanti Polar Lipids, Inc. DPC was dissolved in chloroform at 200 mM, dried under nitrogen and lyophilized

overnight. The dry film was rehydrated in 20 mM deuterated potassium phosphate buffer (d-PBS) with pH 7.4 to a final concentration of 200 mM. The lipids were sonicated at 40°C for 1 hour to form micelles.

4.2.3 Sample preparation

All experiments were performed in deuterated solvents (D_2O and deuterated buffers), rather than water, to ensure that the amide I band was not obstructed by the strong water band in the same region. Purified peptides were dissolved in deuterated hexafluoroisopropanol (d-HFIP) to a final concentration of 1 mM. After 4 h of sonication, the peptides were completely deuterated in the amide II position. For hIAPP fiber preparation, aliquots of the stock solution were dried under vacuum for 1 h to completely remove d-HFIP from the peptide. Once dry, the peptide film was reconstituted in d-PBS, pH 7.4 for final concentrations of 1, 1.5, 2.5, and 5 mM. Fiber initiation began upon addition of buffer, and fibers were allowed to form for 18 h before 2D IR spectra were collected. For rIAPP solution sample preparation, a 10 µL aliquot of the peptide stock solution was dried under vacuum for 1 h to completely remove d-HFIP from the peptide. Once dry, the peptide film was reconstituted in 5 µL of d-PBS, pH 7.4, for a final concentration of 2 mM. For micelle sample preparation, a 10 µL aliquot of the peptide stock solution was dried under vacuum for 1 h to completely remove d-HFIP from the peptide, and 5 µL of the 200 mM DPC solution was added to the dried peptide for a final concentration of rIAPP of 2 mM. For membrane sample preparation, a 10 µL aliquot of the peptide stock solution was dried under vacuum for 1 h to completely remove d-HFIP from the peptide. 2 µL of the 80 mM lipid solution was added to the

dried peptide. An additional 3 µL of d-PBS was also added to give a final concentration of 2 mM rIAPP. All samples were then mixed and placed between two 2 mm thick CaF_2 windows separated by a 56 µm Teflon spacer. All samples were kept in a purge box until and during use. The fiber, solution and membrane experiments were performed at 298 K and the micelle experiments were performed at 303 K. To calculate the transition dipole strength of hIAPP and rIAPP under these conditions, two additional samples were necessary. A sample of pure d-PBS was prepared using the same sample cell as described above. Additionally, L-serine was dissolved in D_2O to a final OD of 0.39 for hIAPP samples and 0.26 for rIAPP samples. The OD of the sample is not critical, as long as it is known. In order to accurately calculate transition dipole strengths between samples, 2D IR spectra of peptide samples were averaged for 15 min to ensure complete purging of the spectrometer box in which the sample was measured. Immediately following a sample measurement, a 2D IR spectrum of L-serine was measured and averaged for 15 min and then a 2D IR spectrum of pure buffer was measured and averaged for 15 min. This process was repeated for each type of hIAPP and rIAPP sample.

4.2.4 Two-dimensional infrared spectroscopy measurements

The two-dimensional infrared (2D IR) spectroscopy set-up consists of a home-built Ti-Sapphire oscillator that seeds a Nd-YLF-pumped femtosecond regenerative amplifier, as described elsewhere.[14,37,38] The 800 nm output is sent to a home-built BBO-based optical parametric amplifier and the generated signal and idler beams are overlapped spatially and temporally in a $AgGaS_2$ crystal for difference frequency mixing

and 6 μm broad-band pulses are generated. The mid-IR light is split into pump and probe beams with a CaF_2 wedge. The pump beam passes through a Ge acousto-optic modulator (AOM) based pulse shaper and splits into two pulses. The pump and probe pulses are then focused onto the sample using parabolic mirrors. All spectra were recorded at T_2 = 0 ps, and all 2D IR spectra were normalized to the intensity of the amide I peak.

4.2.5 Transition dipole strength calculations

Transition dipole strengths of hIAPP fibers and rIAPP in solution, micelle, and membrane were calculated using a combination of 1D and 2D spectroscopies, as described in detail elsewhere.[25] L-serine, previously calculated to have a transition dipole strength of 0.2 D^2 was used as the calibrant molecule. Both linear and 2D IR spectra were collected simultaneously for all peptide samples, L-serine, and the buffer solution. A step-by-step outline of our method for calculating the transition dipole strengths from the data can be found in Appendix 3. It is similar to that previously published, with one additional step explicitly outlined.

4.3 Results

4.3.1 Transition dipole strength of human IAPP fibers

Steady-state 2D IR spectra were collected of human amylin at 1 mM, 1.5 mM, 2.5 mM, and 5 mM. The 2D IR spectra of the human amylin samples are shown in Figure 4. 2a-d. The spectra are typical for those published previously.[1,12,26,39,40] They exhibit a sharp pair of diagonal peaks between 1615-1621 cm^{-1}, which are due to the amyloid β-sheets, and a broader pair of diagonal peaks with a maximum near 1642 cm^{-1}. These latter features are thought to reside from the disordered residues of the loop connecting

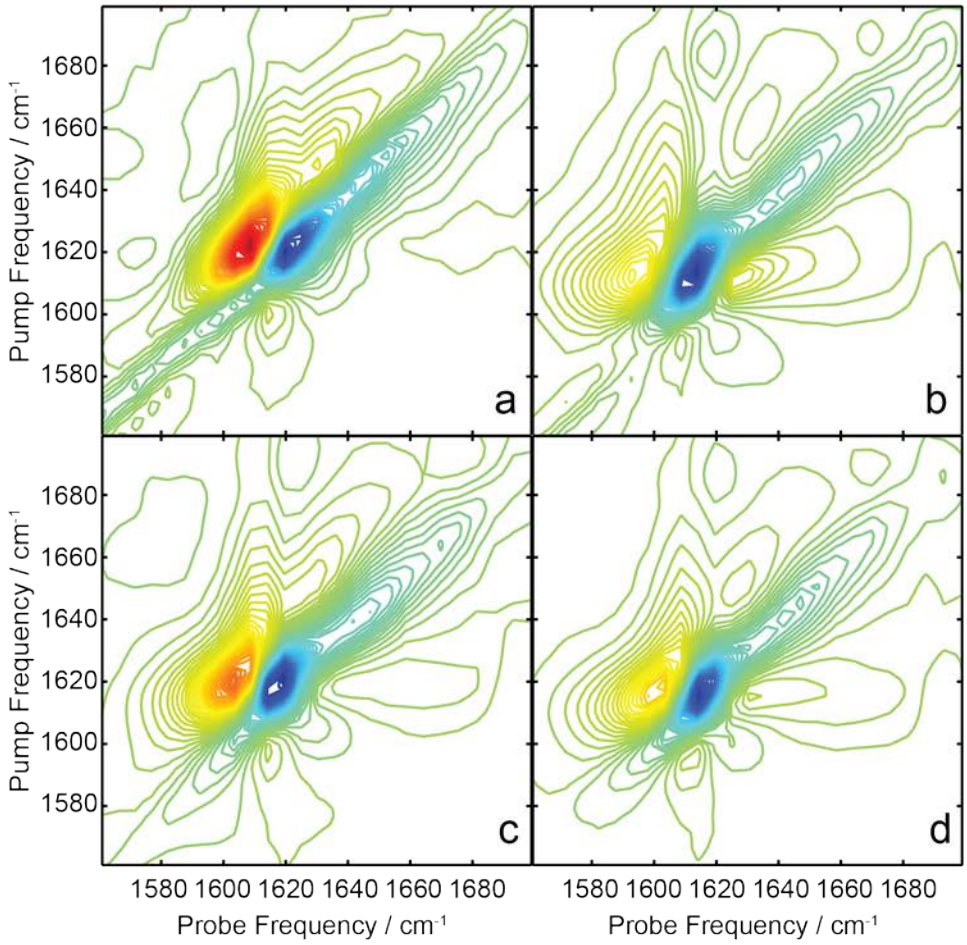

Figure 4.2 (a) 2D IR spectrum of hIAPP fibers, 1 mM. (b) 2D IR spectrum of hIAPP fibers, 1.5 mM. (c) 2D IR spectrum of hIAPP fibers, 2.5 mM. (d) 2D IR spectrum of hIAPP fibers, 5 mM.

the β-sheets and between the two cysteines that form a disulfide bond. These assignments are based primarily on the frequencies at which these features appear, since random coil residues absorb in a similar frequency range.

We determined the transition dipole strength for each of these samples using our previously published method, which is explicitly outlined in Appendix 3. To do so, we need the linear absorption spectrum, 2D IR spectrum, the absorption spectrum of the laser pulses, and a calibrant molecule with a known transition dipole strength. The probe pulse used in the 2D IR measurements provides the linear absorption and pulse spectrum. Figure 4.3 shows diagonal slices through 2D IR and absorption spectra of hIAPP fibers at the four concentrations. The integrated area of the absorption spectra should scale with concentration according to Beer's law, but the 1 and 1.5 mM samples are lower than expected from the average concentration of the sample due to the inherent heterogeneity of mixing during sample preparation. In other places, the concentration is larger than average. In comparison, the 2D IR signals clearly do not scale with concentration, which immediately indicates that the transition dipole of the β-sheet modes is larger than a single amide I oscillator. The heterogeneity in concentration is not a factor in the calculation of the transition dipole strength since the calculation is performed using the 2D IR and absorption spectrum from the same spot in the sample. Table 4.1 lists the frequency of the β-sheet peak, the absorbance, the 2D maximum, and the calculated transition dipole intensity for each of the four samples. The transition dipole strengths range from 0.2 ± 0.01 to 1.5 ± 0.01 D^2.

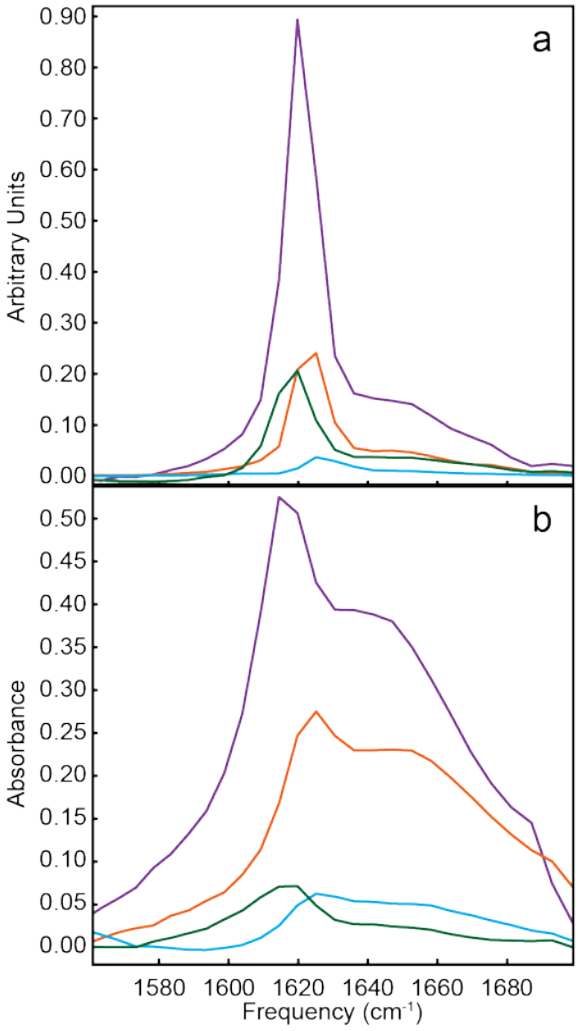

Figure 4.3 (a) Diagonal slices through 2D IR spectra of hIAPP fibers at 1 mM (cyan), 1.5 mM (green), 2.5 mM (orange), and 5 mM (purple). (b) Simultaneously measured absorbance spectra of hIAPP fibers at 1 mM (cyan), 1.5 mM (green), 2.5 mM (orange), and 5 mM (purple).

hIAPP fibers				
Concentration (M)	Frequency (cm^{-1})	Absorbance	2D maximum (arb. units)	Transition Dipole Strength (D^2)
1	1621	0.067	0.037	0.2 ± 0.01
1.5	1614	0.071	0.207	1.5 ± 0.01
2.5	1618	0.275	0.245	0.36 ± 0.01
5	1615	0.525	0.914	0.76 ± 0.01

Table 4.1 Concentration, β-sheet frequency, absorbance, maximum of the 2D IR diagonal slice, and calculated transition dipole strengths of hIAPP fibers.

We note that there is a correlation between β-sheet frequency and transition dipole strength; the lower the frequency the larger the transition dipole. Shown in Figure 4.4 are normalized 2D IR slices. The highest β-sheet mode absorbs at 1621 cm^{-1}, which also has the broadest 2D IR diagonal linewidth, the largest anharmonic shift (not shown), and the smallest transition dipole strength (0.2 ± 0.01 D^2). In contrast, the lowest frequency β-sheet mode absorbs at 1614 cm^{-1}, has the narrowest diagonal linewidth, the smallest anharmonic shift (not shown), and the largest transition dipole strength (1.5 ± 0.01 D^2). The quantities are all related to the delocalization of the normal mode. We come back to this point in the Discussion.

4.3.2 Transition dipole strengths of rat IAPP in solution, micelles, and membranes

The 2D IR spectra of rat amylin in solution, micelles and bilayers are shown in Figure 4.5. All spectra exhibit a broad peak along the diagonal near 1650 cm^{-1} due to the amide I modes in the peptide and a small shoulder at 1591 cm^{-1} from deuterated sidechains, such as arginine, that are known to absorb in this region. Except for the ester stretch in the bilayer sample that begins to absorb at 1680 cm^{-1}, the three spectra are very similar to one another. The maximum absorbance between the samples differs by 2 cm^{-1} or less and there are slight differences in the anti-diagonal linewidths. The FTIR spectra (Figure 4.6b) are similar to one another as well. Using standard empirical assignments based on frequencies and linewidths, one would probably conclude that amylin is random coil in all three environments.

Figure 4.6a shows diagonal slices through 2D IR spectra of rIAPP in solution, micelle, and membrane and Figure 4.6b shows the simultaneously measured absorbance

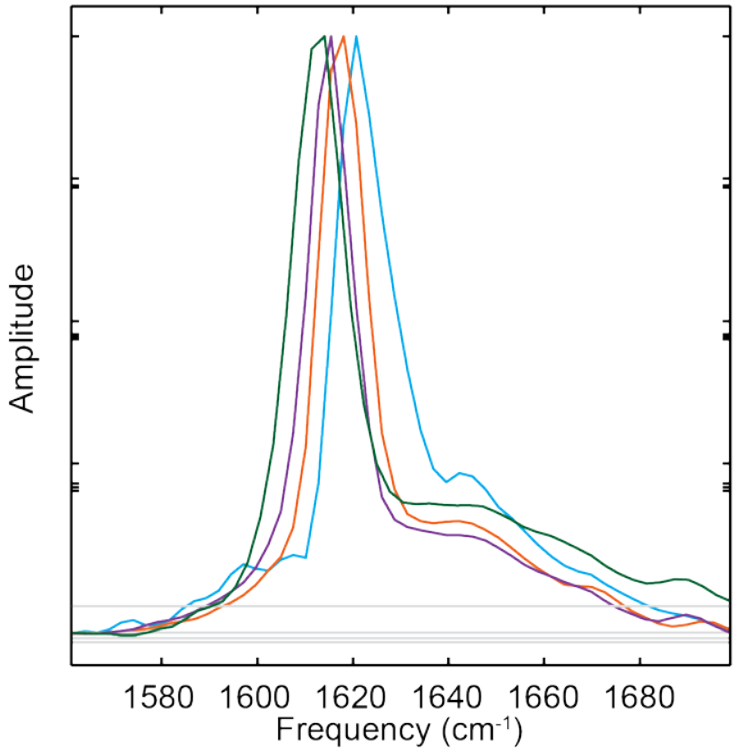

Figure 4.4 Normalized slices through the diagonal of 2D IR spectra of 1 mM (cyan), 1.5 mM (green), 2.5 mM (orange), and 5 mM (purple). The frequency of the β-sheet peak decreases with increasing transition dipole strength. In addition, the diagonal linewidths narrow as the transition dipole strength increases.

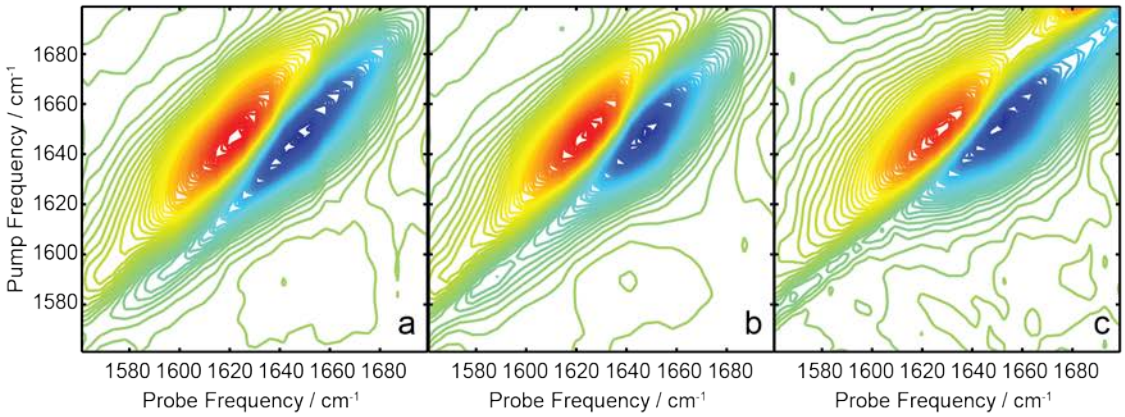

Figure 4.5 (a) 2D IR spectrum of rIAPP in solution. (b) 2D IR spectrum of rIAPP in micelles. (c) 2D IR spectrum of rIAPP in membranes. All slices are normalized to the amide I mode.

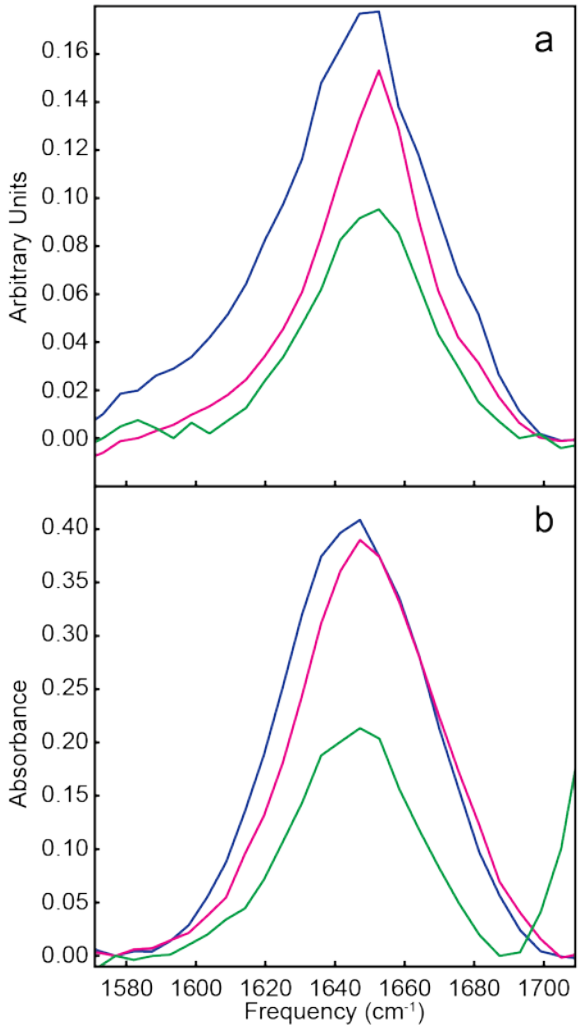

Figure 4.6 (a) Diagonal slices through 2D IR spectra of rIAPP in solution (blue), micelles (magenta), and membranes (green). (b) Simultaneously measured absorbance spectrum of rIAPP in solution (blue), micelles (magenta), and membranes (green).

spectra. Once again, the absorption spectrum does not scale as expected based solely on concentration, because samples made from micelles and vesicles are often not spatially uniform. Thus, calculating transition dipole strengths from the absorption spectrum alone would be quite inaccurate. Following the same procedure as above for the fibers (and as outlined in Appendix 3), the transition dipole strengths were calculated. The transition dipole of rIAPP in solution is $|\mu|^2$=0.15±0.08 D^2 at 1650 cm^{-1}, which is the absorption maximum, in the micelle it is $|\mu|^2$=0.16±0.06 D^2 at 1650 cm^{-1}, and in the membrane it is $|\mu|^2$=0.20±0.07 D^2 at 1652 cm^{-1}. These values are compiled in Table 4.2. Notice that the transition dipole strength progressively increases from solution to micelle to bilayer. Moreover, the transition dipole intensity for a random coil peptide is $|\mu|^2$=0.12±0.013 D^2.[25] Thus, rat amylin is nearly entirely random coil in solution, but progressively adopts a structure in micelles and bilayers that enables the vibrational modes to delocalize. Since the increase in the transition dipole strength occurs at 1650 cm^{-1}, we conclude that it is adopting α-helical character in micelles and bilayers, which is consistent with NMR studies.[41]

Based on our previous work, we know that a soluble α-helices have a transition dipole strength of 0.26 D^2.[25] Thus, in bilayers, rat IAPP might be largely helical. However, in all likelihood, rat IAPP will have both random coil and α-helical contributions to the structure. If so, then the measured $|\mu|^2$ value is an average of the random coil and α-helix transition dipoles, and thus represents a lower bound to the transition dipole strength of any helix that is present. To obtain the transition dipole strength of the helix alone, we repeat our calculation after first subtracting the random

rIAPP				
Sample	Frequency (cm^{-1})	Transition Dipole Strength (D^2)	Percent Random Coil	Calculated Dipole Strength (D^2)
Solution	1650	0.15 ± 0.08		
Micelle	1650	0.16 ± 0.06	0.67	0.55 ± 0.09
Membrane	1652	0.20 ± 0.07	0.35	0.53 ± 0.08

Table 4.2 Sample type, peak frequency, and transition dipole strength of the three types of rIAPP samples. The scaling factors are the calculated to scale the solution spectrum to the micelle spectrum and the solution spectrum to the membrane spectrum. They can be interpreted as the amount of random coil peptide in each sample. After subtracting the scaled solution spectrum from the pure micelle and pure membrane spectra, the transition dipole strength was calculated for the difference spectra and is the calculated dipole strength.

coil contribution to the spectra. To do so, we assume that in solution, rIAPP is 100% random coil, which is consistent with its transition dipole strength. We then subtracted the rIAPP absorption spectrum from the micelle and membrane absorption spectra scaled so that the frequency range between 1614 to 1620 cm^{-1} went to baseline (Figure 4.7a). This region was selected because most helical membrane peptides do not absorb in this region.[21,42] The resulting difference spectrum is the absorption spectrum of the pure helix in the micelle and membrane samples (Figure 4.7b). The scaling factors were 0.67 and 0.35 for the micelles and membrane samples, respectively (Table 4.2), which are a measure of the percent random coil in each sample. Using these scaling factors, the 2D IR spectra are subtracted as well. Finally, the transition dipole strengths are calculated, as done above. In the end, we obtain the transition dipole strength for what we believe to be the α-helix contribution to the structure, which is 0.55 D^2 in the micelles and 0.53 D^2 in the membrane. We note that the two are very similar to one another and that both are roughly twice as large as in the previously measured soluble α-helix, which are points that we discuss below.

4.4 Discussion

4.4.1 Interpretation of transition dipole strengths and participation ratios

The transition dipole strength is a measure of the number of residues over which excitons are delocalized. A single peptide unit, as modeled by N-methylacetamide (NMA), has a transition dipole strength of $|\mu|^2$=0.12 D^2.[25] We consider this value to be equivalent to an uncoupled amide I mode, which is the same value we found for a denatured soluble peptide. Thus, transition dipole strengths greater than 0.12 D^2 indicate

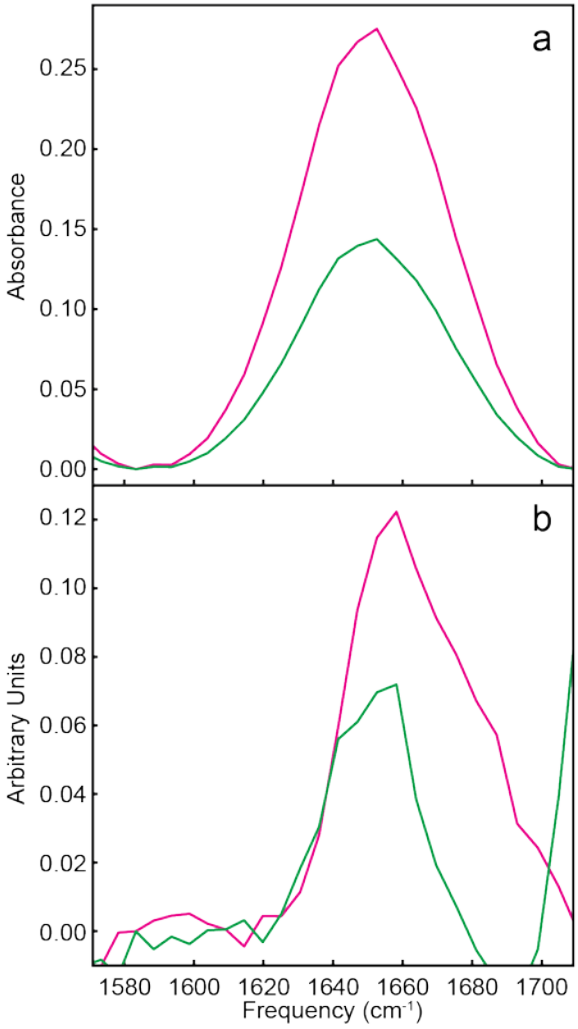

Figure 4.7 (a) Absorbance of rIAPP in solution scaled at 1614-1620 cm^{-1} to absorbance of rIAPP in a micelle (magenta). Scaling the rIAPP in solution to rIAPP in micelle over that frequency range gives a scaling factor of 0.67. Absorbance of rIAPP in solution scaled at 1614-1620 cm^{-1} to absorbance of rIAPP in a membrane (green). Scaling the rIAPP in solution to rIAPP in membrane over that frequency range gives a scaling factor of 0.35. (b) The absorbance of the scaled (to micelle spectrum) rIAPP in solution spectrum subtracted from the pure rIAPP in solution trace (magenta). The absorbance of the scaled (to membrane spectrum) rIAPP in solution spectrum subtracted from the pure rIAPP in solution trace (green).

a peptide has adopted a structure with vibrational coupling large enough to delocalize the amide I vibrational modes. The largest transition dipole measured here was for the 1.5 mM sample of hIAPP, which had $|\mu|^2 = 1.5 \pm 0.01$ D^2, indicating that the amide I mode is delocalized over ~12 amino acids. We discuss the structural implications of this observation below, but the first conclusion from our study is that the amide I vibrational modes can delocalize across an enormous distance.

There are several factors that determine the degree of vibrational delocalization, and hence, the transition dipole strengths. First, there is the structure that sets the coupling constants. To the best of our knowledge, amylin always assumes parallel β-sheets, and so the coupling strengths should be approximately invariant from sample to sample. The coupling constants in perfect parallel β-sheets have been calculated to be as large as 20 cm^{-1}, which is the primary driver for delocalization.[43] Ultimately, the size of the β-sheet determines the number of residues that can participate in a β-sheet vibrational mode, which in the case of amylin, is about 20 residues.[44] Second, there is structural disorder. Structural variations, such as fraying that typically occurs at the edges of β-sheets and the ends of α-helices, alter the coupling constants.[26] This effect is often called "off-diagonal disorder" and usually localizes the vibrational modes. Third, frequency variations caused by the surrounding environment, such as residues exposed to water, will also localize the vibrational modes even if the secondary structure is not altered. This effect is usually called "diagonal disorder" because it changes the diagonal elements of an excitonic Hamiltonian. In essence, the degree of delocalization is a competition between coupling strength and disorder.

In calculations of vibrational normal modes, one often computes the inverse participation ratio, defined as:

$$IPR_\alpha \equiv \left(\sum_j U_{\alpha,j}^4\right)^{-1} \quad (4.1)$$

Where $U_{\alpha,j}$ is the *j*th element of the eigenvector associated with the αth amide I normal mode. The participation ratio is a measure of the number of local vibrations, in our case the amide I modes from each residue, that contribute to the normal mode. For example, Cho used the inverse participation ratio to understand the delocalization of the amide I normal a modes across the strands of a simulated β-hairpin turn[45] and a multistranded β-sheet.[46] The participation ratio is calculated using the eigenvectors of the normal modes, whose coefficients are determined by the competition between coupling and disorder, as discussed above. A participation ratio can be computed from an eigenvector, but one cannot not uniquely back calculate an eigenvector from a participation ratio. For example, IPR_α=1 means that the normal mode is localized on one amino acid, or one peptide strand, while IPR_α=5 is created when the normal mode is delocalized over 5 amino acids or 5 strands.

The experimental transition dipole strengths measured here are closely related to the participation ratio. The transition dipole of the normal mode is created by the vector sum of the local amide I modes, weighted by the coefficients of the eigenstates. The main difference between the transition dipole strengths and the participation ratio is the vector nature of the transition dipoles. Thus, the orientations of the local modes will alter the transition dipoles but not the participation ratio, although they may indirectly influence the participation ratio through the couplings (e.g. transition dipole coupling

depends on orientations). For a given secondary structure with known coupling constants and transition dipoles, then the interpretation of the transition dipole strength can include orientations, which we discuss below. Nonetheless, to a first-order approximation, we can interpret the transition dipole strengths as an experimental measure of the participation ratio by simply dividing the transition dipole strength by that of the local modes. With these concepts in mind, we now turn to the interpretation of the experimental data.

4.4.2 Structural disorder and polymorphs in amyloid fibers

As discussed above, to a first approximation, the transition dipole strength can be considered a measure of the number of residues over which the vibrational modes are delocalized, for which we use the transition dipole strength of NMA, $|\mu|^2=0.12\ D^2$, as the standard for a single peptide unit. In the 1 mM hIAPP fiber sample, the transition dipole strength was measured to be $0.20 \pm 0.01\ D^2$, which indicates that the amide I vibrational modes were delocalized over nearly two amino acids. The 2 mM sample had a transition dipole strength of $0.36 \pm 0.01\ D^2$, which is 3 times that of NMA, revealing that the excitons were delocalized over three residues in the β-sheet. The 5 mM sample had a transition dipole strength of $0.76 \pm 0.01\ D^2$, corresponding to delocalization over ~6 amino acids. The largest transition dipole strength of $1.5 \pm 0.01\ D^2$ was observed in the 1.5 mM sample, which corresponds to delocalization over ~12 amino acids. Thus, the extent of delocalization is enormous.

We note that the transition dipole strength is anti-correlated to the frequency of the β-sheet mode; the larger the transition dipole strength the lower the amide I

frequency, as illustrated in Figure 4.4 and Table 4.1. The smallest transition dipole strength had a β-sheet mode at 1621 cm^{-1}, while the largest was at 1614 cm^{-1}. This experimental observation is in agreement with prior experimental simulations.[43,45,47] Simulations by Cho and coworkers showed that the amide I frequency of parallel and anti-parallel sheets depended largely on the number of strands over which the vibrational modes were delocalized and to a lesser extent over the number of residues in each strand (because interstrand coupling is stronger than intrastrand coupling, e.g. 10 cm^{-1} versus 1 cm^{-1}).[46] Cho did not report absolute transition dipole strengths, but they scale approximately linearly with the number of strands in the β-sheet. Thus, we conclude that the largest transition dipole strength measured here corresponds to vibrational modes that are delocalized over 12 strands in the amyloid β-sheets of the fibers.

We believe that the transition dipole strength is a better measure of delocalization than the frequency itself. Shown in Figure 4.8 is a plot of the measured β-sheet frequency versus the transition dipole strength. Notice that the frequency appears to be reaching an asymptote at 1614 cm^{-1}. The simulations by Cho also predicted asymptotic behavior.[46] Notice that the dipole strengths increase by a factor of 7.5, while the frequency only changes by 7 cm^{-1}. Thus, the frequency is not as sensitive as the transition dipole strength. Moreover, interpretation of the frequency requires knowledge about the environment electrostatics. For instance, β-sheets exposed to water versus buried inside hydrophobic amyloid fibers will certainly have different frequencies even if they are the same size. In contrast, the transition dipole strength of the amide I mode is

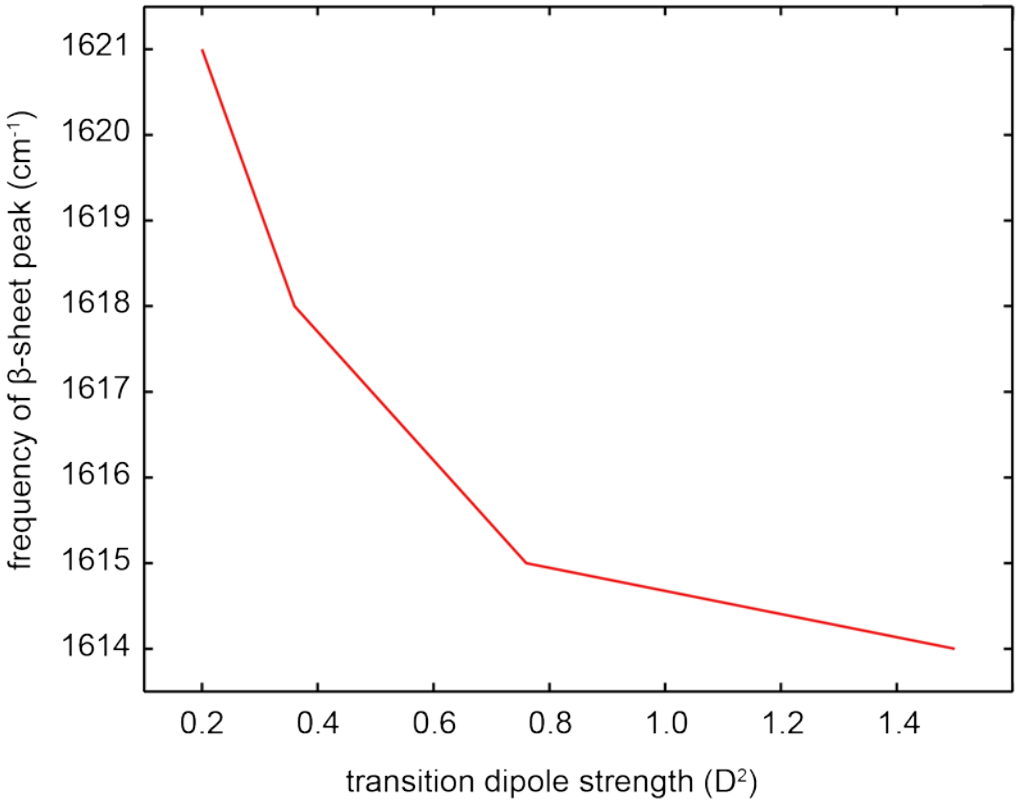

Figure 4.8 Measured β-sheet peak frequency in the four hIAPP fiber samples versus the transition dipole strength measured in each sample.

quite insensitive to its environment or whether it is hydrogen bonded, and thus provides an accurate reference point.[48,49]

Why do fibers formed at different concentrations exhibit different transition dipole strengths and why is there seemingly no correlation between the two? One explanation might be polymorphs which are now being recognized as a common phenomenon of amyloids. Polymorphs are variations in amyloid fiber structure that occur for identical monomers.[50-53] They can differ in the arrangement of the side chains or in the tertiary structure. It is thought that the preparation conditions are responsible for dictating which polymorph forms. Our results might be explained by the conversion of one polymorph into another. However, there is evidence for Aβ that once a polymorph forms, it is kinetically trapped and does not interconvert into another.[51] That result may not hold true for amylin, since we have observed an interconversion between fibers structures in a peptide inhibition study. It might be possible to determine if the samples formed from the different concentrations form polymorphs, but it would be difficult because polymorphs typically exhibit very similar transmission electron microscope images, CD spectra and ThT binding. Another possible explanation for the results is simply the heterogeneity of the sample preparation procedure.

4.4.3 Rat IAPP in membrane bilayers is α-helical like in micelles, but more structurally ordered

As discussed above, the extent of delocalization is determined by a competition between the strength of the coupling and the magnitude of the disorder. Disorder can localize the vibrational modes without altering the secondary structure, such as would

occur by the frequency shifts caused by solvation. As such, the transition dipoles measured here provide lower bounds to the number of amino acids involved in the secondary structure. This statement is most obvious in the context of the amyloid fibers discussed above for which we found at most 12 strands participating in the vibrational modes even though the fibers are formed from hundreds of peptide β-strands. In the case of the helices, which are formed form a single polypeptide, it provides a lower limit to the length of the helix. Considering that the transition dipoles of the helices in the micelle and bilayer were measured to be 0.16 ± 0.06 and 0.20 ± 0.07 D^2, and that the transition dipole is oriented 38° from the helix axis[54], there must be ~7.4 residues, or two complete helix turns, participating in the measured vibrational mode. According to NMR data on rat IAPP in micelles, residues Ala-5 to Ser-23 are helical.[29] In comparison, in our original report using this methodology, for a soluble α-helix, we measured $|\mu|^2$=0.26 D^2 and concluded that the vibrations spanned 3.5 residues, or one complete helix turn. Thus, the increase of the transition dipole strength from 0.15 to 0.53 D^2 is not a reflection of the length of the helix, but instead indicates that the helices themselves are becoming more rigid.

In NMR studies, micelles are often used as approximations to bilayers to study membrane peptides because micelles rotate fast enough that high-resolution NMR spectroscopy can be used rather than solid-state NMR. However, micelles can perturb the peptide structure, by causing curvature or not being a good model for a membrane. The first step towards determining how much α-helix secondary structure is in the samples of rIAPP in micelles and membranes was to scale the absorbance of rIAPP in

solution (assumed to be 100% random coil) to the absorbance of rIAPP in micelles and membranes. The scaling factor between the solution and micelle traces was 0.67, and the scaling factor between the solution and membrane traces was 0.35. This means that 67% of rIAPP in micelles is random coil and 35% of rIAPP in membranes is random coil, corresponding to ~25 and ~13 residues, respectively. After subtracting the solution spectrum from the micelle and membrane spectra, the final transition dipole strength of the α-helix content in rIAPP in micelles was 0.55 D^2, and the transition dipole strength of rIAPP in membrane was 0.53 D^2. Comparing those values to NMA, the transition dipole strength of the α-helix in micelles is ~4.6 times larger, and the transition dipole strength of the α-helix in membrane is ~4.4 times larger. The transition dipole moment of the amide I mode is oriented 38° relative to the helix axis.[55] The measure of delocalization can then be calculated as 4.6 $\cos^{-2}(38°)$ for rIAPP in micelles, meaning that excitons delocalize over ~7.4 residues, or 2 complete turns. Exciton delocalization for rIAPP in membranes spans ~7.1 residues, or just less than 2 complete turns. This is in agreement with previous work that estimated 2 α-helix turns for the extent of exciton delocalization.[54] Based upon previous work suggesting that the N-terminus of rIAPP adopts an α-helix on a micelle, and the work presented here that shows that exciton delocalization spans ~7 residues, it is likely that the α-helix in rIAPP on micelles and membranes spans residues ~8-16. This region is adjacent to the disordered residues between Cys-2 and Cys-7, but before what is considered the turn region in hIAPP. The sequence in the region is identical to that of hIAPP, and thus may provide insight into intermediates in the pathway for hIAPP to disrupt cell membranes.

4.5 Conclusions

To conclude, we have shown that measuring the transition dipole strength is a useful way to determine secondary structures of proteins that otherwise could not be accurately determined. In the case of hIAPP fiber structure, we have shown that this technique can identify polymorphs of the same peptide that would not be definitively revealed based on the β-sheet frequency alone. We show that hIAPP forms fiber polymorphs with vibrational mode delocalization that varies from 2 to 12 residues. We have also shown that the transition dipole strength of rIAPP varies depending on if it is in solution, micelles, or membrane bilayers. In micelles and membranes, vibrational modes delocalize over two helix turns, most likely segregated to the N-terminus of the peptide. Our interpretation of these data works best for excitonic systems in which the local modes are all the same. In the future, this method could be used to identify intermediates in the hIAPP aggregation pathway. While the frequency of the amide I mode may not be drastically changing for every intermediate structure, the transition dipole strength will almost certainly be changing as hIAPP folds.

4.6 Appendix

Step by step instructions for calculating the transition dipole moment of peptides with congested spectra can be found in Appendix 4.

4.7 References

(1) Shim, S.-H.; Gupta, R.; Ling, Y. L.; Strasfeld, D. B.; Raleigh, D. P.; Zanni, M. T. *Proceedings of the National Academy of Sciences* 2009, *106*, 6614-6619.

(2) Ling, Y. L.; Strasfeld, D. B.; Shim, S.-H.; Raleigh, D. P.; Zanni, M. T. *The Journal of Physical Chemistry B* 2009, *113*, 2498-2505.

(3) Vigano, C.; Manciu, L.; Buyse, F.; Goormaghtigh, E.; Ruysschaert, J. M. *Peptide Science* 2000, *55*, 373-380.

(4) Kim, Y. S.; Hochstrasser, R. M. *The Journal of Physical Chemistry B* 2009, *113*, 8231-8251.

(5) Falvo, C.; Zhuang, W.; Kim, Y. S.; Axelsen, P. H.; Hochstrasser, R. M.; Mukamel, S. *The Journal of Physical Chemistry B* 2012, *116*, 3322-3330.

(6) Ding, F.-X.; Xie, H.; Arshava, B.; Becker, J. M.; Naider, F. *Biochemistry* 2001, *40*, 8945-8954.

(7) Ghosh, A.; Qiu, J.; DeGrado, W. F.; Hochstrasser, R. M. *Proceedings of the National Academy of Sciences* 2011, *108*, 6115-6120.

(8) Mukherjee, P.; Kass, I.; Arkin, I. T.; Zanni, M. T. *The Journal of Physical Chemistry B* 2006, *110*, 24740-24749.

(9) Mukherjee, P.; Kass, I.; Arkin, I. T.; Zanni, M. T. *Proc. Natl. Acad. Sci. U. S. A.* 2006, *103*, 3528-3533.

(10) Mukherjee, P.; Krummel, A. T.; Fulmer, E. C.; Kass, I.; Arkin, I. T.; Zanni, M. T. *J. Chem. Phys.* 2004, *120*, 10215-10224.

(11) Woys, A. M.; Lin, Y.-S.; Reddy, A. S.; Xiong, W.; de Pablo, J. J.; Skinner, J. L.; Zanni, M. T. *J. Am. Chem. Soc.* 2010, *132*, 2832-2838.

(12) Middleton, C. T.; Buchanan, L. E.; Dunkelberger, E. B.; Zanni, M. T. *The Journal of Physical Chemistry Letters* 2011, *2*, 2357-2361.

(13) Middleton, C. T.; Marek, P.; Cao, P.; Chiu, C.-c.; Singh, S.; Woys, A. M.; de Pablo, J. J.; Raleigh, D. P.; Zanni, M. T. *Nat Chem* 2012, *advance online publication*.

(14) Middleton, C. T.; Woys, A. M.; Mukherjee, S. S.; Zanni, M. T. *Methods* 2010, *52*, 12-22.

(15) Moran, S. D.; Decatur, S. M.; Zanni, M. T. *J. Am. Chem. Soc.* 2012.

(16) Moran, S. D.; Woys, A. M.; Buchanan, L. E.; Bixby, E.; Decatur, S. M.; Zanni, M. T. *Proceedings of the National Academy of Sciences* 2012, *109*, 3329-3334.

(17) Brovchenko, I.; Singh, G.; Winter, R. *Langmuir* 2009, *25*, 8111-8116.

(18) Mishra, R.; Bulic, B.; Sellin, D.; Jha, S.; Waldmann, H.; Winter, R. *Angewandte Chemie International Edition* 2008, *47*, 4679-4682.

(19) Mishra, R.; Sellin, D.; Radovan, D.; Gohlke, A.; Winter, R. *ChemBioChem* 2009, *10*, 445-449.

(20) Sellin, D.; Yan, L.-M.; Kapurniotu, A.; Winter, R. *Biophys. Chem.* 2010, *150*, 73-79.

(21) Krimm, S.; Bandekar, J. In *Adv. Protein Chem.*; C.B. Anfinsen, J. T. E., Frederic, M. R., Eds.; Academic Press: 1986; Vol. Volume 38, p 181-364.

(22) Barth, A. *Prog. Biophys. Mol. Biol.* 2000, *74*, 141-173.

(23) Chirgadze, Y. N.; Fedorov, O. V.; Trushina, N. P. *Biopolymers* 1975, *14*, 679-694.

(24) Hamm, P. a. Z., Martin T.; Cambridge University Press, New York: 2011.

(25) Grechko, M.; Zanni, M. T. *The Journal of Chemical Physics* 2012, *137*, 184202.

(26) *Examining Amyloid Structure and Kinetics with 1D and 2D Infrared Spectroscopy and Isotope Labeling*; 1 ed.; Buchanan, L., Dunkelberger, EB, Zanni, MT, Ed.; Springer: Heidelberg, 2011; Vol. 1.

(27) Abramavicius, D.; Zhuang, W.; Mukamel, S. *The Journal of Physical Chemistry B* 2004, *108*, 18034-18045.

(28) Nanga, R. P. R.; Brender, J. R.; Xu, J.; Hartman, K.; Subramanian, V.; Ramamoorthy, A. *J. Am. Chem. Soc.* 2009, *131*, 8252-8261.

(29) Nanga, R. P. R.; Brender, J. R.; Xu, J.; Veglia, G.; Ramamoorthy, A. *Biochemistry* 2008, *47*, 12689-12697.

(30) Knight, J. D.; Hebda, J. A.; Miranker, A. D. *Biochemistry* 2006, *45*, 9496-9508.

(31) Cao, P.; Meng, F.; Abedini, A.; Raleigh, D. P. *Biochemistry* 2009, *49*, 872-881.

(32) Williamson, J. A.; Loria, J. P.; Miranker, A. D. *J. Mol. Biol.* 2009, *393*, 383-396.

(33) Williamson, J. A.; Miranker, A. D. *Protein Sci.* 2007, *16*, 110-117.

(34) Hebda, J. A.; Miranker, A. D. *Annual Review of Biophysics* 2009, *38*, 125-152.

(35) Apostolidou, M.; Jayasinghe, S. A.; Langen, R. *J. Biol. Chem.* 2008, *283*, 17205-17210.

(36) Marek, P.; Woys, A. M.; Sutton, K.; Zanni, M. T.; Raleigh, D. P. *Org. Lett.* 2010, *12*, 4848-4851.

(37) Shim, S.-H.; Strasfeld, D. B.; Fulmer, E. C.; Zanni, M. T. *Opt. Lett.* 2006, *31*, 838-840.

(38) Shim, S.-H.; Strasfeld, D. B.; Ling, Y. L.; Zanni, M. T. *Proceedings of the National Academy of Sciences* 2007, *104*, 14197-14202.

(39) Strasfeld, D. B.; Ling, Y. L.; Shim, S.-H.; Zanni, M. T. *J. Am. Chem. Soc.* 2008, *130*, 6698-6699.

(40) Dunkelberger, E. B.; Buchanan, L. E.; Marek, P.; Cao, P.; Raleigh, D. P.; Zanni, M. T. *J. Am. Chem. Soc.* 2012, *134*, 12658-12667.

(41) Brender, J. R.; Lee, E. L.; Cavitt, M. A.; Gafni, A.; Steel, D. G.; Ramamoorthy, A. *J. Am. Chem. Soc.* 2008, *130*, 6424-6429.

(42) Barth, A. *Biochimica et Biophysica Acta (BBA) - Bioenergetics* 2007, *1767*, 1073-1101.

(43) Demirdöven, N.; Cheatum, C. M.; Chung, H. S.; Khalil, M.; Knoester, J.; Tokmakoff, A. *J. Am. Chem. Soc.* 2004, *126*, 7981-7990.

(44) Luca, S.; Yau, W.-M.; Leapman, R.; Tycko, R. *Biochemistry* 2007, *46*, 13505-13522.

(45) Hahn, S.; Ham, S.; Cho, M. *The Journal of Physical Chemistry B* 2005, *109*, 11789-11801.

(46) Lee, C.; Cho, M. *The Journal of Physical Chemistry B* 2004, *108*, 20397-20407.

(47) Cheatum, C. M.; Tokmakoff, A.; Knoester, J. *The Journal of Chemical Physics* 2004, *120*, 8201-8215.

(48) Nicodemus, R. A.; Corcelli, S. A.; Skinner, J. L.; Tokmakoff, A. *The Journal of Physical Chemistry B* 2011, null-null.

(49) Auer, B.; Kumar, R.; Schmidt, J. R.; Skinner, J. L. *Proceedings of the National Academy of Sciences* 2007, *104*, 14215-14220.

(50) Hu, K.-N.; McGlinchey, Ryan P.; Wickner, Reed B.; Tycko, R. *Biophys. J.* 2911, *101*, 2242-2250.

(51) Paravastu, A. K.; Leapman, R. D.; Yau, W.-M.; Tycko, R. *Proceedings of the National Academy of Sciences* 2008, *105*, 18349-18354.

(52) Petkova, A. T.; Leapman, R. D.; Guo, Z.; Yau, W.-M.; Mattson, M. P.; Tycko, R. *Science* 2005, *307*, 262-265.

(53) Tycko, R.; Wickner, R. B. *Acc. Chem. Res.* 2013.

(54) Hamm, P.; Lim, M.; Hochstrasser, R. M. *The Journal of Physical Chemistry B* 1998, *102*, 6123-6138.

(55) Marsh, D.; Müller, M.; Schmitt, F.-J. *Biophys. J.* 2000, *78*, 2499-2510.

CHAPTER 5*

Designing an Amyloid Inhibitor Based on its Aggregation Mechanism

5.1 Abstract

We have synthesized a series of non-natural peptide macrocycles to study the aggregation mechanism of the human islet amyloid polypeptide (hIAPP or amylin) associated with type 2 diabetes. One strand of the macrocycles contains a heptapeptide sequence that matches a segment of hIAPP located primarily within either the disordered loop or the N- or C-terminal β-sheets of the fibers. The second strand of the macrocycle contains a non-natural amino acid that prevents formation of amyloid β-sheets. Of the 5 macrocycles tested, only the macrocycle that matches the disordered loop inhibits the aggregation kinetics. 2D IR spectroscopy with isotope labeling reveals a transient

* Portions of this chapter will be published as part of a paper submitted in the summer of 2013. My contributions are in collaboration with Lauren E. Buchanan, Huong Q. Tran, Pin-Nan Cheng, Chi-Cheng Chiu, Cynthia Tu, Daniel P. Raleigh, Juan J. dePablo, James S. Nowick, and Martin T. Zanni.

oligomeric species with β-sheet content near Ala-25. In the presence of the macrocycle inhibitor, the lifetime of the oligomeric intermediate is increased because the inhibitor stabilizes the intermediate. The presence of an intermediate helps explain long standing questions regarding the fragment studies, kinetics, mutations and inhibition of amylin. This work also demonstrates that an effective strategy for amyloid inhibition may be to design inhibitors that target intermediate states rather than the final fiber structure.

5.2 Introduction

The misfolding of proteins into amyloid fibers is implicated in numerous human diseases, including type 2 diabetes, Alzheimer's disease, and Huntington's disease.[1-5] As a result, there is considerable interest in developing inhibitors of amyloid formation to understand both how their formation can be prevented and the properties that cause them to form in the first place. Many categories of inhibitors have been explored, but the most common are small molecules[6-9] and peptides.[10-15] Amyloid fibers are created by stacks of parallel β-sheets that have interdigitated sidechains. Small molecules like EGCG and resveratrol are thought to bind to the surfaces of the amyloid β-sheets, thereby preventing the side chains from stabilizing the sheets. In contrast, peptide inhibitors are most often designed to replace the monomers in the β-sheet by containing a segment that has high sequence similarity with a segment of the amyloid protein. In addition to this recognition sequence, additional amino acids such as prolines[12-14] or unnatural amino acids[10,11,15] are often included which act as β-sheet breakers to destabilize the adjacent β-sheet or prevent the attachment of additional monomers. Efforts to design peptide inhibitors generally focus on identifying core amyloidogenic regions of amyloid peptides.[16] Mutations are

introduced within this region in either peptide fragments or the full length peptide. N-methylated peptides based on β-amyloid (Aβ)[17-19] and human islet amyloid polypeptide (hIAPP or amylin)[10] have been shown to reduce fibril formation by their respective parent peptides and, in some cases, dissociate preformed fibrils. Proline mutants have also shown promise in both delaying aggregation and reducing overall fiber formation.[12,20] However, similar mutants can have dramatically different inhibition effects and standard techniques, such as transmission electron microscopy (TEM) and thioflavin-T (ThT) fluorescence, do not provide sufficient structural information to understand such differences. In fact, we recently observed two cases in which ThT fluorescence was unaffected by major fiber rearrangements.[14,21]

The strategies discussed above inhibit by targeting the β-sheet features of the fiber. A better target might be structural intermediates that transiently exist along the pathway to fiber formation, if they exist. A few years ago, we used 2D IR spectroscopy to measure the kinetics of individual residues during the aggregation of hIAPP.[22] hIAPP fibers are created by columns of U-shaped monomers, where each column has an N-terminal (residues 8 to 17) and a C-terminal (residues ~25 to 37) parallel β-sheet connected by a disordered turn (Figure 5.1a).[23] By isotope labeling six different positions along the peptide backbone, we found that residues nearest the disordered loop were incorporated into the β-sheets of the fiber faster than were residues near the N- or C-terminals. By comparing the folding times for each residue, we proposed a stepwise aggregation pathway for human amylin. It appears that fiber nucleation occurs near the loop followed by folding down the N- and C- terminal β-sheets, with the C-terminal sheet

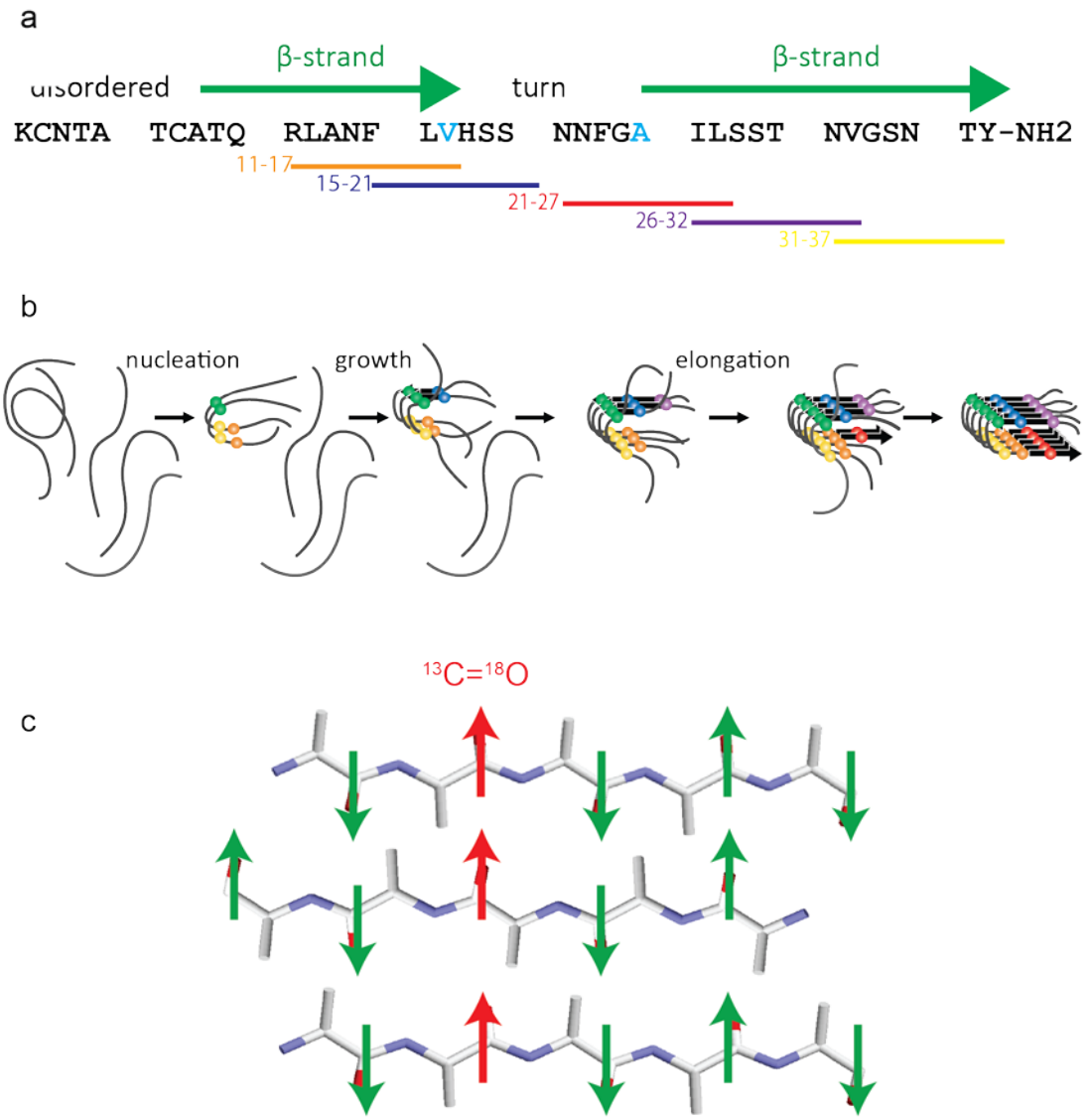

Figure 5.1 Sequence, structural model, and aggregation mechanism of human amylin. (a) Sequence of human amylin with regions of secondary structure indicated. Val-17 and Ala-25, highlighted in cyan, are isotope labeled in these experiments. The residues targeted by the macrocyclic peptides are indicated by the lines under the sequence. (b) Mechanism of amylin aggregation, with thick black arrows representing β-strands and grey strands representing disordered regions. The colored balls indicate the labeled residues used in the original experiment: Ala-8 (purple), Ala-13 (blue), Val-17 (green), Ala-25 (yellow), Leu-27 (orange), and Val-32 (red). (c) View of a parallel β-sheet from the side, illustrating the formation of a linear chain of isotope labeled residues.

taking about twice as long to form (Figure 5.1b). Our data revealed that aggregation of human amylin is not purely a nucleation event, but involves a sequence of secondary structure changes. Thus, the aggregation pathway in Figure 5.1b suggests an alternative strategy for inhibiting amylin fiber formation. Rather than target the final fiber structure, one could instead target an earlier step in the mechanism, such as formation of the disordered loop. If the loop were prevented from forming or were stabilized from evolving further, then the fiber and all the other downstream structures would presumably be inhibited as well.

In this chapter, we test this hypothesis using a series of macrocyclic β-sheet peptides that are homologous to segments of hIAPP. The macrocycles comprise two parallel β-strands connected by two δ-linked ornithines, which mimic β-turns[24] (Figure 5.2). The "lower" strand contains an unnatural amino acid, Hao, and four additional residues which allow for tuning of the macrocycles' properties. The Hao unit was designed as a tripeptide β-strand mimic which templates the folding of the upper strand into a β-strand and blocks the hydrogen-bonding functionality of the lower strand.[25] The "upper" strand contains a heptapeptide sequence from hIAPP, which should cause the macrocycle to hydrogen-bond selectively to the equivalent region of the parent peptide. ThT fluorescence assays and TEMs have shown that macrocycles with similar designs inhibit the aggregation of a tau-derived hexapeptide[15], amyloid-β peptides[26], and a truncated α-synuclein peptide.[26] We find that only the macrocycle targeting the 20-29 part of the turn region of amylin serves as an effective inhibitor, while macrocycles targeting mainly the β-strand regions accelerate

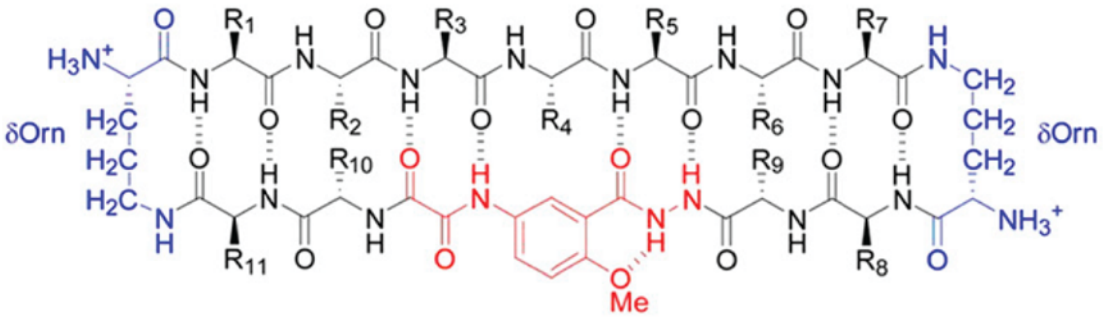

	R1-R7	R8-R11
1a)	amylin 11-17	KFYK
1b)	amylin 15-21	VFYK
1c)	amylin 21-27	KFYV
1d)	amylin 26-32	KFYK
1e)	amylin 31-37	VFYK

Figure 5.2 Design of macrocyclic β-sheet peptides 1a-e. Representation of macrocycles 1a-e highlighting the upper recognition β-strand, the lower blocking β-strand (with the Hao amino acid unit), and the δ-linked ornithine ($^{\delta}$Orn) turn units. The sequences for macrocycles 1a-e are indicated.

aggregation. Using isotope labeled peptides, we learn that the macrocycle that targets the 20-29 region inhibits by increasing the stability of a lag-phase oligomeric species. These results reinforce earlier work suggesting that residues within the region of 20-29 are critical to amylin aggregation.[27-29] They also shed light on previous kinetics and inhibitor studies.[22]

5.3 Experimental

5.3.1 Amylin synthesis

Amylin samples were synthesized on a CEM Liberty1 automated microwave peptide synthesizer using Fmoc solid-phase peptide synthesis and standard trifluoroacetic acid (TFA) cleavage and deprotection protocols, as previously described.[30,31] PAL-PEG-PS resin was used to produce an amidated C-terminus. Starting from ^{13}C C1-labeled amino acids (Cambridge Isotope Laboratories) and ^{18}O water, Fmoc-protected alanine and valine were $^{13}C^{18}O$ isotope labeled at the backbone carbonyl in a procedure also previously reported[32] and incorporated into amylin at positions Ala-25 or Val-17, respectively. Crude peptide was dissolved overnight in dimethylsulfoxide (DMSO) to form the disulfide bond between Cys-2 and Cys-7. Peptides were purified from DMSO by reversed-phase HPLC with a Vydac C18 preparative column and using HCl as the counterion, as described elsewhere.[30]

5.3.2 Macrocycle synthesis

Macrocycle synthesis has previously been described in detail elsewhere.[26] After purification, the macrocycles were lyophilized from 1 mM DCl multiple times until residual TFA had been fully removed.[33]

5.3.3 Sample preparation

Lyophilized amylin was dissolved to a final concentration of 1 mM in deuterated hexafluoroisopropanol (d-HFIP); after 8 hours, the peptides were fully deuterated and any fibers were disaggregated. Lyophilized macrocycles were dissolved to a final concentration of 1 mM in D_2O. Samples were prepared by drying aliquots of stock solution under vacuum and reconstituting them in 2 μL of 20 mM deuterated Tris buffer solution (pD ~ 7.4) to initiate aggregation. The final total peptide concentration was 0.5 mM for pure amylin samples and 1 mM for samples containing equimolar amylin and macrocycle. Samples were placed between CaF_2 windows separated by a 56 μM Teflon spacer and kept in a purge box under dry air to prevent hydrogen exchange from ambient water vapor.

5.3.4 Two-dimensional infrared spectroscopy measurements

The methods for collecting and processing 2D IR spectra are described in detail elsewhere.[34] Briefly, 800 nm pulses were generated by a home-built Ti:sapphire oscillator and amplified in a Nd:YLF-pumped regenerative amplifier. The pulses were sent to a home-built optical parametric amplifier (OPA) with difference frequency generation to produce 60 fs mid-IR pulses. The 6 μm light was split into pump and probe beams and the pump pulse was passed through a Ge acousto-optic modulator (AOM) pulse shaper[35,36] before both beams were focused onto the sample. The signal was detected with an MCT array. For kinetic experiments, there was an approximately 10 minute dead time between initiating aggregation and measuring the first 2D IR spectrum, after which spectra were collected continuously until the aggregation was complete and

the sample had equilibrated. Steady state data was collected either 20 minutes or 5 hours after aggregation was initiated.

5.4 Results

5.4.1 Aggregation of human amylin mixed with macrocyclic peptides

Five macrocycles were designed based on the sequence of human amylin (Figure 5.1a). Macrocycle 1 is a 54-membered ring comprising a heptapeptide recognition β-strand, a blocking β-strand with two dipeptides and a Hao unit, and two δ-linked ornithine ($^{\delta}$Orn) turns (Figure 5.2). The heptapeptide sequences RLANFLV ($hIAPP_{11-17}$), FLVHSSN ($hIAPP_{15-21}$), NNFGAIL ($hIAPP_{21-27}$), ILSSTNV ($hIAPP_{26-32}$), and NVGSNTY ($hIAPP_{31-37}$) were incorporated into the recognition strands of macrocycles 1a-e, respectively. These sequences were chosen to span key regions of hIAPP fibers: macrocycles 1a-b target primarily the N-terminal β-sheet, macrocycle 1c targets the turn region, and macrocycles 1d-e target the C-terminal β-sheet. The residues in the dipeptide sequences of the blocking strand were chosen to match the hydrophobicity and hydrophilicity of the residues in the recognition strand.

To assess the effectiveness of each as an inhibitor, the macrocycles were mixed at equimolar concentrations with monomeric amylin and 2D IR spectra were collected continuously over the course of five hours. Shown in Figure 5.3 are kinetic traces plotting the intensity of the β-sheet fundamental amide I mode, which appears at 1615-1620 cm^{-1} in the 2D IR spectrum. The increase in peak intensity over time is an effective measure of the increase in fiber content of a sample. The macrocycles do not have any spectral features in this range (Appendix 4 Figure A4.1) and so do not contribute

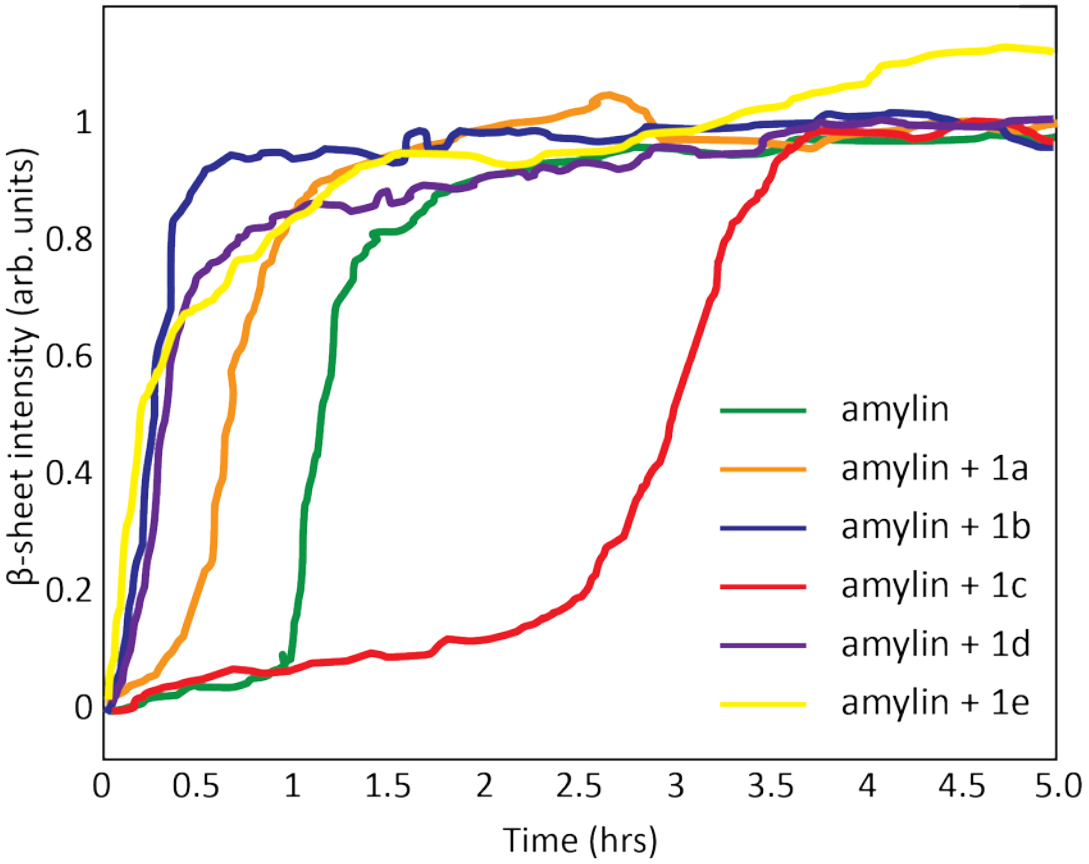

Figure 5.3 Aggregation kinetics of amylin fibril formation with and without macrocycles. Aggregation is monitored by following the amide I peak intensity at 1620 cm^{-1}.

significantly to the intensity measurements. The time-course of amyloid aggregation typically follows a sigmoidal curve, consisting of a lag phase, a growth phase, and an equilibrated phase. The duration of the lag phase is one indicator of inhibition efficiency. Human amylin displays a lag time of about 1 hour before folding commences. Four of the macrocycles significantly accelerate amylin aggregation, reducing the lag time by 50% or more. Macrocycle 1c extends the lag time by 150%, indicating that it is the only macrocycle to inhibit amylin aggregation.

5.4.2 Amylin fiber structure is unaffected by presence of macrocycles

Having established that 4 of the 5 macrocycles seed the formation of fibers, we assess their effect on the final structure of amylin fibers using isotope labeled 2D IR spectroscopy. 2D IR spectroscopy, coupled with isotope labeling, can probe the amyloid structure with residue-level specificity. The principle is illustrated in Figure 5.1c. Isotope labeling the backbone carbonyl of a single residue with $^{13}C=^{18}O$ red-shifts the amide I frequency of that residue by ~54 cm^{-1} and decouples it from the other residues. If the isotope labeled residue lies in a region of the fiber that adopts an in-register parallel β-sheet conformation, then the isotopes will create a linear chain of vibrationally coupled residues. The frequency of the coupled linear chain is shifted from the local mode frequency by twice the coupling strength[37,38] and its intensity scales with the number of residues involved in the vibrational mode.[39] Since the magnitude of the vibrational coupling across strands is very strong, if the labeled residue is involved in a parallel β-sheet then the frequency shift is well resolved from all other features. Moreover, since the coupling strength depends on the exact distance and orientation, it is sensitive to

polymorphs if present. We have previously used 2D IR spectroscopy and isotope labeling to study a peptide drug inhibitor[14], deamidation of amylin[21], and the kinetics of fiber formation.[22] In all of these studies, the ability to resolve individual residues produced observations that are strikingly different from those obtained from ThT fluorescence, TEM and CD spectroscopy for which insufficient structural resolution precluded detailed molecular insights.

Shown in Figures 5.4a and 5.4e are 2D IR spectra of hIAPP isotope labeled at Val-17 or Ala-25, respectively. Val-17 and Ala-25 were selected because they reside on opposite β-strands and fall within the regions targeted by many of the macrocycles. Spectra were collected after at least 5 hours of aggregation to ensure that the samples had fully equilibrated. The largest features in the 2D IR spectra are the pairs of peaks at 1620 cm^{-1}. These are the characteristic β-sheet features created by all the unlabeled residues and are the features that were used to measure the kinetics presented above (Figure 5.3). However, these peaks are largely insensitive to the precise structural details of the fibers because they do not discriminate between residues. For the remainder of the paper, we focus on the isotope label features that appear below 1600 cm^{-1}. The lineshapes of these features and their cross peaks to the uncoupled modes provides information on their solvation and structural heterogeneity[40-42], but for this paper we focus on just their frequency. As such, slices along the diagonal of the 2D IR spectra provide the requisite information, which are shown in Figures 5.4b and 5.4f for the corresponding spectra of Val-17 and Ala-25 labeled peptides. Vertical red lines highlight the frequency of the isotope labeled peaks. Val-17 exhibits a single isotope labeled peak

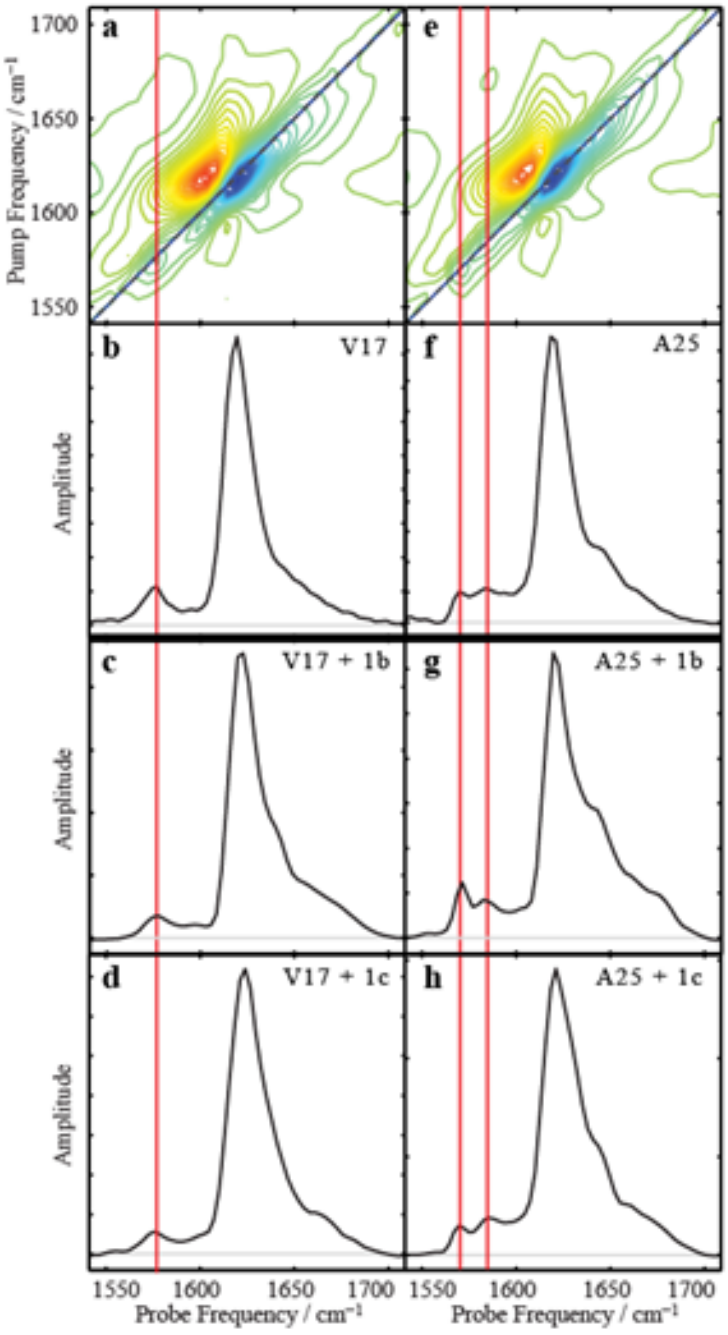

Figure 5.4 Spectra and diagonal slices of amylin fibers formed with or without macrocycles. The columns show data for fibers of human amylin labeled at Val-17 (a-d) and Ala-25 (e-h). Top row: 2D IR spectra of amylin fibers formed in the absence of macrocycles. Second row: diagonal slices through the 2D IR spectra in the top row. Third row: diagonal slices through the 2D IR spectra for amylin fibers formed in the presence of equimolar macrocycle 1b. Fourth row: diagonal slices through the 2D IR spectra for amylin fibers formed in the presence of equimolar macrocycle 1c. Red lines are included to guide the eye to the frequencies of the labeled peaks.

at 1578 cm^{-1}, while Ala-25 exhibits peaks at 1585 cm^{-1} and 1570 cm^{-1}. These spectra are consistent with previously reported data.[22] Their frequencies and intensities indicate that these two labels reside in a parallel β-sheet region of the fibers, as expected from the solid-state NMR structural model.[23] Ala-25 exhibits two peaks caused by two structural polymorphs that differ either in their level of hydration, as has been observed in the 2D IR spectra for Aβ fibers[43], or by slight differences in backbone geometry, as has been resolved with solid-state NMR.[23] Preparation conditions alter the relative abundance of these two polymorphs. For example, aggregation in the presence of 2.5% HFIP produces a single polymorph, as shown in Appendix 4 Figure A4.2.

The slices for amylin mixed with macrocycle 1b (Figure 5.4c and g) are nearly identical to the slices for pure amylin (Figure 5.4b and f). The isotope labeled modes appear at the same frequencies in the pure and mixed samples for both Val-17 and Ala-25. The label frequency depends on many factors, including strength of coupling, structural disorder, and environmental effects.[39,44] Thus, the similarity of the peaks indicates that the final fiber structure of the N- and C-terminal β-sheets is unchanged despite macrocycle 1b accelerating the aggregation process. The same is true for the other macrocycles 1a, 1d, and 1e that accelerate aggregation and is reproducible for all the macrocycles (Appendix 4 Figures A4.3 and A4.4). The slices for amylin mixed with macrocycle 1c (Figures 5.4d and h), which we found acted as an inhibitor, similarly show that the ultimate structure of the amylin fibers formed is unaffected, in spite of the extended lag time. The only differences between the spectra presented are slight changes in the ratio of polymorphs. Thus, we conclude that even though four macrocycles seed

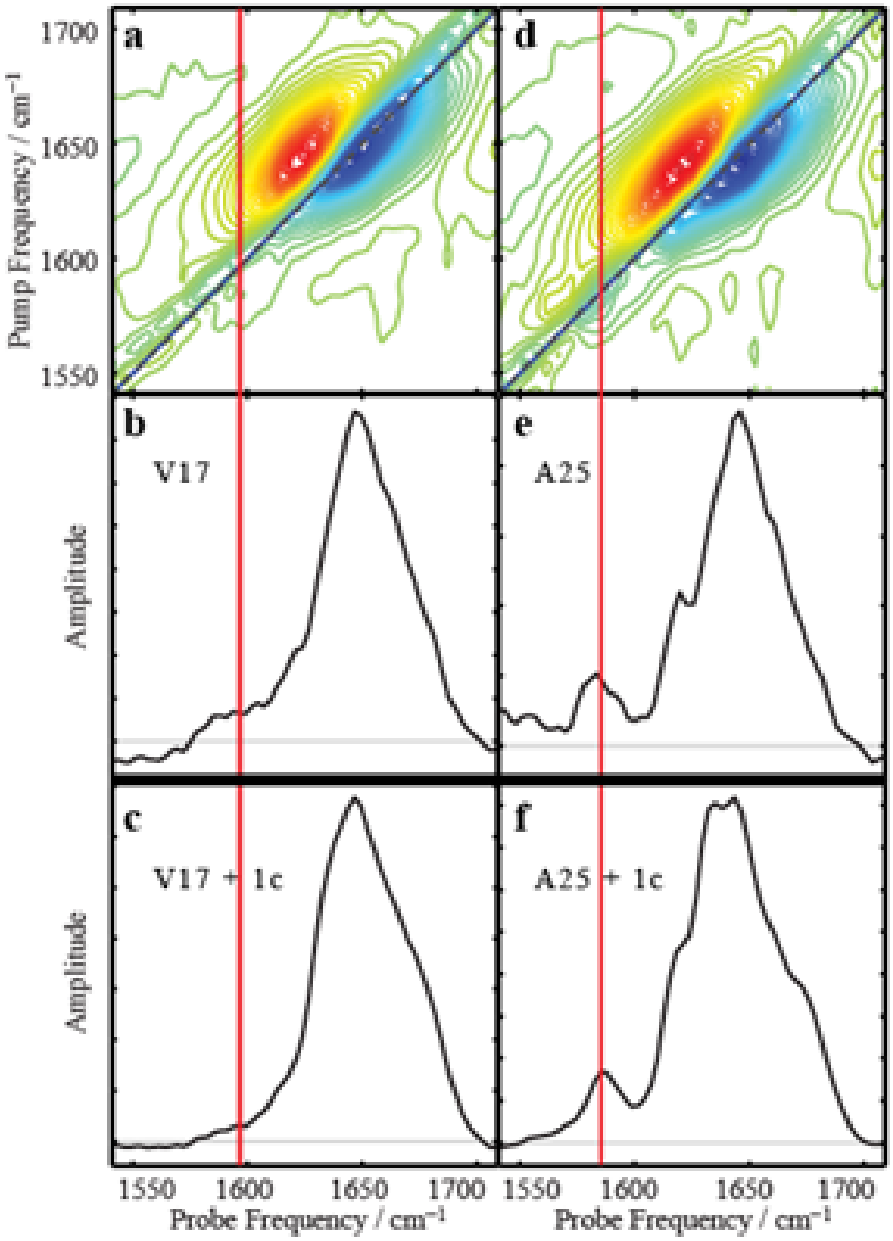

Figure 5.5 Spectra and diagonal slices of amylin during the lag phase, with or without macrocycle 1c. The columns show data for fibers of human amylin labeled at Val-17 (a-c) and Ala-25 (d-f). Top row: 2D IR spectra of lag-phase amylin in the absence of macrocycles. Second row: diagonal slices through the 2D IR spectra in the top row. Third row: diagonal slices through the 2D IR spectra of lag-phase amylin in the presence of equimolar macrocycle 1c. Red lines are included to guide the eye to the frequency of the labeled peak.

the aggregation of amylin and one inhibits, the ultimate structure of the fibers is unchanged.

5.4.3 Inhibition is caused by stabilizing an intermediate with β-sheet structure near Ala-25

Having investigated the structure of the fully formed fibers, we turn to kinetics experiments utilizing isotope labels to investigate the structures during the lag phase. Immediately after aggregation was initiated, 2D IR spectra were collected for Val-17 and Ala-25 with the macrocycles that seed aggregation (Appendix 4 Figure A4.5) and for Val-17 and Ala-25 labeled amylin with and without macrocycle 1c (Figure 5.5 and Appendix 4 Figure A4.6). These spectra are averaged for 10 minutes, which is much shorter than the lag time (Figure 5.3). For macrocycles 1b and 1d-e the isotope labels indicate that β-sheet fiber formation had already occurred at Val-17 and Ala-25, which is consistent with these macrocycles acting as nucleating seeds rather than inhibitors. The spectra of the isotope labels mixed with macrocycle 1a show that, while not complete, aggregation is well underway, which is consistent with the kinetic traces. However, in the case of Val-17 and Ala-25 mixed with 1c, the dominant feature in the unlabeled region of all the spectra is a broad peak centered around 1645 cm^{-1}, indicating that most of the peptide is disordered. There is no appreciable peak at 1620 cm^{-1}, indicating that there are no fully formed amyloid fibers when this spectrum was collected. Regarding the isotope labels, amylin labeled at Val-17 does not have a clear isotope peak, but rather a broad feature near 1595 cm^{-1} (Figure 5.5a and b). Isotope dilutions studies have shown that isotope labeled residues appear between 1590 and 1600 cm^{-1} when fully

decoupled.[14,45] Thus, this frequency indicates that Val-17 residues are uncoupled during the lag phase of amylin aggregation, which indicates that there is no β-sheet at Val-17 during the lag phase. When macrocycle 1c is added to Val-17, the slice is identical to that for the peptide alone (Figure 5.5c), indicating that the macrocycle does not induce β-sheet formation at Val-17 during the lag phase. In contrast, the 2D IR spectrum of Ala-25 labeled peptides shows a strong isotope labeled mode at 1585 cm^{-1} (Figure 5.5d and e). The same labeled mode appears in the lag-phase data for Ala-25 mixed with macrocycle 1c (Figure 5.5f). To confirm that this peak is caused by coupling between the strands of a β-sheet and not by some other effect (such as hydration), we performed isotope dilution experiments. Isotope dilution does not change the structure but eliminates the coupling.[14,45] To perform this test, we measured a 2D IR spectrum of Ala-25 mixed with macrocycle 1c under identical conditions as above, but with only 1 in 3 peptides isotope labeled. The resulting spectrum exhibits the labeled peak at 1595 cm^{-1} (Appendix 4 Figure A4.7), which is what would be expected for uncoupled residues, as discussed above, and indicates that the 1585 cm^{-1} peak for Ala-25 during the lag phase is a result of coupling. As monomeric amylin could not produce such coupling, the spectrum reveals the presence of an aggregated species during the lag phase that has parallel β-sheet at Ala-25. These early aggregates cannot be fully formed amyloid fibers since there is no prominent peak at 1620 cm^{-1}. Furthermore, TEM reveals that the mixture of Ala-25 and macrocycle 1c contains only spherical aggregates during the lag phase, in contrast to the standard fibrils observed after aggregation is complete

(Appendix 4 Figure A4.8). Thus, the lag phase oligomers must be mostly disordered but have local β-sheet structure near Ala-25.

To examine whether or not the macrocycle alters the presence of oligomers during aggregation, Ala-25 aggregation kinetics were collected with and without macrocycle 1c (Figure 5.6). Similar to Figure 5.3, the overall fiber formation is monitored by plotting the unlabeled β-sheet mode intensity at 1620 cm^{-1} as a function of time. Without the macrocycle present (Figure 5.6a), the peptide reaches its half-rise time at t_{50} = 1 h. The increase in intensity at 1570 cm^{-1}, which measures the kinetics of the first polymorph, matches that of the fiber. The intensity increase at 1585 cm^{-1} does not match that of the fiber, because it monitors the development of the second polymorph as well as the oligomeric species. The 1585 cm^{-1} peak is already present at the beginning of data acquisition and continues to gain intensity during the lag phase. It reaches its maximum at about t = 1 h and then decreases in intensity. To better observe the kinetics of the oligomeric species, we subtract off the formation of the polymorph by subtracting the kinetic curve of the unlabeled β-sheet at 1620 cm^{-1} from the kinetic curve of the label at 1585 cm^{-1} (Figure 5.6a, purple). The resulting plot shows that the oligomeric species reaches its maximum population at t = 0.7 h and then decays to baseline by t = 2.5 h, which is when all of the kinetic plots have equilibrated. Subtraction rests on the assumption that both polymorphs have the same kinetics, but that condition must be true; if they followed substantially different aggregation kinetics then it would be unlikely that the first polymorph would match the unlabeled β-sheet kinetics, which measures the

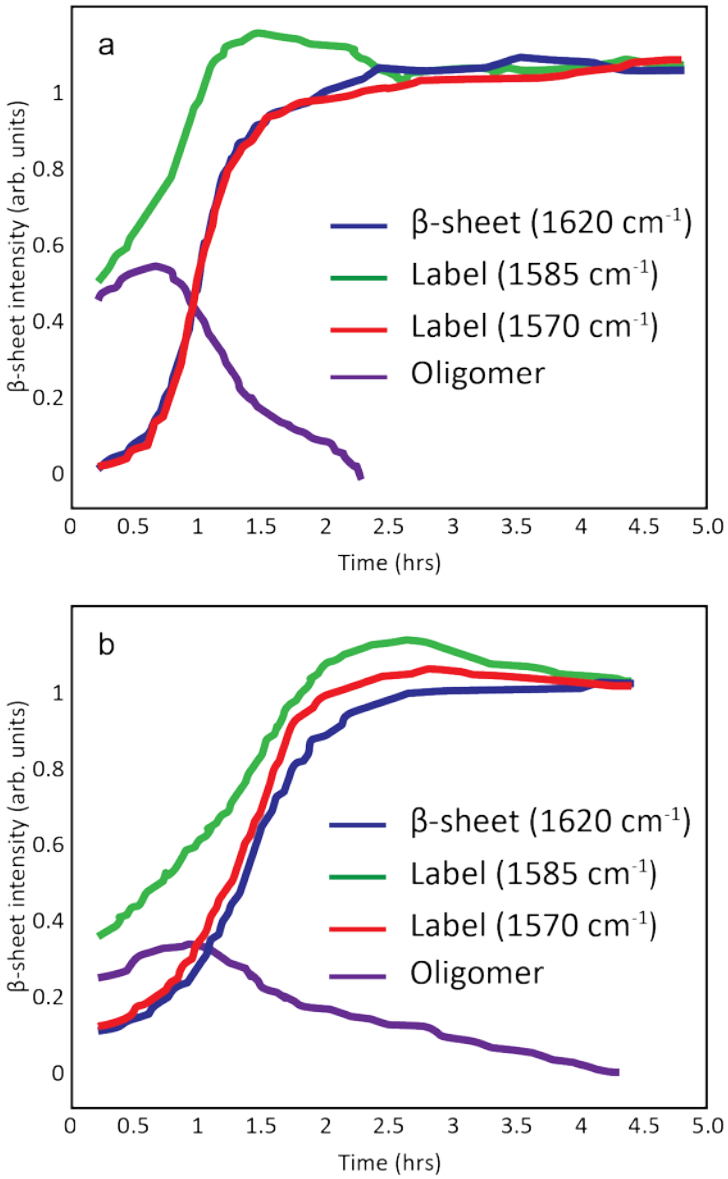

Figure 5.6 Kinetic traces for Ala-25 amylin. Intensity traces for the unlabeled β-sheet, 1585 cm^{-1} isotope, and 1570 cm^{-1} isotope modes during the aggregation of Ala25 amylin alone (a) and with macrocycle 1c (b). The traces were normalized to their values after 5 h of aggregation, when the unlabeled β-sheet peak had fully equilibrated. The unlabeled β-sheet curve was subtracted from the 1585 cm^{-1} isotope curve to generate the kinetic curve of the oligomeric species.

average fibril formation. The rise and then fall of the signal, even without background subtraction, is a clear indication of a β-sheet containing intermediate oligomer.

Shown in Figure 5.6b are kinetics of Ala-25 labeled hIAPP in the presence of macrocycle 1c. In agreement with Figure 5.3 above, macrocycle 1c inhibits aggregation as observed by the increase in the half-rise time to t50 = 1.6 h (the increase in the lag time is not as large as in Figure 5.3 because we used a higher peptide concentration in these samples in order to improve the signal-to-noise). The oligomer content of the sample stays high during the extended lag phase and is present for 4 to 5 hours. Thus, macrocycle 1c extends the lag time of fiber formation and the kinetic lifetime of an oligomeric species with β-sheet near Ala-25.

5.5 Discussion

The experiments reported here shed light on the mechanism by which hIAPP aggregates into amyloid fibers and how that aggregation process might be inhibited. Only one of the five macrocycles studied here acts as an inhibitor of hIAPP aggregation (Figure 5.3). The recognition strand of that macrocycle spans residues 21-27. According to the solid-state NMR structural model, these residues lie within the disordered turn region that connects the N-terminal and C-terminal β-sheets (Figure 5.1a).[23] The sequences of the other macrocycles overlap either fully or more completely with either the N- or C-terminal β-sheets of the fibers. These macrocycles are designed to cap the ends of growing amyloid fibers so as to prevent them from elongating further. They should only attach to the fiber at the exposed ends of β-sheets, since the macrocycles themselves are structurally constrained into β-sheets. Thus, it is quite remarkable that the

only macrocycle that inhibits the aggregation matches the sequence for a region of the fiber that forms a disordered loop and not a β-sheet. It is energetically unfeasible for the macrocycles to match the dihedral angles of the disordered loop. As a result, the 21-27 macrocycle we call 1c must be inhibiting some other way.

First consider the action of the four macrocycles that accelerate aggregation. It is well established that if small amounts of sonicated amyloid fibers are added to a monomeric solution of amyloid forming polypeptides that fibers will immediately form with no lag phase.[46] This occurs because the ends of the fibers act as seeds that overcome the kinetic barrier associated with monomer nucleation. These four macrocycles are acting in a similar manner. They provide a parallel β-sheet template that exactly matches the fiber structure in the β-sheet. As a result, they act as seeds and the kinetics are accelerated, as observed. For amylin, the majority of macrocycles seed aggregation, while for other disease-related and model polypeptides, most macrocycles inhibit fiber formation (clean this sentence up to be consistent with his other work. In fact, maybe we should slightly rework the introduction to include seeding: has he seen seeding in his other studies). In other words, the macrocycles work as intended, in that they do indeed bind to their targeted β-sheet regions. Thus, we would expect that macrocycle 1c would act like the other macrocycles and bind to β-sheets if β-sheets exist between residues 21-27. We have identified oligomers with β-sheet structure at Ala-25 (Figure 5.5) and, furthermore, the lifetime of these oligomers is extended when macrocycle 1c is present (Figure 5.6). Therefore, we conclude that the macrocycle stabilizes these oligomeric intermediates by binding to their β-sheets. We do not know if all 21-27 residues in the

oligomeric species participate in the β-sheet, although several are probably involved because it usually requires at least 3 residues to form stable β-sheets in most soluble proteins.

The effects of macrocycle 1c on the oligomeric species strengthens our evidence for the aggregation mechanism of amylin by providing further detail about on-pathway species. Our previous work studying the kinetics of amylin fiber formation showed that the disordered loop region forms prior to the N- and C-terminal β-sheet .[22] We reached this conclusion because we observed that the sigmoidal kinetics of Val-17 and Ala-25 rose earlier than any of the other residues that we studied. From the ordering of the six residues studied, the mechanism shown in Figure 5.1b was proposed. However, it is synthetically difficult to isotope label most residues in the disordered loopso we did not have a direct measure of the loop kinetics.

In this work, we identified β-sheet formation at Ala-25 during the lag phase prior to the sigmoidal rise of the fibers. No such intermediate is observed for Val-17. We attribute this spectroscopic signature to transient prefibril oligomers, since they are most prominent during the lag phase and disappear as the fibers form. We know that most of the residues in these oligomeric species are disordered since the unlabeled region of the spectra is largely featureless like typical random coil peptides (Figure 5.5). Moreover, these oligomeric species correlate to the presence of small spheres in TEM images (Appendix 4 Figure A4.8).

The discovery of these oligomers suggests an additional step in the hIAPP aggregation mechanism, as illustrated in the free-energy diagram shown in Figure 5.7.

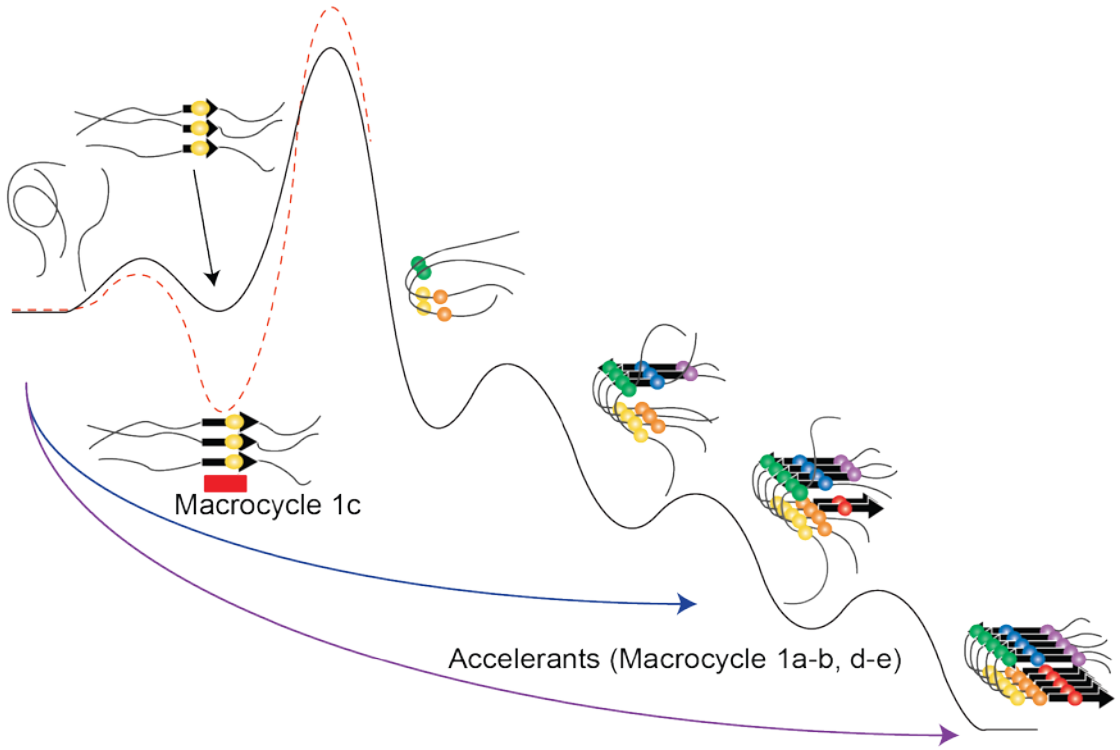

Figure 5.7 Energy landscape for amylin aggregation. The black curves correspond to the pathway by which amylin aggregates normally. The amylin fiber structures are represented as before. The red dashed curve illustrates the effect of macrocycle 1c on the folding pathway. The blue and purple lines indicate alternative folding pathways induced by the addition of accelerating macrocycles.

During the lag phase, amylin must be present in various monomeric folded states and oligomeric species, including the on-pathway oligomer that we identified in this paper. The oligomeric species must occur prior to the formation of the loop, because we know that Val-17 (which lies on the other side of the loop from Ala-25) is incorporated into fibers in conjunction to the decrease in oligomer concentration. Moreover, this oligomeric species must be on-pathway, since we observe its signature with and without macrocycle and trapping of the oligomer by macrocycle 1c delays aggregation. However, we do not know precisely which residues, other than Ala-25, contribute to the β-sheet structure of the oligomers since we cannot label the loop residues themselves. Macrocycle 1b spans residues 15-21, which overlaps with 3 residues of the N-terminal β-sheet and 4 residues of the disordered loop. It would suggest that since this sequence seeds rather than inhibits that residues 18 to 21 of the disordered loop are not part of the oligomeric species. Smaller macrocycles targeting subregions within the loop might allow us to better identify the residues that compose the oligomer.

The observation of this oligomeric species sheds light on a number of previous experiments. For many years, it was thought that amylin fibers were β-sheet between residues 22-27 which have the NFGAIL sequence. This conclusion was derived from studies of fragments of amylin in which it was observed that polypeptides FGAIL, NFGAIL and SNNFGAIL created well-formed fibers, albeit slighty different morphologies.[47] Although some studies have shown that small peptides composed of hIAPP residues 14-20, 15-20, 14-18, and 15-19 aggregate, as well as peptides composed of hIAPP 8-20, 23-27, and 30-37, these aggregates tend to have very different

morphologies from full-length human amylin fibers.[48] Although other regions of the hIAPP sequence have been shown to form aggregates, the NFGAIL region forms fibers most like that of full-length amylin.[47] Moreover, the FGAIL region is the most hydrophobic sequence in amylin and thus it was natural to assume that this region would form the core of amylin fibers. Thus, it was quite surprising when the solid-state NMR structural model was published in which the 21-27 region was largely disordered.[23] The observation of the oligomeric species at Ala-25 helps explain this apparent contradiction. It appears that the hydrophobic NFGAIL region does indeed form parallel β-sheets, which serves as the nucleation region for the polypeptides, but that these β-sheets are less stable than the combined free-energy of the N- and C-terminal β-sheets of the fibers. Thus, the parallel β-sheets of the oligomeric NFGAIL region are ultimately disordered into the loop.

The transition of the NFGAIL region from oligomeric β-sheets into a disordered loop also helps explain our previous work on the kinetics of amylin fiber formation that resulted in the aggregation mechanism shown in Figure 5.1b. Amyloid fibers are thought to form via nucleation so that once a seed is formed, monomers are templated onto the ends. If that is the case, then one would expect that no matter which residue is monitored, all residues would exhibit the same kinetics. Folding of a polypeptide onto the end of a well-formed fiber, which is controlled by diffusion, must be faster than the addition of more monomers. The result is sigmoidal aggregation kinetics. But our kinetics results showed that the timescale for polypeptide folding competed with fiber growth, since different residues exhibited different kinetics. The observation of an

oligomeric species helps explain these kinetics because there must be a large free-energy barrier to transition the oligomeric β-sheet into a disordered loop. Thus, we believe that the free energy surface corresponding to amylin aggregation looks like that shown in Figure 5.7, in which the final fiber structure is more stable than the oligomers, but there is a free energy barrier associated with breaking the oligomeric β-sheets into the disordered loop. Once the turn is formed, aggregation into amyloid fibrils proceeds quickly, giving rise to sigmoidal kinetics. This landscape explains how the 21-27 macrocycle lengthens the lag time and the lifetime of the oligomeric species by stabilizing the oligomer relative to the free energy barrier. The oligomeric species binds more preferentially to the 21-27 macrocycle rather than unstructured monomers because the macrocycle contains a well-ordered recognition strand that more strongly binds to the oligomer. The other four macrocycles circumvent this barrier by catalyzing fiber formation. The curved arrows in Figure 5.7 indicate the alternative pathways taken when the accelerating macrocycles are present. Although inducing β-sheet structure earlier in the aggregation process must change the fiber formation pathway, to within our resolution the final fibers are identical to those formed under standard conditions (Appendix 4 Figures A4.3 and A4.4).

5.6 Conclusions

This study highlights the complexity inherent in designing peptide inhibitors as well as their use in deducing the aggregation pathway of amyloid fibers. It is extremely difficult to obtain precise structural information about amyloid species. One of the best methods is solid-state NMR spectroscopy, which is where the majority of information about amylin fibers comes from. However, solely knowing the fiber structure is not

sufficient when designing inhibitors. We recently found that a polypeptide inhibitor which was designed to inhibit the C-terminal β-sheets of amylin instead prevented the N-terminal sheets from forming.[14] In this study, only one macrocycle of the five proved to be an inhibitor of amylin aggregation. These results cannot be explained without invoking a multiple-step aggregation mechanism. To guide rational drug design, one needs at least residue-specific structural information on the aggregation mechanism. Such information is difficult to obtain because few techniques provide specific structural information on evolving species. In this regards, 2D IR spectroscopy[22], or even just FTIR[49,50], combined with isotope labeling is capable of providing specific structural insights into the aggregation mechanism.

We find that macrocycle 1c extends the lag time of amylin fibril formation by trapping an early oligomeric species consisting of small β-sheets localized near Ala-25 in the turn region. This finding reinforces earlier work suggesting that turn formation is the nucleating step for amylin fibril formation. By stabilizing the oligomeric species, macrocycle 1c increases the energy barrier to fiber nucleation and thus delays aggregation. Thus, future drug design efforts may want to target the turn region in order to improve the efficiency of amylin inhibitors. Although macrocycle 1c does not prevent fibrils from forming in the end, it should be noted that β-sheets present two distinct hydrogen-bonding edges.[15] Macrocycle 1c targets only one of these edges, leaving the other edge free to continue growing. Combining inhibitors which can bind both edges of the β-sheets may prove more effective at inhibiting fiber growth. Heterodivalent linked macrocycles have been shown to be more effective at inhibiting Aβ aggregation than

their individual components, likely due to their ability to bind multiple regions of the Aβ peptide[51]; this approach could prove generally applicable to many amyloid peptides. Fully isotope labeling either the macrocycles or amylin would allow us to characterize their interaction and provide more complete insight into when during the aggregation pathway the macrocycles are bound to amylin. Our studies clearly demonstrate that a thorough understanding of the mechanism by which amyloids aggregate into fibrils is important for rational drug design. On the other hand, studies with compounds such as the macrocyclic peptides used here can provide further insight into the un-inhibited mechanism and reinforce key structures for drugs to target.

5.7 Appendix

Additional information can be found in Appendix 4, including spectra and TEM images of oligomer species. Portions of this chapter will be published as part of Publication 6 in Appendix 5. Most of the data presented in this chapter is included in Publication 6, but there are additional figures, including spectra of additional isotope labeled amylin, and simulations of amylin dimers. That will be in Lauren Buchanan's thesis.

5.8 References

(1) Lorenzo, A.; Razzaboni, B.; Weir, G. C.; Yankner, B. A. *Nature* **1994**, *368*, 756-760.

(2) Wetzel, R. *J. Mol. Biol.* **2012**, *421*, am-490.

(3) Chiti, F.; Dobson, C. M. *Annu. Rev. Biochem.* **2006**, *75*, 333-366.

(4) Selkoe, D. J. *Nat. Cell Biol.* **2004**, *6*, 1054-1061.

(5) Cohen, F. E.; Kelly, J. W. *Nature* **2003**, *426*, 905.

(6) Mishra, R.; Bulic, B.; Sellin, D.; Jha, S.; Waldmann, H.; Winter, R. *Angewandte Chemie International Edition* **2008**, *47*, 4679-4682.

(7) Mishra, R.; Sellin, D.; Radovan, D.; Gohlke, A.; Winter, R. *ChemBioChem* **2009**, *10*, 445-449.

(8) Meng, F.; Abedini, A.; Plesner, A.; Verchere, C. B.; Raleigh, D. P. *Biochemistry* **2010**, *49*, 8127-8133.

(9) Aitken, J. F.; Loomes, K. M.; Konarkowska, B.; Cooper, G. J. S. *Biochem. J.* **2003**, *374*, 779-784.

(10) Sellin, D.; Yan, L.-M.; Kapurniotu, A.; Winter, R. *Biophys. Chem.* **2010**, *150*, 73-79.

(11) Yan, L.-M.; Tatarek-Nossol, M.; Velkova, A.; Kazantzis, A.; Kapurniotu, A. *Proc. Natl. Acad. Sci. U. S. A.* **2006**, *103*, 2046-2051.

(12) Meng, F.; Raleigh, D. P.; Abedini, A. *J. Am. Chem. Soc.* **2010**, *132*, 14340-14342.

(13) Cao, P.; Meng, F.; Abedini, A.; Raleigh, D. P. *Biochemistry* **2010**, *49*, 872-881.

(14) Middleton, C. T.; Marek, P.; Cao, P.; Chiu, C.-c.; Singh, S.; Woys, A. M.; de Pablo, J. J.; Raleigh, D. P.; Zanni, M. T. *Nat Chem* **2012**, *4*, 355-360.

(15) Zheng, J.; Liu, C.; Sawaya, M. R.; Vadla, B.; Khan, S.; Woods, R. J.; Eisenberg, D.; Goux, W. J.; Nowick, J. S. *J. Am. Chem. Soc.* **2011**, *133*, 3144-3157.

(16) Sciarretta, K. L.; Gordon, D. J.; Meredith, S. C. In *Methods Enzymol.*; Indu, K., Ronald, W., Eds.; Academic Press: 2006; Vol. Volume 413, p 273-312.

(17) Hughes, E.; Burke, R. M.; Doig, A. J. *J. Biol. Chem.* **2000**, *275*, 25109-25115.

(18) Gordon, D. J.; Sciarretta, K. L.; Meredith, S. C. *Biochemistry* **2001**, *40*, 8237-8245.

(19) Gordon, D. J.; Tappe, R.; Meredith, S. C. *J. Pept. Res.* **2002**, *60*, 37-55.

(20) Abedini, A.; Meng, F.; Raleigh, D. P. *J. Am. Chem. Soc.* **2007**, *129*, 11300-11301.

(21) Dunkelberger, E. B.; Buchanan, L. E.; Marek, P.; Cao, P.; Raleigh, D. P.; Zanni, M. T. *J. Am. Chem. Soc.* **2012**, *134*, 12658-12667.

(22) Shim, S.-H.; Gupta, R.; Ling, Y. L.; Strasfeld, D. B.; Raleigh, D. P.; Zanni, M. T. *Proceedings of the National Academy of Sciences* **2009**, *106*, 6614-6619.

(23) Luca, S.; Yau, W.-M.; Leapman, R.; Tycko, R. *Biochemistry* **2007**, *46*, 13505-13522.

(24) Nowick, J. S.; Brower, J. O. *J. Am. Chem. Soc.* **2003**, *125*, 876-877.

(25) Nowick, J. S.; Chung, D. M.; Maitra, K.; Maitra, S.; Stigers, K. D.; Sun, Y. *J. Am. Chem. Soc.* **2000**, *122*, 7654-7661.

(26) Cheng, P.-N.; Liu, C.; Zhao, M.; Eisenberg, D.; Nowick, J. S. *Nat Chem* **2012**, *advance online publication*.

(27) Westermark, P.; Engström, U.; Johnson, K. H.; Westermark, G. T.; Betsholtz, C. *Proceedings of the National Academy of Sciences* **1990**, *87*, 5036-5040.

(28) Glenner, G. G.; David Eanes, E.; Wiley, C. A. *Biochem. Biophys. Res. Commun.* **1988**, *155*, 608-614.

(29) Betsholtz, C.; Christmansson, L.; Engström, U.; Rorsman, F.; Svensson, V.; Johnson, K. H.; Westermark, P. *FEBS Lett.* **1989**, *251*, 261-264.

(30) Abedini, A.; Raleigh, D. P. *Org. Lett.* **2005**, *7*, 693-696.

(31) Marek, P.; Woys, A. M.; Sutton, K.; Zanni, M. T.; Raleigh, D. P. *Org. Lett.* **2010**, *12*, 4848-4851.

(32) Marecek, J.; Song, B.; Brewer, S.; Belyea, J.; Dyer, R. B.; Raleigh, D. P. *Org. Lett.* **2007**, *9*, 4935-4937.

(33) Andrushchenko, V. V.; Vogel, H. J.; Prenner, E. J. *J. Pept. Sci.* **2007**, *13*, 37-43.

(34) Middleton, C. T.; Woys, A. M.; Mukherjee, S. S.; Zanni, M. T. *Methods* **2010**, *52*, 12-22.

(35) Shim, S.-H.; Strasfeld, D. B.; Fulmer, E. C.; Zanni, M. T. *Opt. Lett.* **2006**, *31*, 838-840.

(36) Shim, S.-H.; Strasfeld, D. B.; Zanni, M. T. *Optics Express* **2006**, *14*.

(37) Hamm, P.; Zanni, M. T. *Concepts and methods of 2D infrared spectroscopy*; Cambridge, 2010.

(38) Buchanan, L. E.; Dunkelberger, E. B.; Zanni, M. T. In *Protein Folding and Misfolding: Shining Light by Infrared Spectroscopy*; Fabian, H., Naumann, D., Eds.; Springer: Heidelberg, 2011; Vol. 1, p 217-237.

(39) Grechko, M.; Zanni, M. T. *The Journal of Chemical Physics* **2012**, *137*, 184202.

(40) Woys, A. M.; Lin, Y.-S.; Reddy, A. S.; Xiong, W.; de Pablo, J. J.; Skinner, J. L.; Zanni, M. T. *J. Am. Chem. Soc.* **2010**, *132*, 2832-2838.

(41) Wang, L.; Middleton, C. T.; Singh, S.; Reddy, A. S.; Woys, A. M.; Strasfeld, D. B.; Marek, P.; Raleigh, D. P.; de Pablo, J. J.; Zanni, M. T.; Skinner, J. L. *J. Am. Chem. Soc.* **2011**, *133*, 16062-16071.

(42) Kim, Y. S.; Hochstrasser, R. M. *The Journal of Physical Chemistry B* **2009**, *113*, 8231-8251.

(43) Kim, Y. S.; Liu, L.; Axelsen, P. H.; Hochstrasser, R. M. *Proc. Natl. Acad. Sci.* **2009**, *106*, 17751-17756.

(44) Strasfeld, D. B.; Ling, Y. L.; Gupta, R.; Raleigh, D. P.; Zanni, M. T. *The Journal of Physical Chemistry B* **2009**, *113*, 15679-15691.

(45) Kim, Y. S.; Liu, L.; Axelsen, P. H.; Hochstrasser, R. M. *Proceedings of the National Academy of Sciences* **2008**, *105*, 7720-7725.

(46) Padrick, S. B.; Miranker, A. D. *Biochemistry* **2002**, *41*, 4694-4703.

(47) Tenidis, K.; Waldner, M.; Bernhagen, J.; Fischle, W.; Bergmann, M.; Weber, M.; Merkle, M.-L.; Voelter, W.; Brunner, H.; Kapurniotu, A. *J. Mol. Biol.* **2000**, *295*, 1055-1071.

(48) Mazor, Y.; Gilead, S.; Benhar, I.; Gazit, E. *J. Mol. Biol.* **2002**, *322*, 1013-1024.

(49) Petty, S. A.; Decatur, S. M. *J. Am. Chem. Soc.* **2005**, *127*, 13488-13489.

(50) Petty, S. A.; Decatur, S. M. *Proc. Natl. Acad. Sci. U. S. A.* **2005**, *102*, 14272-14277.

(51) Cheng, P.-N.; Spencer, R.; Woods, R. J.; Glabe, C. G.; Nowick, J. S. *J. Am. Chem. Soc.* **2012**, *134*, 14179-14184.

CHAPTER 6*

2D IR Cross Peaks Reveal Hydrogen-Deuterium Exchange with Single Residue Specificity

6.1 Abstract

A form of chemical exchange, hydrogen-deuterium exchange (HDX), has long been used as a method for studying the secondary and tertiary structure of peptides and proteins using mass spectrometry and NMR spectroscopy. Using 2D IR (two dimensional infrared) spectroscopy, we resolve cross peaks between the amide II band and a $^{13}C^{18}O$ isotope labeled amide I band, which we show measures HDX with site-specific resolution. By rapidly scanning 2D IR spectra using mid-IR pulse shaping, we monitor the kinetics of HDX exchange on-the-fly. For the antimicrobial peptide, ovispirin, bound to membrane bilayers, we find that the amide II peak decays with a biexponential with

* This chapter was originally published as the following: Dunkelberger, Emily B., Woys, Ann M., Zanni Martin T., "2D IR Cross Peaks Reveal Hydrogen-Deuterium Exchange with Single Residue Specificity", *J. Phys. Chem. B*, 2013, 10.1021/jp402942s.

rate constants of 0.54 ± 0.02 and 0.12 ± 0.01 min^{-1}, which is a measure of the overall HDX in the peptide. The cross peaks between Ile-10 labeled ovispirin and the amide II mode, which specifically monitor HDX kinetics at Ile-10, decay with a single rate constant of 0.36 ± 0.1 min^{-1}. Comparing this exchange rate to theoretically determined exchange rates of Ile-10 for ovispirin in a solution random coil configuration, the exchange rate at Ile-10 is at least 100 times slower, consistent with the known α-helix structure of ovispirin in bilayers. Because backbone isotope labels produce only a very small shift of the amide II band, site-specific HDX cannot be measured with FTIR spectroscopy, which is why 2D IR spectroscopy is needed for these measurements.

6.2 Introduction

Two-dimensional infrared (2D IR) spectroscopy correlates vibrational modes, which provides information about molecular structure and dynamics. One recent development in 2D IR spectroscopy is the study of chemical exchange processes that occur on the femto/picosecond timescales.[1-11] If two different molecular configurations absorb at two different frequencies, then the dynamics of the cross peaks between the two reveal the timescale at which one configuration exchanges into the other. A beautiful example is from the Fayer group, who applied this principle to study the phenol hydroxyl stretch in a benzene solvent mixture.[7] By varying the waiting time in the vibrational echo pulse sequence, Fayer showed that the time dependence of the intensity of the cross peaks reports on the dissociation time of the solute-solvent complex, which occurred in only 8 ps. Such information cannot be obtained from linear spectroscopy, like FTIR spectroscopy, because FTIR spectroscopy solely reports on the equilibrium

concentrations. To obtain kinetics, one needs to know the exchange rate, which is contained in the cross peaks of 2D IR spectra. In this article, we utilize a variant of chemical exchange to study hydrogen-deuterium exchange (HDX) in a polypeptide. We show that by using isotope labeling and monitoring the cross peaks in rapidly scanned 2D IR spectra, we obtain single-residue exchange information. Such information cannot be obtained from FTIR spectroscopy.

The principle behind HDX is that the amide proton on each amino acid is in rapid exchange with hydrogen atoms in the solvent. Shown in Figure 6.1a is a protonated peptide bond. After adding deuterium atoms to the sample using D_2O, amide protons exchange with solvent deuterium atoms, if they are solvent accessible and in a conformation that allows proton exchange. This isotopic exchange does not perturb the structure of the protein, but does provide information on which amide bonds are solvent exposed or protected by internal hydrogen bonds, thereby providing insights into the secondary and tertiary structure of peptides. The rate of exchange also depends on other factors. In general, HDX is strongly pH-dependent; base-catalyzed HDX is more effective than acid-catalyzed exchange, as evidenced by measuring HDX rates in poly-alanine as a function of pH.[12-15] At physiological pH, HDX occurs in random coil and solvent exposed residues on the timescale of milliseconds-seconds.[13] Exchange times are longer for proteins with regular secondary structures. A good example is human serum albumin, a globular peptide with α-helix, β-turn, and extended chain secondary structures. The residues in the β-turns are relatively unstructured and were shown to be most exposed to deuterated solvent, thus they exchanged rapidly, on the order of less than two

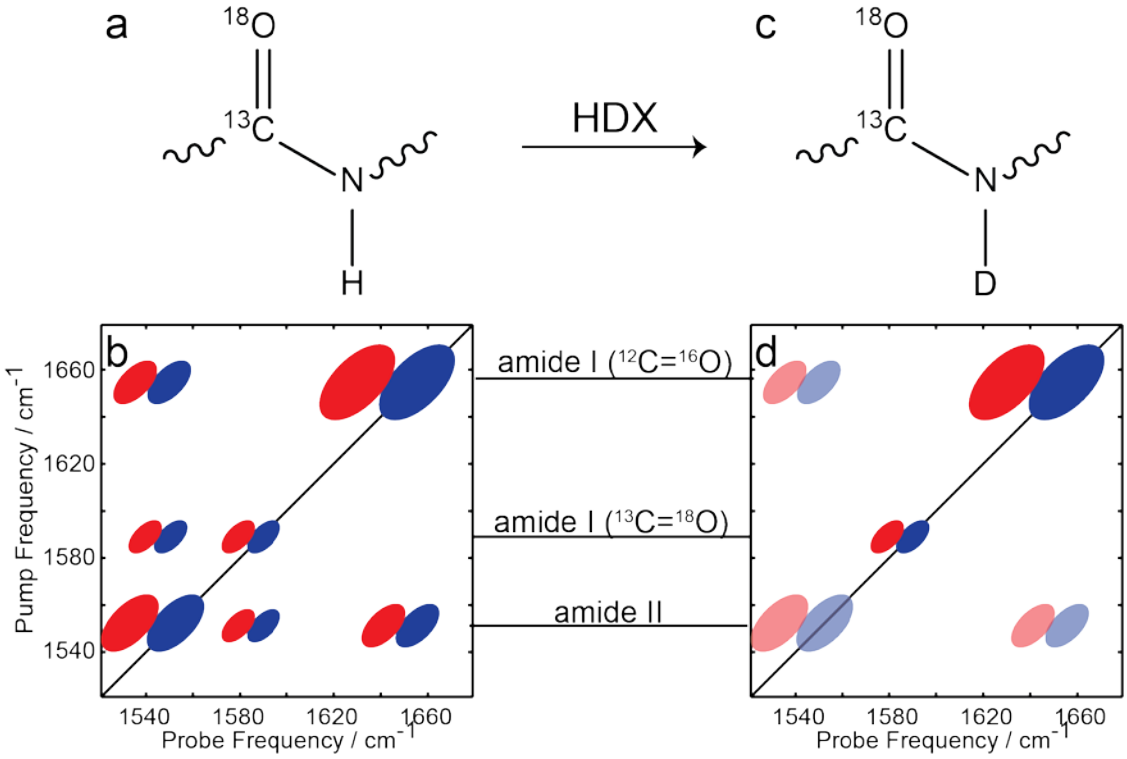

Figure 6.1 Schematic for how 2D IR spectroscopy and isotope labeling provides site-specific HDX. (a) A protonated peptide unit with a single $^{13}C^{18}O$ isotope label and (b) the corresponding 2D IR spectrum for the entire protein. (c) The corresponding protein and (d) 2D IR spectrum after HDX has deuterated the isotope labeled peptide unit. Peaks always appear in pairs in 2D IR spectra (blue is for fundamental transitions and red is for overtone and combination band transitions). The large amide I peaks have contributions from all of the unlabeled residues in the protein while the $^{13}C^{18}O$ amide I peaks are much smaller because there is only 1 labeled residue. Cross peaks between the unlabeled amide I and amide II are shown, which are typical of all proteins that are not fully deuterated. In (b) cross peaks also appear between the $^{13}C^{18}O$ label and the amide II because the labeled residue is protonated. In (d), these cross peaks are absent because the labeled residue is protonated and the amide II and its cross peaks are also weaker (shown shaded) because some, but not all, of the protein has exchanged. The above scenario is for a residue that exchanges faster than the average.

minutes. Random coil residues exchanged on the order of 30 minutes, and α-helix residues, the most structured portion of the protein, exchanged over a few hours. Nearly 25% of the peptide never exchanged in the four hour experimental window due to the high stability its hydrophobic core.[16] HDX can take even longer or cease to happen in transmembrane proteins.[17,18] Previous studies have shown that residues in a transmembrane protein that lie in the center of the membrane bilayer do not undergo HDX in 3-4 days following sample exposure to deuterium, but residues on the surface can exchange rapidly, and thus provide information about membrane protein structure.

The key to obtaining detailed structural information from HDX is to measure exchange rates on individual residues. To this end, solid-state and solution NMR spectroscopies are very good methods. They have been used extensively to study the structure of a variety of peptides.[14,17,19-21] Electrospray ionization mass spectrometry (ESI-MS) is another good tool to measure HDX to determine the structure of membrane bound peptides and amyloid peptides.[18,22-25] NMR spectroscopy and mass spectrometry techniques often require conditions which may be perturbative, such as low pH to slow down HDX or quenching to stop it. Nonetheless, the information that one obtains from residue-by-residue HDX exchange kinetics has provided important insights into many problems in structural biology.

Fourier transform infrared (FTIR) spectroscopy is also often used to measure HDX,[16,26-31] but unlike NMR spectroscopy and mass spectrometry, it does not provide residue-level structural information even when using isotope labels. As such, it is often difficult to obtain precise structural information from the kinetics. The problem is as

follows. The amide I mode is composed primarily of C=O stretch motions with a little CN stretch and typically absorbs between 1620 and 1680 cm^{-1}, depending on the secondary structure(s) of the protein. [32] If a single residue is $^{13}C^{18}O$ isotope labeled, then it is largely decoupled from the other amide I modes and residues near 1590 cm^{-1}, which is why $^{13}C^{18}O$ labeling is often used in FTIR and 2D IR spectroscopy to obtain residue-level structural resolution. However, the amide I mode frequency depends very little on whether the peptide group is protonated or deuterated. At most, there is an 8 cm^{-1} difference between the frequency of the amide I mode when there is a hydrogen atom in the amide position and when there is a deuterium atom in the amide position; thus it is not a good mode for monitoring HDX.[16,32] In contrast, the amide II mode is mostly CN stretch and NH bend motions. Because of the bend, its frequency is highly dependent on whether the nitrogen is protonated or deuterated. If protonated, the amide II mode absorbs at ~1550 cm^{-1}.[32] If deuterated, it absorbs at ~1450 cm^{-1} (Figure 6.1c and d), which is often called the amide II' band. Thus, the amide II mode is very sensitive to HDX. However, it alone does not provide residue-level structural information because isotope labeling with ^{13}C or ^{18}O has no effect on the amide II frequency and ^{15}N only produces a red shift of 13-15 cm^{-1}, which is much smaller than the amide II linewidth and so cannot typically be resolved for polypeptides larger than a few residues.[33,34] Thus, FTIR spectroscopy cannot obtain site-specific HDX on proteins, because neither the amide I nor the amide II modes alone contain the necessary site-specificity and HDX sensitivity.

In this chapter, we illustrate how one can take advantage of the coupling between the amide I and II vibrational modes in order to obtain residue-specific HDX using 2D IR spectroscopy. Our study builds on previous work using 2D IR spectroscopy and cross peaks between the amide I and amide II/II' modes to resolve HDX of different secondary structures in proteins.[35,36] In combination with isotope labeling, one can also obtain site-specific HDX rates. Because the amide I and II modes both contain CN stretching motions, they are strongly coupled, and so the typical 2D IR spectrum exhibits large cross peaks between the two bands.[33,37] We take advantage of this fact to determine whether or not an isotope labeled residue is coupled to the amide II. Our scheme is illustrated in Figure 6.1. Figure 6.1b has a schematic 2D IR spectrum for a protonated peptide with a single $^{13}C^{18}O$ isotope label. As such, there are large diagonal peaks for all the unlabeled residues that would appear somewhere between 1620 and 1680 cm^{-1} depending on the secondary structure, which we chose to be 1650 cm^{-1} in this example. The single isotope labeled residue would appear at 1590 cm^{-1}, regardless of the secondary structure because it is largely decoupled from the other modes. A large amide II band would appear at ~1550 cm^{-1}, since all the residues are protonated. Cross peaks between the unlabeled amide I and amide II are shown, which are typical of all proteins that are not fully deuterated. These cross peaks have been measured previously using 2D IR spectroscopy.[33,35-38] The cross peaks that we are interested in appear between the $^{13}C^{18}O$ label and the amide II. These cross peaks appear because, before the addition of D_2O, the labeled residue is protonated. Shown in Figure 6.1d is a schematic for how the spectrum might look a few minutes after the addition of D_2O. The peaks along the diagonal would

not change frequency, but the amide II mode would decrease in intensity as would its cross peaks to the amide I mode as amide hydrogen atoms exchange for deuterium atoms. If the isotope labeled residue has undergone HDX (which is the scenario we illustrate in Figure 6.1d), then the isotope labeled amide I mode is no longer coupled with the amide II mode, so that the cross peaks between these modes disappear. Thus, by monitoring the decay of the cross peaks between the labeled amide I and the amide II modes, one can measure the kinetics of HDX for a particular residue, because those particular cross peaks only report on the protonation state of the single isotope labeled residue, not the average of all the residues. Ideally, one would also monitor the cross peaks between the isotope labeled and the amide II' mode, which would increase with HDX, but that band currently lies outside our experimentally accessible frequency range.

In this chapter, we apply this approach to the antibiotic peptide ovispirin bound to lipid bilayers. Ovispirin is a surface bound α-helical peptide whose structure is known from solid-state NMR, 2D IR, and molecular dynamics and thus is a good test system for our approach.[39,40] By initially measuring 2D IR spectra in H_2O, we observe cross peaks between the amide I and amide II modes as well as between the isotope label and amide II modes. Upon deuterating the sample via addition of D_2O, the cross peaks between the amide I and amide II decrease in intensity as amide hydrogen atoms exchange for deuterium atoms, like illustrated in Figure 6.1. At the same time, the cross peak between the isotope label and amide II also decreases in intensity, because the amide hydrogen located on the same amino acid as the isotope label has exchanged for deuterium. In addition, Arg residues in ovispirin also become deuterated, which create new diagonal

peaks. For all discussions in this paper, the $^{13}C^{18}O$ labeled residue will be described as 'isotope label(ed)', and while exchanging hydrogen atoms for deuterium atoms is also a form of isotope labeling, this will be described as HDX.

6.3 Experimental

6.3.1 Peptide synthesis and isotope labeling Ile-10

Ovispirin, with the sequence H_2N-KNLRRIIRKII<u>*</u>HIIKKYG-COOH, was synthesized using standard FMOC peptide synthesis techniques. One $^{13}C^{18}O$ carbonyl group was incorporated into Ile-10. To synthesize the isotope labeled residue, FMOC-protected Ile, labeled with ^{13}C in the carbonyl position, underwent acid-catalyzed exchange with $^{18}OH_2$, to produce the fully-labeled carbonyl group. Further details of the isotope labeling procedure can be found elsewhere.[41-43] Following peptide synthesis, ovispirin was purified by HPLC using a 0.1% TFA water/acetonitrile solvent system. Masses were confirmed using MALDI-MS.[39]

6.3.2 Preparation of membranes

For membrane studies, a mixture of 1-palmitoyl-2-oleoly-sn-glycero-3-phosphocholine (POPC)/1-palmitoyl-2-oleoyl-sn-glycero-3-phosphoglycerol (POPG) (Avanti Polar Lipids) was produced. The lipids were purchased as chloroform solutions, and mixed at a molar of 3:1 POPC:POPG. The mixture was dried under a stream of nitrogen for four hours and lyophilized overnight. The dry film was rehydrated in 0.1 mM phosphate buffer that contained isotope labeled ovispirin, and the final peptide-to-lipid ratio was larger than 1:21.[39] A complete description of ovispirin synthesis, purification, and incorporation into membranes can be found elsewhere.[39]

6.3.3 Two-dimensional infrared spectroscopy

A home-built Ti:Sapphire oscillator was used to seed a Nd:YLF-pumped regenerative amplifier, producing ultra-fast (~60 fs) 800 nm pulses. The 800 nm light was sent to a Type II BBO crystal-based optical parametric amplifier, producing signal and idler beams. The signal and idler were difference frequency mixed in a $AgGaS_2$ crystal and produced 6 μm limited bandwidth mid-IR light. The mid-IR light was specifically tuned to the frequency of the isotope labeled amide I peak (~1595 cm^{-1}). Due to the bandwidth of the mid-IR light, the amide II' mode was not observed. The mid-IR light was split into pump and probe pulses; the pump passed through a Ge-based mid-IR pulse shaper before overlapping with the probe and focused to a spot of ~120 μm at the sample cell. The probe was then directed to a monochromator and the signal was detected with a HgCdTe detector. All spectra were collected with parallel pump probe polarization. Further details of the experimental setup and pulse shaper can be found elsewhere.[44,45]

6.3.4 Sample preparation

Experiments were performed first by measuring spectra of Ile-10 ovispirin hydrated in H_2O. A total of 2 μL of sample was deposited in 0.5 μL increments onto the same spot in the center of a CaF_2 window, and excess H_2O was removed under a gentle stream of nitrogen between each deposit. Bulk water was removed from the sample to reduce the signal from the water bend mode that absorbs near the amide I carbonyl mode. The sample was then covered with half of a CaF_2 window, sliced across the diameter. The sample was placed in the spectrometer such that the laser beam passed through the

sample and both CaF_2 windows, within 2 mm of the edge of the half-window. Data collection was then initiated and after a few minutes we added 2 μL of D_2O to the sample cell at the edge of the half-window. The D_2O was whisked between the two CaF_2 windows by capillary action in a fraction of a second. Using our rapid-scan pulse shaping technology, a 2D IR spectrum was collected every 0.4 s. Thus, the HDX exchange process was monitored continuously for 1 h with nearly no dead time. All diagonal slices are normalized to the unlabeled amide I band. All pump and probe slices shown in later figures are normalized to the Ile-10 amide I band, and all kinetics traces are normalized to the kinetics of the Ile-10 amide I band. The Ile-10 amide I band remains virtually unchanged during HDX, and thus by normalizing the kinetic features to this peak, any random laser fluctuations are eliminated from the data.

The HDX rates measured in this experiment exceed the permeability coefficient of water across a membrane.[46-48] HDX light scattering experiments of vesicles measured the permeability coefficient of water to be ~10^{-6}-10^{-7} cm/s[47], while other experiments measured the permeability coefficient to be ~10^{-1}-10^{-3} cm/s.[46,48]. The water permeability is dependent on lipid chain length, temperature, and vesicle size. However, estimating the thickness of a 3:1 mixture of POPC:POPG lipids to be 30 Å, water will permeate the membranes in this experiment in no more than ~2 s, and likely much faster. Thus, the exchange rates measured are not dependent on the mixing time of D_2O and the sample.

6.4 Results

Shown in Figure 6.2 are 2D IR spectra of Ile-10 labeled ovispirin in both H_2O and D_2O (30 min after D_2O addition), along with respective diagonal slices through the

spectra. Consider the spectrum in H_2O. The pair of diagonal peaks at 1654 cm^{-1} is due to the unlabeled ($^{12}C^{16}O$) amide I modes, the C-terminus carboxyl group, and various side chains. The pair of diagonal peaks at 1587 cm^{-1} is the $^{13}C^{18}O$ isotope labeled amide I mode of Ile-10. The diagonal peaks at 1547 cm^{-1} are due to the amide II mode.[32] Other important features to point out are the cross peaks at (ω_{pump},ω_{probe})=(1654, 1547) cm^{-1} and its conjugate (small-dash boxes). This set of cross peaks has been measured previously using 2D IR spectroscopy and contain many overlapping peaks since they result from coupling between the unlabeled amide I and the amide II mode.[35,36,49] The peaks that we are interested in are those connecting the isotope labeled amide I mode to the amide II mode, which appear at (ω_{pump},ω_{probe})=(1587, 1547) and (1547, 1587) cm^{-1} (solid boxes). These cross peaks are created by coupling from a single residue in the peptide.

Shown in Figure 6.2 is a spectrum (d) and diagonal slice (c) of Ile-10 ovispirin taken 30 min after addition of D_2O. The linewidth of the unlabeled amide I peak changes upon deuteration, due to the small shift in frequency of the amide I mode upon HDX (<8 cm^{-1}); however, this frequency shift is not significant enough to use as a measure of HDX. Thus, HDX cannot be measured by the unlabeled amide I mode. The amide II mode has decreased by a factor of 3 in intensity. Additional features appear along the diagonal at 1607 cm^{-1} due to deuteration of the $(CN_3H_5)^+$ Arg sidechain (large-dash box). Ovispirin contains three Arg residues, and so the deuterated sidechain features prominently along the diagonal of the 2D IR spectrum. Original experiments performed on ovispirin were performed strictly in H_2O in order to avoid overlap of the Arg

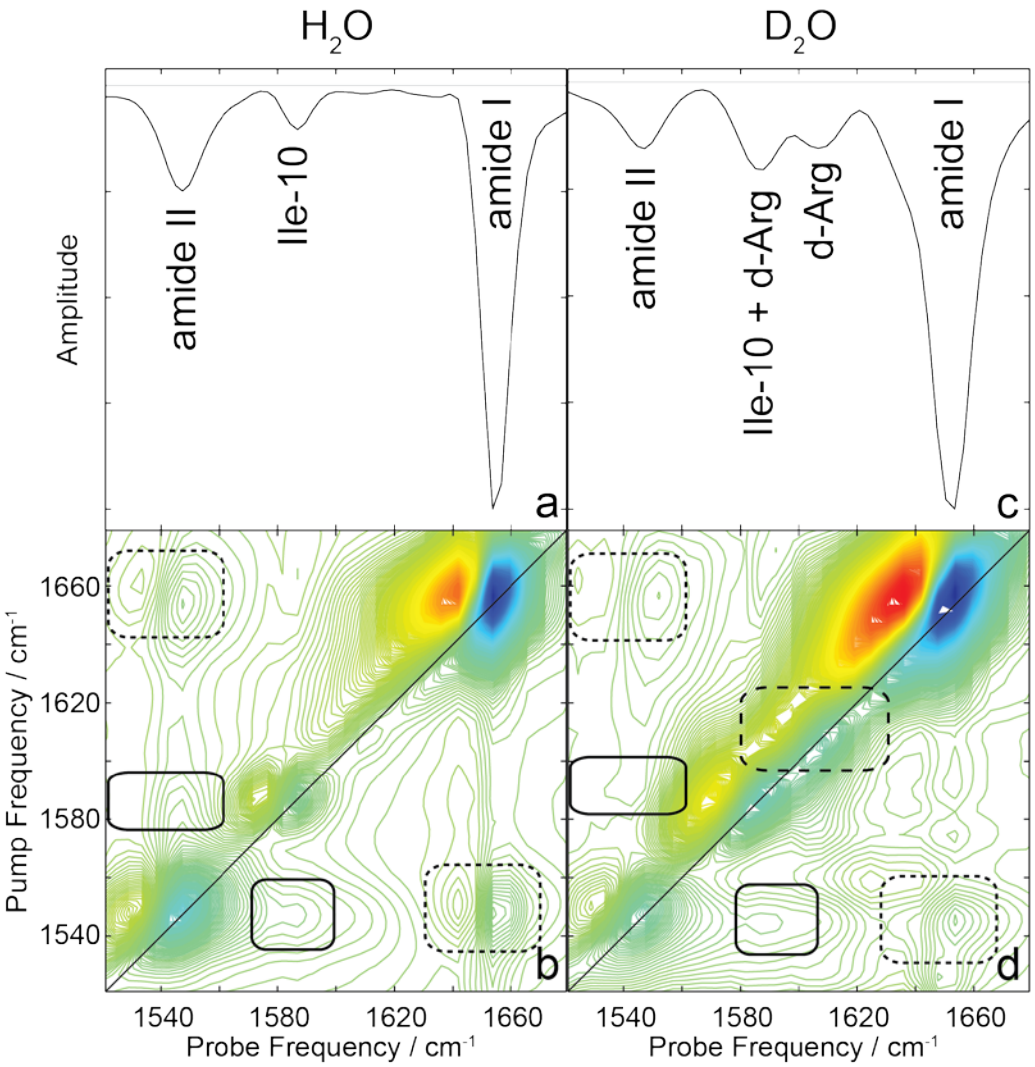

Figure 6.2 (a) Diagonal slice through the 2D IR spectrum below. (b) 2D IR spectrum of Ile-10 ovispirin in H_2O. Spectrum (b) shows the unlabeled amide I, isotope labeled amide I, and amide II modes along the diagonal. Cross peaks between the amide I and amide II modes are highlighted with small-dash boxes. Cross peaks between Ile-10 and amide II modes are highlighted with solid boxes. (c) Diagonal slice through the 2D IR spectrum below. (d) 2D IR spectrum of Ile-10 ovispirin in D_2O. Spectrum (d) shows the unlabeled amide I, isotope labeled amide I, and amide II modes along the diagonal. Also along the diagonal, enclosed with a large-dash box, is the peak arising from the deuterated sidechain on Arg at 1607 cm^{-1}. Cross peaks between the amide I and amide II modes are highlighted with small-dash boxes. Cross peaks between Ile-10 and amide II modes are highlighted with solid boxes.

sidechain with the $^{13}C^{18}O$ isotope label.[39] But overlap is not a problem here since the cross peaks are still well-resolved, as we show below.

In addition to changing the intensities of the amide II and Arg sidechain peaks, HDX causes the intensities of the cross peaks to change as well. With the decrease in intensity of the amide II peak, the cross peaks between the unlabeled amide I and amide II ($\omega_{pump},\omega_{probe}$)=(1653, 1547) and (1547, 1653) cm^{-1} drop in intensity (small-dash boxes), but these features are difficult to interpret as mentioned above. More interestingly, the cross peaks between the isotope label amide I and amide II peaks ($\omega_{pump},\omega_{probe}$)=(1587, 1547) cm^{-1} and its conjugate, have decreased in intensity, indicating that HDX has occurred at Ile-10.

Shown in Figure 6.3b and 3c are expanded ranges of the spectra from Figure 6.2, highlighting the Ile-10/amide II cross peaks. To determine the extent of exchange, slices through the pump axes at 1587 cm^{-1} (dashed line) in H_2O and D_2O were compared (Figure 6.3a). The two slices in Figure 6.3a point out one cross peak between Ile-10 and the amide II (large-dash boxes in Figures 6.3a, b, and c) that changes intensity upon deuteration. The blue trace shows a dip in the spectrum near 1547 cm^{-1}, corresponding to the fundamental of the isotope label amide I/amide II cross peak, while the red trace has no resolvable negative peak. Comparing the intensities of these two traces in this region, the cross peak intensity between the isotope labeled amide I and amide II modes decreases by a factor of 4.3 upon HDX. The two slices in Figure 6.3d are slices through the probe axes at 1587 cm^{-1} of Ile-10 in H_2O and D_2O. The important feature in Figure 6.3d, enclosed by a small-dash box, is the other cross peak between Ile-10 and the amide

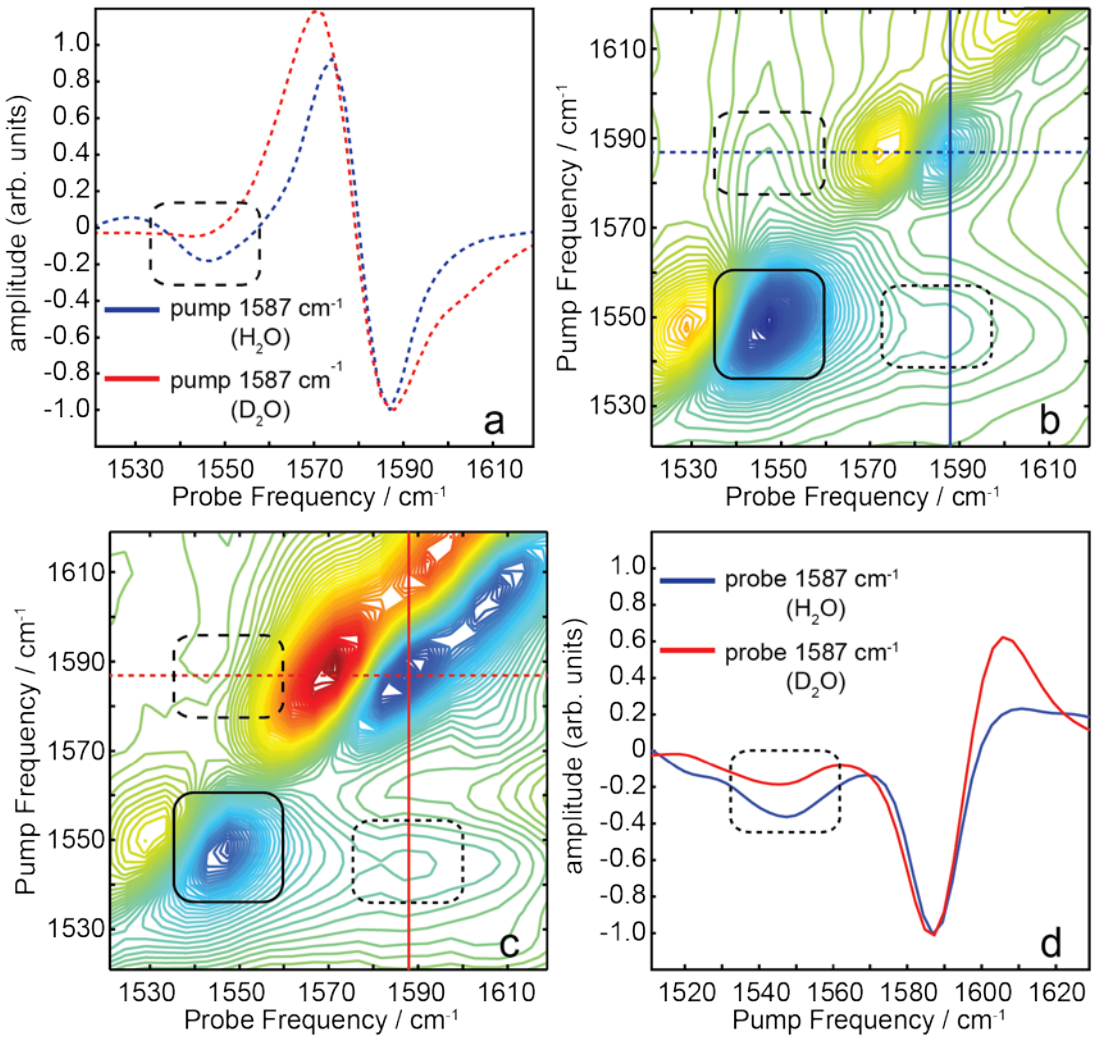

Figure 6.3 (a) Slices through the pump axis at 1595 cm^{-1} (blue, dashed, H_2O) and 1596 cm^{-1} (red, dashed, D_2O). (b) 2D IR spectrum of Ile-10 labeled ovispirin in H_2O. The dashed blue line at ω_{pump}=1587 cm^{-1} designates the pump slice shown in blue in (a) and the solid blue line at ω_{probe}= 1587 cm^{-1} designates the probe slice shown in blue in (d). (c) 2D IR spectrum of Ile-10 labeled ovispirin in D_2O. The dashed red line at ω_{pump}= 1587 cm^{-1} designates the pump slice shown in red in (a) and the solid red line at ω_{probe}=1547 cm^{-1} designates the probe slice shown in red in (d). (d) Slices through the probe axis at 1587 cm^{-1} (blue, H_2O) and 1587 cm^{-1} (red, D_2O). All solid black boxes enclose amide II peaks on the diagonal of 2D IR spectra. All large-dash boxes enclose cross peaks between isotope labeled amide I and amide II modes in the upper part of the 2D IR spectra. All small-dash boxes enclose cross peaks between isotope labeled amide I and amide II modes in the lower part of the 2D IR spectra.

II. In Figure 6.3d at ω_{probe}=1587 cm^{-1} in H_2O, the cross peak between the amide II and isotope label amide I is well resolved (blue). However, upon addition of D_2O, the intensity of the cross peak decreases by a factor of 2 between the blue and red traces. The other major difference between the blue and red traces in Figure 6.3d is in the region of ω_{pump} >1600 cm^{-1}. The only signal in this part of the spectra comes from the overtone of deuterated Arg sidechains; in the blue trace (H_2O), Arg is not deuterated and thus there is very little intensity in this part of the spectrum, while in the red trace (D_2O), Arg is deuterated and the slice goes through the deuterated Arg overtone peak, giving a positive peak above 1600 cm^{-1}. The amide II peak (enclosed with a solid black box in the 2D IR spectra) appears at 1547 cm^{-1} in both H_2O and D_2O. After addition of D_2O and 30 min of exchange time, the amide II peak decreases in intensity by a factor of 3 (slice comparison is not shown). One would expect that the change in intensity of cross peaks above and below the diagonal should be equivalent. However, the cross peaks above the diagonal at (ω_{pump},ω_{probe})= (1587, 1547) cm^{-1} have destructive interference from the diagonal peak of the isotope/Arg combination peak at (ω_{pump},ω_{probe})=(1587, 1571) cm^{-1}. One could do multi-peak fits to separate overlapping modes.[50] However, we have chosen to concentrate on the cross peaks below the diagonal because they have less overlap with the diagonal peaks.

Using the rapid-scan capabilities of our pulse shaper, we measured the kinetics of HDX following the addition of D_2O to a sample that is originally protonated. As explained in the Experimental, the instrumental dead time is less than a fraction of a second and so for all purposes of this paper, the peptides are immediately exposed to

D_2O. In addition, since spectra are collected every 0.4 s, the data points are congested in Figure 6.4 to form one smooth line. Figure 6.4 shows three kinetics traces: the decay of the intensity of the amide II peak ($\omega_{pump},\omega_{probe}$)=(1547, 1547) cm^{-1} (a, blue), the growth of the intensity of the arginine peak ($\omega_{pump},\omega_{probe}$)=(1607, 1607) cm^{-1} (b, green), and the decay of the intensity of the amide II/isotope labeled amide I cross peak ($\omega_{pump},\omega_{probe}$)=(1547, 1588) cm^{-1} (c, red). Each of these traces shows the change in peak intensity at given pump and probe frequencies immediately after HDX initiation. The kinetics trace of the amide II peak was fit to a biexponential decay function with an offset that separated the exchange rates into two sub-populations of exchangeable amide hydrogen atoms and one population that did not exchange (Equation 6.1).

$$y = aexp^{-bx} + cexp^{-dx} + e \quad (6.1)$$

The coefficients *a*, *c*, and *e* represent the fraction of residues that exchange with the rate constant 1/*b* (population *a*), 1/*d* (population *c*), or do not exchange at all (population *e*). The coefficients are unitless, while *b* and *d* have units of min^{-1}. The fit to the amide II data is shown in Figure 6.4a (cyan), and reveals a fast time constant of 0.54 ± 0.02 min^{-1} and the slower constant of 0.12 ± 0.01 min^{-1} (Table 6.1). The amide II band is not adequately fit by a single exponential, which indicates that there are a range of HDX timescales in the peptide. In contrast, the kinetics traces of the arginine peak and cross peak were fit to a single exponential decay function (Equation 6.2) and those fits are shown in Figure 6.4b (light green) and Figure 6.4c (magenta), respectively.

$$y = aexp^{-bx} + e \quad (6.2)$$

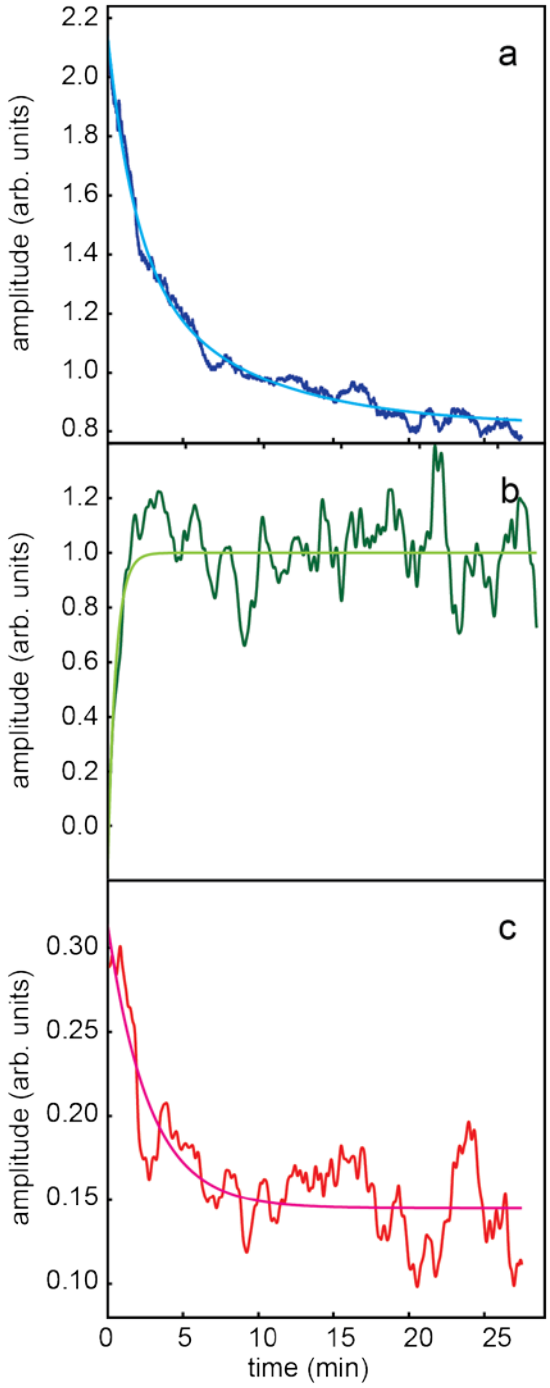

Figure 6.4 (a) Decay of the intensity at (ω_{pump},ω_{probe})=(1547, 1547) cm^{-1} immediately following addition of D_2O to the sample (blue). Biexponential fit (cyan). (b) Rise of the intensity at (ω_{pump},ω_{probe})=(1607, 1607) cm^{-1} immediately following addition of D_2O to the sample (dark green). Single exponential fit (light green). (c) Decay of the intensity at (ω_{pump},ω_{probe})=(1547, 1588) cm^{-1} immediately following addition of D_2O to the sample (red). Single exponential fit (magenta).

Peak	frequency (cm^{-1}) (ω_{pump}, ω_{probe})	a	b (min^{-1})	T (min)	c	d (min^{-1})	T (min)	e
Amide II	1547, 1547	0.75 ± 0.02	0.54 ± 0.02	1.9 ± 0.07	0.57 ± 0.02	0.12 ± 0.01	8.3 ± 0.7	0.82 ± 0.03
Arginine	1607, 1607	1.18 ± 0.063	1.96 ± 0.15	0.51 ± 0.04				0
Cross peak	1547, 1588	0.17 ± 0.028	0.36 ± 0.1	2.8 ± 1				0.15 ± 0.02

Table 6.1 Coefficients of the biexponential fit (Equation 6.1) to the amide II trace and single exponential fit (Equation 6.2) to the arginine trace and the isotope label amide I/amide II cross peak trace shown in Figure 6.4. Decay times (T) are also given.

The coefficient *a* is the fraction of residues that decay with the rate constant 1/*b*, and *e* is the fraction of residues that do not exchange. Variables *a* and *e* are unitless and *b* has units of min^{-1}. The rate constant for exchange of the arginine peak is 1.96 ± 0.15 min^{-1} and for the cross peak is 0.36 ± 0.1 min^{-1} (Table 6.1). All fitted variables and decay times are given in Table 6.1. Kinetics of the cross peak in the upper half of the spectrum are not shown because of the previously described interference with the overtone of the Ile-10/Arg peak.

6.5 Discussion

Upon HDX of ovispirin, the amide II peak decreased intensity, as expected. This observation follows previous IR experiments showing that upon deuteration of a protein, the amide II peak intensity decreases and the amide II' peak increases. While the laser bandwidth and center frequency prevented observation of the amide II' peak, the amide II peak decreased by a factor of 3 over 1 h. The decay of the amide II peak is shown in Figure 6.4a and can be considered the average HDX kinetics for the entire peptide because the amide II mode has contributions from every residue in the peptide. The biexponential fit suggests that 6 residues exchange with a rate of 0.54 ± 0.02 min^{-1}, 5 residues exchange with a rate of 0.12 ± 0.01 min^{-1}, and 7 residues do not exchange, although this is only an approximation. Nonetheless, it is consistent with other experimental techniques; when individual residues are not resolved, multistep kinetics are observed.[18,24,51,52] In transmembrane domain proteins, the overall deuterium content has been fit to a triexponential function where the first class of hydrogen atoms exchange rapidly (less than 1 min), the second class exchange slower (on the order of tens of

minutes), and the third class virtually never exchanges.[18,51] Ovispirin is not a transmembrane peptide and it lies mostly parallel to the membrane surface; however, multiple classes of hydrogen atoms likely exist for this mostly α-helical surface-bound peptide. The residues that lie completely outside the with membrane will likely have the fastest exchange, residues in the most ordered secondary structure deep in the membrane will likely have the slowest exchange, and then residues somewhat exposed to solvent or in a less ordered secondary structure will have intermediate exchange rates. While we do not fit our data to a triexponential function, the fast exchanging hydrogen atoms exchange in 1.9 ± 0.07 min, the intermediate exchanging hydrogen atoms exchange in 8.3 ± 0.7 min, and it is likely there is a third, longer exchanging sub-population of amide hydrogen atoms that decay on the 1 h or longer timescale. After 1 h of HDX, the amide II peak has decayed and appears not to be changing, but there is still a peak at the amide II frequency in the 2D IR spectrum (not shown). This suggests that while exchange has become very slow, not every amide II hydrogen atom has exchanged for a deuterium atom.

As described above, upon HDX of Ile-10 ovispirin, an additional peak grows in along the diagonal of the 2D IR spectrum at 1607 cm^{-1} (Figure 6.2d). This additional peak can be attributed to deuteration of the guanidyl group of Arg sidechains, of which ovispirin has three. Previously reported values of deuterated Arg sidechain frequencies are 1587 cm^{-1} and 1610 cm^{-1} in solution and 1582 cm^{-1} and 1610 cm^{-1} in a micelle.[53] The two frequencies derive from degenerate CN stretch modes in the guanidyl group. The Arg peak in Figure 6.2d derives from one of the degenerate modes, while the other is likely absorbing in the same position as the Ile-10 peak at 1587 cm^{-1}. Intensity from

deuterated Arg is contributing to the intensity of Ile-10 along the diagonal and could impact the scaling factors used to produce the slices in Figure 6.3. The rapid increase in intensity of the Arg sidechain diagonal peaks shown in Figure 6.4b suggests that the three Arg residues rapidly exchanged hydrogen atoms for deuterium atoms, in 0.51 ± 0.04 min with an exchange constant of 1.96 ± 0.15 min^{-1}, and therefore the three Arg residues in ovispirin must be highly solvent exposed. According to structures from ssNMR and 2D IR spectroscopies, the three Arg residues are all solvent exposed; this follows suit with the three Arg residues rapidly undergoing HDX with nearby water molecules.[39,40] Monitoring HDX of sidechains can provide a way of ensuring the peptide is exposed to D_2O.

HDX rates of sidechain hydrogen atoms in Arg have rarely been studied; to our knowledge there has been one circular dichroism spectroscopy study of HDX rates of the hydrogen atoms in Arg sidechains in solution[54] and a few NMR spectroscopy studies that measured the HDX rates of the hydrogen atoms in Arg sidechains in proteins.[55,56] The Arg sidechain has two types of exchangeable hydrogen atoms, and thus two different exchange rates; however, these rates only differ by an order of magnitude at low pH (~2) and are the same order of magnitude at higher pH (>3.5).[54] At pH ~3.5 both exchange rates are ~0.5 sec^{-1}, and it can be assumed that the exchange rates increase by an order of magnitude with each increasing pH unit.[13] At neutral pH, the exchange rate of the sidechain hydrogen atoms can be estimated to be ~0.5 x 10^4 sec^{-1}, which is extremely fast. In protein systems, using NMR spectroscopy, the HDX rates of hydrogen atoms in Arg sidechains has been measured to be 10^2-10^3 sec^{-1}.[56] Although the HDX rate of Arg

in solution has not been measured at neutral pH and thus cannot be directly compared, it must be very fast. Comparing the estimated exchange rate in solution with that measured in ovispirin, the Arg sidechains are protected from HDX in the peptide. It has not been common practice to measure HDX rates of sidechain hydrogen atoms, and thus measure protection factors, likely because exchange happens too quickly for most NMR spectroscopy techniques to capture. However, IR spectroscopy can capture fast HDX rates, and could be used to measure sidechain protection factors.

The most structurally interesting cross peaks in these 2D IR spectra are between the isotope label and amide II peaks, shown in Figure 6.3 (dashed boxes). By monitoring the intensity of these cross peaks over time, site-specific HDX was monitored in real-time. Amide I/amide II coupling has been shown to be strongest within one peptide unit and has been measured in the model molecule NMA.[33,49,57] The Ile-10/amide II cross peak must then derive from coupling between those two modes on the same amino acid; therefore if the cross peak intensity decreases after addition of D_2O, the amide proton on Ile-10 must undergo HDX. The amide hydrogen atom of Ile-10 exchanged for deuterium with an exchange constant of 0.36 ± 0.1 min^{-1}, corresponding to 2.8 ± 1 min after deuterated buffer was added to the sample (Figure 6.4c), and this gives insight into the structure of ovispirin on a membrane. HDX rates are a function of temperature, pH, as well as the residues adjacent to the amide group of interest. The rate of HDX for a variety of peptide sequences at various temperatures and pH has been measured, and attempts to use that data to extrapolate protection factors have been fruitful.[58] The protection factor at a given residue is a ratio of the rate of HDX of that residue in a

solvated unstructured peptide compared to the rate of HDX under experimental conditions such as in a secondary structure or membrane. Theoretically determined HDX rates of Ile-10 were calculated using a program written by Englander, which is derived from a series of papers looking at the rate of HDX under a variety of experimental conditions.[58,59] Comparing the theoretical rate of exchange at Ile-10 in a random coil (6.7 x 10^{-1} s^{-1}) to the experimentally measured exchange rate of 0.36 min^{-1} (Table 6.1), gives the protection factor of 113. Solvent exposed residues with no secondary structure have typical protection factors of 1, soluble alpha-helices have protection factors ranging from 2-20[60], globular proteins with some secondary structure have protection factors of 0.5-2000[61], and membrane bound alpha-helices have protection factors of 3-2000[19,62]. Thus, the protection factor measured for Ile-10 is consistent with that residue being located in an α-helical membrane peptide where the hydrogen bonded secondary structure and amphipathic membrane protect Ile-10 from HDX.

Previous 2D IR spectroscopy measurements and molecular dynamics simulations solved the structure of ovispirin on a membrane; in addition to the three Arg residues being fully solvated, Ile-10 was found to lie in a largely homogeneous electrostatic environment.[39] From MD simulations, it was found that Ile-10 resides near a kink in the helix that denatures ovispirin over the next 6 residues. This explains why it is not as greatly protected from solvent as one might imagine being a hydrophobic amino acid in a membrane-bound α-helix.[39] Ultimately, kinks cause decreased protection factors, and the effect of kinks in transmembrane peptides has been previously studied.[24] A single proline was incorporated into the most hydrophobic region of the peptide to determine what

effect this α-helix destabilizer and hydrogen bond breaking residue would have on the rate of HDX, particularly for the residues located in the transmembrane region of the peptide. Overall, the HDX rate of the peptide with the proline mutation was one order of magnitude larger than the non-mutated peptide, showing that the proline kink disrupted the lipid acyl chains enough to allow for faster overall HDX. Although Ile-10 lies in a largely inhomogeneous environment, it is consistent that the kink in ovispirin disrupts the membrane such that HDX is allowed at that residue. Although further experiments could be done to more precisely measure the rate of HDX in random coil ovispirin, we believe this protection factor makes sense for this system. Protection factors on the same order of magnitude have been measured for a 129-residue α-helix/β-sheet protein and a membrane-bound α-helical peptide.[62,63]

6.6 Conclusions

To conclude, we have shown that it is possible to measure on-the-fly HDX rates in the membrane-bound peptide, ovispirin, using a combination of rapid-scan pulse shaping 2D IR spectroscopy and non-invasive isotope labeling in the amide I mode of one residue in ovispirin. In contrast to linear IR spectroscopy, 2D IR spectroscopy allows one to measure coupled modes through the observation of cross peaks in a 2D IR spectrum. As such, we have monitored the kinetics of cross peaks between the isotope labeled amide I mode at Ile-10 and the amide II mode, which decreases intensity upon HDX. Ten minutes after HDX initiation by addition of deuterated buffer to the sample, the Ile-10/amide II cross peak in the lower half of the 2D IR spectrum decreased by a factor of 2. We calculated a protection factor of 113, which suggests that the Ile-10

amide group undergoes HDX at a rate 100 times slower than it would in solution. Our results are consistent with 2D IR and NMR spectroscopy derived structural models of ovispirin. These results show that 2D IR spectroscopy can be used to obtain site-specific HDX in the same manner as one might use NMR spectroscopy or mass spectrometry, although it can be done on-the-fly for membrane peptides without the need for quenchers or for slowing down the rates by lowering the pH. Our experiments illustrate another possible way in which 2D IR spectroscopy can be used to study protein and peptide structures that we believe will find use during the course of other isotope labeled 2D IR experiments, such as measuring the protection factors for one complete helix turn in ovispirin or measuring the rate of HDX at various time points in the folding process of isotope labeled amylin, the amyloidogenic polypeptide implicated in Type II diabetes.

6.7 Acknowledgments

Support for this research was provided by the National Institutes of Health Grant DK79895.

6.8 References

(1) Bredenbeck, J.; Helbing, J.; Nienhaus, K.; Nienhaus, G. U.; Hamm, P. *Proceedings of the National Academy of Sciences* **2007**, *104*, 14243-14248.

(2) Woutersen, S.; Mu, Y.; Stock, G.; Hamm, P. *Chem. Phys.* **2001**, *266*, 137-147.

(3) Fayer, M. D. *Annu. Rev. Phys. Chem.* **2009**, *60*, 21-38.

(4) Kwak, K.; Rosenfeld, D. E.; Chung, J. K.; Fayer, M. D. *The Journal of Physical Chemistry B* **2008**, *112*, 13906-13915.

(5) Moilanen, D. E.; Wong, D.; Rosenfeld, D. E.; Fenn, E. E.; Fayer, M. D. *Proceedings of the National Academy of Sciences* **2009**, *106*, 375-380.

(6) Zheng, J.; Fayer, M. D. *The Journal of Physical Chemistry B* **2008**, *112*, 10221-10227.

(7) Zheng, J.; Kwak, K.; Asbury, J.; Chen, X.; Piletic, I. R.; Fayer, M. D. *Science* **2005**, *309*, 1338-1343.

(8) Zheng, J.; Kwak, K.; Chen, X.; Asbury, J. B.; Fayer, M. D. *J. Am. Chem. Soc.* **2006**, *128*, 2977-2987.

(9) Ghosh, A.; Remorino, A.; Tucker, M. J.; Hochstrasser, R. M. *Chem. Phys. Lett.* **2009**, *469*, 325-330.

(10) Kim, Y. S.; Hochstrasser, R. M. *Proc. Natl. Acad. Sci. U. S. A.* **2005**, *102*, 11185-11190.

(11) Kim, Y. S.; Hochstrasser, R. M. *The Journal of Physical Chemistry B* **2006**, *110*, 8531-8534.

(12) Jeng, M.-F.; Englander, S. W. *J. Mol. Biol.* **1991**, *221*, 1045-1061.

(13) Englander, S. W.; Mayne, L. *Annu. Rev. Biophys. Biomol. Struct.* **1992**, *21*, 243-265.

(14) Dempsey, C. E. *Prog. Nucl. Magn. Reson. Spectrosc.* **2001**, *39*, 135-170.

(15) Eriksson, M. A.; Härd, T.; Nilsson, L. *Biophys. J.* **1995**, *69*, 329-339.

(16) Wu, Y.; Murayama, K.; Ozaki, Y. *The Journal of Physical Chemistry B* **2001**, *105*, 6251-6259.

(17) Cotten, M.; Fu, R.; Cross, T. A. *Biophys. J.* **1999**, *76*, 1179-1189.

(18) Demmers, J. A. A.; Haverkamp, J.; Heck, A. J. R.; Koeppe, R. E.; Killian, J. A. *Proceedings of the National Academy of Sciences* **2000**, *97*, 3189-3194.

(19) Dempsey, C. E.; Handcock, L. J. *Biophys. J.* **1996**, *70*, 1777-1788.

(20) Dempsey, C. E.; Butler, G. S. *Biochemistry* **1992**, *31*, 11973-11977.

(21) Hoshino, M.; Katou, H.; Yamaguchi, K.-i.; Goto, Y. *Biochimica et Biophysica Acta (BBA) - Biomembranes* **2007**, *1768*, 1886-1899.

(22) Hansen, R. K.; Broadhurst, R. W.; Skelton, P. C.; Arkin, I. T. *J. Am. Soc. Mass Spectrom.* **2002**, *13*, 1376-1387.

(23) Zhang, A.; Qi, W.; Good, T. A.; Fernandez, E. J. *Biophys. J.* **2009**, *96*, 1091-1104.

(24) Demmers, J. A. A.; van Duijn, E.; Haverkamp, J.; Greathouse, D. V.; Koeppe, R. E.; Heck, A. J. R.; Killian, J. A. *J. Biol. Chem.* **2001**, *276*, 34501-34508.

(25) Lanman, J.; Prevelige Jr, P. E. *Curr. Opin. Struct. Biol.* **2004**, *14*, 181-188.

(26) Vigano, C.; Smeyers, M.; Raussens, V.; Scheirlinckx, F.; Ruysschaert, J. M.; Goormaghtigh, E. *Biopolymers* **2004**, *74*, 19-26.

(27) Dzwolak, W.; Loksztejn, A.; Smirnovas, V. *Biochemistry* **2006**, *45*, 8143-8151.

(28) Beevers, A. J.; Kukol, A. *Protein Sci.* **2006**, *15*, 1127-1132.

(29) Ding, F.-X.; Xie, H.; Arshava, B.; Becker, J. M.; Naider, F. *Biochemistry* **2001**, *40*, 8945-8954.

(30) Earnest, T. N.; Herzfeld, J.; Rothschild, K. J. *Biophys. J.* **1990**, *58*, 1539-1546.

(31) Ludlam, C. F.; Arkin, I. T.; Liu, X. M.; Rothman, M. S.; Rath, P.; Aimoto, S.; Smith, S. O.; Engelman, D. M.; Rothschild, K. J. *Biophys. J.* **1996**, *70*, 1728-1736.

(32) Krimm, S.; Bandekar, J. In *Adv. Protein Chem.*; C.B. Anfinsen, J. T. E., Frederic, M. R., Eds.; Academic Press: 1986; Vol. Volume 38, p 181-364.

(33) Maekawa, H.; Poli, M. D.; Moretto, A.; Toniolo, C.; Ge, N.-H. *The Journal of Physical Chemistry B* **2009**, *113*, 11775-11786.

(34) Fillaux, F.; de Lozé, C. *Chem. Phys. Lett.* **1976**, *39*, 547-551.

(35) DeFlores, L. P.; Ganim, Z.; Nicodemus, R. A.; Tokmakoff, A. *J. Am. Chem. Soc.* **2009**, *131*, 3385-3391.

(36) DeFlores, L. P.; Tokmakoff, A. *J. Am. Chem. Soc.* **2006**, *128*, 16520-16521.

(37) Maekawa, H.; Ge, N.-H. *The Journal of Physical Chemistry B* **2010**, *114*, 1434-1446.

(38) Rubtsov, I. V.; Wang, J.; Hochstrasser, R. M. *Proceedings of the National Academy of Sciences* **2003**, *100*, 5601-5606.

(39) Woys, A. M.; Lin, Y.-S.; Reddy, A. S.; Xiong, W.; de Pablo, J. J.; Skinner, J. L.; Zanni, M. T. *J. Am. Chem. Soc.* **2010**, *132*, 2832-2838.

(40) Yamaguchi, S.; Huster, D.; Waring, A.; Lehrer, R. I.; Kearney, W.; Tack, B. F.; Hong, M. *Biophys. J.* **2001**, *81*, 2203-2214.

(41) Middleton, C. T.; Woys, A. M.; Mukherjee, S. S.; Zanni, M. T. *Methods, In Press, Corrected Proof*.

(42) Torres, J.; Adams, P. D.; Arkin, I. T. *J. Mol. Biol.* **2000**, *300*, 677-685.

(43) Torres, J.; Kukol, A.; Goodman, J. M.; Arkin, I. T. *Biopolymers* **2001**, *59*, 396-401.

(44) Shim, S.-H.; Strasfeld, D. B.; Fulmer, E. C.; Zanni, M. T. *Opt. Lett.* **2006**, *31*, 838-840.

(45) Shim, S.-H.; Strasfeld, D. B.; Zanni, M. T. *Opt. Express* **2006**, *14*, 13120-13130.

(46) Saito, H.; Shinoda, W. *The Journal of Physical Chemistry B* **2011**, *115*, 15241-15250.

(47) Jansen, M.; Blume, A. *Biophys. J.* **1995**, *68*, 997-1008.

(48) Lande, M. B.; Donovan, J. M.; Zeidel, M. L. *The Journal of General Physiology* **1995**, *106*, 67-84.

(49) DeFlores, L. P.; Ganim, Z.; Ackley, S. F.; Chung, H. S.; Tokmakoff, A. *The Journal of Physical Chemistry B* **2006**, *110*, 18973-18980.

(50) Zanni, M. T.; Asplund, M. C.; Hochstrasser, R. M. *The Journal of Chemical Physics* **2001**, *114*, 4579-4590.

(51) Stelzer, W.; Poschner, B. C.; Stalz, H.; Heck, A. J.; Langosch, D. *Biophys. J.* **2008**, *95*, 1326-1335.

(52) Yamamoto, T.; Takao, T.; Izumi, S.; Gekko, K. *Journal of the Mass Spectrometry Society of Japan* **2007**, *55*, 333-338.

(53) Ghosh, A.; Tucker, M. J.; Hochstrasser, R. M. *The Journal of Physical Chemistry A* **2011**, *115*, 9731-9738.

(54) Takahashi, T.; Nakanishi, M.; Tsuboi, M. *Anal. Biochem.* **1981**, *110*, 242-249.

(55) Thakur, A.; Chandra, K.; Dubey, A.; D'Silva, P.; Atreya, H. S. *Angew. Chem.* **2013**, *125*, 2500-2503.

(56) Segawa, T.; Kateb, F.; Duma, L.; Bodenhausen, G.; Pelupessy, P. *ChemBioChem* **2008**, *9*, 537-542.

(57) Hayashi, T.; Mukamel, S. *The Journal of Physical Chemistry B* **2007**, *111*, 11032-11046.

(58) Bai, Y.; Milne, J. S.; Mayne, L.; Englander, S. W. *Proteins: Struct., Funct., Bioinf.* **1993**, *17*, 75-86.

(59) Connelly, G. P.; Bai, Y.; Jeng, M.-F.; Englander, S. W. *Proteins: Struct., Funct., Bioinf.* **1993**, *17*, 87-92.

(60) Rohl, C. A.; Baldwin, R. L. *Biochemistry* **1994**, *33*, 7760-7767.

(61) Kuroda, Y.; Endo, S.; Nagayama, K.; Wada, A. *J. Mol. Biol.* **1995**, *247*, 682-688.

(62) Halsall, A.; Dempsey, C. E. *J. Mol. Biol.* **1999**, *293*, 901-915.

(63) Lacroix, E.; Bruix, M.; López-Hernández, E.; Serrano, L.; Rico, M. *J. Mol. Biol.* **1997**, *271*, 472-487.

CHAPTER 7*

Conclusions and Future Work

7.1 Introduction

When I started working on the hIAPP project, I was a fourth year graduate student. Up to that point, I had built up the Wyvern laser table (Chapter 2) and completed hydrogen-deuterium exchange (HDX) experiments (Chapter 6). The site-specific folding mechanism of hIAPP had just been solved[2], and the next direction we took with hIAPP was to determine if any small molecules or small peptides could inhibit aggregation. Although we had to take a detour to determine that our entire stock of expensive isotope labeled peptides had become deamidated (Chapter 3), in the process we learned how to synthesize isotope labeled amino acids and peptides. Since then, we have made great strides towards learning about how small macrocyclic β-sheet molecules

* Portions of this chapter will be published as part of a paper submitted in the summer of 2013. My contributions are in collaboration with Lauren E. Buchanan, Huong Q. Tran, Wenting Cai, and Martin T. Zanni.

inhibit fiber formation (Chapter 5). However, there is still much work to be done both in understanding how hIAPP aggregates, using other small molecule inhibitors, and in using HDX experiments to elucidate the structure of peptides, both membrane-bound and aggregates. There are ongoing projects that I am leaving, and future projects to explore that will be discussed below.

7.2 Expose the aggregation mechanism of human amylin

The site-specific folding mechanism of hIAPP was determined by measuring the kinetics of folding at six different positions in the peptide. It was determined that out of the residues studied, Val-17 folded first, folding before the unlabeled peptide. Next, Ala-25 and Leu-27 formed β-sheets, followed by Ala-13, Ala-8, and finally, Val-32 (Figure 5.1).[2] While this study yielded the highest-resolution folding mechanism for human amylin, it still did not address the possibility of early-stage oligomeric species that have been shown to be more toxic than final-stage fibers.[3] In order to learn more about the mechanism of aggregation, and to possibly prevent aggregation, the next step was to mix hIAPP with possible small molecule or small peptide-based inhibitors to see what affect they had on amylin aggregation.

7.2.1 Current project: Discovery of amylin oligomers by the use of β-sheet macrocycles

In the process of mixing amylin with β-sheet macrocycles, one result stood out as indicating the presence of an early stage oligomeric species. At early times, pure Ala-25 had a high-frequency, coupled isotope label peak that persisted for ~2.5 h, while Ala-25 mixed with macrocycle 1c had the same high-frequency, coupled isotope label peak that

persisted for ~4 h (Figure 5.6). This peak, although higher in frequency than the isotope peak in the final fiber structure of Ala-25, was shown to be due to coupling at Ala-25. The coupling must be weaker than in the final fiber structure; nonetheless, it showed that hIAPP forms β-sheets at early times, before the rest of the peptide has assembled into fibers. We call this early-stage coupled species an oligomer. The addition of the macrocycle extended the lifetime of the oligomer.

Work is ongoing to determine if any other C-terminal residues in hIAPP also form this early-stage oligomer. Other isotope labeled peptides have been synthesized at Phe-23, Gly-24, and Leu-27, targeting the hydrophobic, and highly amyloigenic NFGAIL region. Early results show that for Phe-23, the isotope label couples at early times, and the coupled peak disappears as the peptide forms β-sheet aggregates. Experiments are still being conducted on Gly-24 and Leu-27. However, these preliminary results suggest that the oligomer species persists from at least Phe-23 to Ala-25. In the future, it might be beneficial to prevent this oligomer from forming, rather than trying to inhibit the formation of full-length fibers, as this oligomer may prove to be the more toxic species.

7.2.2 Current project: FDA-approved drug, pramlintide, aggregates

Previously, it was shown that rat amylin (rIAPP), the rat form of human amylin, did not form fibers, despite only differing from hIAPP at six amino acids (Figure 7.1a).[4-7] Three of mutations of hIAPP to rIAPP are at positions A25, S28, and S29, which all mutate to prolines. Proline, a well-established hydrogen-bond and β-sheet blocker, is thought to prevent the C-terminus of rIAPP from forming β-sheets, thus blocking the rest of the peptide from aggregating. Pramlintide, a synthetic mutant of hIAPP contains the

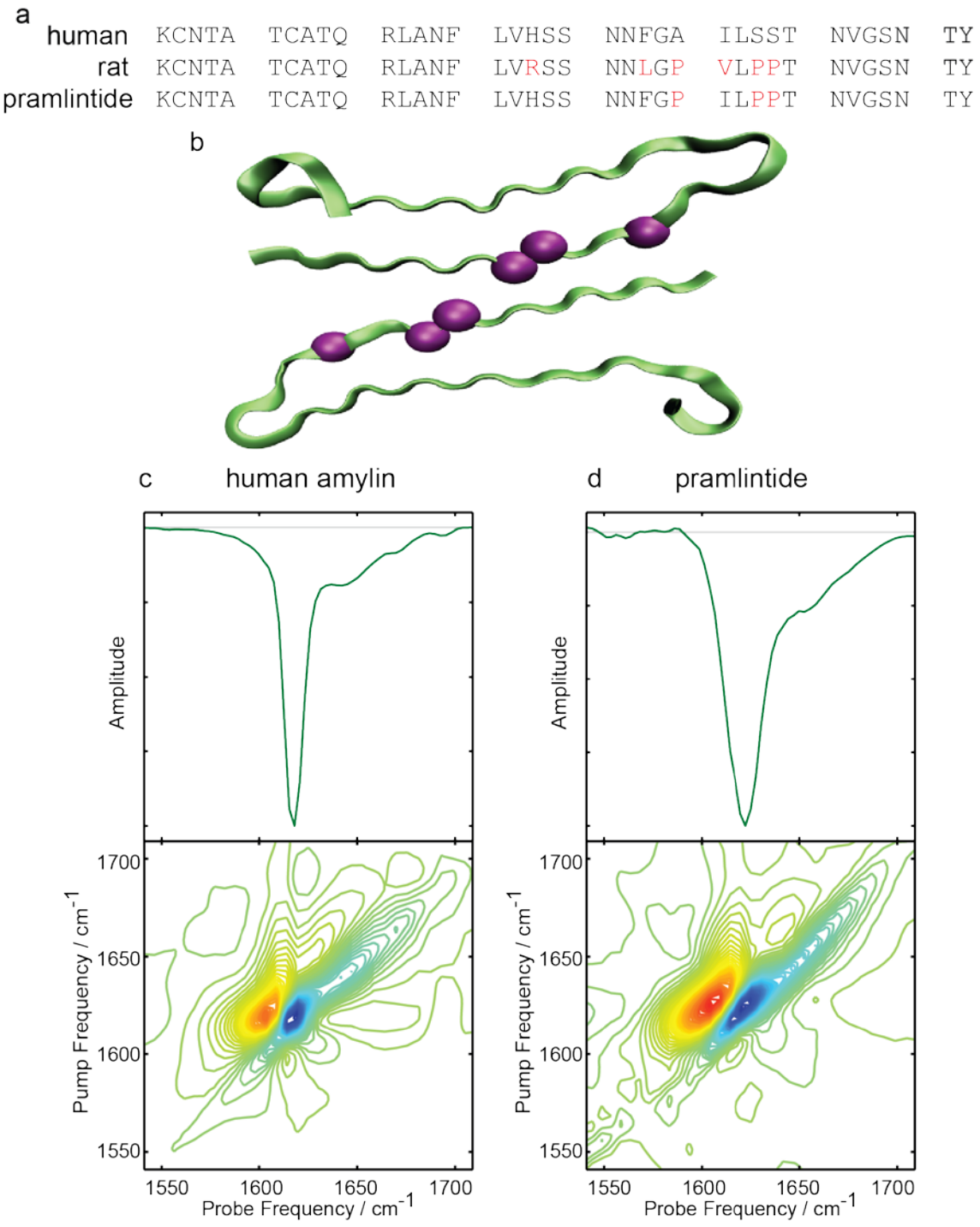

Figure 7.1 (a) Sequence of human amylin, rat amylin, and pramlintide. (b) Human amylin fiber structure, as determined my solid-state NMR.[1] The three mutations from hIAPP to pramlintide (A25P, S28P, and S29P) are highlighted in purple. (c) 2D IR spectrum and diagonal slice of unlabeled hIAPP fibers. (d) 2D IR spectrum and diagonal slice of unlabeled pramlintide. The pramlintide looks very similar to hIAPP fibers.

three proline mutations (shown in purple) in rIAPP, but retains the rest of the hIAPP sequence (Figure 7.1a and b).[8-12] Pramlintide is an FDA approved hormone replacement therapy for Type 2 diabetics. It is thought to work because it does not form insoluble aggregates at the concentrations at which it is administered.[12] However, we have shown that pramlintide does aggregate into β-sheets, depending on the experimental conditions.

We have synthesized unlabeled pramlintide and Ala-13 labeled pramlintide. Early results show that the propensity for pramlintide to form fibers is dependent upon the buffer conditions: in 20 mM pH 7.4 Tris buffer, pramlintide does not fold into β-sheets and remains random coil over the course of a three day experiment (not shown), however, in 20 mM pH 7.4 phosphate buffer, pramlintide forms β-sheets that are very similar to unlabeled hIAPP fibers, as shown in Figure 7.1. While 1 mM hIAPP fibers usually fold into equilibrated fibers in 8 h, 1 mM pramlintide took at least 24 hours to form β-sheets. In addition, the coupling in hIAPP fibers is stronger than in pramlintide because the β-sheet peak in hIAPP is narrow and at a lower frequency, 1618 cm^{-1} (Figure 7.1c) and for pramlintide is broader and at a higher frequency, 1622 cm^{-1} (Figure 7.1d).

Furthermore, we have shown that under conditions at which pramlintide aggregates (pH 7.4 phosphate buffer, 1 mM), Ala-13 becomes coupled, proving that at least the N-terminus of pramlintide forms β-sheets (Figure 7.2). This sample still contains some random coil peptide, as evidenced by the absorbance near 1650 cm^{-1}; however, this spectrum was collected 24 h after aggregation initiation. If left to aggregate longer, more random coil peptide would have been converted to β-sheet. In addition to the random coil peak, there is a peak at 1626 cm^{-1}, suggesting that some of the

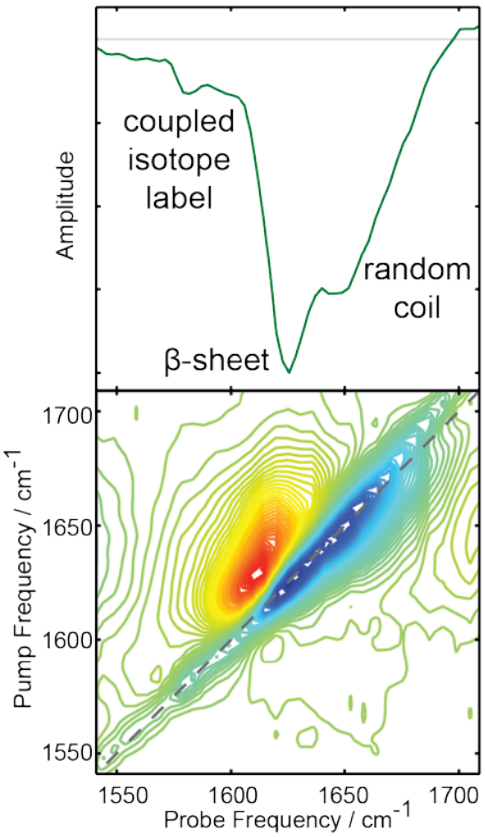

Figure 7.2 2D IR spectrum and diagonal slice of Ala-13 labeled pramlintide. Regions of the diagonal slice are labeled according to secondary structure. This particular sample of pramlintide has random coil (1650 cm^{-1}), β-sheet (1626 cm^{-1}), and the Ala-13 label is coupled into β-sheets (1583 cm^{-1}).

peptide is in β-sheets, and the peak at 1583 cm^{-1} is due to Ala-13 coupling in β-sheets. This result is somewhat expected because the N-terminus of pramlintide and hIAPP are identical. If pramlintide folds into β-sheets similar to those of hIAPP, it makes sense that Ala-13 would strongly couple in pramlintide as it does in hIAPP.

Mixing experiments have also been done on unlabeled pramlintide and Val-17 and Ala-25 labeled hIAPP to determine if pramlintide acted as a good fiber inhibitor, similar to rIAPP.[4] When pramlintide was mixed with equimolar labeled hIAPP, fibers formed at both Val-17 and Ala-25 (Figure 7.3 and 7.4, respectively). Immediately after fiber initiation, the peptides were random coil (Figure 7.3a and 7.4a), demonstrated by the large broad peaks near 1650 cm^{-1}, and after 24 h, the peptides folded into β-sheets (Figure 7.3b and 7.4b), confirmed by the narrow peaks near 1620 c m^{-1}. The spectra were not collected continuously for either of these samples, so it is impossible to know how long it took for these fibers to form. However, fibers formed faster in these mixed samples of pramlintide than pure pramlintide. This suggests that the driving force for hIAPP to form fibers is stronger than the ability of the three proline mutations in pramlintide to block fiber formation. Moreover, the final fiber structure contained coupled isotope labels (Figure 1.4a) at both Val-17 (1579 cm^{-1}) and Ala-25 (1584 cm^{-1} and 1571 cm^{-1}), suggesting that the mixed fiber structure contains parallel β-sheets at both positions.

Another mixing experiment involved mixing equimolar unlabeled hIAPP with Ala-13 labeled pramlintide. The final fiber spectrum is shown in Figure 7.5. There is a strongly coupled unlabeled β-sheet peak at 1619 cm^{-1}, and no coupled isotope labeled

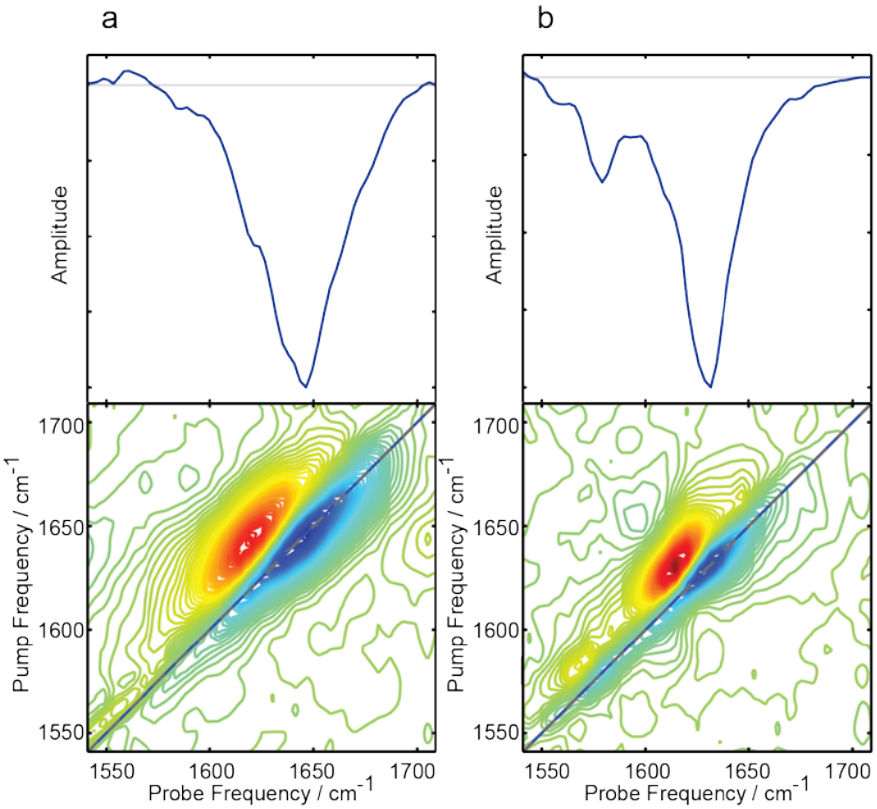

Figure 7.3 (a) 2D IR spectrum and diagonal slice of Val-17 labeled hIAPP and unlabeled pramlintide mixed in equimolar parts. Spectrum is collected immediately after fiber initiation by addition of phosphate buffer. (b) 2D IR spectrum and diagonal slice of Val-17 labeled hIAPP and unlabeled pramlintide mixed in equimolar parts. Spectrum is collected 24 h after fiber initiation by addition of phosphate buffer. The mixture is random coil in (a), and contains β-sheet in (b). Val-17 is coupled after 24 h, as shown by the low frequency peak at 1579 cm^{-1}.

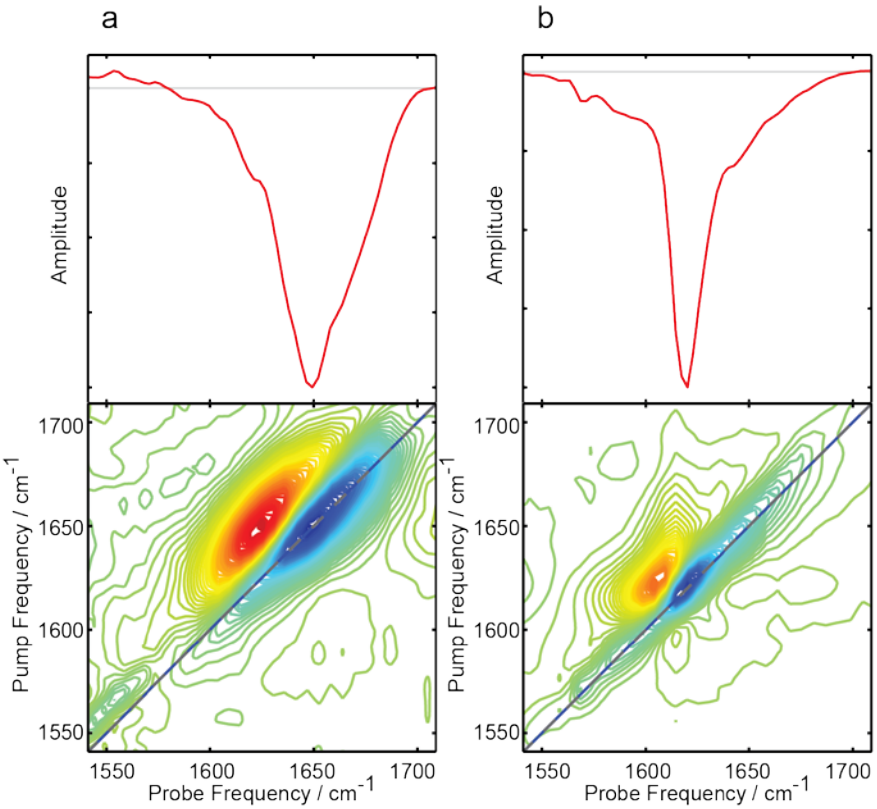

Figure 7.4 (a) 2D IR spectrum and diagonal slice of Ala-25 labeled hIAPP and unlabeled pramlintide mixed in equimolar parts. Spectrum is collected immediately after fiber initiation by addition of phosphate buffer. (b) 2D IR spectrum and diagonal slice of Ala-25 labeled hIAPP and unlabeled pramlintide mixed in equimolar parts. Spectrum is collected 24 h after fiber initiation by addition of phosphate buffer. The mixture is random coil in (a), and contains β-sheet in (b). Ala-25 is coupled after 24 h, as shown by the low frequency peaks at 1584 cm^{-1} and 1571 cm^{-1}.

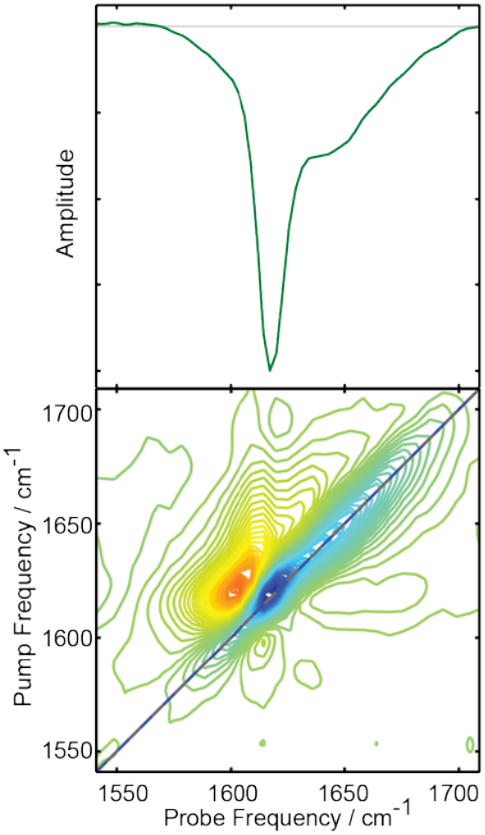

Figure 7.5 2D IR spectrum and diagonal slice of unlabeled hIAPP mixed with Ala-13 labeled pramlintide. Spectrum was collected 24 h after initiation of fiber formation by addition of phosphate buffer. The mixture has formed β-sheets, but Ala-13 is not coupled, as shown by the lack of coupled isotope label peak at low frequencies.

peak at low frequency. This result suggests that the mixture forms a fiber structure with β-sheets, but coupling is broken at Ala-13 (Figure 1.4b). This is probably due to the hIAPP and pramlintide monomers folding together such that Ala-13 labeled pramlintide intercalates into the fiber structure, breaking the coupling at Ala-13.

One additional experiment has been performed, measuring the kinetics of pramlintide under the conditions at which it is administered to diabetics. The typical dosage is 60 μg (~150 μM) and pramlintide is stored in pH 4 acetic acid solution. Once pramlintide is injected into a diabetic, it diffuses throughout the body, but it is important that it hasn't aggregated before injection. We find that under storage conditions, pramlintide folds, but on the very slow timescale. Spectra were collected immediately after fiber initiation by addition of buffer, 12 h after initiation and 36 h after initiation (Figure 7.6). 2D IR spectra and diagonal slices collected at various time points in the folding process show that pramlintide may pass through an α-helical intermediate on the way to fiber formation. At t=0 h, the sample is predominately random coil, as evidenced by the broad peak at 1652 cm^{-1}. After 12 h, the peak narrows, suggesting a new structure has formed, possibly an α-helix. Thirty-seven hours after fiber initiation, the spectrum has a narrow peak at 1620 cm^{-1}, indicating the presence of a β-sheet.

7.2.3 Future experiment: Presence of C-terminal β-sheets in pramlintide

To date, no experiments have shown that pramlintide aggregates. To ensure that the β-sheet signal in Figure 7.1d is due to both N and C-terminal β-sheets in pramlintide, an amino acid on the C-terminus of pramlintide should be isotope labeled. If, when pramlintide aggregates, the isotope label is strongly coupled, we can conclude that the C-

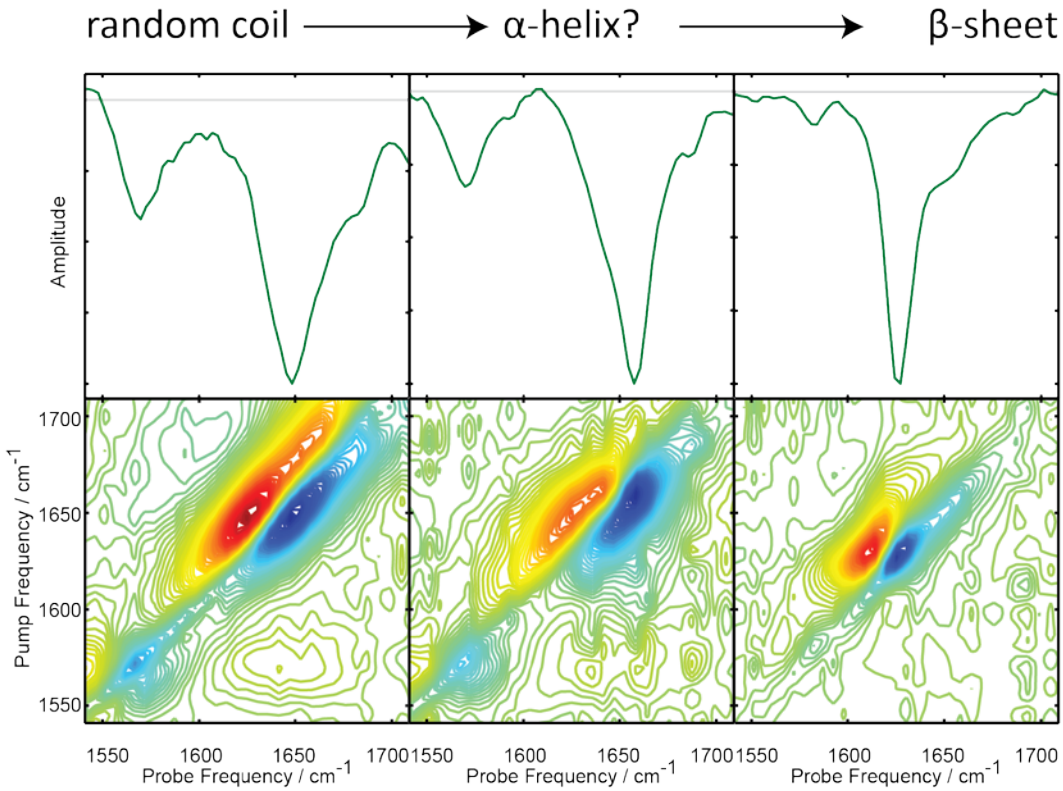

Figure 7.6 2D IR spectra and diagonal slices of unlabeled pramlintide measured in pH 4 acetate buffer. Immediately after addition of buffer to pramlintide, the peptide is random coil. The low frequency peak in the random coil spectrum is due to the buffer. After 12 h, the amide I mode shifts to slightly higher frequency, and the band narrows. This suggests that the peptide might be passing through an α-helix intermediate. After 36 h, the amide I band shifts to lower frequency, and the band narrows, suggesting that under acidic conditions, unlabeled pramlintide folds into β-sheets.

terminus of pramlintide forms β-sheets, just as Ala-13 showed that the N-terminus of pramlintide forms β-sheets. Further hIAPP and pramlintide mixing experiments should be performed to determine the composition and structure of the fibers formed in Figures 7.3, 7.4, and 7.5.

7.3 Use hydrogen-deuterium exchange experiments to explore the interactions between human and rat amylin

HDX experiments have been shown to be useful for studying the structure of a soluble, membrane, and amyloid peptides and proteins.[13-16] The rate at which the amide hydrogen atom exchanges for a deuterium atom is a good metric for determining the solvent exposure or secondary structure at that residue.[17-20] HDX experiments have been used to identify oligomeric species in the folding mechanism for a similar amyloidogenic peptide, Aβ.[21] More recently, a HDX experiment, using NMR spectroscopy, was performed on hIAPP fibers aiming to identify the amino acids involved in β-sheets in the final fiber structure.[22] The measured protection factors match reasonably well with previously calculated 2D IR diagonal lineshapes for amylin fibers, calculated from an MD simulation based on the solid state NMR structure of amylin fibers.[1,22,23]

7.3.1 Future experiment: HDX experiment of labeled hIAPP and rIAPP

One HDX experiment that I wanted to accomplish during graduate school involved mixing isotope labeled hIAPP with rIAPP. Previously, it was shown that 8 h after hIAPP and rIAPP are mixed, rIAPP disrupts the N-terminus β-sheets in hIAPP fibers, but the C-terminus β-sheet remains intact.[4] At 24 h after mixing, the hIAPP fibers

remain intact and rIAPP actually forms its own fibers, possibly on the outside of the hIAPP fibers.[4]

To test the hypothesis that after 24 hours rIAPP forms fibers on the outside of hIAPP fibers, a straightforward HDX experiment could be performed. By measuring 2D IR spectra of Ala-13 and Ile-26 labeled hIAPP, the cross peaks between the amide II/Ala-13 and amide II/Ile-26 modes could be monitored as a function of time after adding H_2O to fibers formed in D_2O. The amide II mode would increase intensity with time, and the cross peak between the isotope label and amide II mode would report on the exchange rate of the hydrogen atom for a deuterium atom in the amide position. The exchange rate for Ala-13 would be expected to be much faster than that of Ile-26, and it has been shown that Ile-26 exchanges ~5 times slower than Ala-13.[22] The next experiment is to mix Ala-13 and Ile-26 labeled hIAPP with rIAPP in D_2O. After 8 h, rIAPP should have disrupted the N-terminus, and Ala-13 would no longer reside in a β-sheet. Conversely, rIAPP should not have disrupted the C-terminus, and Ile-26 would remain in an intact β-sheet. After 24 h, both Ala-13 and Ile-26 should be coupled, as it has been suggested that 24 h after hIAPP and rIAPP are mixed, the hIAPP fibers are intact and rIAPP forms fibers outside the hIAPP fibers.[4] At 24 h after mixing, H_2O could be added to the sample, and the HDX rate could be measured. If rIAPP truly forms its own fibers on the outside of hIAPP fibers, the HDX exchange rate for N-terminal Ala-13 should slow dramatically. Residues on the C-terminus of hIAPP, that lie protected in the hydrophobic center of the fiber have much slower exchange rates, while residues on the N-terminus exchange much faster, some almost immediately.[22] Assuming that rIAPP forms fibers outside the hIAPP

fibers, all N-terminal amino acids in hIAPP would become protected, and their exchange rate would slow. Quantifying the exchange rates throughout several residues on the N-terminus of hIAPP would provide a picture of where rIAPP fibers form.

7.4 References

(1) Luca, S.; Yau, W.-M.; Leapman, R.; Tycko, R. *Biochemistry* **2007**, *46*, 13505-13522.

(2) Shim, S.-H.; Gupta, R.; Ling, Y. L.; Strasfeld, D. B.; Raleigh, D. P.; Zanni, M. T. *Proceedings of the National Academy of Sciences* **2009**, *106*, 6614-6619.

(3) Fändrich, M. *J. Mol. Biol.* **2012**, *421*, 427-440.

(4) Middleton, C. T.; Marek, P.; Cao, P.; Chiu, C.-c.; Singh, S.; Woys, A. M.; de Pablo, J. J.; Raleigh, D. P.; Zanni, M. T. *Nat Chem* **2012**, *advance online publication*.

(5) Reddy, A. S.; Wang, L.; Lin, Y.-S.; Ling, Y.; Chopra, M.; Zanni, M. T.; Skinner, J. L.; De Pablo, J. J. *Biophys. J.* **2010**, *98*, 443-451.

(6) Ling, Y. L.; Strasfeld, D. B.; Shim, S.-H.; Raleigh, D. P.; Zanni, M. T. *The Journal of Physical Chemistry B* **2009**, *113*, 2498-2505.

(7) Knight, J. D.; Hebda, J. A.; Miranker, A. D. *Biochemistry* **2006**, *45*, 9496-9508.

(8) Hekman, C.; DeMond, W.; Dixit, T.; Mauch, S.; Nuechterlein, M.; Stepanenko, A.; Williams, J. D.; Ye, M. *Pharm. Res.* **1998**, *15*, 650-658.

(9) Hekman, C. M.; DeMond, W. S.; Kelley, P. J.; Mauch, S. F.; Williams, J. D. *J. Pharm. Biomed. Anal.* **1999**, *20*, 763-772.

(10) Hollander, P. A.; Levy, P.; Fineman, M. S.; Maggs, D. G.; Shen, L. Z.; Strobel, S. A.; Weyer, C.; Kolterman, O. G. *Diabetes Care* **2003**, *26*, 784-790.

(11) Day, C. *The British Journal of Diabetes & Vascular Disease* **2005**, *5*, 151-154.

(12) Cort, J. R.; Liu, Z.; Lee, G. M.; Huggins, K. N. L.; Janes, S.; Prickett, K.; Andersen, N. H. *Protein Engineering Design and Selection* **2009**, *22*, 497-513.

(13) Cotten, M.; Fu, R.; Cross, T. A. *Biophys. J.* **1999**, *76*, 1179-1189.

(14) Hoshino, M.; Katou, H.; Yamaguchi, K.-i.; Goto, Y. *Biochimica et Biophysica Acta (BBA) - Biomembranes* **2007**, *1768*, 1886-1899.

(15) Carulla, N. l.; Zhou, M.; Giralt, E.; Robinson, C. V.; Dobson, C. M. *Acc. Chem. Res.* **2010**, *43*, 1072-1079.

(16) DeFlores, L. P.; Tokmakoff, A. *J. Am. Chem. Soc.* **2006**, *128*, 16520-16521.

(17) Englander, S. W.; Krishna, M. M. G. *Nat. Struct. Mol. Biol.* **2001**, *8*, 741-742.

(18) Englander, S. W.; Mayne, L. *Annu. Rev. Biophys. Biomol. Struct.* **1992**, *21*, 243-265.

(19) Englander, S. W.; Sosnick, T. R.; Englander, J. J.; Mayne, L. *Curr. Opin. Struct. Biol.* **1996**, *6*, 18-23.

(20) Krishna, M. M. G.; Hoang, L.; Lin, Y.; Englander, S. W. *Methods* **2004**, *34*, 51-64.

(21) Zhang, A.; Qi, W.; Good, T. A.; Fernandez, E. J. *Biophys. J.* **2009**, *96*, 1091-1104.

(22) Alexandrescu, A. T. *PLoS One* **2013**, *8*, e56467.

(23) Wang, L.; Middleton, C. T.; Singh, S.; Reddy, A. S.; Woys, A. M.; Strasfeld, D. B.; Marek, P.; Raleigh, D. P.; de Pablo, J. J.; Zanni, M. T.; Skinner, J. L. *J. Am. Chem. Soc.* **2011**, *133*, 16062-16071.

APPENDIX 1

Supporting Information for Chapter 2 Experimental Methods: Tips and Tricks-Alignment of the Wyvern

Since the Wyvern oscillator and regenerative amplifier (regen) were prototypes, they did not come with instruction manuals, alignment procedures, or troubleshooting guides. Therefore, much time was spent trying to figure out how to best align the optics in this system. Although an instruction manual was eventually written for this laser, I am including some details below.

Shown in Figure A1.1 is the beam path of the light through the oscillator, stretcher, regen, and compressor. This diagram is not strictly correct, as the Millennia is now housed outside the laser box and the Faraday Isolator (EOT) has been moved to be located near the Ti:Sapphire crystal. Nonetheless, Figure A1.1 is a fairly accurate

diagram of the beam path. Figure A1.2 shows the labeling scheme for every optic in the laser system.

Two parts of the Wyvern system that needed the most attention in terms of realignment were the stretcher and regen. While the oscillator consistently lost mode-lock because of temperature fluctuations, the optics were fairly simple to align and the alignment procedure was

similar to that on the Black table (the homebuilt oscillator). The stretcher and regen beam paths, however, were unique to the Zanni group, and thus it was important to develop a method to aligning these optics.

Shown in Figure A1.3a is the beam path through the stretcher with the optics labeled. The beam path from the oscillator is S-SM1 to S-SM2 to S-L to S-I1 to S-SM3 to S-SM4 to S-G to S-M1 to S-M2 to S-M1 to S-G to S-M3and then reversed. Some important notes are that the grating (S-G) should never be translated and its angle should never be adjusted. In addition, unlike other stretchers, the beams are generally not centered on the optics. It is nearly impossible to eliminate all clipping, particularly on S-M2. This is normal; do not try to center the beams and do not worry about minor clipping on S-M2.

Figure A1.3b shows the faces of S-G (grating), S-M1 (curved mirror), S-M2 (folding mirror), and S-M3 (retroreflector). The red spots on the optics show what the stretched beam should look like upon each reflection starting when the beam first hits S-G (grating) and continuing through the optics and retroreflections. The instructions for detailed alignment are as follows:

1. Use S-SM1 and S-SM2 to center the beam on S-L and S-I1. The beam should be centered horizontally on mirror S-SM3, but offset vertically to hit near the top edge.

2. Use S-SM3 to center the beam horizontally on mirror S-SM4, but again offset vertically towards the top edge. The beam should just pass over the corner of grating S-G with as little clipping as possible.

3. To temporarily reduce the number of beams and facilitate alignment, place a card in front of the folding mirror S-M2.

4. Using the diagrams above as a guide, adjust S-SM4, S-G, and S-M1 sequentially to get spots 1-3.

5. Move card from S-M2 to the retroreflector S-M3, ensuring that the edge of the card does not rise above the edge of mirror.

6. Adjust S-M2 to get spots 4-5.

7. Remove card from S-M3 and tweak S-M2 further so that spot 6 hits as high on the retroreflector S-SM3 as possible with minimal clipping.

8. Adjust S-M3 to get align spots 7-11.

When properly aligned, the beam should exit the stretcher on roughly the same path on which it entered. The beams should generally pass just over other optics without clipping. The stretcher output should have a slight downward tilt that allows it to be picked off by PP-SM1.

Figure A1.4 shows the beam path and optics labels for the regen. The regen has several unique optics that should first be described. PP-PC is a pockels cell that acts as a

half-waveplate when on. A-W1 is a half-waveplate that rotates the seed bean (light from the oscillator) by 90°. Rotating this waveplate by 45° rotates the polarization of the light by 90°. A-TFP is a thin film polarizer that transmits horizontally polarized light and reflects vertically polarized light. A-W2 is a quarter-waveplate. This optic with rotate linearly polarized light to circularly polarized light and vice-versa. Again, when set to 45°, this waveplate rotates the polarization of light; when set to 0°, the polarization does not change. A-PC is another pockels cell that acts as a quarter-waveplate when on.

The seed, coming from the oscillator is horizontally polarized after exiting the stretcher. PP-PC is the first pockels cell and it selects a single pulse to enter the regen to be amplified. The selected pulse passes through PP-PC, is rotated to vertically polarized light, and then is rotated back to horizontally polarized light by A-W1. All other pulses are transmitted through the pockels cell as horizontally polarized light and rotated by A-W1 to vertically polarized light. Then, the selected pulse is transmitted through A-TFP because it is horizontally polarized, while the vertically polarized light is rejected and reflected to the wall of the laser box. The selected pulse then passes through A-W2 and converted to circularly polarized light, passes through A-PC while it is off, reflects off A-CM1, passes through A-PC while it is off again, then back through A-W2 to be converted to vertically polarized light. Then, the light comes to A-TFP and is now reflected off the thin film polarizer because it is vertically polarized.

Now, the seed is set to be overlapped with the beam from the pump laser. A-PC traps a pulse in the cavity by turning on (this timing is controlled by the computer and can be changed for maximum power). The vertically polarized light in the cavity is

reflected off A-TFP and through A-W2 to become circularly polarized. The pulse then passes through an on A-PC which converts the polarization to horizontal. The light reflects off A-CM1, then back through A-PC, where is becomes circularly polarized. The light then passes through A-W2 and becomes vertically polarized. Again, the pulse reflects off A-TFP and back to the regen cavity where it passes through the cryogenically cooled Ti:Sapphire crystal. The polarizations of light in the regen can be very confusing. However, knowing these polarizations is very helpful in determining where beams are becoming misaligned or where power is being lost.

The overall beam path from the pump (Empower laser) is as follows: AP-L1 to AP-P1 to AP-SM1 to AP-L2 to A-CM7 to A-I4 to A-CM5 to A-CM6 to A-CM5 to A-CM4 to A-CM3 to A-CM2 to A-TFP to A-W2 to A-PC to A-CM1 to A-PC to A-W2 to A-TFP to A-SM2 to A-I2 to A-I1 to A-SM1 to PP-PC. To align and optimize the regen cavity when there is already some lasing, perform the following steps:

1. Ensure the pump beam is roughly centered on AP-L1 and AP-P1. Use AP-SM1 to center the beams on two irises, I4 and A-I3.

2. Block the seed beam and place a power meter between A-I1 and A-I2, facing A-I2. Rotate A-W2 by 45°.

3. Tweak the cavity end mirrors, A-CM1 and A-CM9 to optimize the power. Use only small adjustments. The mounts on these optics are very nice, but the power is very sensitive to small changes in alignment. Go slow.

4. Remove the power meter and rotated A-W2 back to 0°. Further small adjustments to A-CM1 and A-CM9 can be made if thought necessary.

There may be times in which the laser is not lasing. In that case, the following directions should be followed:

1. Turn the Empower down to ~12 A. Do not increase this power above 15 A. Doing so puts the optics in danger of burning.

2. Rotate A-W2 to 0° to defeat A-PC, which should remain off.

3. Place a card in from of A-I2 and scan the pump beam around the cryo-cell with AP-SM1. Watch for a flash of red on the card, which indicates the regen cavity is lasing.

4. Once there is a stable spot on the card, optimize the cavity, as described above.

Occasionally, the entire cavity may need realigned. It is best to align the cavity using the seed beam, as it is small and not too divergent. Follow these instructions:

1. Use PP-SM2 and PP-SM3 to center the seed on irises A-I1 and A-I2, respectively.

2. Rotate A-W1 to 0° so the seed can reach A-CM1. The spot should be in the bottom left corner of the mirror. It will not be centered. Do not be alarmed.

3. Look between A-I1 and A-I2 for the back reflection. Use A-CM1 to overlap the reflection with the incoming beam.

4. Rotate A-W2 to 45° to minimize the back reflection and direct the seed into the cavity.

5. Use A-CM4 and A-CM5 to center the seed on irises A-I3 and A-I4, respectively. Make passing through the cryo-cell level and parallel to the table. (As the beam passes from A-CM5 to A-I3, there will be some clipping on A-CM6 which should be minimized as much as possible)

6. Block the beam with a black beam block in front of A-CM9 and look at the image of the scatter on the camera. It should be very weak. Move A-CM5 slightly to make sure the scatter spot is the correct one; there can be false images.

7. Turn on the pump. Use AP-SM1 to roughly align the pump with the seed (vertical alignment won't be perfect).

8. Turn off the pump and unblock A-CM9. Use A-CM9 to overlap the back reflection of the seed with the incoming beam.

9. To check the overall alignment of the two arms of the cavity, place a card in front of C-SM1. Rotate A-W2 to 0° and there should be a spot on the card reflected from the arm with end mirror A-CM1. Rotate A-W2 to 45° and there should be a spot on the card reflected from A-CM9. If the cavity is properly aligned, the two spots should overlap.

10. Rotate A-W2 back to 0° and turn on the pump laser to ~12 A (no higher than 15 A). Look for lasing.

11. Use the instructions above to optimize the alignment of the cavity.

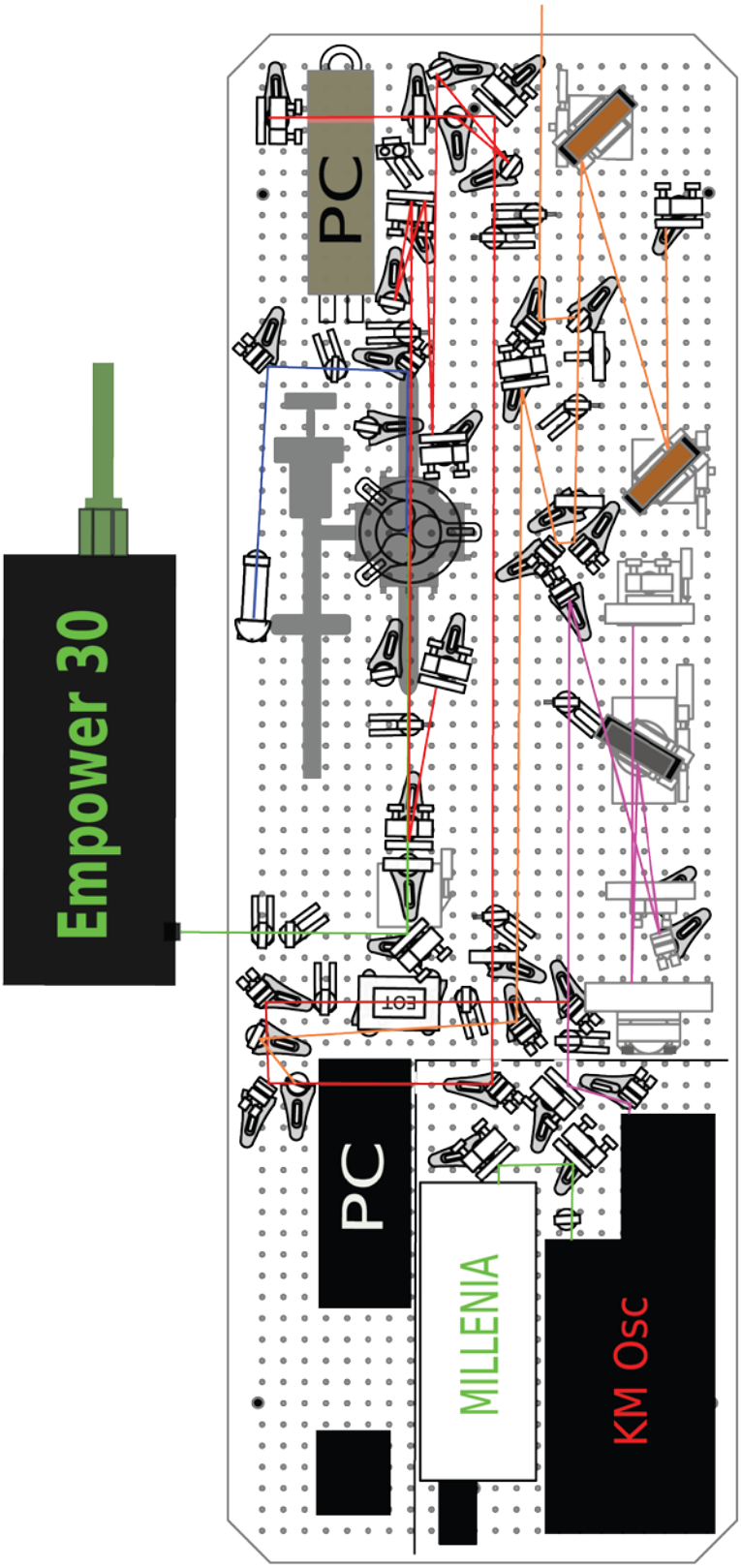
PC
Empower 30
PC
MILLENIA
KM Osc

Figure A1.1 Beam path of the stretcher (purple), regenerative amplifier (red), compressor (orange), and regen pump (green). The Millennia laser that pumps the KM oscillator is now located outside the laser box. The Empower 30 pumps the regen. The two boxes labeled PC are the two pockels cells.

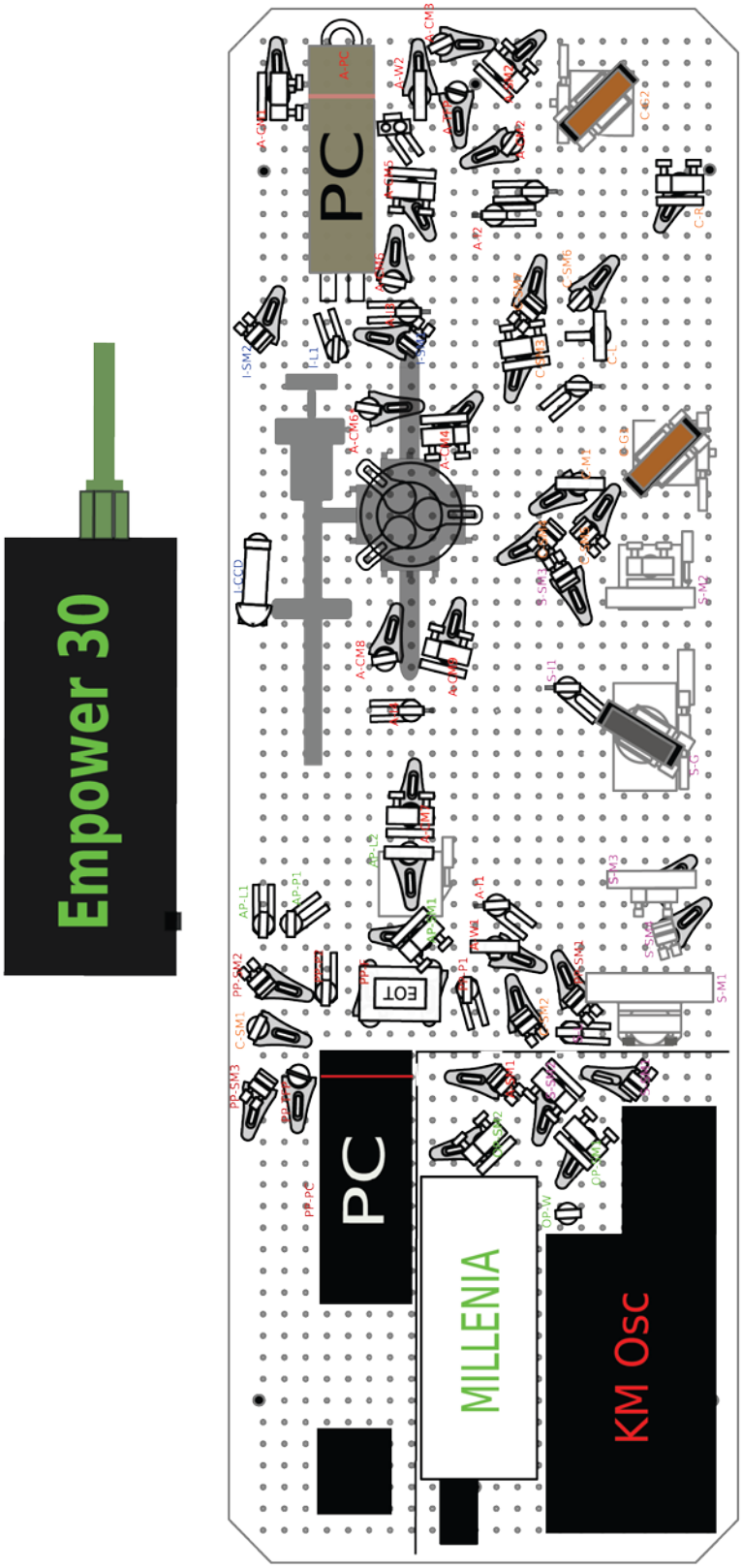
Empower 30
PC
PC
MILLENIA
KM Osc
EOT

Figure A1.2 Labeling scheme for every optic in the Wyvern setup.

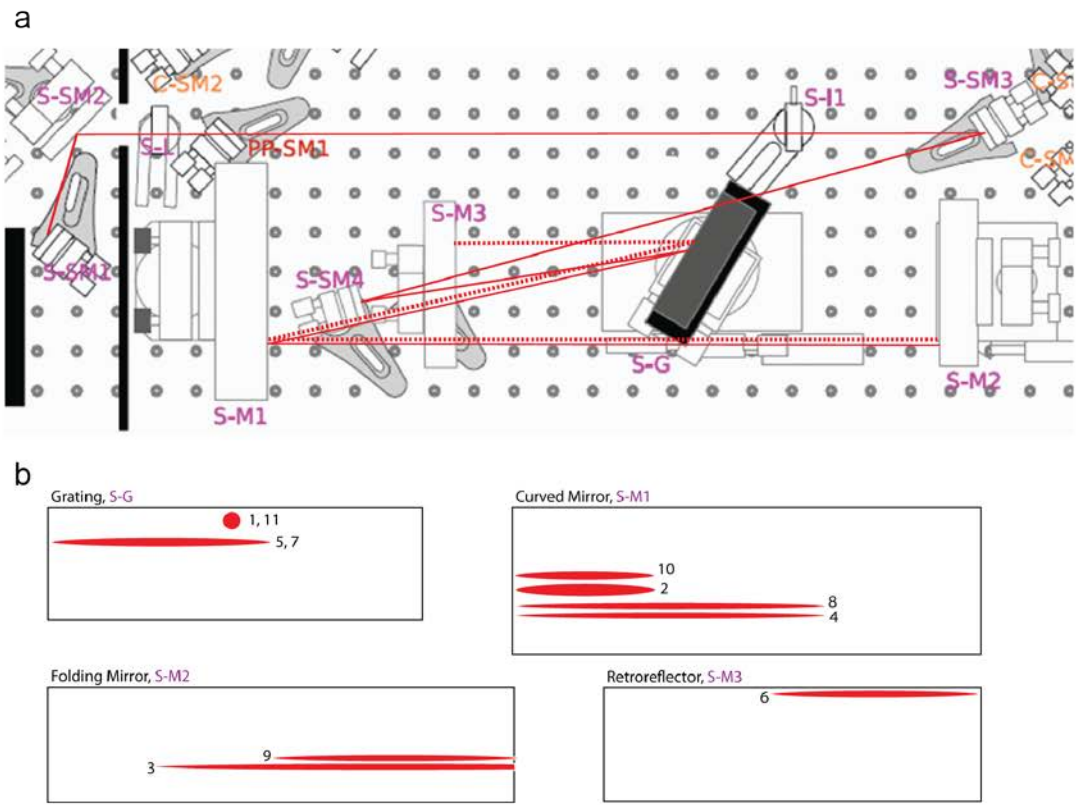

Figure A1.3 (a) Beam path and optics labeles for the optics in the stretcher. (b) Faces of the grating (S-G), curved mirror (S-M1), folding mirror (S-M2), and retroreflector (S-M3) in the stretcher. The red spots are representations of the size, shape, and location of each spot on those optics when the stretcher is properly aligned. The spots are labeled numerically, in the order in which the spots are created. A full description of the alignment procedure is in the text.

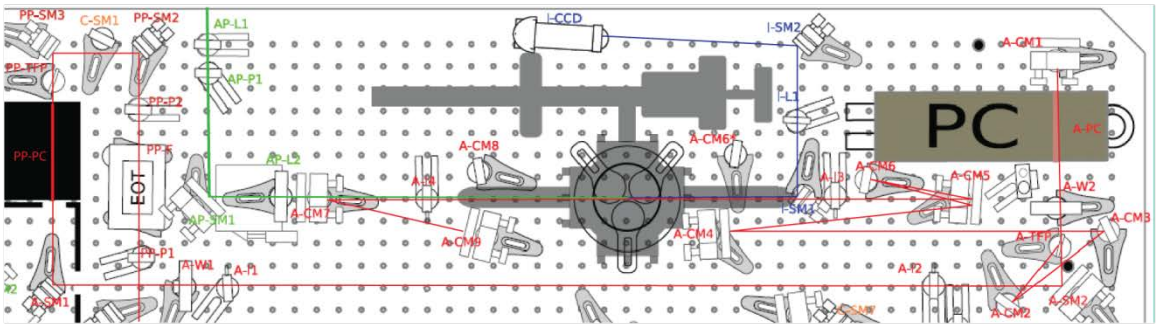

Figure A1.4 Beam path and optics labels of the seed alignment through PP-PC (pockels cell #1), and the regen alighment. A full description of the alignment procedure is in the text.

APPENDIX 2

Supporting Information for Chapter 3

Deamidation Accelerates Amyloid Formation and Alters Amylin Fiber Structure

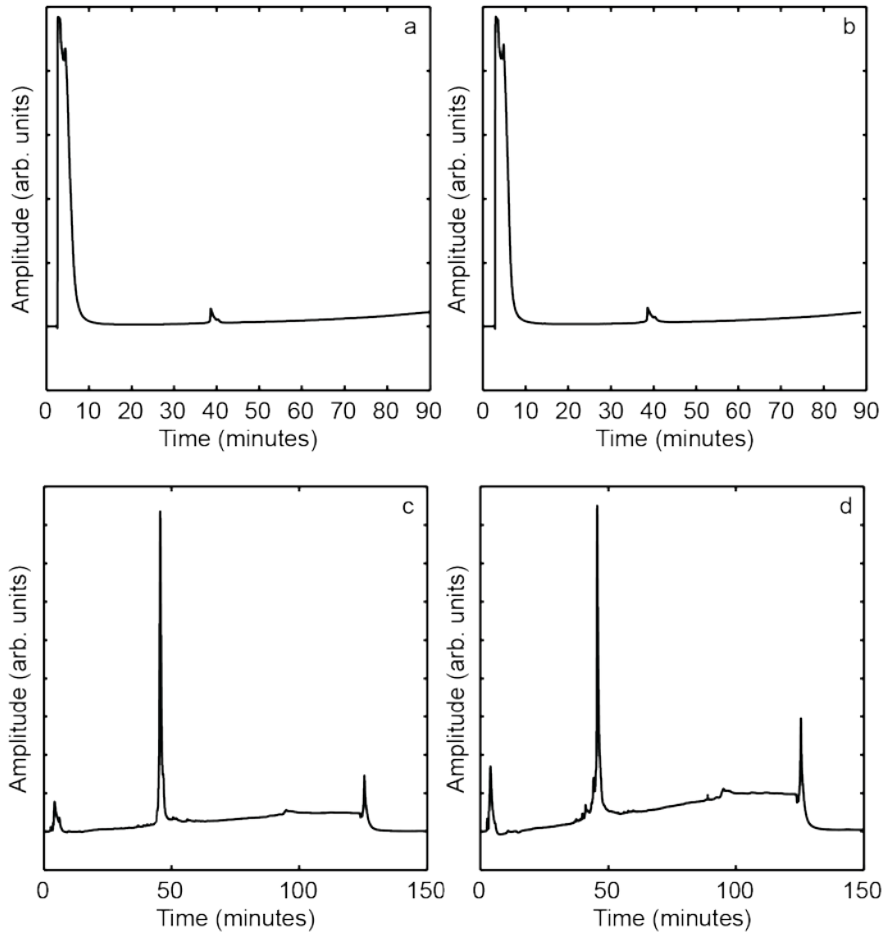

Figure A2.1 HPLC chromatograms of deamidated peptides. (a) Ala-8. (b) Ala-13. (c) Leu-16. (d) Leu-27.

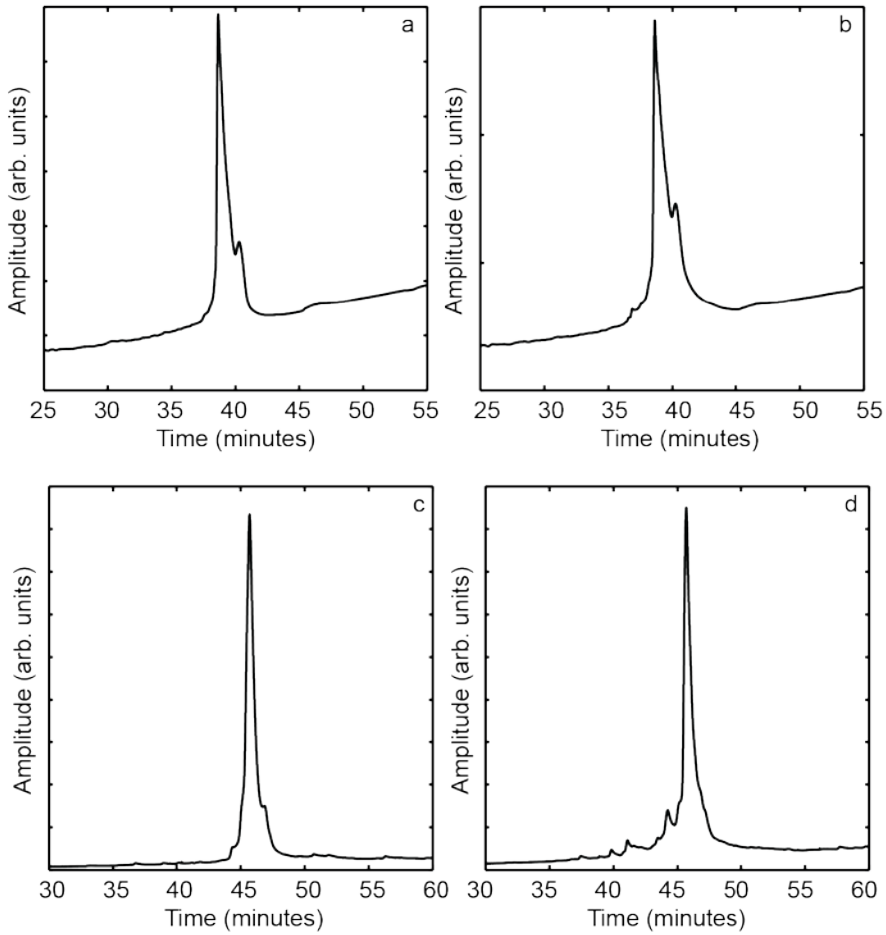

Figure A2.2 Enlarged HPLC chromatograms of deamidated peptides. (a) Ala-8. (b) Ala-13. (c) Leu-16. (d) Leu-27.

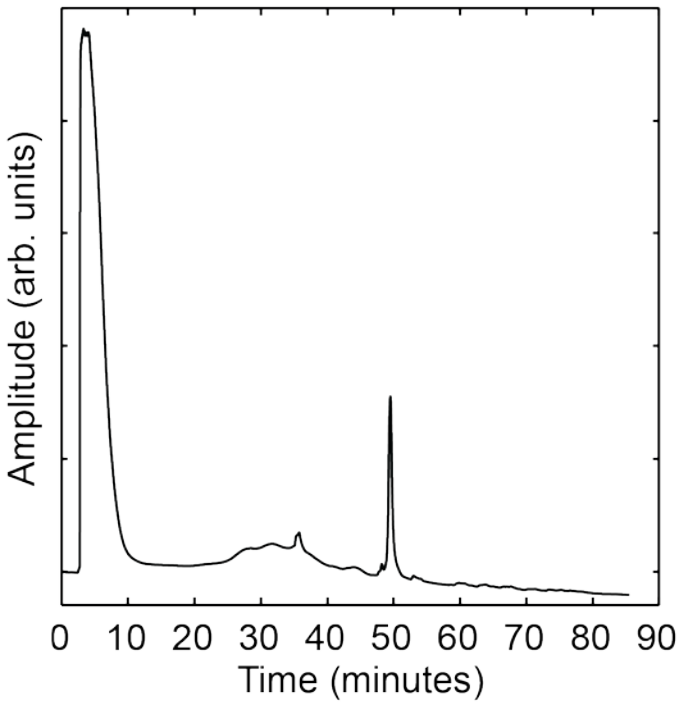

Figure A2.3 HPLC chromatogram of deamidated Ala-13 purified using buffers at pH 5.

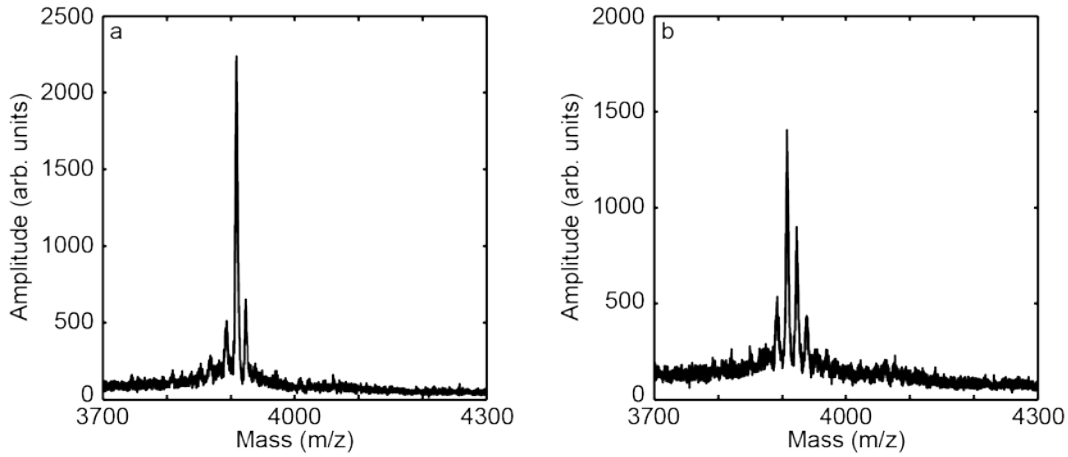

Figure A2.4 (a) MALDI-MS spectrum after 1 hour of the methyl esterification reaction. The ratio of the methylated hIAPP peak to the native hIAPP peak is 0.29. (b) MALDI-MS spectrum after 3 hours of the methyl esterification reaction. The ratio of the methylated hIAPP peak to the native hIAPP peak is 0.64.

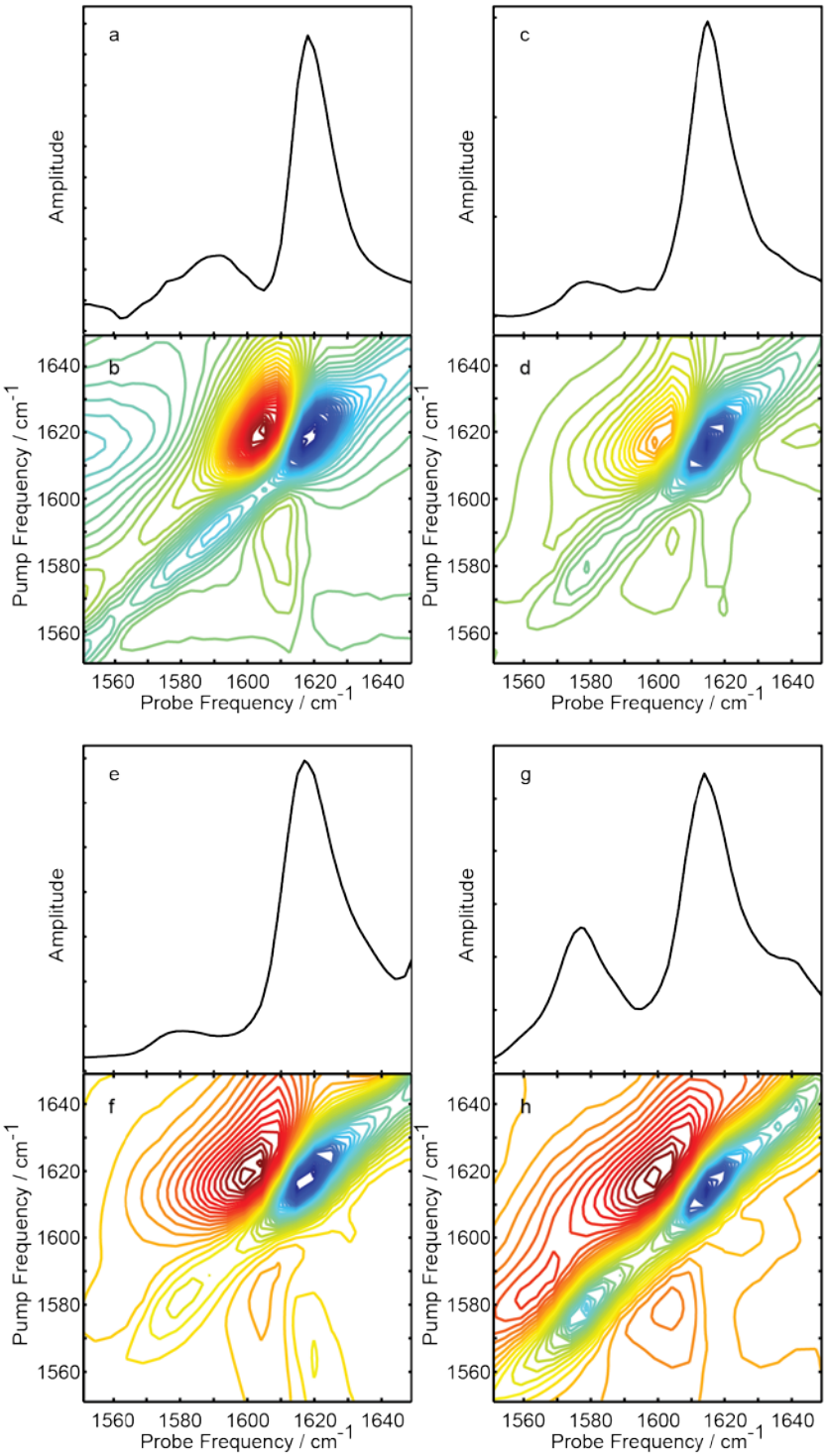

Figure A2.5 2D IR spectra and diagonal slices of unmodified peptides. (a) and (b) Ala-8. (c) and (d) Ala-13. (e) and (f). Leu-16. (g) and (h) Leu-27.

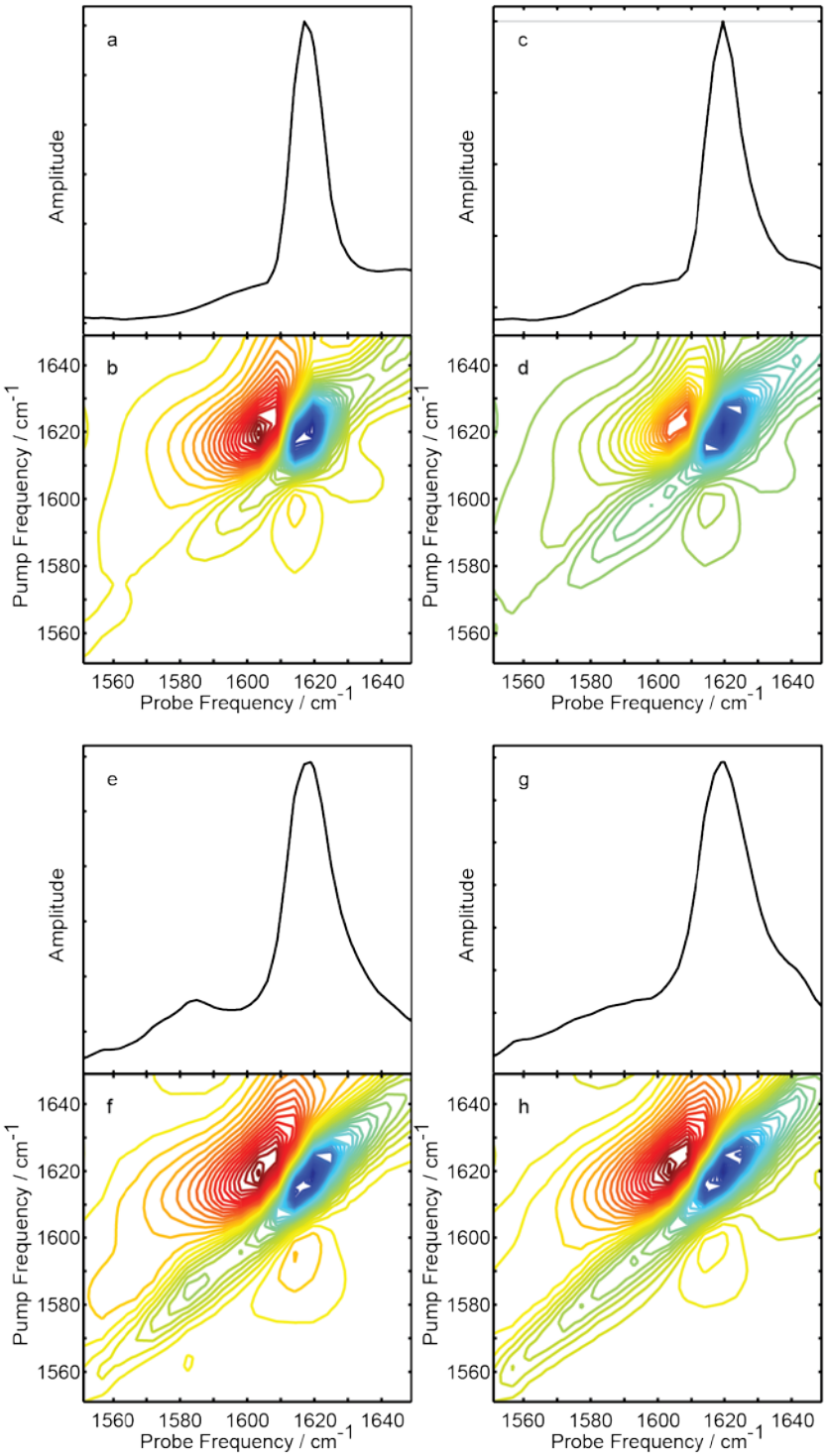

Figure A2.6 2D IR spectra and diagonal slices of deamidated peptides. (a) and (b) Ala-8. (c) and (d) Ala-13. (e) and (f). Leu-16. (g) and (h) Leu-27.

APPENDIX 3

Supporting Information for Chapter 4

Infrared Spectroscopy Provides Extended Vibrational Modes that Reveal Secondary Structures of Amyloid Proteins

The following step-by-step instructions are meant as a guide for calculating the transition dipole moment for peptides and proteins.

1. Measure a 1D and 2D IR spectrum of the sample of interest, in this case hIAPP fibers or rIAPP in solution, micelles, or membranes, the buffer, in this case deuterated potassium phosphate buffer, and a calibrant molecule, in this case L-serine.

2. Acquire the voltage (1D spectrum) of V_{sample} and V_{buffer} (Figure A3.1), using an array detector. Shown in Figure A3.1 are the voltage spectra for rIAPP in solution (blue) and buffer (magenta). Acquire the voltage of the calibrant molecule as well, $V_{calibrant}$ (green).

3. Calculate the optical density (*OD*) of the sample according to the equation:

$$OD = -log\left(\frac{V_{sample}}{V_{buffer}}\right) \quad \text{(A3.1)}$$

The new *OD* spectrum will likely have a distorted baseline, and could look like the spectrum shown in Figure A3.2 of rIAPP in solution (blue). Also, calculate the *OD* of the calibrant molecule, replacing V_{sample} with $V_{calibrant}$ Equation A3.1.

4. Subtract the baseline by fitting the spectra in Figure A3.2 to a second order polynomial trendline near the frequency of the sample and the calibrant, in this case near 1650 cm^{-1} for rIAPP in solution, and near 1625 cm^{-1} for L-serine.

5. The actual absorbance spectrum of the calibrant is obtained by subtracting the trendline, and this spectrum of serine is shown in Figure A3.3. The $OD_{calibrant}$ is the maximum intensity of the absorbance spectrum.

6. Acquire the diagonal slice of the 2D IR absorptive spectrum of the calibrant. The diagonal slice through the 2D IR spectrum of serine is shown in Figure A3.4. The $\Delta OD_{calibrant}$ is measured as the maximum intensity of the diagonal slice.

7. The actual absorbance spectrum of the sample is obtained by subtracting the trendline, and this spectrum of rIAPP in solution is shown in Figure A3.5.

8. Acquire the diagonal slice of the 2D IR absorptive spectrum of the sample. The diagonal slice through the 2D IR spectrum of rIAPP in solution is shown in Figure A3.6. It is possible that there could be scatter in the diagonal slice. If so, repeat the baseline subtraction procedure of fitting a polynomial trendline to the baseline near the sample and subtracting the trendline to get the actual diagonal slice.

9. Calculate $|\mu|^2$ of the sample using the following equation:

$$|\mu|^2 = \frac{\frac{\Delta OD_{sample}}{OD_{sample}}}{\frac{\Delta OD_{calibrant}}{OD_{calibrant}}} * |\mu_{calibrant}|^2 \quad \text{(A3.2)}$$

To do this calculation, divide the spectrum from Figure A3.6 (2D IR diagonal slice, ΔOD) by the spectrum from Figure A3.5 (absorbance spectrum, OD). Then, calculate $\Delta OD_{calibrant}/OD_{calibrant}$. Divide the ratio of the two spectra by the calculated calibrant value. Last, multiply by the transition dipole strength of the calibrant that in this case is 0.20 D^2 for L-serine. The maximum value in the spectrum of $\Delta OD_{sample}/OD_{sample}$ is the transition dipole strength of the sample.

10. If the sample is purely one type of secondary structure, the procedure for measuring transition dipole strength is complete. Otherwise, if the sample contains multiple secondary structures, the structural distribution can be calculated. For instance, rIAPP in

solution is assumed to be 100% random coil, while rIAPP in membranes is at least partially α-helical. To calculate the % α-helix in the membrane sample, and the transition dipole strength of the α-helix distribution, first scale the absorbance spectrum of the solution ($OD_{solution}$) to the absorbance spectrum of the membrane ($OD_{membrane}$), as shown in Figure A3.7 and by Equation A3.3. The purely random coil (solution) spectrum should be scaled to the distributed (membrane) spectrum only at frequencies, ω, of pure random coil.

$$SF = \frac{OD_{membrane}(\omega)}{OD_{solution}(\omega)} \quad \text{(A3.3)}$$

11. The calculated scaling factor (*SF*) between the solution spectrum and membrane spectrum is a measure of the percent of the membrane spectrum that is α-helical. The scaled solution spectrum is then subtracted from the membrane spectrum, shown in Figure A3.8.

$$OD_{membrane} - SF * OD_{solution} \quad \text{(A3.4)}$$

12. The 2D IR diagonal slice of the solution spectrum is then scaled by the scaling factor calculated in step 10. The resulting scaled 2D IR diagonal slice is then normalized to $OD_{calibrant}/\Delta OD_{calibrant}$.

$$|\mu^2| = \frac{\left(\Delta OD_{membrane} * \frac{OD_{calibrant}}{\Delta OD_{calibrant}}\right) - \left(\Delta OD_{solution} * \frac{OD_{calibrant}}{\Delta OD_{calibrant}} * SF\right)}{OD_{membrane} - SF * OD_{solution}} \quad \text{(A3.5)}$$

This equation gives the new transition dipole strength of the α-helix portion of the membrane spectrum.

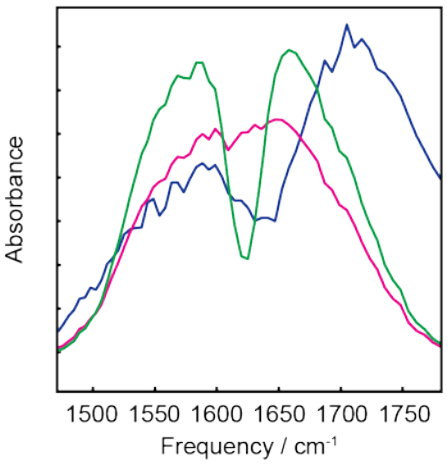

Figure A3.1 Voltage (1D spectrum) of V_{sample} (rIAPP in solution, blue), V_{buffer} (magenta), and $V_{calibrant}$ (L-serine, green). Step 2.

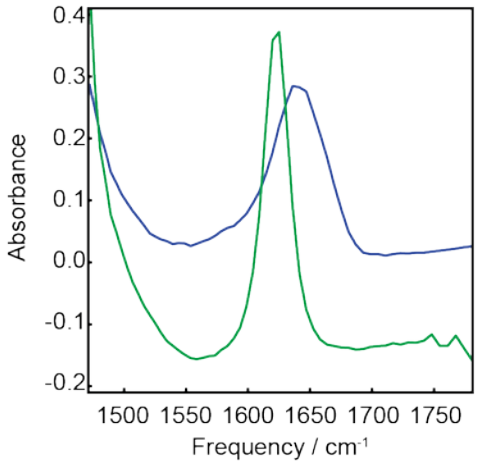

Figure A3.2 *OD* spectrum of rIAPP in solution (blue) and L-serine (green). The spectra are calculated using Equation A3.1, and may have a distorted baseline. Step 3.

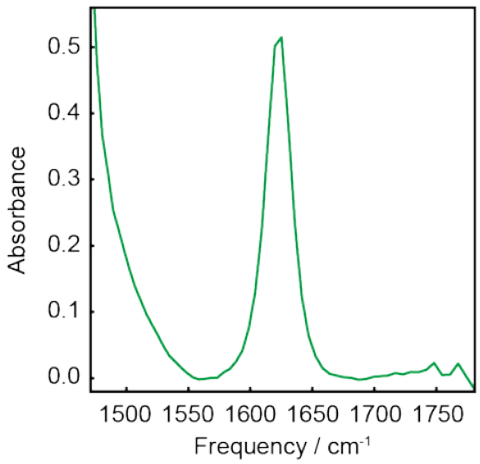

Figure A3.3 Absorbance spectrum (*OD*) of L-serine after baseline subtraction. Steps 4 and 5.

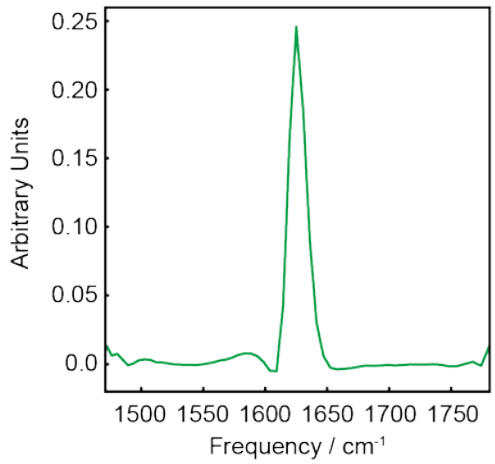

Figure A3.4 Diagonal slice through a 2D IR spectrum (ΔOD) of L-serine. Step 6.

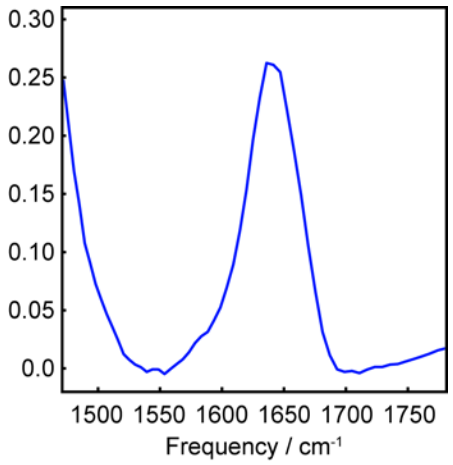

Figure A3.5 Absorbance spectrum (*OD*) of rIAPP after baseline subtraction. Steps 4 and 7.

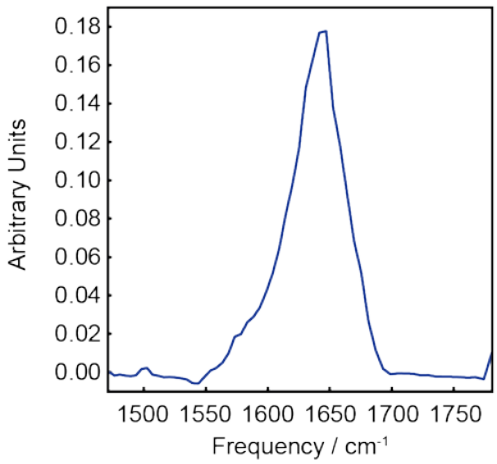

Figure A3.6 Diagonal slice through a 2D IR spectrum (ΔOD) of rIAPP. Step 8.

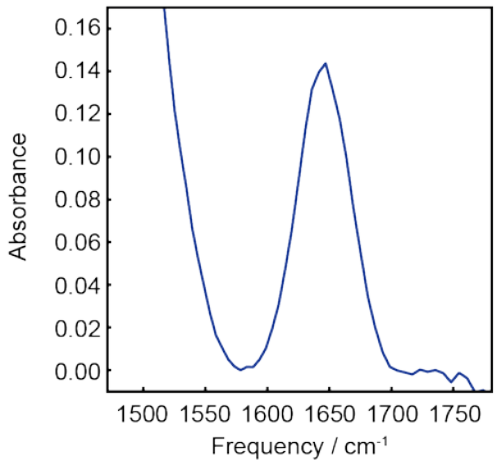

Figure A3.7 Scaled absorbance spectrum of rIAPP in solution ($OD_{solution}$) to rIAPP in membranes ($OD_{membrane}$) according to Equation A3.3. Step 10.

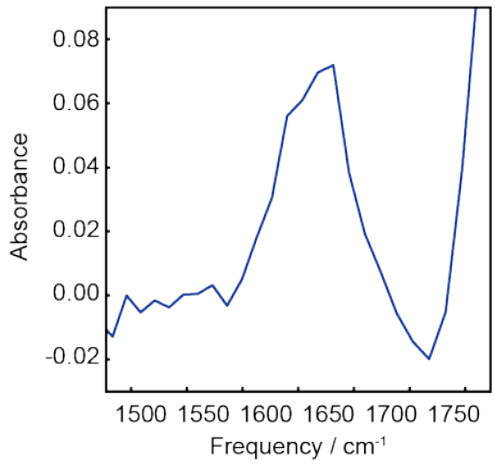

Figure A3.8 Scaled rIAPP in solution spectrum subtracted from the rIAPP in membranes spectrum, according to Equation A3.4. Step 11.

APPENDIX 4

Supporting Information for Chapter 5

Designing an Amyloid Inhibitor Based on its Aggregation Mechanism

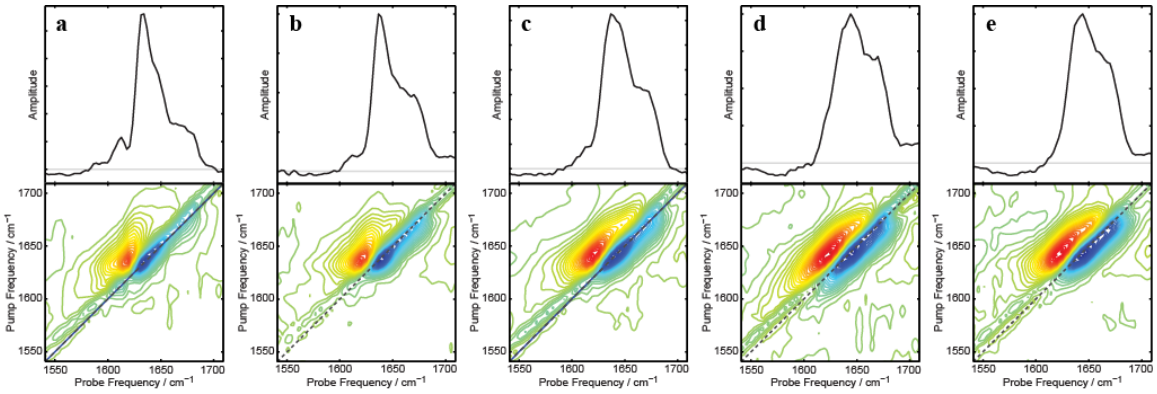

Figure A4.1 Spectra and diagonal slices of pure macrocycles. Macrocycles 1a-e (a-e).

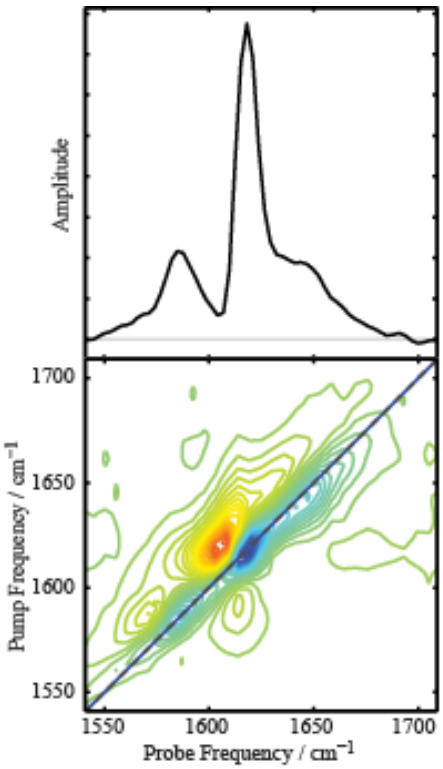

Figure A4.2 Spectra and diagonal slice of Ala-25 amylin fibers formed in 2.5% HFIP.

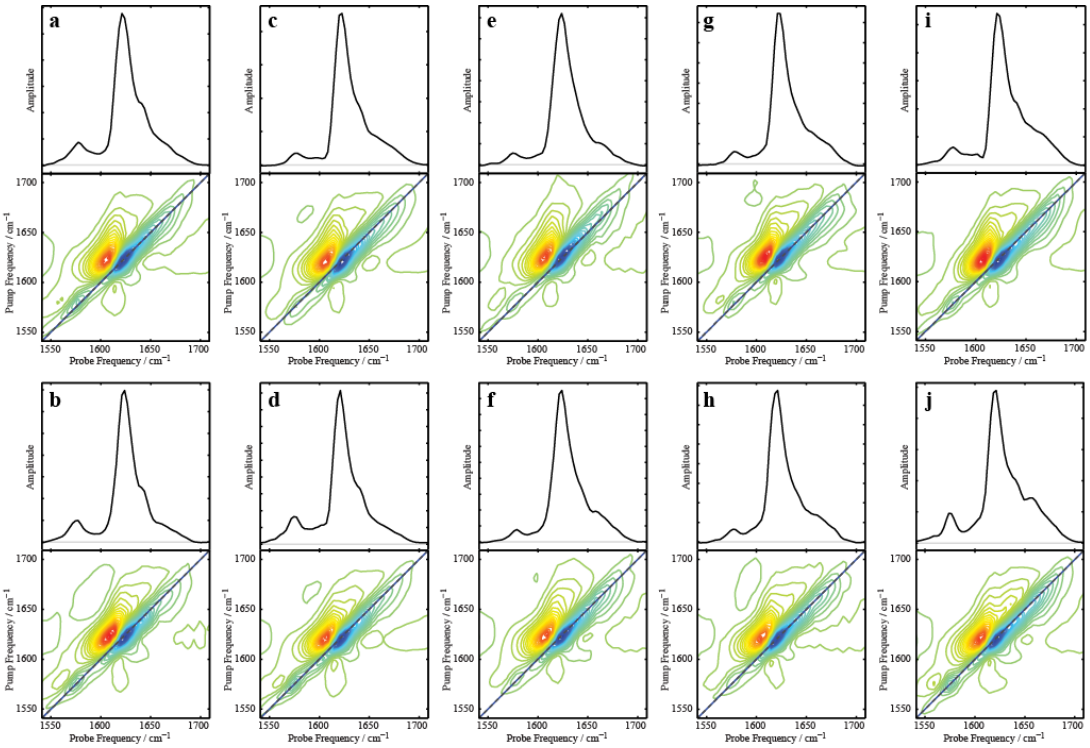

Figure A4.3 Fiber spectra and diagonal slices of Val-17 amylin mixed with macrocycles 1a-e. Spectra were collected after 5 h of aggregation for Val-17 amylin mixed with macrocycles 1a (a,b), 1b (c,d), 1c (e,f), 1d (g,h), and 1e (i,j).

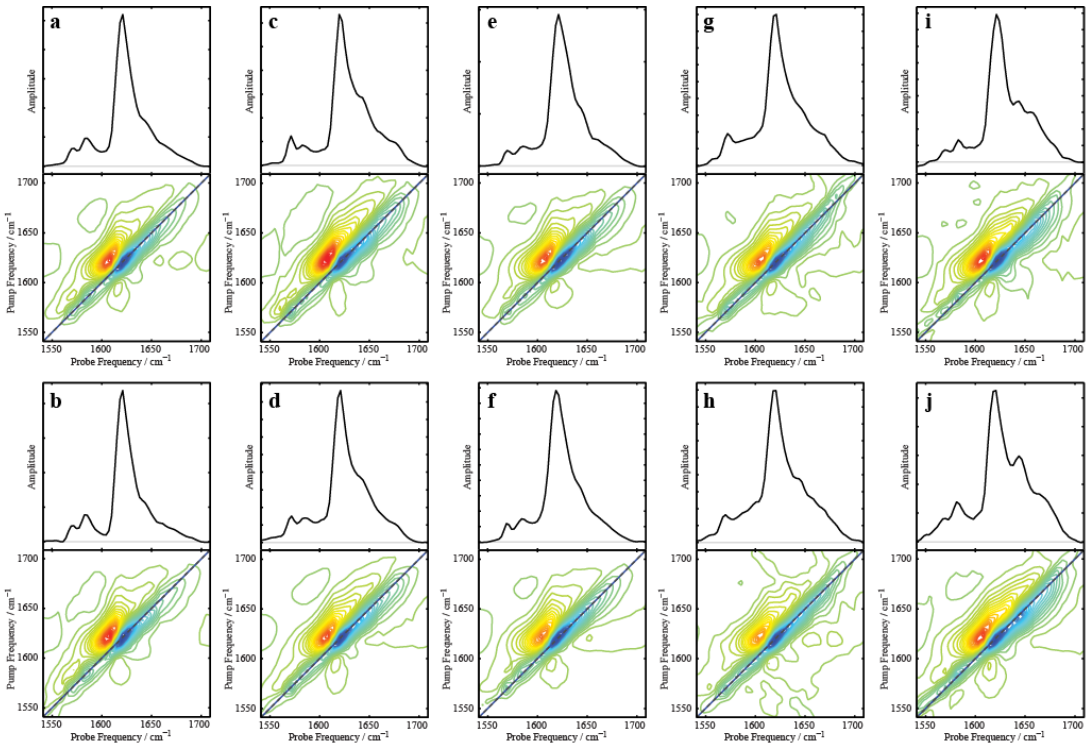

Figure A4.4 Fiber spectra and diagonal slices of Ala-25 amylin mixed with macrocycles 1a-e. Spectra were collected after 5 h of aggregation for Ala-25 amylin mixed with macrocycles 1a (a,b), 1b (c,d), 1c (e,f), 1d (g,h), and 1e (i,j).

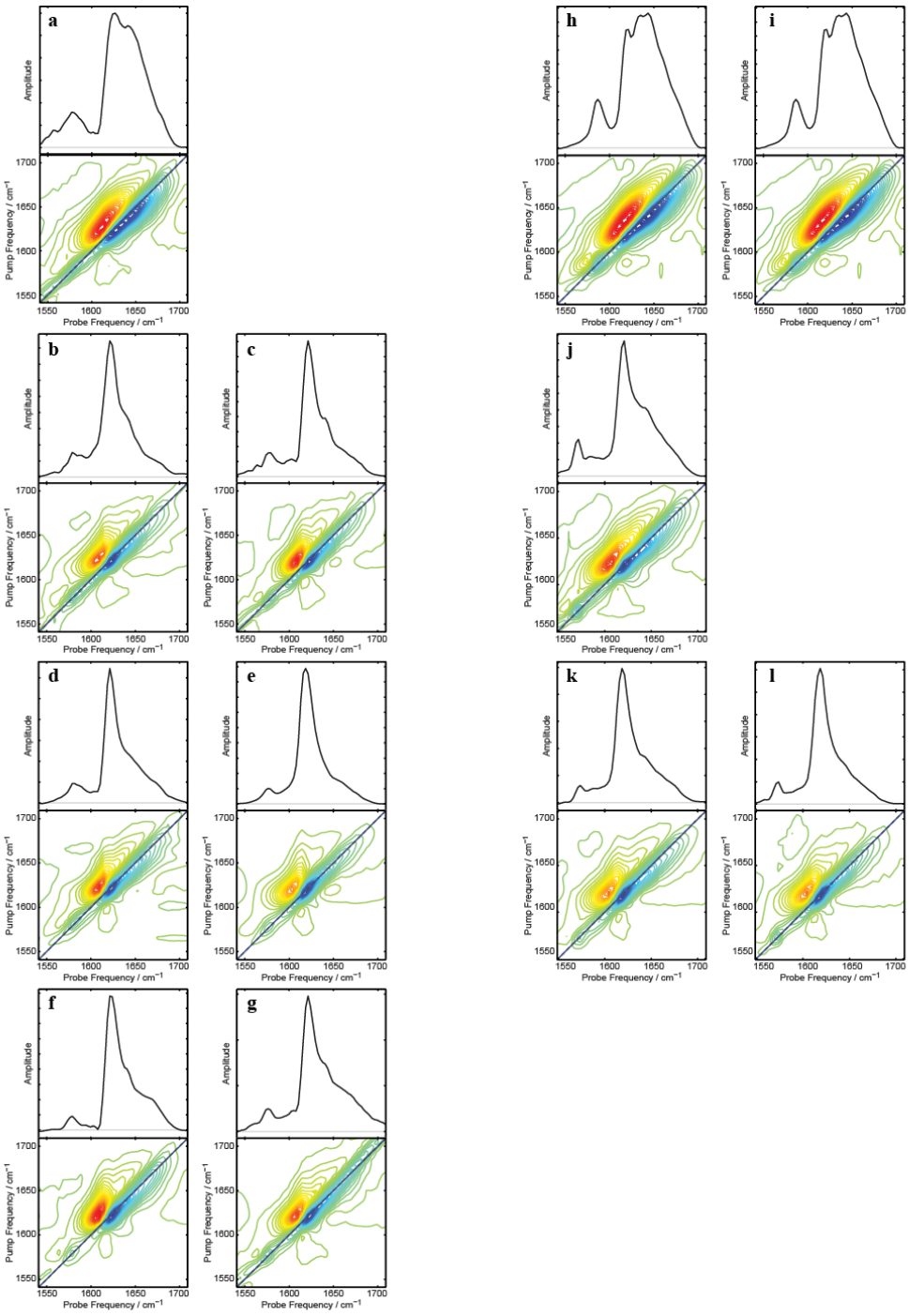

Figure A4.5 Early spectra and diagonal slices of Val-17 and Ala-25 amylin mixed with accelerating macrocycles. Spectra were collected after 20 min of Val-17 amylin mixed with macrocycles 1a (a), 1b (b,c), 1d (d,e), and 1e (f,g) and of Ala-25 amylin mixed with macrocycles 1a (h,i), 1b (j), and 1d (k,l).

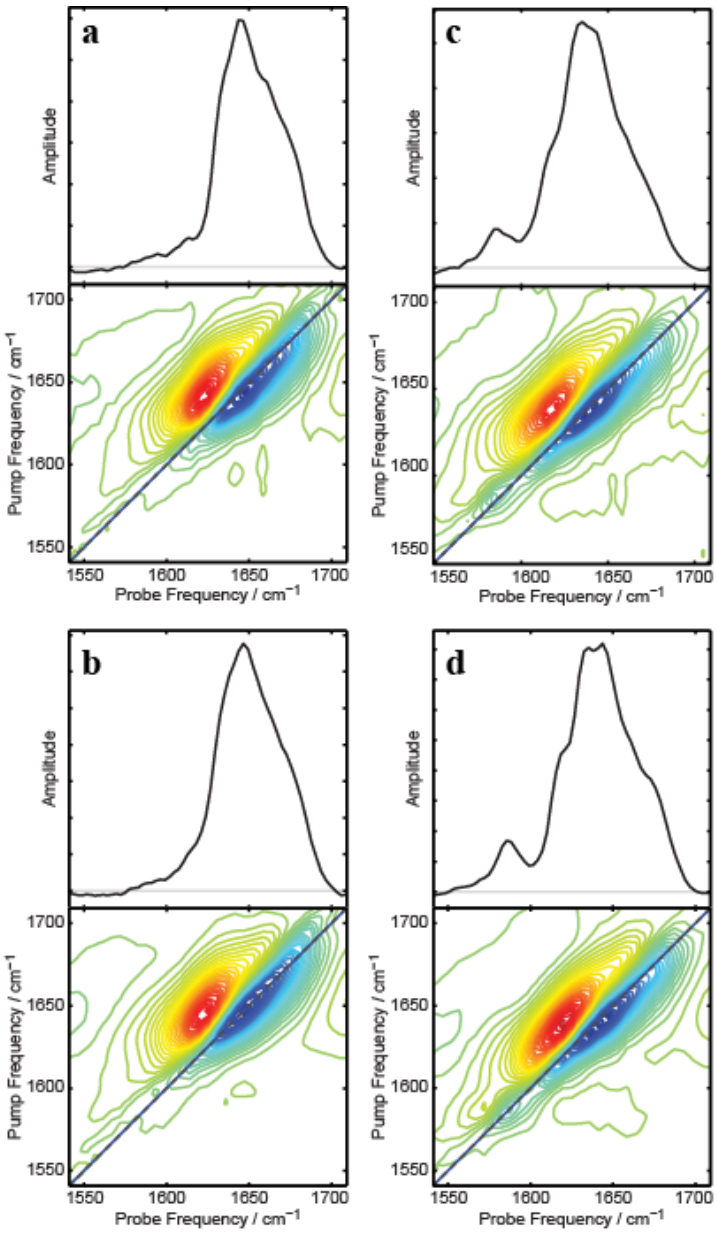

Figure A4.6 Lag phase spectra and diagonal slices of Val-17 and Ala-25 amylin mixed with macrocycle 1c. Spectra were collected after 15 min of aggregation for Val-17 (a,b) and Ala-25 (c,d) mixed with macrocycle 1c.

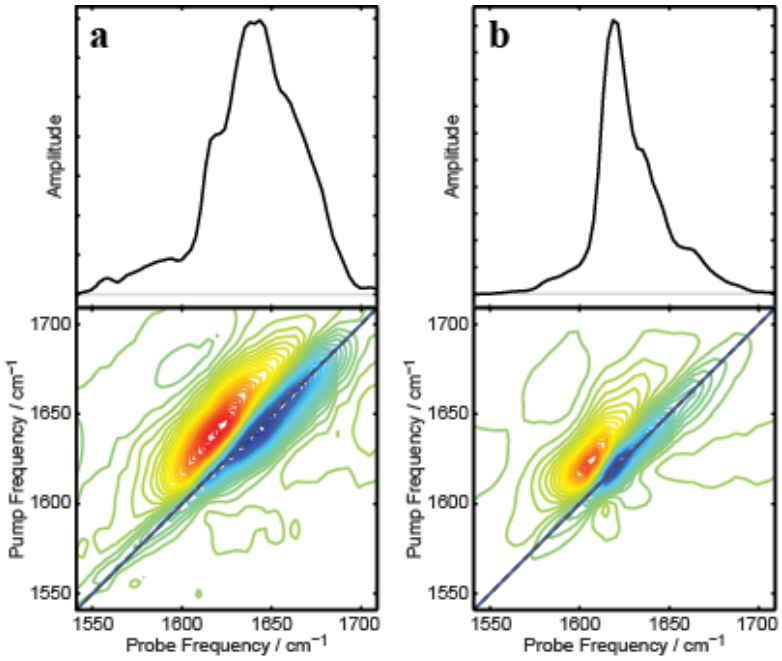

Figure A4.7 Spectra of dilute labeled Ala-25 amylin mixed with macrocycle 1c. Spectra were collected after 15 min (a) and 5 h (b).

Transmission electron microscopy (TEM) was performed at the University of Wisconsin Medical School Electron Microscope Facility. Samples were prepared as for spectroscopy experiments, although sample volumes were scaled up to 40 uL. A 2 uL aliquot was removed to monitor aggregation via 2D IR and 2 uL aliquots were flash frozen at various points during aggregation to allow correlation of 2D IR spectra with TEM images. Aliquots were thawed immediately before obtaining TEM images and stained using the negative stain Nano-W (methylamine tungstate) (Nanoprobes, inc) in a two-step staining procedure. The samples were placed on a pioloform coated 300 mesh thinbar Cu grid and viewed on a Philips CM120 electron microscope at 80 kV. Images were documented with an SIS (Olympus-Soft Imaging Systems) MegaView III digital camera. Multiple images were collected for each sample. Apparent widths of aggregates were measured using Adobe illustrator by drawing lines across the aggregates and calculating the length of the lines according to the resolution of each image. One hundred measurements were made for each sample and the results collected in histograms.

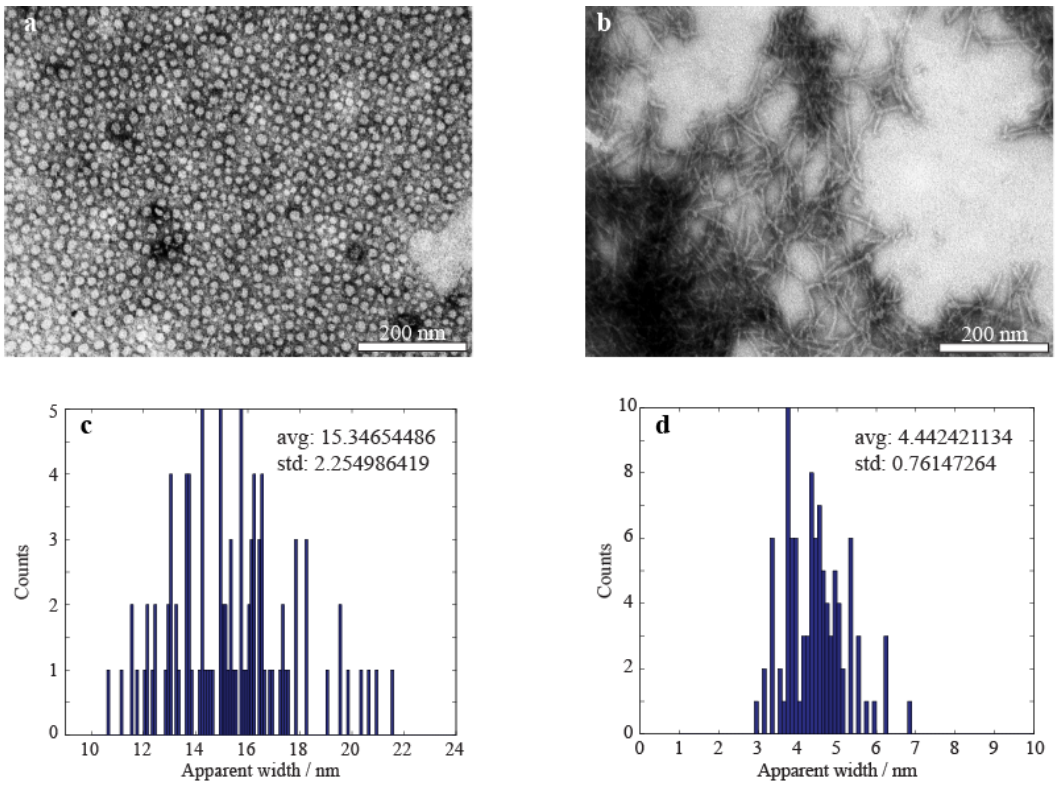

Figure A4.8 TEM and statistical analysis of Ala-25 amylin mixed with macrocycle 1c. (a) TEM of lag-phase aggregates. (b) TEM of fibrils. (c) Histogram of lag-phase aggregate diameters. (d) Histogram of fiber widths. The scale bars on the TEM images represent 200 nm.

APPENDIX 5

8. **Dunkelberger, Emily B.**, Grechko, Maxsim, Zanni, Martin T., "Infrared Spectroscopy Provides Extended Vibrational Modes that Reveal Secondary Structures of Amyloid Proteins", *in preparation*.

7. Buchanan, Lauren E., **Dunkelberger, Emily B.**, Cai, Wenting, Tran, Huong Q., Zanni, Martin T., "The Human Amylin Mutant Pramlintide forms N and C Terminal β-Sheets" *in preparation*.

6. Buchanan, Lauren, E., **Dunkelberger, Emily B.**, Tran, Huong Q., Cheng, Pin-Nan, Chiu, Chi-Cheng, Tu, Cynthia, Raleigh, Daniel P., dePablo, Juan J., Nowick, James S., Zanni, Martin T., "2D IR Spectroscopy Reveals a Non-Amyloid Intermediate in the Aggregation Pathway of Human Amylin" *in preparation*.

5. **Dunkelberger, Emily B.**, Woys, Ann M., Zanni, Martin T., "2D IR Cross Peaks Reveal Hydrogen-Deuterium Exchange with Single Residue Specificity", *accepted to JPC*.

4. Wang, Lu, Buchanan, Lauren E., **Dunkelberger, Emily B.**, dePablo, Juan J., Zanni, Martin T., Skinner, James L., in *Ultrafast Infrared Vibrational Spectroscopy*, "Ultrafast Infrared Spectroscopy of Amylin Solution and Fibrils", Fayer, M.D. Ed., Taylor & Francis, 2013.

3. **Dunkelberger, Emily B.**, Buchanan, Lauren E., Marek, Peter, Cao, Ping, Raleigh, Daniel P., Zanni, Martin T., "Deamidation Accelerates Amyloid Formation and Alters Amylin Fiber Structure", *J. Am. Chem. Soc.*, **2012**, *134* (30), 12658.
Featured in Chemical and Engineering News, online July 6, 2012

2. Middelton, Chris T., Buchanan, Lauren E., **Dunkelberger, Emily B.**, Zanni, Martin T., "Utilizing Lifetimes to Suppress Random Coil Features in 2D IR Spectra of Peptides", *J. Phys. Chem. Lett.*, **2011**, *2* (18), 2357.

1. Buchanan, Lauren E., **Dunkelberger, Emily, B.**, Zanni, Martin T., in *Protein Folding and Misfolding: Shining Light by Infrared Spectroscopy*, "Examining Amyloid Structure and Kinetics with 1D and 2D Infrared Spectroscopy and Isotope Labeling", Fabian, H., Naumann, D., Eds., Springer: Heidelberg, 2011, Vol 1, 217-237.